Exploring Charge Transport Properties of Copper-based Chalcogenides and their Carbon Composites for Dye Wastewater Treatment

A Thesis submitted to

Jadavpur University

by

Mainak Das

in partial fulfillment of the requirements for the degree of

Doctor of Philosophy (Ph.D.)

(Science)

Department of Physics

Jadavpur University

Kolkata, India

2025

যাদবপুর বিশ্ববিদ্যালয়
কলকাতা - ৭০০ ০৩২, ভারত

JADAVPUR UNIVERSITY
KOLKATA-700 032, INDIA

FACULTY OF SCIENCE : DEPARTMENT OF PHYSICS

CERTIFICATE FROM THE SUPERVISOR

This is to certify that the thesis entitled "**Exploring Charge Transport Properties of Copper-based Chalcogenides and their Carbon Composites for Dye Wastewater Treatment**" submitted by Sri **Mainak Das** who got his name registered on **11.11.2020** (Index No.: 56/20/Phys./27) for the award of Ph. D. (Science) degree of Jadavpur University, is absolutely based upon his own work under the supervision of **Prof. Partha Pratim Ray** and that neither this thesis nor any part of it has been submitted for either any degree/diploma or any other academic award anywhere before.

Partha Pratim Ray
(Prof. Partha Pratim Ray) 30/04/2025

Dr. Partha Pratim Ray
Professor
Department of Physics
Jadavpur University

This thesis is dedicated to my parents

for their endless love, support and encouragement.

ACKNOWLEDGEMENT

I thank everyone who have been closely attached to me during this period of pursuing the doctoral degree. It would not have been possible without the support, guidance, and encouragement of many individuals and institutions to whom I am deeply indebted. I am truly honoured and appreciative for the courageous support and guidance that shaped my academic journey.

Firstly, I utilise this opportunity to express my gratitude towards Prof. Partha Pratim Ray for providing me the chance to undergo the Ph.D. degree under his guidance. His guidance and skills have been invaluable throughout my Ph.D. path. The invaluable ideas, critical comments, and steadfast encouragement helped shape the direction of my research. I am extremely grateful for the time and effort he spent in offering constructive criticism, which considerably boosted the quality and rigour of this research work. I am blessed to have undergone the whole process in this ambience of Jadavpur University that provided me a thorough and apt research experience through the presence of required machinery and technology.

Thereafter, during my period here I have received useful anecdotes from faculty members which have proved to be lessons for life. I would like to express my deepest gratitude to Prof. Sanjay Kumar for his wisdom and insights, which have enhanced my learning experience. I have always valued our conversations, during which Prof. Sanjay Kumar kindly offered his knowledge and provided useful advices. Throughout my Ph.D. tenure, I had the opportunity to collaborate with renowned professionals such as Prof. Dirtha Sanyal (VECC, Kolkata), Prof. Raju Mondal (IACS, Kolkata), Dr. Saikat Kumar Seth (Jadavpur University, Kolkata), Prof. Shouvik Chattopadhyay (Jadavpur University, Kolkata), Prof. Mohammad Hedayetullah Mir (Aliah University, Kolkata), and Dr. Bhaskar Biswas (University of North Bengal). Working with these specialists was not only a rewarding experience, but also provided as means of obtaining essential information and expertise.

I acknowledge the help and support from Department of Physics, especially previous and current HODs, administrative personnel, and the research and Ph.D. sections. Their administrative support was helpful. I am grateful to Prof. Sukhen Das, Dr. Saikat Kumar Seth, Dr. Kaustav Das and Prof. Joydeep Chowdhury for their excellent recommendations and generous offer of lab facilities. Mr. Manojit Dey (DEO, Research Section) and Mr. Azizur Rahaman (Ph.D. Cell) deserve special thanks for their invaluable administrative help. Furthermore, it is necessary to acknowledge the financial assistance granted by UGC through the NET-JRF program, which has been critical in enabling my research efforts. I am appreciative for the possibilities and resources made possible by their generosity.

Sincere gratitude is offered to all of my lab mates, a supportive group that has been crucial in my academic journey. Dr. Arka Dey, Dr. Sayantan Sil, and Dr. Joydeep Datta deserve special mention for going above and beyond their jobs as lab seniors to provide crucial guidance and support during my Ph.D. tenure. I am also grateful for the knowledge and ideas provided by other elders, such as Dr. Animesh Layek, Dr. Joydeep Dhar, Dr. Mrinmay Das, Dr. Rajkumar Jana, and Dr. Nur Amin Hoque. Besides the research works, I've cherished engaging conversations with them and they have been very supportive in various matters.

I would like to express my gratitude to my lab partners, who have made significant contributions to my thesis. Together, the friendships formed in the lab and the productive scientific exchanges have improved my Ph.D. experience. Sometimes more than often, one feels

by oneself during this venture. Not so, when there are friends around. I thank Dr. Dhananjoy Das from the bottom of my heart for his support throughout and for being present in the thick and thin of times. It is needless to say, that the connections built here are to last lifetime. I would also want to express my appreciation to my other lab colleagues, Mr. Animesh Biswas, Dr. Pubali Das, Dr. Baishakhi Pal, Dr. Jitendra Saha, Mr. Ramjan Sk, Mr. Supravat Ghosh, and Mr. Srikanta Malik, for the bond and happy times that have characterised our collective group experience.

Despite the hectic schedule of a doctoral student, my stay at Jadavpur University has been anything but monotonous. Instead, because of my amazing friends, who have brought joy and vitality into my life, it has developed into an enthralling experience that is painted with a multitude of hues. The company of people like Dr. Tanmoy Chakraborty, Dr. Dhananjoy Mondal, Ms. Mousumi Pramanik, Ms. Dipanwita Das, Dr. Tousif Riaz, Dr. Saikat Shyamal, Dr. Soma Rani Das, has made my journey colourful and delightful, and I consider myself privileged to be surrounded by them. Note of thanks to the people who hold great impression just by their presence. I am fortunate to have the presence of one such personality, Ms. Moisilee Dutta. I am sincerely thankful to her for all the academic and philosophical pursuits. The tune of her Sarod playing brought a melody to the monotonous pace of Ph.D. life. There are many other juniors to whom I express my thanks for the various interactions and exchanges of words.

I would like to extend my sincere appreciation towards two of my close friends from college days, Mr. Anirban Sen and Ms. Mahasweta Bhattacharya, for having faith upon me even before I believed in myself. Your constant encouragement, thoughtful advice, and shared confidence played a pivotal role in my decision to pursue a Ph.D. It was through your motivation and support that I found the courage to take this leap. Thank you for being the spark that lit the path towards this academic journey. Anirban Sen, my former roommate, with whom I shared memories in Visva Bharati, Santiniketan. Our friendship endures despite the passage of over a decade, and we still encourage one another and share personal stories. Both of your companionship made this journey not only bearable but memorable. Thank you for your patience, understanding, and unwavering encouragement.

Last but most important, I take up this opportunity to acknowledge the countless measures taken up by my family to be in support of my work throughout this long period and always being there irrespective of the outcome. I am forever indebted towards my parents for standing beside me. Everything was made possible by my mother Mrs. Maya Das, whose relentless persistence led me to fulfill my passion in academics. I deeply acknowledge the pivotal role taken up by her in all my endeavours. I joyfully appreciate the supportive roles of my father Mr. Swapan Das and my sister Mrs. Lopita Das during this long venture. I am thankful to Mr. Sandip Das who stood beside as a brother whenever need arisen with words of hope.

As I reach the end of this long and rewarding journey, I find myself reflecting on all the people who have walked alongside me, lifted me up, and helped me to move forward- sometimes with advice, sometimes with some word of encouragement, and often with the simple gift of presence. This journey has been a transformative experience and I extend my sincere gratitude to all individuals and entities that have contributed, whether significantly or modestly, to this academic endeavour.

Mainak Das.

(Mainak Das)

Table of Contents

***Chapter 7*: Effect of enhanced carrier mobility of reduced graphene oxide-copper selenide (rGO-CuSe) nanocomposite towards efficient charge transfer in the visible light driven photodegradation of Methylene Blue dye**

List of Abbreviations

3-D	Three Dimensional
AC	Alternating Current
B. E.	Binding Energy
BET	Brunauer–Emmett–Teller
CB	Conduction Band
CNT	Carbon Nanotube
CVD	Chemical Vapour Deposition
DC	Direct Current
DI	Deionized
DMF	Dimethyl formamide
EDX	Energy Dispersive X-ray Spectroscopy
EIS	Electrochemical Impedance Spectroscopy
e-h$^+$	Electron-hole
FEG-TEM	Field Emission Gun Transmission Electron Microscopy
PVD	Physical Vapour Deposition
GO	Graphene oxide
HRTEM	High Resolution Transmission Electron Microscopy
HT	Hydrothermal
IPA	Isopropyl alcohol
I-V	Current-voltage
IR	Infrared
IS	Impedance Spectroscopy
ITO	Indium tin oxide
JCPDS	Joint Committee on Powder Diffraction Standards
kV	Kilovolt
LED	Light Emitting Diode
LUMO	Lowest Unoccupied Molecular Orbital
MB	Methylene Blue
MS	Metal-Semiconductor
NCs	Nanocomposites
NPs	Nanoparticles
OHT	One-pot hydrothermal
PL	Photoluminescence
R.T.	Room temperature
rGO	Reduced graphene oxide
RhB	Rhodamine B
RCS	Reduced graphene oxide copper selenide
SAED	Selected Area Electron Diffraction
SDs	Schottky Diodes
SMU	Source Measuring Unit
SCLC	Space Charge Limited Current
S.I.	Supplementary Information
ST	Solvothermal

T-CuS	Carbon nanotube-copper sulfide
TE	Thermionic Emission
TEM	Transmission Electron Microscopy
TGA	Thermogravimetric Analysis
UV	Ultraviolet
VB	Valence Band
wt.%	Weight Percent
XPS	X-ray Photoelectron Spectroscopy
XRD	X-ray Diffraction

***

Preface

In the 21st century, the discharge of dye-containing wastewater into aquatic environments, predominantly by the textile industry, has emerged as a significant environmental concern, resulting in various ecological issues. Advanced oxidation processes (AOPs), particularly photo-induced catalytic decomposition, have gained prominence as a cost-effective and environmentally sustainable method for wastewater treatment. While metal oxides and chalcogenides, such as titanium dioxide (TiO_2), copper oxide (CuO), copper sulfide (CuS), copper telluride (CuTe), and copper selenide (CuSe), have been utilized for photocatalytic dye degradation, their limitations—including low surface-to-volume ratios and short lifetimes of photo-generated electron-hole pairs—have necessitated the exploration of remedial techniques. An effective approach by two different carbon nanomaterials, identified in the literature include the synthesis of carbon nanotube-based composites of CuS and the graphene-based composite of CuSe. The present thesis compiles and organizes our research, which is based on carbon nanotubes (CNTs), reduced graphene oxide (rGO), copper sulfide (CuS), and copper selenide (CuSe), into eight chapters, each contributing to a deeper understanding of these effective methodologies.

Chapter 1 provides an overview about the nanomaterials and nanocomposites. A brief introduction of carbon nanotubes and its properties, the synthesis methods of graphene since its 2004 discovery. The unique characteristics of carbon nanomaterials, its versatile role in synthesizing inorganic nanocomposites, and its applications in wastewater management are discussed. A comprehensive review of copper nanomaterials-based semiconductors, focusing on CuS, CuSe, and their carbon (CNT, rGO) composites, is presented.

Chapter 2 introduces the theoretical overview of some characterization techniques, the theory of Schottky barrier formation and fabrication technique of Schottky diode with introductory insights into their electrical study. The theoretical background of impedance spectroscopy is briefly outlined.

Chapter 3 investigates the synthesis of copper sulfide (CuS) via two different methods. The structural, optical and electrical properties of the materials were analysed. Schottky barrier diode were fabricated and the charge transport properties were analysed via current-voltage measurement and impedance spectroscopy. The particle size and the crystallinity by different synthesis method enhances the device performance and charge transport. This highlights the charge transport of CuS-based photovoltaic devices and a better perception of the synthesis procedure-dependent conduction mechanism.

Chapter 4 is dedicated to the synthesis of copper sulfide (CuS) and its composite with carbon nanotubes (CNT-CuS). It explores the fabrication of Schottky barrier diodes utilizing both pristine CuS and CNT-CuS. A comprehensive analysis of charge transfer properties and an examination of metal-semiconductor interfaces through bias-dependent impedance spectroscopy yield valuable insights into the advancement of optoelectronic device applications.

Chapter 5 investigates the influence of enhanced carrier mobility in carbon nanotubes on the photodegradation of azo dyes. The current-voltage characteristics of CuS and CNT-CuS Schottky devices, along with an analysis of charge transport parameters, contribute to a nuanced understanding of the underlying mechanisms. Furthermore, this chapter extends to the simulated solar light-induced photocatalytic performance of both materials in the degradation of the azo dye Rhodamine B (RhB). A comprehensive analysis is presented to elucidate the role of carrier mobility in extending photo-induced charge separation, thereby promoting efficient charge transfer and enhancing the photodegradation process.

Chapter 6 presented the charge transport properties of reduced graphene oxide-copper selenide (rGO-CuSe) based Schottky diodes by tuning the rGO content over bare CuSe. The performance of the fabricated diodes was analysed with incorporation of different weight percentage of rGO. Space charge limited current theory was used to determine various charge transport properties like carrier mobility, transit time, and diffusion length to provide valuable insights in the development of electronic device applications.

Chapter 7 introduces the overall charge separation characteristics of hexagonal copper selenide (CuSe), with the objective of maximizing efficiency in the catalytic degradation of dyes. Additionally, it investigates the influence of enhanced carrier mobility provided by reduced graphene oxides (rGO) on the photo-degradation of Methylene Blue (MB) azo dyes. The research employs the spatial-charge-limited conduction (SCLC) theory to extract the mobility of each catalyst, thereby offering a nuanced exploration of how charge carrier mobility affects photocatalytic degradation efficiency. This analysis transcends traditional macroscopic parameters by emphasizing microscopic factors such as mobility and transit time, which are crucial for a comprehensive understanding of the photocatalytic process.

Chapter 8 encapsulates the entirety of the research, providing a succinct conclusion to the conducted study. This chapter also signifies a critical juncture as we consider future directions. Our focus shifts towards the shape-dependent copper chalcogenides and rare earth doped metal oxide synthesis to attain deeper insights into their electrical and charge transport characteristics. We have to fabricate Schottky diode to determine different charge transport parameters and investigate their role towards the photo decomposition of various azo and non azo dyes.

All the references cited in this thesis are given in the following format:

Journals: Authors, *Journal Name*, Year, **Volume,** Pages.

Example: G. Carullo, F. Galligano and F. Aiello, *MedChemComm*, 2017, **8**, 492-500.

Books: Authors, *Title*, Publisher, Publisher Location, Year.

Example: S T Beckett, *Science of Chocolate*, Royal Society of Chemistry, Cambridge, 2000.

30th April, 2025

Kolkata, India.

Mainak Das

(**Mainak Das**)

Introduction to copper-based nanomaterials with their carbon composites

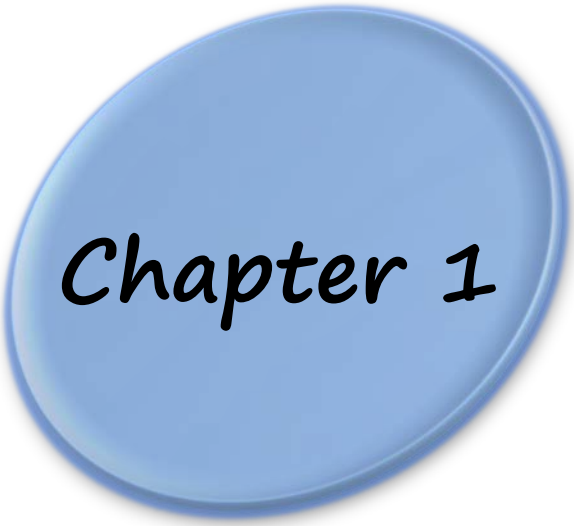

1.1. Nanomaterials and Nanocomposites

The history of nanomaterials can be traced back to the formation of nanostructures in early meteorites, a process that occurred following the Big Bang. Subsequently, natural processes led to the evolution of various other nanostructures, such as skeletal remains and seashells[1,2]. Additionally, nanoscaled smoke particles were generated during the use of fire by early humans. However, systematic scientific investigation of nanomaterials commenced much later. Michael Faraday's synthesis of colloidal gold particles in 1857 represents one of the earliest documented scientific contributions to the field[3]. For over 70 years, researchers have been exploring the properties and applications of nanostructured catalysts. By the early 1940s, precipitated and fumed silica nanoparticles were produced and marketed in the United States and Germany as alternatives to ultrafine carbon black for rubber reinforcement purposes[4,5].

Both industry and academia have demonstrated significant interest in nanomaterials over the past three decades[6,7]. The impetus for this interest stems from the need for solutions in practical applications, where existing methodologies are facing limitations. Advancements in characterization and processing techniques have facilitated scientists' assessment of theoretical research on nanomaterials, thereby providing more sophisticated tools for investigating and manipulating the nanoscale environment[8,9]. Generally, materials that possess at least one dimension within the nano meter range (1 nm = 10^{-9} m) are classified as nanomaterials[10]. This dimensional scale, which exists between the atomic and microscale, imparts new physical and chemical properties to materials. Such properties become particularly pronounced when the nanomaterial has at least one dimension ranging from 1 to 100 nm[11].

It has become widely acknowledged that the term "nanomaterial" pertains to a specific range of dimensions characterized by their nanoscale properties. Nanomaterials can be classified as either natural or engineered (synthesized) nanomaterials. Naturally occurring examples include volcanic ash and soot from forest fires[12–14]. Engineered nanomaterials can be further categorized based on their shape and composition. The structural characteristics of their constituent components, as well as the dimensionality that extends beyond the nanoscale, provide a useful framework for their classification. Nanomaterials are generally categorized into zero-dimensional (0-D) materials (such as

quantum dots and nanoparticles), one-dimensional (1-D) materials (including carbon nanotubes, nanorods, and nanowires), two-dimensional (2-D) materials (such as nanofilms), and three-dimensional (3-D) materials, which arise when 0-D, 1-D, and 2-D nanomaterials interact to form interfaces (such as powders, fibrous structures, multilayered systems, and polycrystalline materials)[15,16]. The diverse arrangements of nanomaterials can give rise to a wide spectrum of nanostructures, each characterized by distinct observable shapes and dimensions. For instance, a linear or planar arrangement of nanoparticles of a specific composition leads to the formation of one-dimensional or two-dimensional nanostructured materials, respectively[17]. Moreover, methodologies for the production of nanodevices can be informed by the assembly of ordered arrays of nanostructures[18]. Generally, the surface area of a nanomaterial exerts a more significant influence on its performance than its composition. Recent advancements in nanotechnology enable the development of nanomaterials that enhance the quality of life. Notable examples of engineered nanomaterials include carbon nanotubes (CNTs), carbon nanofibers (CNFs), graphene, fullerenes, silica, clay, as well as various metal and metal oxide nanomaterials.

Due to their exceptional properties, nanomaterials are frequently integrated with bulk polymeric materials to augment their characteristics. Nanocomposites are defined as the combination of two or more phases or components with distinct physical or chemical characteristics, wherein at least one component exists at the nanometer scale, resulting in properties that differ from those of the individual components. The enhanced properties of these nanocomposites, as compared to their respective micro composites, are primarily attributed to the size effects of the involved nanomaterials[19]. The specialized category of nanocomposites entails the dispersion of at least one discontinuous nanosized phase within a continuous medium, commonly referred to as the matrix. Nanocomposites can be classified based on the type of matrix material utilized, including polymer matrix composites, metal matrix composites, and ceramic matrix composites. In polymer matrix composites, the dispersion of nanofillers within the bulk polymer matrix is a critical consideration. Enhanced properties are associated with a homogeneous dispersion of nanoparticles. However, the weak van der Waals interactions among the nanomaterials lead to a propensity for particle agglomeration, which negatively impacts the material's properties. For example, a homogeneous dispersion of carbon nanotubes (CNTs), graphene, carbon nanofibers (CNFs), and clay

within the polymer matrix has been shown to improve mechanical, thermal, electrical, optical, gas barrier, and flame-retardant properties of the nanocomposites[20–22]. It is now well-established that the surface modification or functionalization of nanomaterials can significantly enhance their dispersion within a polymer matrix[23,24]. Recent studies have demonstrated that the incorporation of compatibilizers can also improve the dispersion of nanomaterials within the polymer matrix[21]. To develop high-performance lightweight composites for advanced applications, surface modification and functionalization of nanomaterials strengthen the interfacial interactions or compatibility between the filler and the matrix. This improvement in dispersion facilitates effective stress transfer between the matrix and the filler.

1.2. Advantages of Nanomaterials

A diverse array of fields, including electronics, sensors, energy devices, medicine, cosmetics, and catalysis, have significantly benefited from the unique optical, magnetic, electrical, and chemical properties exhibited by nanomaterials[25–27]. For instance, advancements in nanomaterials have facilitated the development of various electronic devices, such as organic light-emitting diodes (OLEDs), plasma displays, and nanotransistors. In the realm of energy, nanomaterials have been instrumental in the enhancement of solar cells, fuel cells, and high-performance portable batteries. Furthermore, the incorporation of nanomaterials into polymers has resulted in the production of materials that are both stronger and lighter, enabling the development of smart uniforms, nonwetting textiles, fire-retardant fabrics, self-cleaning and self-healing materials, as well as lightweight, high-performance military aircraft and automobiles[28]. The large surface area and high gas sensitivity of metallic-based nanomaterials render them particularly suitable for applications in gas sensors and hydrogen storage devices[29]. The utilization of nanopesticides, nanofertilizers, and nanoherbicides in agriculture presents potential advantages for crop management[30]. Moreover, the field of nanocatalysis is experiencing rapid expansion, with nanomaterials emerging as a favorable choice for catalysts due to their substantial surface area and exceptional surface activity.

1.3. Challenges and Opportunities

Although nanomaterials have a wide range of applications, numerous challenges remain to be addressed. There is considerable concern regarding the effects of nanoparticles on human and animal health. To alleviate safety concerns associated with nanoparticles, further investigation is necessary, as many questions regarding this domain remain unanswered. For instance, the inhalation of nanoparticles may cause lung irritation and elevate the risk of lung damage, potentially leading to cancer. The agglomeration of nanoparticles, driven by weak van der Waals forces, is particularly concerning. To preserve the distinctive properties of nanoparticles, technologies must be developed to maintain their separation.

The cost of nanomaterials and their associated products is significantly higher than that of conventional materials. It has been proposed that the cost of nanomaterials could be reduced by expanding their application across various new fields, thereby increasing their production rates. Furthermore, the potential development of atomic weapons, which could have catastrophic consequences, necessitates a thorough understanding of nanomaterials. Consequently, it is imperative that nanomaterials are utilized in a constructive manner.

The extensive use of nanoparticles in agriculture raises significant concerns, as their release into the environment may adversely affect animals, plant growth, and soil fertility. Prior to employing metallic-based nanoparticles in gas sensors and hydrogen storage applications, it is critical to control their structure and chemistry, which presents a substantial challenge. Moreover, issues pertaining to the need for new materials, performance enhancement, extended product lifespan, and pricing persist. Collectively, these factors underscore the necessity for the development of new and advanced technologies to enhance the performance of nanomaterials.

1.4. Promises of inorganic materials in Photo responsive-electronic devices and photocatalysis application

The influence of inorganic materials on civilization is extensive and multifaceted, particularly regarding their promising applications in photoelectronic systems. These materials are essential to the advancement of technologies that drive economic growth, enhance quality of life, and promote environmental sustainability due to their remarkable

electrical and optical properties. Inorganic semiconductor materials have ushered in a new era of innovation and progress in photoelectronic devices, offering unparalleled advantages across various technological domains and societal dimensions. Characterized by their exceptional optical and electrical properties, these materials serve as the foundation for the development of high-efficiency solar cells, light-emitting diodes (LEDs), photodetectors, laser diodes, and other devices[31–38]. These examples exemplify the unique attributes of inorganic materials, which extend their applicability across a broad spectrum of applications. Furthermore, these materials can be seamlessly integrated with contemporary technologies, such as Complementary Metal-Oxide-Semiconductor (CMOS) techniques, to enable the creation of hybrid devices that leverage the benefits of both inorganic and organic compounds[39–41]. In recent years, the incorporation of inorganic LEDs has played a significant role in enhancing the brightness and energy efficiency of consumer display technologies[42–45]. Inorganic quantum dots, for instance, are utilized to improve the brightness and color purity of displays, resulting in advancements in television and smartphone screens[46–48]. The exceptional efficacy, durability, tunable properties, and versatility of inorganic semiconductor materials render them critical to the progression of modern technology. Consequently, the promises offered by inorganic materials are numerous, encompassing energy production, economic development, environmental sustainability, and the overall well-being of humanity.

Solar energy is increasingly recognized as a viable alternative to fossil fuels, primarily due to its remarkable efficiency in directly converting sunlight into electricity. This transition contributes to the reduction of air pollution, the mitigation of climate change, and the decrease of greenhouse gas emissions, thereby enhancing both environmental and public health[49,50]. The pursuit of renewable energy materials represents a compelling objective for scientists and researchers. It is evident that the production of renewable energy constitutes one of the most significant societal impacts of inorganic materials. A critical element of the global shift toward sustainable energy is the utilization of solar cells, which are predominantly composed of silicon and other inorganic semiconductors[51–54].

Environmentally, these materials contribute to a circular economy by minimizing ecological footprints through non-toxic manufacturing processes and comprehensive recycling programs. Their durability decreases electronic waste. Continuous research and

development in this domain facilitate ongoing innovation, promoting sustainable progress and enhancing global quality of life on a daily basis. Undoubtedly, these advancements significantly improve performance and efficiency, which are essential for the progress of photoelectronic devices.

Technology enhances devices' capabilities to meet the evolving demands of society, particularly through chemical modifications of materials. A fundamental concept in the modification of inorganic materials is doping, which involves the introduction of controlled impurities into a material's crystal lattice to alter its electrical properties. For instance, doping silicon with phosphorus or boron results in n-type and p-type materials[55], respectively, thus optimizing the performance and efficiency of optoelectronic devices. Nanostructuring represents another critical modification technique, utilizing manipulation at the nanoscale to enhance specific characteristics and leverage quantum mechanical phenomena. The size and surface properties of nanomaterials, such as quantum dots and nanowires, confer unique optical and electrical attributes. Specifically, nanowires and nanotubes exhibit increased surface areas and enhanced charge transport channels, which improve light absorption and efficiency in photodetectors and solar cells. Conversely, quantum dots provide tunable emission wavelengths, making them ideal for high-definition displays and biomedical imaging applications. Surface passivation is also a vital modification method that mitigates charge carrier recombination by applying thin layers of oxides or nitrides to semiconductor surfaces. This technique enhances the stability and performance of inorganic materials in electronic devices; for example, the passivation of CuS with titanium dioxide (TiO_2) prolongs carrier lifetime[56] and boosts device efficiency by reducing the presence of recombination centers. Furthermore, inorganic components can be combined with other materials, such as polymers or ceramics, to create composite materials that exhibit synergistic properties unattainable by individual elements alone. These composites are employed in photonic devices to enhance durability, lower production costs, and expand application possibilities.

Another significant method for altering inorganic materials is alloying, a process that involves the combination of two or more elements to produce alloys with specific characteristics. For instance, $Cu(In,Ga)Se_2$ (CIGS) is synthesized by alloying copper indium selenide ($CuInSe_2$) with gallium (Ga). By varying the concentration of gallium, the

band gap can be modulated from approximately 1.0 eV ($CuInSe_2$) to 1.7 eV ($CuGaSe_2$)[57–59]. This tuning enhances the alignment with the solar spectrum, thereby increasing the efficiency of solar cells[60]. In applications where specific emission wavelengths are requisite, such adjustments are critical for optimizing the performance of light-emitting diodes (LEDs) and laser diodes. Furthermore, thin film techniques such as chemical vapor deposition (CVD) and molecular beam epitaxy (MBE) play a pivotal role in the modification of inorganic materials through the deposition of precise layers with regulated properties. These techniques facilitate the production of high-quality thin films, which are essential for developing advanced photovoltaic systems that utilize multi-junction solar cells with elevated conversion efficiencies. Additionally, it is imperative for photoelectronic devices to account for the sustainability of the inorganic nanomaterials employed in their fabrication to mitigate environmental impact, conserve resources, and ensure long-term viability—an aspect that is increasingly critical in the context of technological advancement.

One significant area of interest is the enhancement of mitigation strategies for global environmental pollution, particularly concerning air and water contamination. Over the past two to three decades, the photocatalytic degradation of environmental pollutants through the conversion of solar energy into chemical energy has garnered substantial attention. Heterogeneous photocatalysts offer numerous advantages over alternative photocatalytic materials, as they are often cost-effective, stable, non-toxic, and capable of functioning effectively under ambient temperature and pressure conditions[61]. The integration of photocatalysts with geopolymers has been explored within the construction industry to develop self-cleaning coatings for buildings, where key considerations include aesthetic appeal and the associated costs of maintenance[62].

In recent years, the rapid pace of industrial development and population growth has led to the depletion of traditional fossil fuels and an increase in CO_2 emissions, thereby precipitating dual challenges: the greenhouse effect and the energy crisis[63–65]. Addressing these issues necessitates the advancement of clean energy, which has emerged as one of the foremost challenges of the 21st century[66–69]. Among the various sources of clean energy, solar energy is particularly notable for its sustainability and long-term stable supply performance[70,71]. Photocatalysis, recognized as an accessible and environmentally benign energy conversion technique, has emerged as a significant area

of research[72]. A variety of photocatalysts have been developed to date[73–77]. A suitable photocatalyst must satisfy two primary criteria: (1) a broad light-excitation range coupled with high optical absorption capacity[78]and (2) efficient charge transfer and separation of photoelectrons and holes[79–81]. However, achieving these requirements simultaneously poses significant challenges for many conventional photocatalytic materials due to inherent limitations. Consequently, several methodologies have been developed to overcome the constraints associated with traditional photocatalysts, which can be classified into two categories: (1) modifying existing photocatalysts to broaden their light-excitation range and enhance visible-light absorption and (2) creating semiconductor heterojunctions. The synergistic effects at the interface of these heterojunctions can effectively facilitate the transfer and separation of photogenerated electron-hole pairs[82–87]. Inorganic photocatalysts possess high electron transport capabilities, favourable magnetic properties, and substantial mechanical strength. However, their wide bandgaps necessitate high photo-excitation energy, resulting in low sunlight utilization efficiency. Additionally, the photogenerated carriers excited by inorganic photocatalysts tend to recombine readily, thereby restricting the effective utilization of single inorganic photocatalysts within photocatalytic applications. Conversely, organic photocatalysts exhibit narrow bandgaps, requiring less photoexcitation energy while offering greater sunlight utilization efficiency. Furthermore, organic photocatalysts are generally more cost-effective and easier to synthesize. The band structures of organic photocatalysts can also be tailored through modifications of the functional groups within their molecular frameworks. However, these materials often demonstrate structural instability and limited electron transport efficiency. The combination of inorganic and organic photocatalysts to form inorganic-organic hybrid photocatalysts presents a promising solution[88]. In this context, we regard the integration of organic and inorganic components as the creation of inorganic-organic hybrid materials[89–92]. These hybrid materials exhibit characteristics derived from both inorganic and organic components, while the synergistic effects at their interface significantly influence their overall properties[93–95]. As a result, inorganic-organic hybrid materials are characterized by exceptional mechanical, thermal, optical, and catalytic properties. Schmidt *et* al.[96] first introduced the concept of inorganic-organic hybrid materials in 1984, which has since garnered significant interest from researchers. Various hybrid

materials incorporating different organic components in conjunction with inorganic materials have been synthesized employing various methodologies[97].

1.5. Copper (Cu)-based materials and chalcogenides

Crystalline silicon is a cost-effective semiconductor material in the electronic industry. In the pursuit of low-cost alternatives, various thin-film compound semiconductor materials are frequently employed, offering distinct advantages over silicon. In recent years, the application of copper-based nanoparticles has generated considerable interest within the semiconductor industry. Metal chalcogenides represent a distinct class of inorganic chemical compounds, characterized by the presence of at least one chalcogen anion and at least one additional electropositive metal element. While all elements within Group VIA of the periodic table are classified as chalcogens, the designation "metal chalcogenide" is predominantly applied to sulfides, selenides, and tellurides, instead of oxides and compounds containing polonium. A metal chalcogenide is a class of semiconductor materials that has garnered significant scholarly attention due to its diverse properties, which encompass optical, electrical, chemical, thermal, and mechanical characteristics. These materials are notable for their low and tunable band gaps, as well as their optical configurations, which facilitate enhanced conversion efficiency. Copper chalcogenide bonds exhibit a strong covalent character, despite the fact that the chalcogenides are often regarded as divalent anions (S^{2-}, Se^{2-}, or Te^{2-}) in certain contexts. Within a fundamental lattice cell, the chalcogen atoms form the framework of a regular lattice, while the copper atoms display a degree of disorder, exhibiting liquid-like behavior as they occupy random positions within the chalcogen lattice[98]. These materials have garnered significant interest due to their diverse applications in semiconductors, photoconductors, thermoelectric materials, and solar cells. The binary copper sulfide system encompasses several crystal phases, including monoclinic ($Cu_{31}S_{16}$ and $Cu_{1.94-1.97}S$), cubic (Cu_9S_5 and $Cu_{1.8}S$), orthorhombic (Cu_7S_4 and $Cu_{1.75}S$), triclinic ($Cu_{58}S_{32}$ and $Cu_{1.81}S$), and hexagonal (CuS) structures. In contrast, the binary copper selenide system comprises cubic (Cu_2Se and $Cu_{1.8}Se$), tetragonal (Cu_3Se_2), hexagonal (CuSe and $Cu_{0.87}Se$), and orthorhombic (Cu_5Se_4 and $CuSe_2$) phases. Furthermore, the known crystal phases of copper tellurides include hexagonal (Cu_2Te), tetragonal (Cu_7Te_4, Cu_4Te_3, and Cu_3Te_2), orthorhombic (CuTe), and pyrite-type ($CuTe_2$) structures[99,100]. Binary chalcogenides, such as CuS and CuSe, are considered promising candidates for photovoltaic and

optoelectronic devices due to their non-toxicity, abundance in the Earth's crust, and the tunability of the copper to chalcogen ratio[101,102].

1.5.1. Copper Sulfide (CuS)

Copper sulfide nanoparticles (NPs) attract increasing attention due to unique chemical, optical and electronic properties. CuS has hexagonal crystalline structure[103] with lattice constants of $a = b = 3.792$ Å and $c = 16.344$ Å. There exist several stable phases of the compound, including CuS (covellite), Cu_2S (chalcocite), $Cu_{1.75}S$ (anilite), $Cu_{1.96}S$ (djurleite), and $Cu_{1.8S}S$ (digenite). The bandgap energy of Cu_xS compounds is observed to vary between 1.2 and 2.5 eV depending on upon the specific composition (x)[104,105]. Efforts to synthesize copper sulfide have been undertaken utilizing various methodologies, including chemical synthesis, hydrothermal processes, thermolysis, solvothermal methods, physical vapor deposition, and template-assisted growth etc. CuS has been synthesized in various structural forms, including bulk crystals, thin films, nanofibers, quantum dots, nano-flakes, and nanoparticles. They have gained significant attention in nanotechnology due to their tunable bandgap, high conductivity, and strong light absorption. Currently, $Cu_{2-x}S$ is being investigated for a wide range of applications, including biosensors, solar cells, optoelectronics, photocatalysis, and is utilized as a cathode material in lithium rechargeable batteries.[106]

1.5.2. Copper Selenide (CuSe)

Copper selenide is a significant compound within the category of first-row transition metal chalcogenides and exhibits a range of compositions, including both stoichiometric and non-stoichiometric forms. It is found in various crystalline structures, including cubic Cu_2Se (bellidoite), orthorhombic Cu_2Se, monoclinic Cu_2Se, tetragonal Cu_3Se_2 (umangite), face-centered cubic $Cu_{2-x}Se$ (berzelianite), hexagonal CuSe, $Cu_{0.87}Se$ (klockmannite), orthorhombic Cu_5Se_4 (athabascaite), and $CuSe_2$[107,108]. Copper selenides exhibit a variety of crystallographic phases, including monoclinic, cubic, tetragonal, and hexagonal structures. Copper selenides are widely recognized as semiconductors exhibiting both direct and indirect band gap. Notably, the value of their band gap (E_g) is influenced by variations in their stoichiometries or phases ranging from 1.1 eV to 2.7 eV[109,110]. The composition of copper selenide (CuSe), along with the arrangement of atoms within its crystalline structure, significantly influences its electronic, chemical, and thermal

properties. Variations in size regimes and morphologies are employed to modulate these properties. To attain the desired characteristics through morphological and structural modifications, various synthetic methods have been adopted. The routes for synthesis include chemical bath deposition (CBD), electrodeposition (ED), microwave synthesis, the sol-gel method, dip coating, sputtering, spin coating, the colloidal method, solid-state reaction, hydrothermal synthesis, and vapor-based methods. Researchers have dedicated considerable effort to the development of hierarchically designed copper selenide nanostructures for a variety of photoelectric applications. Copper selenide (CuSe) is a significant chalcogenide material that exhibits a diverse array of applications in thermoelectric and photovoltaic-based energy harvesting[111,112]. Additionally, it plays a crucial role in the photocatalytic degradation of dyes for water purification, fabrication of electrodes for batteries[113], and in photo-ablation therapy[114].

1.6. Cabon-based Nanomaterials/ Allotropes

Carbon is a unique and indispensable element in our ecosystem. Carbon, in its various forms and singular entity, has been utilized in technology and human life for several centuries. Over the past two and a half decades, conjugated carbon nanomaterials, particularly carbon nanotubes, fullerenes, activated carbon, and graphite, have emerged as significant energy materials due to their unique properties. Owing to their exceptional chemical, mechanical, electrical, and thermal characteristics, carbon nanostructures have recently been applied across a wide range of fields, including drug delivery, electronics, composite materials, sensors, field emission devices, and energy storage and conversion. Carbon science has garnered significant attention in contemporary research, particularly within the domains of nanoscience, materials science, engineering, and technology. In these fields, carbon nanostructures are recognized for their diverse low-dimensional allotropes of carbon, which include graphite, activated carbon, carbon nanotubes, the C60 family of buckyballs, polyaromatic molecules[115], and graphene[116,117]. Chemically speaking, various allotropes of carbon can be formed due to the valence characteristics of carbon atoms. This phenomenon occurs when carbon atoms establish covalent bonds with one another[118]. To elucidate this phenomenon the concept of allotropes is utilised which are defined as elements that are chemically identical yet display significant variations in their physical properties. Consequently, when atoms in a substance consisting solely of one type of atom are organized differently, an allotrope is formed. As

a result, several allotropes and forms of carbon have been identified (Fig. 1.1), including graphene, buckminsterfullerene, and carbon nanotubes. This diversity results in carbon possessing the highest number of identified allotropes compared to any other element.

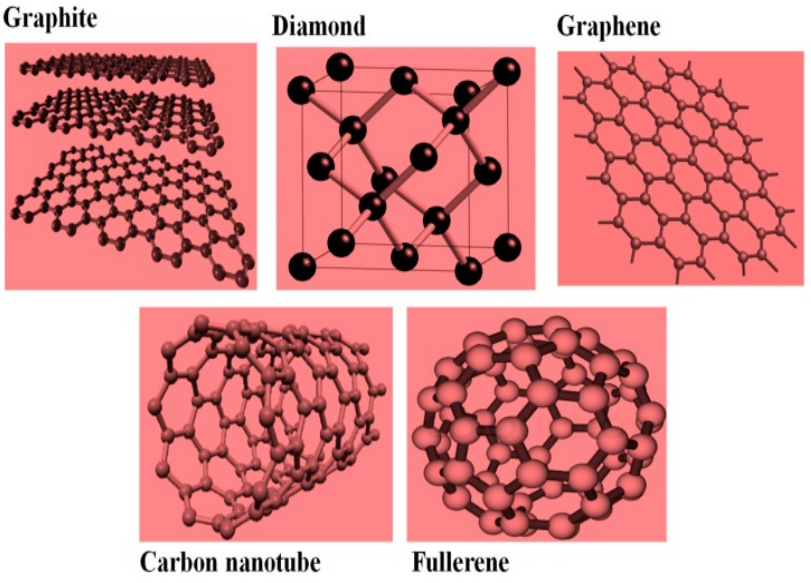

Fig. 1.1: Structural illustration of some 0-, 1-, 2- and 3-dimensional carbon nanomaterials with sp^2 and sp^3 hybridization allotropes occurring in different crystallographic forms. (Ref. [119])

1.6.1. Brief description of Carbon nanotubes (CNTs)

Carbon nanotube is one of the most important nano-allotropes of carbon. Carbon nanotube is an one-dimensional tube or cylindrical nanocarbon. It is simply a rolled graphene nanosheet with sp^2-bonded carbon atoms. Depending upon the numbers of rolled overlapping cylinders, carbon nanotube can be named as single-walled carbon nanotube (SWCNT), double-walled carbon nanotube (DWCNT), and multiwalled nanotube (MWCNT). These are tubular carbon molecules with excellent mechanical, chemical, electrical, and thermal properties. Carbon nanotubes are considered as excellent nano-reinforcing materials for polymer matrix due to their 1D cylindrical geometry (nano-meter size diameter, high aspect ratio, and high specific surface area) and remarkable mechanical properties. Their outstanding properties such as excellent mechanical strength, electrical conductivity, and thermal properties resulted in a great deal of attention for the preparation of composites.

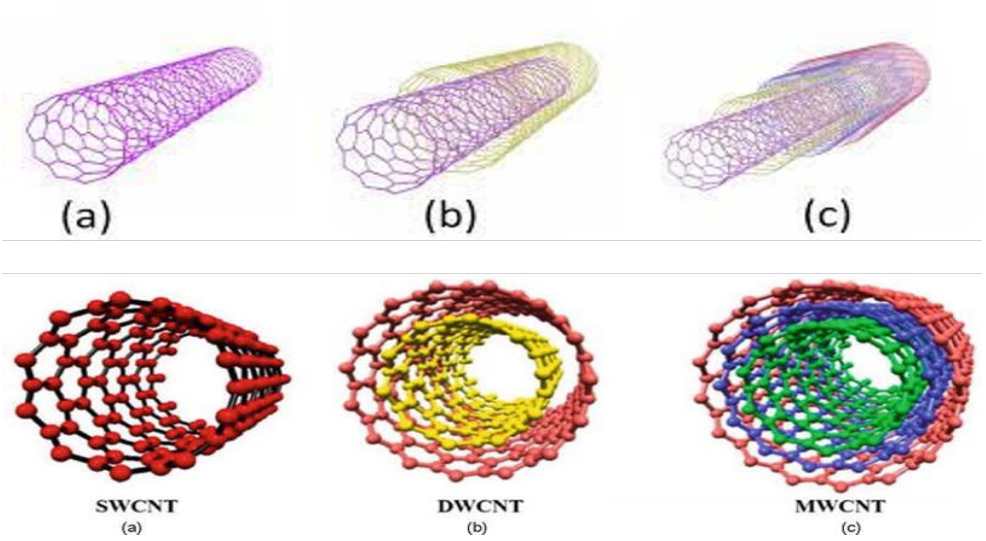

Fig. 1.2: Surface and internal view of (**a**) single-walled CNTs, (**b**) double-walled CNTs, and (**c**) multi-walled CNTs. (Ref. [120])

From the structural point of view, carbon nanotubes are categorized into two groups: single-walled carbon nanotubes (SWCNTs) and multi-walled carbon nanotubes (MWCNTs). The result of weak van der Waals forces comes from carbon nanotubes tends to accumulate and prevent well dispersion in the matrix. Carbon nanotubes have excellent surface properties like enormous surface area, high aspect ratio, and marvellous electrical and mechanical properties.

CNTs have many applications in wastewater treatment systems and have been widely utilized as adsorbents for many water pollutants[121]. This applicability is due to their excellent electronic properties, mechanical properties, high chemical stability and high thermal stability. They also have high specific adsorption surface area, layered structure, and hollowness, and thereby make the perfect adsorbent with adjustable surface chemistry and are easy to reuse. CNTs were also used in nanofiltration membranes and in nano sensors.

1.6.2. Introduction of reduced graphene oxides (rGO)

Typically, a novel material with exceptional qualities appears every few times, capturing the interest of the international scientific community. The discovery of graphene, a remarkable substance, in 2004 caused a great deal of enthusiasm among researchers[122–124]. Graphene's adventure began in 2004 when it was isolated via the 'Scotch Tape' method, which was created by Geim and Novoselov[125]. Subsequently, studies highlighting

its distinct mechanical, electrical, and physical characteristics—ascribed to the long-range π-conjugation—have led to an exponential rise in study on this material[126–128]. The basic building block of all graphitic carbon forms is graphene, which is defined as a two-dimensional honeycomb lattice made of sp^2-hybridized carbon (C) atoms[129]. Bilayer and few-layer graphene formations are also of great interest, despite the fact that they are usually thought of as single-layer sheets. Graphene sheets may be rolled and coiled to create zero-dimensional fullerenes and one-dimensional nanotubes, respectively, or stacked to create three-dimensional graphitic structures (Fig. 1.3). Research on graphene over the last ten years has indicated a wide range of possible uses, such as improved battery longevity[130], Schottky diodes[131], solar cells[132], corrosion prevention strategies[133], circuit boards[134], display panels[135], and various developments in medical technologies[136].

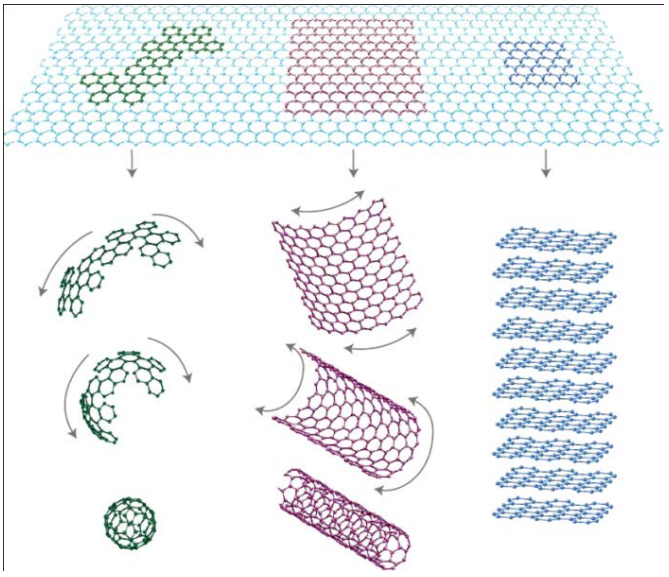

Fig. 1.3: Graphene: the parent of all graphitic forms: fullerene (bottom left); carbon nanotubes (CNT) (bottom centre); and graphite (bottom right). (Ref. [128])

The integration of graphene into the current framework of semiconductor device technologies is greatly facilitated by its natural compatibility with thin film processing. In addition to creating rectifying junctions with a number of semiconductor materials, graphene is easily scaled and exhibits low contact resistance when interacting with widely used metals. The creation of graphene-inorganic semiconductor nanocomposite materials has garnered a lot of scholarly interest because of these attractive characteristics[137]. Applications for optoelectronic and electrochemical devices, as well as the study of processes at the micro and nanoscale, depend heavily on inorganic semiconductors. They are crucial for clarifying the connection between the size and

dimensionality of particles and the functional characteristics of the device. Because of their high aspect ratio, great mechanical stability, and low work function, inorganic semiconductors' intrinsic nanostructure makes them ideally suited for a variety of electrical system applications[138]. Achieving widespread integration of nano-electronic devices is the main driving force behind the integration of graphene with inorganic semiconductors[139]. Charge transfer in composite systems may be improved by adding graphene to inorganic semiconductors, which is a very beneficial property for electronic devices. The production of graphene and its inorganic semiconducting nanocomposites will be investigated in this thesis, along with thorough characterisations. The main emphasis will be on using the synthesised graphene-based nanocomposites in Schottky diode applications and for the photocatalysis of azo dyes.

1.7. Discovery and Historical Overview of Graphene

Recognising graphene as the smallest layer limit of graphite is essential to know the direction of graphene research. Reports showing increasingly fewer graphite layers have been published for a number of years prior to the notable developments in this area. In 2004, Geim and his colleagues at the University of Manchester made a significant contribution by elevating graphene to a prominent position. They used the well-known 'Scotch Tape technique' (Fig. 1.4) to successfully separate single-layer samples from graphite throughout this crucial year[140].

The naturally occurring material graphite, which has been around for around 500 years, became very important in the Middle Ages because of the modest dispersion forces between its sheets and its layered structure, which made it perfect for making writing instruments. It has been used in a variety of applications, including industrial blast furnaces and electrodes, because to its unique qualities, which include high thermal conductivity (about 3000 W/mK) and in-plane electrical conductivity (approximately 104 $\Omega^{-1}cm^{-1}$)[141]. Over a million tonnes of graphite are presently needed annually worldwide.

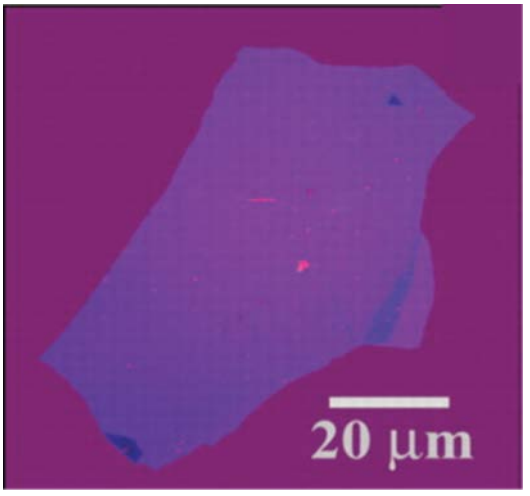

Fig. 1.4: The single (mono)-layer graphene, first discovered by Geim and his colleagues at Manchester University. The image displays a few-layer graphene flakes, with enhanced optical contrast achieved through an interference effect at a meticulously selected oxide thickness. (Ref.[125])

1.8. Synthesis of Graphene

Several methods have been used to synthesise graphene. A number of approaches have been used in the long-standing goal of creating ultra-thin carbon films. Graphite oxide was synthesised by Brodie[142] and Staudenmaier[143] in the late 1850s and 1898, respectively. There has been widespread usage of the well-known Hummers process, which was created by W.S. Hummers in 1958 as a stand-alone synthesis of graphite oxide[144]. In 1962, chemically reduced graphene oxides were reported to be produced[145]. The effective production of monolayer graphene using silicon carbide by A.J. Van Bommel et al. in 1975 marked a significant advancement[146]. These early studies, however, were unable to clarify the unique characteristics of graphene[122].

Research has also been done on the mechanical exfoliation of multilayer materials to create thin samples. Ruoff's team carved tiny pillars into highly ordered pyrolytic graphite (HOPG) in 1999 using an atomic force microscope (AFM) tip[147]. The thinnest slab they managed to produce, however, was more than 200 nm, or around 600 layers. By moving the pillars to a tipless cantilever and imprinting the slabs onto SiO_2, Kim et al. enhanced this technique. This development made it possible to produce slabs as thin as 10 nm, or around 30 layers[148].

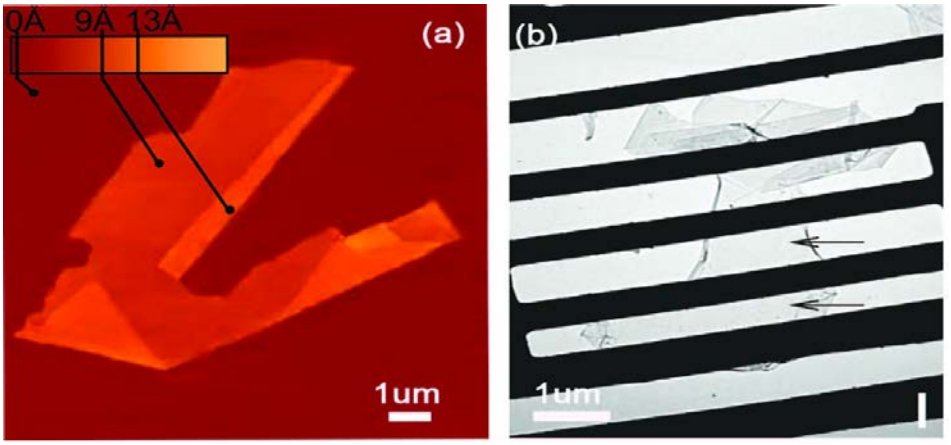

Fig. 1.5: The inception of single-layer graphene through mechanical exfoliation. (a) Atomic force microscopy displaying the substrate graphene step-height (<1 nm) and a folded step-height (0.4 nm) (Ref. [140]) (b) Transmission electron microscopy (TEM), capturing a free-standing graphene film with etched underlying substrate (Ref. [149]).

Enoki's Tokyo group transformed nano-diamonds into nanometer-sized graphene on HOPG in 2001 by using high temperatures (~ 1600 °C)[150]. A new era in graphene research began in 2004 when Geim, Novoselov, and colleagues developed a much easier method, despite the fact that this method proved helpful for creating thin samples. They created the 'Scotch-Tape technique,' which helped isolate single-layer graphene for the first time (Fig. 1.5). Geim and Novoselov's groundbreaking contributions to the field of two-dimensional atomic physics earned them the 2010 Nobel Prize in Physics[149].

1.8.1. Mechanical Exfoliation or Cleavage Method

Commercially accessible sheets of Highly Orientated Pyrolytic Graphite (HOPG) are used as the first raw material in the process. Using standard cellulose tape, layers of a graphite flake are repeatedly cut off before the tape is applied to a silicon substrate for material deposition. Nevertheless, a single layer is thinner than the layers sticking to the tape. Given that mechanical exfoliation might result in a complex combination of thick slabs that makes single layer identification challenging, the successful isolation of a single-layer graphene sheet by mechanical cleavage is simply an accident. The excellent mechanical and electrical characteristics of the graphene generated by mechanical exfoliation are maintained due to the high quality of the initial single-crystal graphite source[151]. Graphene's numerous applications require large-scale synthesis, which this approach is not the ideal for.

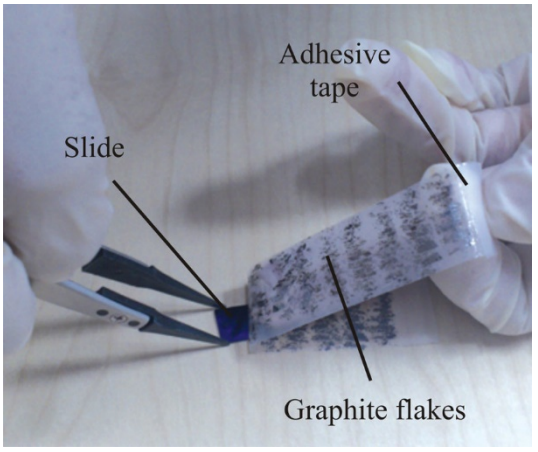

Fig. 1.6: 'Scotch tape' method. (Ref. [152])

Alternative large-scale synthesis processes have been proposed, including ion implantation[153], chemical-vapor deposition (CVD)[154,155], liquid-phase exfoliation[156,157], and epitaxial growth on a silicon carbide substrate[158]. Lee et al. found that graphene created using CVD techniques has 90% of the theoretical strength of pure graphene[159]. However, these approaches are less commonly used than the alternative methods of exfoliating graphite oxide and then decreasing it. Currently, one of the most widely used methods for large-scale graphene synthesis is the 'Hummers' method and its several variants[144]. In this thesis, the modified Hummers method was used to synthesise graphene, or, more specifically, reduced graphene oxide (rGO), which is discussed separately in the following section.

1.8.2. Chemical Vapour Deposition (CVD)

Few-layer graphene sheets were successfully synthesised for the first time in 2006 using Chemical Vapour Deposition (CVD)[160]. Graphene films were created by pyrolysing camphor, a natural hydrocarbon source, on Ni substrates. However, the films tended to fold, with a minimum layer count of 20. Recent advancements have confirmed that graphene creation via CVD is reproducible. According to a number of studies, CVD is the most promising method for producing graphene on a big scale. Notably, the introduction of certain gases, such NH_3, makes graphene doping possible during CVD development[161]. Additionally, lowering the growth temperature is made possible by the use of plasma in CVD techniques. In these circumstances, the direction of the electric field is influenced by the plasma sheath, which causes graphene to grow vertically onto the substrate. Plasma-enhanced CVD (PECVD) is a novel method for producing huge amounts of freestanding few-layer graphene.

1.8.3. Chemical Derivation

A technique for producing graphite oxide was first presented by Hummers and Offeman in 1958. It involved treating graphite for two hours at temperatures lower than 45 °C with an anhydrous combination of H_2SO_4, $NaNO_3$, and $KMnO_4$. Graphitic sheets are intercalated as a result of this process, and they can break down into few-layer or even single-layer graphene when heated. The breaking of graphite oxide into separate layers is further facilitated by subsequent ultrasonic treatment. The phenol, carbonyl, and epoxy groups that are added during oxidative intercalation improve the graphite oxide suspension's colloidal stability[151]. Nevertheless, graphene produced using this chemical process has different electrical characteristics than graphene produced by mechanical exfoliation. The electrical structure of graphene oxide (GO) produced by the chemical process appears to be semiconductive because of structural flaws, but mechanically exfoliated graphene layers show semi metallic characteristics. To restore the relevant characteristics of graphene, GO must be chemically reduced, usually with sodium borohydrate ($NaBH_4$)[162] or hydrazine (N_2H_4)[163]. The reduced substance is known as reduced graphene oxide (rGO), and when it dissolves in water, its brown hue changes to black. Total removal of oxygen atoms, and hence total chemical reduction, is not possible even if it becomes less hydrophilic following reduction. As a result, the final product continues to be in a state between graphene and graphene oxide. According to X-ray photoelectron spectroscopy (XPS), the precise structures of graphene are not entirely restored by thermal annealing (up to 1100 °C) or chemically reducing GO with hydrazine [Fig. 1.7 (a-d)]. However, residual hydroxyl functional groups are present after reduction by $NaBH_4$ [Fig. 1.7 (e-j)]. Chemical derivation is not regarded as a practical synthesis method when the original graphene structure is important; instead, physical exfoliation ought to be used. Nevertheless, rGO synthesis produces a state in between graphene and graphene oxide (GO), despite its intrinsic simplicity and suitable characteristics. rGO thin films are a potential element for upcoming applications as a transparent conductor due to its conductivity and transparency[164]. Despite being straightforward and not requiring complex synthesis conditions, chemical exfoliation has drawbacks. The handling of graphene sheets or amorphous graphene flakes as a matrix for inorganic semiconductors is made easier by the fact that rGO produces high end product yields and may be kept in a water-based solution or as a powder after drying. For the production of reduced graphene oxide in the current thesis, chemical derivation has been selected.

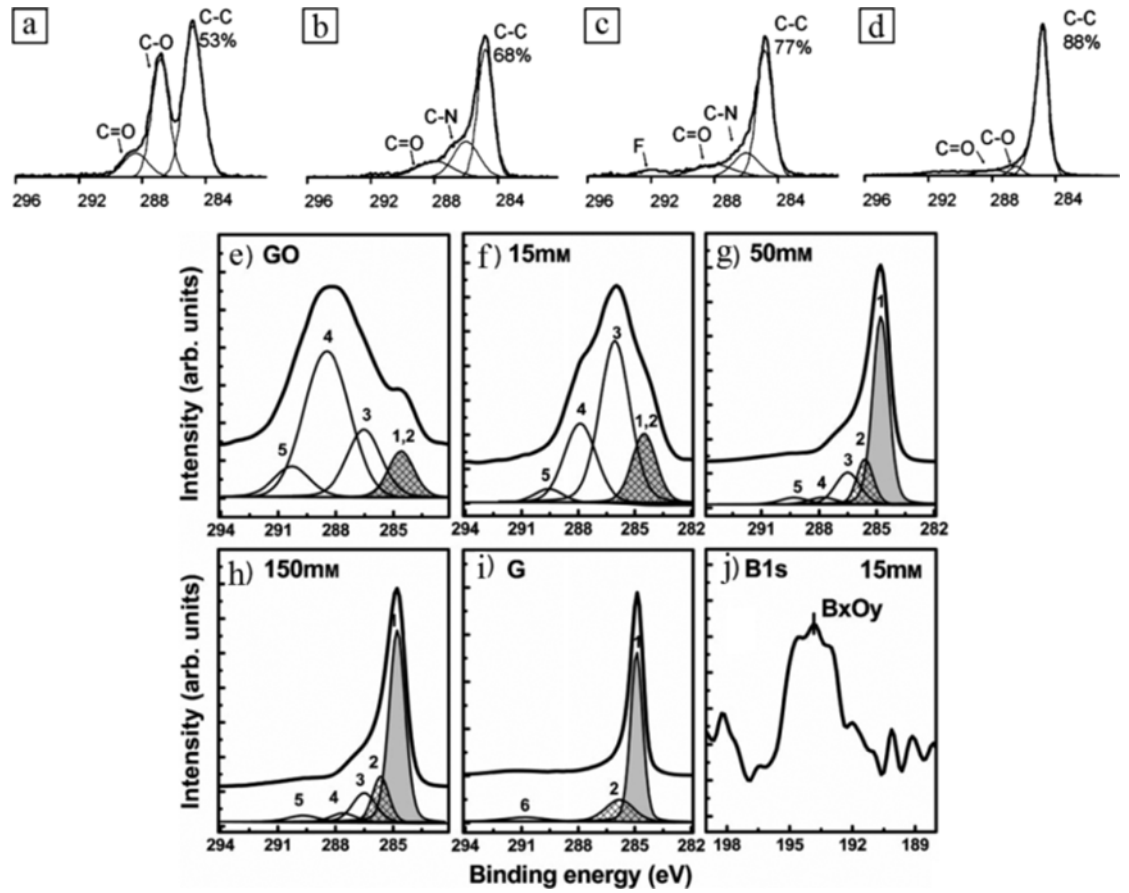

Fig. 1.7: X-ray photoelectron spectroscopy (XPS) reveals the impact of various reduction treatments on graphene oxide (GO). Images a–d show deconvoluted results indicating the presence of C–C, C–N, C–O and C=O species; approximately at B.E. of 284.8, 285.7, 286.2 and 287.8 eV respectively, with the percentage of deoxidized carbon (C–C, ~284.5 eV). (a) Non-reduced. (b) Hydrazine-Vapour-treated. (c) Hydrazine Vapour and annealed at 400 °C. (d) Thermal annealing in a vacuum (1100 °C). The C–N signal observed in images b and c indicates the formation of hydrazone groups resulting from hydrazine treatment. The presence of an F signal at around 292 eV in image (c), is attributed to contamination from the vacuum system. (e) C 1s peak of graphene oxide. (f–i) Reduced graphene oxide (rGO) was synthesized using sodium borohydride ($NaBH_4$) concentrations of (f) 15 mM (g) 50 mM and (h) 150 mM and (i) graphite. The curves were fitted considering C=C (peak-1), C–C (peak-2), C–O/C–O–C (hydroxyl and epoxy groups, peak-3), C=O (carbonyl groups, peak-4), O–C=O (carboxyl groups, peak-5) and π–π* (peak-6) species. (j) B 1s peak in the XPS spectra of rGO originated from 15 mM $NaBH_4$. (Images a–d and e-j from Ref. [165] and [162] respectively).

1.8.4. Alternative Methods

Using ultrasonication to treat graphite dispersions in an appropriate liquid solution is an alternate technique for producing graphene sheets by accomplishing physical exfoliation. By dispersing graphite into N-methyl pyrrolidone (NMP), Hernandez et al. were the first to report the exfoliation of graphene sheets[166]. Furthermore, a suspension of thin graphitic platelets made up of single-layer graphene flakes may be produced by

dispersing natural graphite crystals in dimethylformamide (DMF) and then sonicating them to exfoliate them[167]. A well-dispersed combination of graphene and a few-layer graphite remains in the residual solution when centrifugation is used to remove huge, thick graphene flakes, even if there are plenty of them in the suspension.

The graphene produced using this process has characteristics in common with those obtained using chemical processes. However, by skipping the oxidation stage in the liquid-phase exfoliation process, the product is protected against restrictions or deterioration of its electrical characteristics caused by defects. Graphene suspensions must be deposited onto a solid substrate with the aid of heat treatment in order to produce dry graphene using this method. Another option is liquid-phase exfoliation in water, which calls for the addition of strong surfactants such as sodium dodecylbenzene sulfonate (SDBS). In order to stabilise the dispersion and stop aggregation, these surfactants can be adsorbed onto individual single-layer graphene sheets. The solvent's expense and the propensity for individual sheets to overlap are disadvantages, though.

The thermal expansion of graphite oxide is another technique for creating functionalised graphene sheets[137]. Starting with the treatment of natural graphite flakes in an oxidising solution of H_2SO_4, HNO_3, and $KClO_3$, this procedure is comparable to the Hummers technique. Following the completion of the reaction, the resultant material is combined with extra water, rinsed with HCl, and then rinsed many times with water until the filtrate's pH approaches neutral. This process requires that the graphite be fully oxidised and heated to an extremely high temperature in order to produce single-layer graphene. By releasing CO_2, the heating process breaks down graphite oxide into separate sheets.

1.9. Properties of Graphene

Numerous studies have been carried out to investigate the special physical characteristics of graphene since the beginning of the graphene revolution. Early research indicated that graphene has a very high carrier mobility in the 2000–5000 cm^2/Vs range[168]. Recent developments have shown that suspended graphene solutions can have charge carrier mobility of up to 230,000 cm^2/Vs under ideal circumstances[151,169]. For uses like field-effect transistors (FETs), graphene's exceptional electron-transport capacity places it in a prominent position. By 2010, graphene FETs were reported to be able to operate at 100

GHz, and more recent research indicates that they may be able to operate at frequencies as high as terahertz (THz)[170].

Graphene's remarkable optical transparency, which may reach up to 97.7%[140], increases the potential uses of the material, especially for sophisticated technologies like holographic data storage[171] and transparent electrodes in solar cells[172]. In addition to these qualities, graphene has a high Young's modulus of more than ~1 TPa, which guarantees excellent mechanical characteristics[173]. It also has a very large specific surface area of 2630 m^2/g[174] and a good thermal conductivity that approaches 5000 $Wm^{-1}K^{-1}$ [175]. Interested readers can consult the references supplied for in-depth studies, even if a thorough investigation of these qualities is outside the purview of this debate.

1.10. Carbon nanomaterial-based Inorganic Composites

Carbon nanotubes (CNTs) are significant carbon-based materials. A single-walled carbon nanotube (SWCNT) can be conceptualized as a seamless cylinder formed by the rolling of a graphene sheet, whereas a multi-walled carbon nanotube (MWCNT) consists of multiple concentric SWCNTs. Due to their exceptional properties, carbon nanotubes (CNTs) have been the subject of extensive research and have garnered significant attention over the past decade.

Inorganic nanomaterials, encompassing elemental substances and a wide range of compounds, represent a significant category of nanomaterials characterized by diverse properties in the fields of optics, electronics, magnetics, and catalysis. The properties of inorganic nanomaterials can be further optimized through the modulation of their composition, structure, and morphology.

Composite materials based on carbon nanotubes (CNTs) and inorganic nanomaterials integrate the unique characteristics and functionalities of both component types. Additionally, they may exhibit novel properties resulting from the cooperative effects between the two material classes[176–178]. Consequently, these composite materials demonstrate significant potential for applications across various fields like in catalysis, energy conversion, sensor etc.

As previously mentioned, graphene and its inorganic nanocomposites show great potential for electronic devices. However, despite its remarkable properties, challenges

have emerged regarding graphene's electrical and optical characteristics in high-speed electronic applications, primarily due to the absence of a bandgap. Graphene is inherently a zero-bandgap semiconductor, characterized by charge conjugation symmetry between electrons and holes, along with carriers that possess a chirality-like internal degree of freedom, similar to ultra-relativistic elementary particles. These factors contribute to the limitations observed in its application[179].

To overcome these obstacles, scientists realised that integrating graphene nanosheets with certain inorganic semiconductors might mitigate or even eradicate the zero-gap drawbacks. Techniques including strain-induced curvature and size constrictions were used to create an electrical band gap in graphene. It was later discovered that this goal may be successfully accomplished by adding nanoscale inorganic semiconductors[180,181]. There are notable differences in the compatibility of graphene with other inorganic semiconducting materials due to the production process, even though several inorganic semiconductors have shown compatibility with graphene to produce composites. This leads to significant changes in the final composites' optical and electrical characteristics.

The charge transport characteristics of these composite materials are significantly impacted by graphene. Charge carriers in common inorganic semiconductors are activated by light irradiation. Smooth charge separation and transport are made possible by the subsequent electronic interactions between graphene and the semiconductor. As the electron conductor, graphene prevents the composite's electrons and holes from recombining quickly. By using these benefits, hybrid graphene-inorganic semiconductor materials have become very attractive choices for use in photochemistry, electrochemistry, and optoelectronics, possibly transforming the composites and electronics sectors.

Particle size and the band gap energy of semiconductor materials, such quantum dots, are closely related; when the particle size shrinks, the band gap rises as a result of quantum confinement phenomena[182]. Many copper-based semiconductors, including CuO, CuS, $CuInSe_2$, CuSe, and CuTe, exhibit this phenomenon, where variations in quantum dot size cause a shift in the absorption threshold[183]. Semiconducting copper nanoparticles, such CuS and CuSe, are interesting prospects for a variety of applications due to their unique optical and electrical features resulting from quantum confinement.

However, the zero-bandgap characteristic of graphene limits its potential[137]. As a result, hybrid structures that combine graphene and group I–VI semiconductors have been investigated to harness on synergistic benefits and show better performance than individual materials.

In this thesis, the carbon nanotube-copper sulphide (CNT-CuS) microstructures are synthesised, characterised, optimised, and used in practical applications. Additionally, reduced graphene oxide-copper selenide (rGO-CuSe) microstructures are included and their use in thin-film Schottky barrier diodes is investigated, with a focus on how graphene and carbon nanotubes affect the inorganic semiconductors' charge transport and photoresponse characteristics.

1.10.1. Copper Sulfide (CuS) and carbon nanotube (CNT)

Composite materials with enhanced charge mobility and optical responsiveness are made by combining carbon nanotube (CNT) with copper sulfide (CuS), a semiconductor with an energy range of 1.3–2.4 eV. Utilising the semiconducting qualities of CuS and the multifunctional qualities of CNT like, high electrical and thermal conductivities, high mechanical strength and excellent structural flexibility, the combination of the two creates hybrid structures with improved electrical conductivity, thermal and physical stability, and optical qualities. When combined with advantageous energy band locations, the quick creation of electron-hole (e-h+) pairs following photo-excitation allows CuS nanoparticles combined with carbon nanotubes to perform better in dye degradation processes. Aiming to better comprehend the synergistic interactions between CuS and CNT, ongoing research endeavours are focused on improved materials for modern physics applications.

1.10.2. Copper Selenide (CuSe) and Graphene Oxide

Copper Selenide (CuSe), a semiconductor with an energy range of 2.4−2.6 eV, is combined with graphene oxide (GO) to create composite materials that exhibit improved charge mobility and optical responsiveness. The integration of CuSe and GO capitalizes on the semiconducting properties of CuSe and the multifunctional characteristics of GO, leading to hybrid structures that demonstrate enhanced electrical conductivity, physical and thermal stability, and superior optical properties. The rapid generation of electron-hole (e-h+) pairs upon photo-excitation, coupled with favourable energy band positions,

enables CuSe nanoparticles decorated with graphene to achieve enhanced performance in dye degradation processes. Ongoing research efforts aim to deepen the understanding of the synergistic interactions between CuSe and GO, particularly in the context of advanced materials for contemporary applications in physics.

1.11. Synthesis of copper-based nanoparticles and their carbon nanocomposites

Recently, in modern technology and nanoscience, a fundamental aspect is the synthesis of various nanomaterials. Consequently, there has been a significant increase in publications addressing the synthesis of nanoparticles in recent times. Several inorganic nanoparticles have been synthesized using a variety of synthetic strategies. Moreover, significant efforts have been made to selectively synthesize nanoparticles of various shapes, sizes, and dimensionalities. Various physical as well as chemical method of synthesis techniques has adopted to synthesis copper-based nanoparticles. Electrochemical deposition, sol-gel, hydrothermal, and chemical reduction are belonging to the chemical route and sputtering, physical vapor deposition, laser ablation, pulsed laser deposition, electrodeposition, ball milling, spark discharge generation, pulsed wire discharge are procedures that belong to the Physical synthesis methods[184]. In this thesis the solvothermal, hydrothermal and co-precipitation methods have been adopted for the synthesis of copper-based nanoparticles and their carbon-based nanocomposites and hence these methods are described in the following section.

1.11.1. Solvothermal, Hydrothermal and Co-precipitation method

Solvothermal, hydrothermal and co-precipitation methods are commonly used technique to synthesize inorganic nanoparticles. Hydrothermal synthesis pertains to the generation of materials via chemical reactions conducted in aqueous solutions at temperatures exceeding the boiling point of water. In contrast, solvothermal synthesis involves the preparation of materials in nonaqueous solutions at comparably elevated temperatures whereas the co-precipitation method is generally performed at low temperature, sometimes at the room temperature.

In the hydrothermal method chemical reactions occur in a sealed vessel containing an aqueous solution heated above the boiling point of water, which establishes high-pressure conditions that promote the formation of nanomaterials with controlled morphology and

size. The solvothermal synthesis process is similar to hydrothermal synthesis, employs an organic solvent, such as ethanol or methanol etc, in place of water. This approach facilitates the synthesis of materials that may not be soluble in aqueous environments. In co-precipitation, rapid mixing of aqueous solutions containing the desired metal precursors result in a sudden alteration in solubility, which facilitates the precipitation of nanoparticles.

The particle size distribution of the synthesized materials and the nucleation rates during the synthesis procedure can be effectively adjusted by manipulating various reaction parameters including reaction temperature, concentration, pressure, pH, time duration, and reaction cell fill volume. A significant array of inorganic materials from diverse classes has been synthesized using hydrothermal, solvothermal, and co-precipitation methods, including metal chalcogenides, oxides, and other materials. In this thesis, we have synthesized copper sulfide (CuS) and copper sulfide-carbon nanotube composite (CNT-CuS) via solvothermal and co-precipitation methods and copper selenide (CuSe) and copper selenide-reduced graphene oxide (rGO-CuSe) composite via hydrothermal technique.

1.12. Application of Carbon nanomaterials and their Composites

Since 2004, there has been a notable increase in the number of scholarly papers about carbon nanomaterials, indicating important turning points and the growing trend in graphene research publications. Depending on their intrinsic qualities, different kinds of carbon materials, produced in different ways, provide unique benefits for a wide range of applications. A range of prospective technologies is illustrated by the many uses of carbon-based composites in Fig. 1.8. The practical uses of graphene and carbon nanotubes and its nanocomposites will be briefly discussed in the next section.

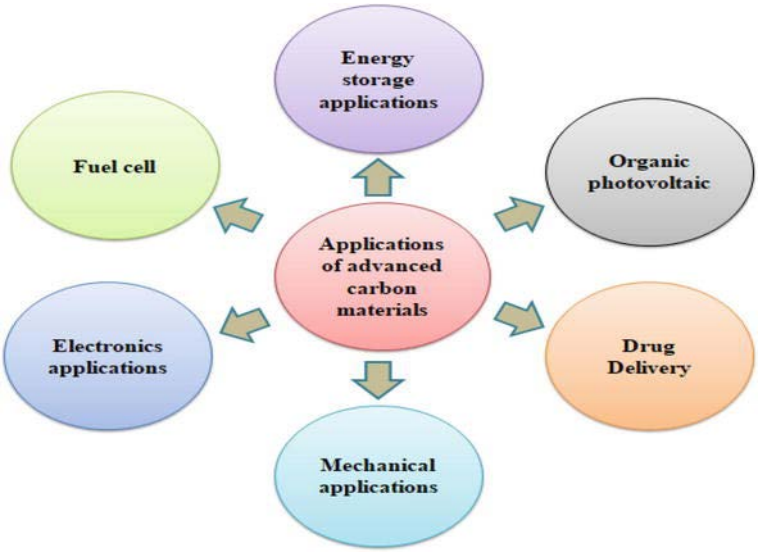

Fig. 1.8: Schematic representation of diverse applications of carbon-based composite materials (Ref.[185]).

1.12.1. High-speed Electronics

High-speed electronics are a perfect fit for carbon nanocomposites because of their extraordinarily high conductivity. Among them graphene has this advantage, its zero band-gap prevents it from being widely used commercially in electrical equipment. For electrical devices to have "on and off" states, a band-gap is clearly required. The twisting of the graphene sheet[186] is the reason why bilayer graphene does not have a band-gap, according to recent research. However, scientists have been able to create ultra-thin graphene transistors[187]. In graphene transistors, a self-aligning Co_2Si-Al_2O_3 nanowire has been used as a gate, notably exhibiting high operating frequencies of 100–300 GHz[188] and avoiding device deterioration. This development highlights how quickly carbon nanocomposite research is progressing and suggests that high-speed graphene transistors may soon appear in consumer products.

1.12.2. Solar Cells

Carbon nanomaterials have significant applications in solar cells, a domain that is essential for future energy solutions. The integration of carbon nanomaterials into various types of solar cells can augment the performance of photovoltaic technologies, leading to improvements in both efficiency and stability. The widespread utilization of platinum-based electrodes in contemporary solar cell technologies presents two significant challenges: the limited availability of platinum necessary for the production of solar cells on a planetary scale and the associated high costs. The hollow tubular structure

of CNT with high specific area, excellent thermal and electrical conductivity is suitable for electrode materials in the photovoltaic solar cells. Graphene, another two-dimensional carbon nanomaterial has similar properties like CNT and has outstanding optical properties, with a light transmittance of 97.7% that is independent of wavelength, makes it an excellent transparent electrode material compared to ITO. The light weight, higher specific surface area, higher conductivity and good transparency of graphene make it alternative to transparent conductive oxide to the field of solar cell, similar to CNTs. The current density–voltage (J–V) characteristics of the dye-sensitized solar cells (DSSCs) incorporating graphene (G) and multi-walled carbon nanotubes (MWCNTs), recorded under conditions of 1000 W/m^2 air mass 1.5 global (AM 1.5 G) irradiation with an efficiency (η) of 4.1%, surpasses those obtained from platinum-based solar cells, as reported by Wahyuono et al[189]. While large-scale commercial applications continue to be a prospective development, any advancements in green energy are highly anticipated. Graphene nanocomposites, including Graphene-CdS and Graphene-TiO_2, demonstrate significant potential for enhancing the performance of solar cells[190,191]. The enhanced durability and stability observed in the study indicate that flexible perovskite solar cells (PSCs) are entirely compatible with carbon materials, thereby contributing to the advancement of low-cost, flexible PSCs.

1.12.3. Smart Windows and OLED Displays

The technology behind Liquid Crystal Display (LCD) Smart Windows involves a layer of liquid crystals placed between two flexible electrodes, typically made of a polymer and graphene. Graphene also functions as a flexible counter electrode for organic light-emitting diodes (OLEDs). Current OLED technologies often use indium tin oxide (ITO) counter electrodes, which are scarce and fragile, presenting significant challenges. In contrast, graphene is abundant and flexible, offering a clear advantage. The potential commercial use of graphene in OLED devices has attracted interest from multinational companies such as Samsung, paving the way for flexible touch screens in mobile and tablet devices. Ongoing research indicates a future where curved screens may become standard in mobile phones, potentially evolving into flexible three-dimensional displays—a concept that seemed inconceivable just a decade ago.

1.12.4. Electrochemical Sensors

Carbon nanomaterials, exhibit remarkable electrochemical properties that have facilitated sensing applications, as the novel carbon-derived nanomaterials possess attributes that are unattainable in their bulk counterparts. This enables them to function with enhanced sensitivity and selectivity in challenging environments, as well as over a broader spectrum of temperatures and dynamic ranges. Specifically, graphene, CNTs, and diamond have emerged as the most extensively utilized polymorphs of carbon for electrochemical sensing applications in recent years. Moreover, excellent properties of carbon nanomaterials, such as large surface-to-volume ratio, high conductivity, and electron mobility at room temperature, have led to numerous advances in electrochemical sensors. The study conducted by Li and Lee [192] has demonstrated a two-fold enhancement in the detection limit of a DNA sensing system, achieving approximately 140 picomolar sensitivity. Furthermore, the incorporation of functionalized multi-walled carbon nanotubes (MWCNTs) into the sensing system has substantially decreased the fabrication time.

1.12.5. Supercapacitors

Supercapacitors (SCs) exhibit superior power densities; however, these devices typically maintain a moderate level of specific energy. To enhance their energy densities, various strategies have been employed, including the utilization of different electrolytes and electrode materials to improve capacitive performance, thereby resulting in increased energy densities. Carbon materials have been modified to enhance their specific surface area (SSA) and optimize their surface chemistry and porous structure. However, carbon remains the most widely utilized active material in commercially available supercapacitor devices, primarily due to the inferior power densities associated with conducting polymers and transition metal oxide-based nanomaterials. This characteristic is a fundamental advantage that underlies the preference for supercapacitors in numerous high-power delivery applications[193,194]. Carbon-based materials are extensively employed in supercapacitors owing to their superior physical, chemical, and electrochemical properties, which include an exceptionally high surface area, the ability to control porous structures, excellent electrical conductivity, chemical inertness, structural stability, the capability for functionalization, and the versatility in producing a diverse array of

composites[195,196]. Among various carbon-based materials, activated carbon (AC), graphene, and carbon nanotubes (CNT) are the most extensively utilized as electrode materials for supercapacitors (SCs). Nevertheless, they demonstrate potential as sustainable energy solutions for electric vehicles, trains, and potentially aircraft.

1.12.6. Schottky Barrier Diodes

Schottky diodes are essential electronic components within contemporary technology, providing the foundational basis for a range of applications, including solar cells, photodetectors, clamped transistors, metal-semiconductor field-effect transistors (MESFETs), high electron mobility transistors (HEMTs), microwave mixers, RF attenuators, rectifiers, varactors, Zener diodes, and various integrated circuits[197]. The enhancement of Schottky junction performance has the potential to significantly improve the functionality of these devices. Schottky barriers, which are formed at metal-semiconductor junctions, typically employ metals such as aluminium, silver, gold, or platinum. By harnessing the semi-metallic properties of graphene as well as CNT, it may be possible to substitute traditional metals in the fabrication of Schottky diodes. Indeed, existing literature highlights the exceptionally promising performance of Schottky diodes featuring graphene electrodes [131,198]. In addition to functioning as a metal electrode within the Schottky barrier, graphene-inorganic nanocomposites, including graphene oxide–Fe_3O_4 and carbon nanotube-CuS, have exhibited favourable results in Schottky diode applications[199,200]. Notwithstanding these advancements, there remains substantial opportunity for further improvement and exploration of carbo nanomaterials-inorganic semiconductor nanocomposites in Schottky diodes, which may yield diverse prospects for future technologies. As previously discussed, this thesis focuses on the synthesis of carbon allotropes based-inorganic semiconductors and their application in a Schottky barrier diode, thereby establishing a foundation for the subsequent discourse on the theory and configuration of Schottky barrier diodes.

1.12.7. Photocatalysis and Wastewater Treatment

Cabon nanomaterials such as carbon nanotube and graphene and its composites have emerged as promising materials for a variety of applications, including photocatalysis and wastewater treatment. Their distinctive properties, including a large surface area and excellent electrical conductivity, render them attractive candidates for addressing

environmental challenges. In the realm of photocatalysis, carbon-based materials function as efficient catalysts that promote chemical reactions under light irradiation. The incorporation of graphene and CNT with semiconductor photocatalysts such as TiO_2, ZnO, and CdS can significantly enhance photocatalytic activity due to improved light absorption and charge carrier separation. Furthermore, carbon composites demonstrate enhanced stability and recyclability, making them suitable for practical applications in wastewater treatment. The integration of graphene as well as CNT into membranes or adsorbents facilitates the removal of pollutants from water through adsorption or photocatalytic degradation. Additionally, carbon-based materials exhibit excellent antibacterial properties, further augmenting their effectiveness in wastewater disinfection. Overall, the application of carbon nanomaterials and its composites in photocatalysis and wastewater treatment holds substantial promise for mitigating environmental pollution and promoting sustainable water management practices. Ongoing research in this field seeks to optimize synthesis methods, explore novel composite materials, and scale up production for practical implementation.

***

References

1. X. Li, *JOM*, 2007, **59**, 71–74.

2. X. Li and P. Nardi, *Nanotechnology*, 2004, **15**, 211–217.

3. *Philos Trans R Soc Lond*, 1857, **147**, 145–181.

4. B. Mubeen, A. Hasnain, J. Wang, H. Zheng, S. A. H. Naqvi, R. Prasad, A. ur Rehman, M. A. Sohail, M. Z. Hassan, M. Farhan, M. A. Khan and M. Moustafa, *Coatings*, 2023, **13**, 212.

5. S. Gupta, M. Mohan and R. K. Srivastva, *50 th INDIAN GEOTECHNICAL CONFERENCE 17 th-19 th*, 2015.

6. Y. Yin and D. Talapin, *Chem Soc Rev*, 2013, **42**, 2484.

7. A. E. Shalan, A. S. H. Makhlouf and S. Lanceros-Méndez, 2022, pp. 3–14.

8. Alexei Nabok, *Organic and Inorganic Nanostructures*, 2005.

9. J. K. Patel, A. Patel and D. Bhatia, in *Emerging Technologies for Nanoparticle Manufacturing*, Springer International Publishing, Cham, 2021, pp. 3–23.

10. C. Rao and A. Cheetham, *Nanomaterials Handbook*, CRC Press, 2006.

11. C. N. R. Rao, A. Müller and A. K. Cheetham, *The Chemistry of Nanomaterials Synthesis, Properties and Applications in 2 Volumes*, 2004.

12. S. Prasad, V. Kumar, S. Kirubanandam and A. Barhoum, *Emerging applications of nanoparticles and architectural nanostructures: Current prospects and future trends*, 2018.

13. A. Barhoum, M. L. García-Betancourt, J. Jeevanandam, E. A. Hussien, S. A. Mekkawy, M. Mostafa, M. M. Omran, M. S. Abdalla and M. Bechelany, *Nanomaterials*, 2022, **12**, 177.

14. D. B. Resnik, *AMA J Ethics*, 2019, **21**, E363-369.

15. C. Lv, X. Zhang, Y. Liu, T. Zhang, H. Chen, J. Zang, B. Zheng and G. Zhao, *Chem Soc Rev*, 2021, **50**, 3957–3989.

16. G. Paramasivam, V. V. Palem, T. Sundaram, V. Sundaram, S. C. Kishore and S. Bellucci, *Nanomaterials*, 2021, **11**, 3228.

17. D. Roy, A. K. Srivastava, K. Mukhopadhyay and E. P. Namburi, *Novel Defence Functional and Engineering Materials (Ndfem) Volume 1: Functional Materials for Defence Applications*, 2024, vol. 1.

18. C. N. R. Rao and A. K. Cheetham, *J Mater Chem*, 2001, **11**, 2887–2894.

19. Vladimir. Pokropivny, *Introduction to nanomaterials and nanotechnology*, Tartu University Press, 2007.

20. N. Domun, H. Hadavinia, T. Zhang, T. Sainsbury, G. H. Liaghat and S. Vahid, *Nanoscale*, 2015, **7**, 10294–10329.

21. J. Parameswaranpillai, G. Joseph, K. P. Shinu, S. Jose, N. V. Salim and N. Hameed, *RSC Adv*, 2015, **5**, 25634–25641.

22. L. Liu, M. Yu, J. Zhang, B. Wang, W. Liu and Y. Tang, *J Mater Chem C Mater*, 2015, **3**, 2326–2333.

23. E. Glogowski, R. Tangirala, T. P. Russell and T. Emrick, *J Polym Sci A Polym Chem*, 2006, **44**, 5076–5086.

24. W. R. Glomm, *J Dispers Sci Technol*, 2005, **26**, 389–414.

25. Z. Liu, J. Xu, D. Chen and G. Shen, *Chem Soc Rev*, 2015, **44**, 161–192.

26. W. Yang, P. Wan, H. Meng, J. Hu and L. Feng, *CrystEngComm*, 2015, **17**, 2989–2995.

27. V. Chabot, D. Higgins, A. Yu, X. Xiao, Z. Chen and J. Zhang, *Energy Environ Sci*, 2014, **7**, 1564.

28. R. Bogue, *Assembly Automation*, 2011, **31**, 106–112.

29. S. K. Gupta, A. Joshi and M. Kaur, *Journal of Chemical Sciences*, 2010, **122**, 57–62.

30. C. R. Chinnamuthu and P. M. Boopathi, *Madras Agricultural Journal*, 2009, **96**, 17–31.

31. H. J. Snaith, *J Phys Chem Lett*, 2013, **4**, 3623–3630.

32. A. Kojima, K. Teshima, Y. Shirai and T. Miyasaka, *J Am Chem Soc*, 2009, **131**, 6050–6051.

33. W. Xu, Q. Hu, S. Bai, C. Bao, Y. Miao, Z. Yuan, T. Borzda, A. J. Barker, E. Tyukalova, Z. Hu, M. Kawecki, H. Wang, Z. Yan, X. Liu, X. Shi, K. Uvdal, M. Fahlman, W. Zhang, M. Duchamp, J.-M. Liu, A. Petrozza, J. Wang, L.-M. Liu, W. Huang and F. Gao, *Nat Photonics*, 2019, **13**, 418–424.

34. S. Yakunin, M. Sytnyk, D. Kriegner, S. Shrestha, M. Richter, G. J. Matt, H. Azimi, C. J. Brabec, J. Stangl, M. V. Kovalenko and W. Heiss, *Nat Photonics*, 2015, **9**, 444–449.

35. H. Dong, C. Ran, W. Gao, N. Sun, X. Liu, Y. Xia, Y. Chen and W. Huang, *Adv Energy Mater*, DOI:10.1002/aenm.202102213.

36. H. Dong, C. Ran, W. Gao, M. Li, Y. Xia and W. Huang, *eLight*, 2023, **3**, 3.

37. J. C. Ince, M. Peerzada, L. D. Mathews, A. R. Pai, A. Al-qatatsheh, S. Abbasi, Y. Yin, N. Hameed, A. R. Duffy, A. K. Lau and N. V. Salim, *Adv Compos Hybrid Mater*, 2023, **6**, 130.

38. M. Dada and P. Popoola, *Beni Suef Univ J Basic Appl Sci*, 2023, **12**, 66.

39. W. Honda, T. Arie, S. Akita and K. Takei, in *2015 Transducers - 2015 18th International Conference on Solid-State Sensors, Actuators and Microsystems (TRANSDUCERS)*, IEEE, 2015.

40. H. Chen, Y. Cao, J. Zhang and C. Zhou, *Nat Commun*, 2014, **5**, 4097.

41. S. Kumagai, H. Murakami, K. Tsuzuku, T. Makita, C. Mitsui, T. Okamoto, S. Watanabe and J. Takeya, *Org Electron*, 2017, **48**, 127–131.

42. L. F. Weber, *IEEE Transactions on Plasma Science*, 2006, **34**, 268–278.

43. T. Wu, C.-W. Sher, Y. Lin, C.-F. Lee, S. Liang, Y. Lu, S.-W. Huang Chen, W. Guo, H.-C. Kuo and Z. Chen, *Applied Sciences*, 2018, **8**, 1557.

44. X. Lv, K. H. Loo, Y. M. Lai and C. K. Tse, *IEEE Transactions on Industrial Electronics*, 2014, **61**, 4665–4673.

45. F. Templier, *J Soc Inf Disp*, 2016, **24**, 669–675.

46. V. Wood and V. Bulović, *Nano Rev*, 2010, **1**, 5202.

47. V. Wood, M. J. Panzer, J. Chen, M. S. Bradley, J. E. Halpert, M. G. Bawendi and V. Bulović, *Advanced Materials*, 2009, **21**, 2151–2155.

48. M. K. Choi, J. Yang, T. Hyeon and D.-H. Kim, *npj Flexible Electronics*, 2018, **2**, 10.

49. H. L. Tuller, *Mater Renew Sustain Energy*, 2017, **6**, 3.

50. M. Grätzel, *Philosophical Transactions of the Royal Society A: Mathematical, Physical and Engineering Sciences*, 2007, **365**, 993–1005.

51. N. A. Ludin, N. I. Mustafa, M. M. Hanafiah, M. A. Ibrahim, M. Asri Mat Teridi, S. Sepeai, A. Zaharim and K. Sopian, *Renewable and Sustainable Energy Reviews*, 2018, **96**, 11–28.

52. K. Ranabhat, L. Patrikeev, A. A. evna Revina, K. Andrianov, V. Lapshinsky and E. Sofronova, *Journal of Applied Engineering Science*, 2016, **14**, 481–491.

53. M. Tao, *Electrochem Soc Interface*, 2008, **17**, 30–35.

54. M. P. Paranthaman, W. Wong-Ng and R. N. Bhattacharya, Eds., *Semiconductor Materials for Solar Photovoltaic Cells*, Springer International Publishing, Cham, 2016, vol. 218.

55. S. Kohiki, M. Nishitani, T. Negami and T. Wada, *Appl Phys Lett*, 1993, **62**, 1656–1657.

56. M. Z. U. Shah, M. Sajjad, H. Hou, S. ur Rahman and A. Shah, *J Energy Storage*, 2022, **55**, 105651.

57. W. Hörig, W. Möller, H. Neumann, E. Reccius and G. Kühn, *physica status solidi (b)*, DOI:10.1002/pssb.2220920142.

58. S.-H. Wei, S. B. Zhang and A. Zunger, *Appl Phys Lett*, 1998, **72**, 3199–3201.

59. B. Schumann, H. Neumann, A. Tempel, G. Kühn and E. Nowak, *Kristall und Technik*, 1980, **15**, 71–76.

60. A. M. Gabor, J. R. Tuttle, D. S. Albin, M. A. Contreras, R. Noufi and A. M. Hermann, *Appl Phys Lett*, 1994, **65**, 198–200.

61. K. Santhi, C. Rani and S. Karuppuchamy, *J Alloys Compd*, 2016, **662**, 102–107.

62. E. Boonen and A. Beeldens, *European Transport Research Review*, 2013, **5**, 79–89.

63. J. Low, B. Dai, T. Tong, C. Jiang and J. Yu, *Advanced Materials*, 2019, **31**, 1802981.

64. Q. Xie, W. He, S. Liu, C. Li, J. Zhang and P. K. Wong, *Chinese Journal of Catalysis*, 2020, **41**, 140–153.

65. K. Dai, J. Lv, J. Zhang, G. Zhu, L. Geng and C. Liang, *ACS Sustain Chem Eng*, 2018, **6**, 12817–12826.

66. Y. Wang, S. Wang and X. W. (David) Lou, *Angewandte Chemie International Edition*, 2019, **58**, 17236–17240.

67. L. Sun, Y. Zhou, X. Li, J. Li, D. Shen, S. Yin, H. Wang, P. Huo and Y. Yan, *Chinese Journal of Catalysis*, 2020, **41**, 1573–1588.

68. Z. Zhao, X. Li, K. Dai, J. Zhang and G. Dawson, *J Mater Sci Technol*, 2022, **117**, 109–119.

69. H. Li, N. Wells, B. Chong, B. Xu, J. Wei, B. Yang and G. Yang, *Chem Eng Sci*, 2021, **229**, 116069.

70. D. Ren, R. Shen, Z. Jiang, X. Lu and X. Li, *Chinese Journal of Catalysis*, 2020, **41**, 31–40.

71. Y. Huo, Y. Yang, K. Dai and J. Zhang, *Appl Surf Sci*, 2019, **481**, 1260–1269.

72. X. Li, X. Wu, S. Liu, Y. Li, J. Fan and K. Lv, *Chinese Journal of Catalysis*, 2020, **41**, 1451–1467.

73. T. Hu, K. Dai, J. Zhang and S. Chen, *Appl Catal B*, 2020, **269**, 118844.

74. Y.-J. Liu, L. Geng, Y. Kang, W.-H. Fang and J. Zhang, *Chinese Journal of Catalysis*, 2021, **42**, 1332–1337.

75. X. Li, T. Hu, J. Zhang, K. Dai and C. Liang, *Ceram Int*, 2021, **47**, 7169–7176.

76. T. Jiang, K. Wang, T. Guo, X. Wu and G. Zhang, *Chinese Journal of Catalysis*, 2020, **41**, 161–169.

77. L. Liu, K. Dai, J. Zhang and L. Li, *J Colloid Interface Sci*, 2021, **604**, 844–855.

78. Y. Yang, H. Tan, B. Cheng, J. Fan, J. Yu and W. Ho, *Small Methods*, 2021, **5**, 2001042.

79. C. Xue, H. An, G. Shao and G. Yang, *Chinese Journal of Catalysis*, 2021, **42**, 583–594.

80. Y. Xia and J. Yu, *Chem*, 2020, **6**, 1039–1040.

81. M. Xia, X. Yan, H. Li, N. Wells and G. Yang, *Nano Energy*, 2020, **78**, 105401.

82. J. Wei, Y. Chen, H. Zhang, Z. Zhuang and Y. Yu, *Chinese Journal of Catalysis*, 2021, **42**, 78–86.

83. Z. Li, Y. Yang, K. Dai, J. Zhang and L. Lu, *Appl Surf Sci*, 2019, **469**, 505–513.

84. Y. Ren, Y. Li, X. Wu, J. Wang and G. Zhang, *Chinese Journal of Catalysis*, 2021, **42**, 69–77.

85. Y. Huo, J. Zhang, K. Dai and C. Liang, *ACS Appl Energy Mater*, 2021, **4**, 956–968.

86. H. Wu, D. Wang, P. Zhou, M. Xie, J. Jing, Y. Xu and J. Xie, *Sep Purif Technol*, 2021, **274**, 119004.

87. X. Fei, H. Tan, B. Cheng, B. Zhu and L. Zhang, *Acta Physico Chimica Sinica*, 2020, **0**, 2010027–0.

88. Y. Huang, J. Liang, C. Wang, S. Yin, W. Fu, H. Zhu and C. Wan, *Chem Soc Rev*, 2020, **49**, 6866–6883.

89. X. Li, J. Liu, J. Huang, C. He, Z. Feng, Z. Chen, L. Wan and F. Deng, *Acta Physico Chimica Sinica*, 2020, **0**, 2010030–0.

90. H. Zhao, Y. Li, B. Zhang, T. Xu and C. Wang, *Nano Energy*, 2018, **50**, 665–674.

91. X. Chen, X. Ke, J. Zhang, C. Yang, K. Dai and C. Liang, *Ceram Int*, 2021, **47**, 13488–13499.

92. N. Zhao, L. Yan, X. Zhao, X. Chen, A. Li, D. Zheng, X. Zhou, X. Dai and F.-J. Xu, *Chem Rev*, 2019, **119**, 1666–1762.

93. Z. Q. Zhuo, F. Pan and W. L. Yang, *Fujian Institute of Research of the Structure of Matter*, 2019, preprint, DOI: 10.14102/j.cnki.0254-5861.2011-2677.

94. F. Mei, K. Dai, J. Zhang, L. Li and C. Liang, *J Colloid Interface Sci*, 2022, **608**, 1846–1856.

95. I. B. Krylov, E. R. Lopat'eva, I. R. Subbotina, G. I. Nikishin, B. Yu and A. O. Terent'ev, *Chinese Journal of Catalysis*, 2021, **42**, 1700–1711.

96. H. Schmidt, *J Non Cryst Solids*, 1985, **73**, 681–691.

97. H. Yang, J. feng Zhang and K. Dai, *Chinese Journal of Catalysis*, 2022, **43**, 255–264.

98. I. Kriegel, J. Rodríguez-Fernández, A. Wisnet, H. Zhang, C. Waurisch, A. Eychmüller, A. Dubavik, A. O. Govorov and J. Feldmann, *ACS Nano*, 2013, **7**, 4367–4377.

99. C. Coughlan, M. Ibáñez, O. Dobrozhan, A. Singh, A. Cabot and K. M. Ryan, *Chem Rev*, 2017, **117**, 5865–6109.

100. Y. Zhao and C. Burda, *Energy Environ. Sci.*, 2012, **5**, 5564–5576.

101. B. Barman, K. C. Handique, Y. Nanung and P. K. Kalita, *Mater Today Proc*, 2021, **46**, 6213–6217.

102. G. Xiao, J. Ning, Z. Liu, Y. Sui, Y. Wang, Q. Dong, W. Tian, B. Liu, G. Zou and B. Zou, *CrystEngComm*, 2012, **14**, 2139.

103. S. Wang, J. Ning, L. Zhao, B. Liu and B. Zou, *J Cryst Growth*, 2010, **312**, 2060–2064.

104. D. E. Ortiz-Ramos, A. I. Martínez-Enríquez and L. A. González, *Mater Sci Semicond Process*, 2019, **89**, 18–25.

105. S. V. Bagul, S. D. Chavhan and R. Sharma, *Journal of Physics and Chemistry of Solids*, 2007, **68**, 1623–1629.

106. J.-S. Chung and H.-J. Sohn, *J Power Sources*, 2002, **108**, 226–231.

107. E. Andrade, V. M. García, P. K. Nair, M. T. S. Nair, E. P. Zavala, L. Huerta and M. F. Rocha, *Nucl Instrum Methods Phys Res B*, 2000, **161–163**, 635–640.

108. V. M. García, P. K. Nair and M. T. S. Nair, *J Cryst Growth*, 1999, **203**, 113–124.

109. S. Thanikaikarasan, D. Dhanasekaran and K. Sankaranarayanan, *Chinese Journal of Physics*, 2020, **63**, 138–148.

110. H.-I. Hsiang, W.-H. Hsu, L.-H. Lu, Y.-L. Chang and F.-S. Yen, *Mater Res Bull*, 2013, **48**, 715–720.

111. X. Q. Chen, Z. Li and S. X. Dou, *ACS Appl Mater Interfaces*, 2015, **7**, 13295–13302.

112. L. Yang, Z.-G. Chen, G. Han, M. Hong, L. Huang and J. Zou, *J Mater Chem A Mater*, 2016, **4**, 9213–9219.

113. J.-L. Yue, Q. Sun and Z.-W. Fu, *Chemical Communications*, 2013, **49**, 5868.

114. C. M. Hessel, V. P. Pattani, M. Rasch, M. G. Panthani, B. Koo, J. W. Tunnell and B. A. Korgel, *Nano Lett*, 2011, **11**, 2560–2566.

115. J. Deng, Y. You, V. Sahajwalla and R. K. Joshi, *Carbon N Y*, 2016, **96**, 105–115.

116. M. J. Allen, V. C. Tung and R. B. Kaner, *Chem Rev*, 2010, **110**, 132–145.

117. A. K. Geim and K. S. Novoselov, *Nat Mater*, 2007, **6**, 183–191.

118. J. Pang, A. Bachmatiuk, I. Ibrahim, L. Fu, D. Placha, G. S. Martynkova, B. Trzebicka, T. Gemming, J. Eckert and M. H. Rümmeli, *J Mater Sci*, 2016, **51**, 640–667.

119. S. Nasir, M. Hussein, Z. Zainal and N. Yusof, *Materials*, 2018, **11**, 295.

120. T. V. Patil, D. K. Patel, S. D. Dutta, K. Ganguly, A. Randhawa and K.-T. Lim, *Applied Sciences*, 2021, **11**, 9550.

121. M. Sajid, M. Asif, N. Baig, M. Kabeer, I. Ihsanullah and A. W. Mohammad, *Journal of Water Process Engineering*, 2022, **47**, 102815.

122. E. P. Randviir, D. A. C. Brownson and C. E. Banks, *Materials Today*, 2014, **17**, 426–432.

123. C. N. R. Rao, H. S. S. Ramakrishna Matte, R. Voggu and A. Govindaraj, *Dalton Transactions*, 2012, **41**, 5089.

124. Y. Zhang, L. Zhang and C. Zhou, *Acc Chem Res*, 2013, **46**, 2329–2339.

125. K. S. Novoselov, A. K. Geim, S. V. Morozov, D. Jiang, Y. Zhang, S. V. Dubonos, I. V. Grigorieva and A. A. Firsov, *Science (1979)*, 2004, **306**, 666–669.

126. K. S. Novoselov, A. K. Geim, S. V. Morozov, D. Jiang, M. I. Katsnelson, I. V. Grigorieva, S. V. Dubonos and A. A. Firsov, *Nature*, 2005, **438**, 197–200.

127. Y. Zhang, Y.-W. Tan, H. L. Stormer and P. Kim, *Nature*, 2005, **438**, 201–204.

128. A. K. Geim and K. S. Novoselov, *Nat Mater*, 2007, **6**, 183–191.

129. M. J. Allen, V. C. Tung and R. B. Kaner, *Chem Rev*, 2010, **110**, 132–145.

130. X. Zhao, C. M. Hayner, M. C. Kung and H. H. Kung, *Adv Energy Mater*, 2011, **1**, 1079–1084.

131. C.-C. Chen, M. Aykol, C.-C. Chang, A. F. J. Levi and S. B. Cronin, *Nano Lett*, 2011, **11**, 1863–1867.

132. H. Wang, K. Sun, F. Tao, D. J. Stacchiola and Y. H. Hu, *Angewandte Chemie International Edition*, 2013, **52**, 9210–9214.

133. D. Prasai, J. C. Tuberquia, R. R. Harl, G. K. Jennings, B. R. Rogers and K. I. Bolotin, *ACS Nano*, 2012, **6**, 4540–4540.

134. W. J. Hyun, O. O. Park and B. D. Chin, *Advanced Materials*, 2013, **25**, 4729–4734.

135. Z. Radivojevic, P. Beecher, C. Bower, S. Haque, P. Andrew, T. Hasan, F. Bonaccorso, A. C. Ferrari and B. Henson, in *Proceedings of the 2012 Virtual Reality International Conference*, ACM, New York, NY, USA, 2012, pp. 1–3.

136. A. Bonanni and M. Pumera, *ACS Nano*, 2011, **5**, 2356–2361.

137. N. Gao and X. Fang, *Chem Rev*, 2015, **115**, 8294–8343.

138. X. Fang, Y. Bando, U. K. Gautam, C. Ye and D. Golberg, *J. Mater. Chem.*, 2008, **18**, 509–522.

139. J. Hass, R. Feng, T. Li, X. Li, Z. Zong, W. A. de Heer, P. N. First, E. H. Conrad, C. A. Jeffrey and C. Berger, *Appl Phys Lett*, DOI:10.1063/1.2358299.

140. D. A. C. Brownson, D. K. Kampouris and C. E. Banks, *Chem Soc Rev*, 2012, **41**, 6944.

141. P. Delhaes, *Graphite and Precursors*, CRC Press, 2000.

142. B. C. Brodie, *Philos Trans R Soc Lond*, 1859, **149**, 249–259.

143. L. Staudenmaier, *Berichte der deutschen chemischen Gesellschaft*, 1898, **31**, 1481–1487.

144. W. S. Hummers and R. E. Offeman, *J Am Chem Soc*, 1958, **80**, 1339–1339.

145. H. P. Boehm, A. Clauss, G. O. Fischer and U. Hofmann, *Z Anorg Allg Chem*, 1962, **316**, 119–127.

146. A. J. Van Bommel, J. E. Crombeen and A. Van Tooren, *Surf Sci*, 1975, **48**, 463–472.

147. X. Lu, M. Yu, H. Huang and R. S. Ruoff, *Nanotechnology*, 1999, **10**, 269–272.

148. Y. Zhang, J. P. Small, W. V. Pontius and P. Kim, *Appl Phys Lett*, 2005, **86**, 073104.

149. J. C. Meyer, A. K. Geim, M. I. Katsnelson, K. S. Novoselov, T. J. Booth and S. Roth, *Nature*, 2007, **446**, 60–63.

150. A. M. Affoune, B. L. V. Prasad, H. Sato, T. Enoki, Y. Kaburagi and Y. Hishiyama, *Chem Phys Lett*, 2001, **348**, 17–20.

151. C. Soldano, A. Mahmood and E. Dujardin, *Carbon N Y*, 2010, **48**, 2127–2150.

152. R. Van Noorden, *Nature*, 2012, **483**, S32–S33.

153. S., H. W. and G. J. A. Garaj, *Appl Phys Lett*, 2010, **97**, 183103–183106.

154. S. Bae, H. Kim, Y. Lee, X. Xu, J.-S. Park, Y. Zheng, J. Balakrishnan, T. Lei, H. Ri Kim, Y. Il Song, Y.-J. Kim, K. S. Kim, B. Özyilmaz, J.-H. Ahn, B. H. Hong and S. Iijima, *Nat Nanotechnol*, 2010, **5**, 574–578.

155. D. A. C. Brownson and C. E. Banks, *Physical Chemistry Chemical Physics*, 2012, **14**, 8264.

156. M. Lotya, P. J. King, U. Khan, S. De and J. N. Coleman, *ACS Nano*, 2010, **4**, 3155–3162.

157. M. Lotya, Y. Hernandez, P. J. King, R. J. Smith, V. Nicolosi, L. S. Karlsson, F. M. Blighe, S. De, Z. Wang, I. T. McGovern, G. S. Duesberg and J. N. Coleman, *J Am Chem Soc*, 2009, **131**, 3611–3620.

158. Y. Zhu, V. W. Yu and G. Galli, *Nano Lett*, 2023, **23**, 11453–11460.

159. G.-H. Lee, R. C. Cooper, S. J. An, S. Lee, A. van der Zande, N. Petrone, A. G. Hammerberg, C. Lee, B. Crawford, W. Oliver, J. W. Kysar and J. Hone, *Science (1979)*, 2013, **340**, 1073–1076.

160. P. R. Somani, S. P. Somani and M. Umeno, *Chem Phys Lett*, 2006, **430**, 56–59.

161. D. Wei, Y. Liu, Y. Wang, H. Zhang, L. Huang and G. Yu, *Nano Lett*, 2009, **9**, 1752–1758.

162. H. Shin, K. K. Kim, A. Benayad, S. Yoon, H. K. Park, I. Jung, M. H. Jin, H. Jeong, J. M. Kim, J. Choi and Y. H. Lee, *Adv Funct Mater*, 2009, **19**, 1987–1992.

163. C. Gómez-Navarro, R. T. Weitz, A. M. Bittner, M. Scolari, A. Mews, M. Burghard and K. Kern, *Nano Lett*, 2007, **7**, 3499–3503.

164. D. Li, M. B. Müller, S. Gilje, R. B. Kaner and G. G. Wallace, *Nat Nanotechnol*, 2008, **3**, 101–105.

165. H. A. Becerril, J. Mao, Z. Liu, R. M. Stoltenberg, Z. Bao and Y. Chen, *ACS Nano*, 2008, **2**, 463–470.

166. Y. Hernandez, V. Nicolosi, M. Lotya, F. M. Blighe, Z. Sun, S. De, I. T. McGovern, B. Holland, M. Byrne, Y. K. Gun'Ko, J. J. Boland, P. Niraj, G. Duesberg, S. Krishnamurthy, R. Goodhue, J. Hutchison, V. Scardaci, A. C. Ferrari and J. N. Coleman, *Nat Nanotechnol*, 2008, **3**, 563–568.

167. P. Blake, P. D. Brimicombe, R. R. Nair, T. J. Booth, D. Jiang, F. Schedin, L. A. Ponomarenko, S. V. Morozov, H. F. Gleeson, E. W. Hill, A. K. Geim and K. S. Novoselov, *Nano Lett*, 2008, **8**, 1704–1708.

168. K. S. Novoselov, D. Jiang, F. Schedin, T. J. Booth, V. V. Khotkevich, S. V. Morozov and A. K. Geim, *Proceedings of the National Academy of Sciences*, 2005, **102**, 10451–10453.

169. K. I. Bolotin, K. J. Sikes, Z. Jiang, M. Klima, G. Fudenberg, J. Hone, P. Kim and H. L. Stormer, *Solid State Commun*, 2008, **146**, 351–355.

170. Y.-M. Lin, C. Dimitrakopoulos, K. A. Jenkins, D. B. Farmer, H.-Y. Chiu, A. Grill and Ph. Avouris, *Science (1979)*, 2010, **327**, 662–662.

171. X. Li, Q. Zhang, X. Chen and M. Gu, *Sci Rep*, 2013, **3**, 2819.

172. K. S. Kim, Y. Zhao, H. Jang, S. Y. Lee, J. M. Kim, K. S. Kim, J.-H. Ahn, P. Kim, J.-Y. Choi and B. H. Hong, *Nature*, 2009, **457**, 706–710.

173. C. Lee, X. Wei, J. W. Kysar and J. Hone, *Science (1979)*, 2008, **321**, 385–388.

174. Y. Zhu, S. Murali, W. Cai, X. Li, J. W. Suk, J. R. Potts and R. S. Ruoff, *Advanced Materials*, 2010, **22**, 3906–3924.

175. A. A. Balandin, S. Ghosh, W. Bao, I. Calizo, D. Teweldebrhan, F. Miao and C. N. Lau, *Nano Lett*, 2008, **8**, 902–907.

176. G. G. Wildgoose, C. E. Banks and R. G. Compton, *Small*, 2006, **2**, 182–193.

177. V. Georgakilas, D. Gournis, V. Tzitzios, L. Pasquato, D. M. Guldi and M. Prato, *J Mater Chem*, 2007, **17**, 2679.

178. X. Peng, J. Chen, J. A. Misewich and S. S. Wong, *Chem Soc Rev*, 2009, **38**, 1076.

179. M. I. Katsnelson and K. S. Novoselov, *Solid State Commun*, 2007, **143**, 3–13.

180. M. Y. Han, J. C. Brant and P. Kim, *Phys Rev Lett*, 2010, **104**, 056801.

181. D. I. Son, B. W. Kwon, D. H. Park, W.-S. Seo, Y. Yi, B. Angadi, C.-L. Lee and W. K. Choi, *Nat Nanotechnol*, 2012, **7**, 465–471.

182. L. E. Brus, *J Chem Phys*, 1984, **80**, 4403–4409.

183. S. Dagher, Y. Haik, A. I. Ayesh and N. Tit, *J Lumin*, 2014, **151**, 149–154.

184. V. Molahalli, A. Sharma, K. Bijapur, G. Soman, A. Shetty, B. Sirichandana, B. G. M. Patel, N. Chattham and G. Hegde, 2024, pp. 1–33.

185. A. Bashir, A. Mehvish and M. Khalil, in *21st Century Advanced Carbon Materials for Engineering Applications - A Comprehensive Handbook*, IntechOpen, 2021.

186. K. S. Kim, A. L. Walter, L. Moreschini, T. Seyller, K. Horn, E. Rotenberg and A. Bostwick, *Nat Mater*, 2013, **12**, 887–892.

187. C. Mattevi, F. Colléaux, H. Kim, Y.-H. Lin, K. T. Park, M. Chhowalla and T. D. Anthopoulos, *Nanotechnology*, 2012, **23**, 344017.

188. L. Liao, Y.-C. Lin, M. Bao, R. Cheng, J. Bai, Y. Liu, Y. Qu, K. L. Wang, Y. Huang and X. Duan, *Nature*, 2010, **467**, 305–308.

189. R. A. Wahyuono, G. Jia, J. Plentz, A. Dellith, J. Dellith, F. Herrmann-Westendorf, M. Seyring, M. Presselt, G. Andrä, M. Rettenmayr and B. Dietzek, *ChemPhysChem*, 2019, **20**, 3336–3345.

190. F. W. Low and C. W. Lai, *Renewable and Sustainable Energy Reviews*, 2018, **82**, 103–125.

191. Q. Wu, H. Zhao, F. Huang, J. Hou, H. Cao, Z. Liu, S. Peng and G. Cao, *Journal of Physical Chemistry C*, 2017, **121**, 18430–18438.

192. J. Li and E.-C. Lee, *Sens Actuators B Chem*, 2017, **239**, 652–659.

193. J. Chaparro-Garnica, D. Salinas-Torres, M. J. Mostazo-López, E. Morallón and D. Cazorla-Amorós, *Journal of Electroanalytical Chemistry*, 2021, **880**, 114899.

194. C. Zhao, C. Zhao, Q. Liu, X. Liu, X. Lu, C. Pang, Y. Liu, Z. Liu and A. Ying, *Nanoscale*, 2021, **13**, 12697–12710.

195. R. Wang, X. Li, Z. Nie, Y. Zhao and H. Wang, *J Energy Storage*, 2021, **38**, 102479.

196. J. G. Ruiz-Montoya, Lady V. Quispe-Garrido, J. C. Calderón Gómez, A. M. Baena-Moncada and J. M. Gonçalves, *Sustain Energy Fuels*, 2021, **5**, 5332–5365.

197. A. Di Bartolomeo, *Phys Rep*, 2016, **606**, 1–58.

198. D. Sinha and J. U. Lee, *Nano Lett*, 2014, **14**, 4660–4664.

199. Ö. Metin, Ş. Aydoğan and K. Meral, *J Alloys Compd*, 2014, **585**, 681–688.

200. M. Das, D. Das, S. Ghosh, R. Sk, A. Biswas and P. P. Ray, *Journal of Materials Science: Materials in Electronics*, 2024, **35**, 1143.

***

Theoretical Analysis of structural and optical characterization technique: Fabrication of Schottky Barrier Diodes with Introductory Insights into their Electrical Study and Impedance Spectroscopy

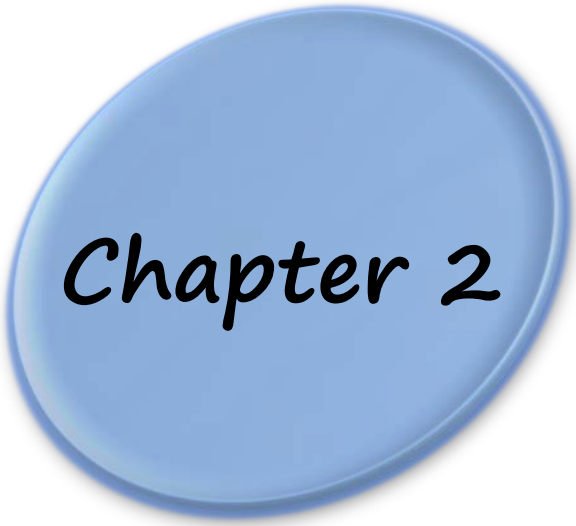

The fundamental theories and related parameters associated with the material characterization, as well as the theory pertaining to the metal-semiconductor contact have been explored in this chapter. The way of analysis and understanding of the mechanism of charge transport within the Schottky device is illustrated in this part.

2.1. Crystallite size and strain from Powder X-Ray Diffraction

Powder X-Ray diffraction analysis (PXRD) is a non-destructive laboratory technique that provides detailed information about the crystallographic structure, chemical composition, and physical properties of a chemical compound. It is based on the constructive interference of monochromatic X-rays of CuK_α radiation having wavelength 1.54Å. The Fourier analysis of diffraction spectra obtained from the powder crystal sample, informs about all the details of crystal (e.g. lattice dimension; crystallite size; and crystal-strain). Few analytical methods utilised for such purposes are illustrated aptly in the following sections:

2.1.1. Debye-Scherrer and Williamson-Hall Method

The Scherrer equation, sometimes referred to as the Debye-Scherrer equation, has been a helpful and pronounced tool for estimating crystallite size. The width of the diffraction peak pattern could enable to get information about the average dimension of material using Debye-Scherrer equation, developed from the famous Bragg's Diffraction law. The equation that helps to estimate crystal dimension, can be stated as

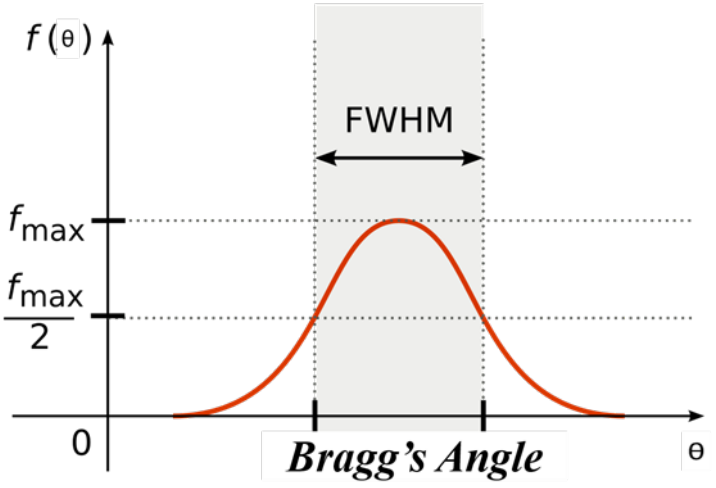

Fig. 2.1: full-width half maxima (FWHM) or the integral breadth of the peak

$$\beta_s = \frac{K\lambda}{D\cos\theta_{hkl}} \quad (2.1)$$

Here, β_s is the full-width at half maxima (FWHM) or the integral breadth of the peak (hkl plane) due to the crystallite size contribution (Fig. 2.1), K is considered as near about 1, D is the average thickness of the crystal which is normal to the hkl plane. θ is Bragg's angle and λ is the wavelength of CuK_α radiation. It is crucial to remember that the Scherrer equation interprets the size of the crystallite, not the aggregation of polycrystalline crystals[1]. Crystallite, in general, denotes the discrete diffracting zone that coherently scatters the applied X-ray.

However, the lattice distortion also plays a role in the broadening of the diffraction peak in addition to the size of the crystallite. Compressive and tensile stresses as well as compositional gradient within the sample could be the source of this distortion[1]. The bending or shearing in the crystals can be used to illustrate the coexistence of stress and strain gradients in the crystal. Peak broadening can also occasionally be attributed to variations in unit cell dimensions with negligible compositional differences in different crystals. If we consider the differential Bragg equation with respect to the d-spacing and the diffraction angle, then

$$\left|\frac{\Delta d}{d}\right| = \cot\theta\Delta\theta \Rightarrow \Delta(2\theta) = 2\left|\frac{\Delta d}{d}\right|\tan\theta \quad (2.2)$$

Around the Bragg maximum, the fractional spread in the d spacing is considered to be 2η, and then the stress-induced broadening due to the strain (η) is expressed by[1]

$$\beta_\eta = 4\eta\tan\theta \quad (2.3)$$

Hence, the broadening on the peak is convoluted by the effects of crystallite size (D) and stress. Thus, the total broadening can be written as,

$$\beta = \frac{K\lambda}{D\cos\theta} + 4\eta\tan\theta \quad (2.4)$$

Or,

$$\beta\cos\theta = \frac{K\lambda}{D} + 4\eta\sin\theta \quad (2.5)$$

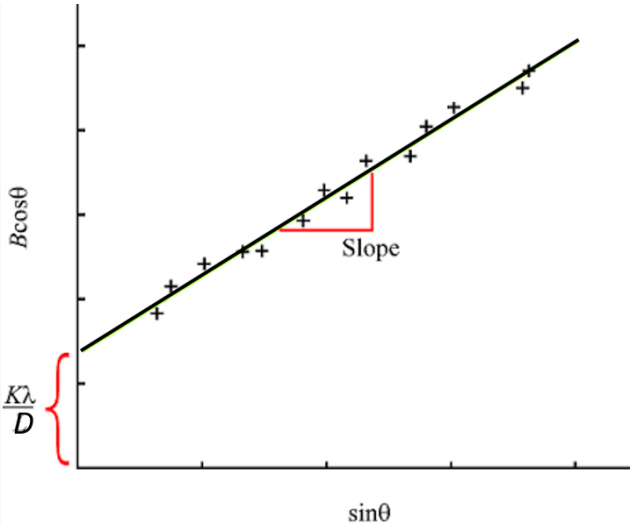

Fig. 2.2: Williamson-Hall plot

the plot of βcosθ versus sinθ which is also referred as Williamson-Hall plot[2], For a particular hkl plane, yields the values of crystallite size and strain deduced from the intercept and slope (Fig. 2.2), respectively. The effect of low angle reflections has decreased due to the dependency of stress broadening on tanθ. W-H plots are usually applied to smaller unit cell materials.

2.2. Determination of optical parameters from UV-Vis data: A theoretical study

The absorption coefficient, the optical energy band gap, the refractive index and the optical conductivity of the materials can be derived from the UV-Vis spectroscopy data, which could enable one to get better information about the optical characteristics of the materials.

2.2.1 Absorption coefficient and Optical Band gap

Beer Lambert's law states that the light's intensity drops exponentially with the depth in the material i.e., $I = I_0 e^{-\alpha d}$, where I is the intensity of light after passing through the sample, I_0 is the initial light intensity, α is the linear absorption coefficient, and d is the path travelled by the light. Generally, I/I_0 is defined as transmittance. So, absorbance A can be stated as

$$A = \log\left(\frac{I_0}{I}\right) = \log\left(\frac{I_0}{I_0 e^{-\alpha d}}\right) = \log e^{\alpha d} = \frac{\alpha d}{2.303}$$
$$\Rightarrow \alpha = \frac{2.303A}{d} \qquad (2.6)$$

Tauc developed an equation to determine the optical band gap energy in the late 70's of the nineteenth century, which can be expressed as[3],

$$\alpha h\nu = c\left(h\nu - E_g\right)^{\gamma} \qquad (2.7)$$

Here c is a constant related to valence band and conduction band[4], h is the Planck's constant, ν is the frequency of light and E_g is the band gap energy. γ is associated to the electronic transition nature. The values of band gap E_g can be estimated from the extrapolation of the linear region of the $(\alpha h\nu)^{1/\gamma}$ versus hν graph to the photon energy axis. The value of γ can be 1/2, 2, 3/2, 3 for the direct allowed, indirect allowed, direct forbidden and indirect forbidden transition, respectively, and can be obtained from the differential expression:

$$\frac{d[\ln(\alpha h\nu)]}{d[h\nu]} = \frac{\gamma}{h\nu - E_g} \qquad (2.8)$$

There is a discontinuity that corresponds to the band gap energy in the plot of $d[\ln(\alpha h\nu)]/d[h\nu]$ versus hν. This energy value is used in the plot of $\ln[(\alpha h\nu)]$ versus $\ln[h\nu - E_g]$, and the slope of the plot gives the value of γ.

2.3. Introduction of Schottky Barrier Diodes (SBD)

In the year 1874, Braun revealed first time the systematic analysis of conduction between metal and semiconductor (lead sulfide)[5]. By 1904, point-contact rectifiers in various configurations had begun to find practical applications. Based on the band theory of solids, Wilson developed the transport theory for semiconductors in 1931[6], which was later applied to metal-semiconductor contacts. But, in 1931 Walter Hans Schottky noticed the formation of a potential barrier between the metal-semiconductor contacts[7]. In 1938, Schottky and Mott proposed a model to quantify the shape of the barrier and the barrier height[8,9]. These metal-semiconductor diodes were not effectively

imitated or precisely dependable and were replaced by the p-n junction during the 1950s. However, semiconductor and vacuum technology is currently used to create reproducible and reliable metal-semiconductor contacts.

2.3.1. Energy-Band Relation

The interfacial contact between a metal and a semiconductor can lead to two distinct devices: the Ohmic junction or the Schottky (rectifying) junction. This outcome depends on the type of semiconductor (n-type or p-type) and the relative positions of the Fermi level in both the metal and semiconductor. For a n-type semiconductor, the contact is said to be rectifying only if its work function (ϕ_s) is less than the metal work function (ϕ_m), i.e., if $\phi_s < \phi_m$. Conversely, if $\phi_s > \phi_m$, the metal-n-type semiconductor contact is Ohmic. The situation is reversed for p-type semiconductors. A metal-p-type semiconductor contact will be rectifying, if $\phi_s > \phi_m$ and non-rectifying, if $\phi_s < \phi_m$. The subsequent section will explore into the formation of Schottky junctions.

When a metal establishes contact with a semiconductor, a potential barrier is created at the metal-semiconductor (MS) interface. This kind of barrier forms when the charges separate at the interface, leading to the formation of a high-resistance region in the semiconductor, depleted of mobile carriers. Schottky and Mott presented the initial model to elucidate the barrier height. The process of barrier formation is depicted in the energy band diagrams in Fig. 2.1. In Fig. 2.1(a), the band diagram illustrates a metal and an n-type semiconductor with work functions ϕ_m and ϕ_s, respectively, where $\phi_s < \phi_m$ and the vacuum level serve as the reference point. The work function of the semiconductor undergoes variation due to the fluctuation in the Fermi level caused by doping. Nevertheless, the electron affinity χ_s of a semiconductor remains unaffected by doping. Both the work functions and the electron affinity are measured and denoted in units of electron volts (eV).

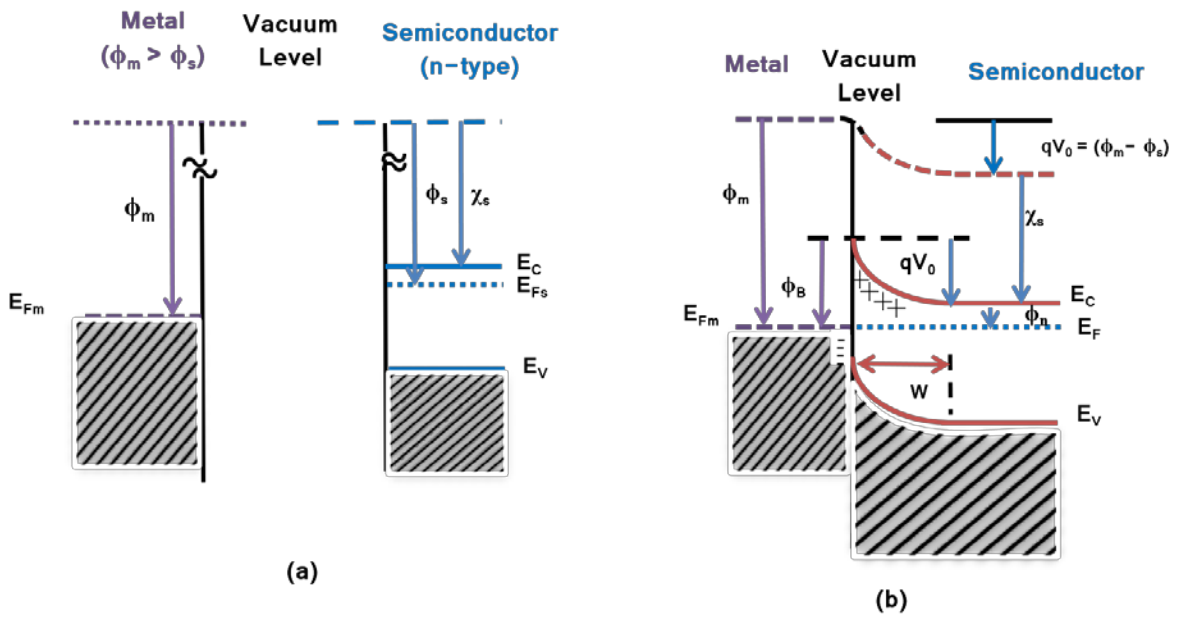

Fig. 2.3: Energy band diagrams depicting the contact of a metal with an n-type semiconductor, where $\phi_m > \phi_s$. Neutral materials when (a) they are separate from one another and (b) in the thermal equilibrium after contact formation. (Ref.[10])

The energy band diagram, shown in Fig. 2.3(b), represents the equilibrium state after the metal-semiconductor (MS) contact has been established. Upon intimate contact, electrons from the CB of the semiconductor, possessing higher energy than the metal electrons, migrate into the metal until the Fermi levels on both sides align. Consequently, the free electron concentration near the boundary decreases, leading to an increased separation between the CB edge (E_C) and the Fermi level (E_F), causing E_C to bend upwards [Fig. 2.3(b)]. This electron transfer results in a positive charge of ionized donors left in the semiconductor region, depleting it of mobile electrons. Simultaneously, a narrow layer of negative charge forms on the metal region, creating an electric field aligning from the semiconductor region to the metal. As the band gap of the semiconductor remains unchanged upon metal contact, the valence band (VB) edge (E_V) moves up parallel to E_C. The vacuum level in the semiconductor undergoes similar variations as E_C, gradually approaching the metal's vacuum level to maintain continuity. The degree of band bending equals the gap between the two vacuum levels, equivalent to the distance between the two work functions $qV_i = (\phi_m - \phi_s)$, where V_i is the contact potential difference or built-in potential of the junction. An electron transitioning from the semiconductor to the metal must cross a potential barrier of qV_i. However, when viewed from the metal region to the semiconductor, the barrier value changes and is given by:

$$\phi_B = \phi_m - \chi_s \tag{2.9}$$

Considering,

$$\phi_s = \chi_s + \phi_n \tag{2.10}$$

the barrier becomes,

$$\phi_B = qV_i + \phi_n \tag{2.11}$$

where $\phi_n = (E_C - E_F)$ and q represents the electronic charge. Here, eq. 2.9 was formulated by Schottky and independently by Mott, referred to as the Schottky limit. The rectifying nature of the MS contact will be explored in the following section.

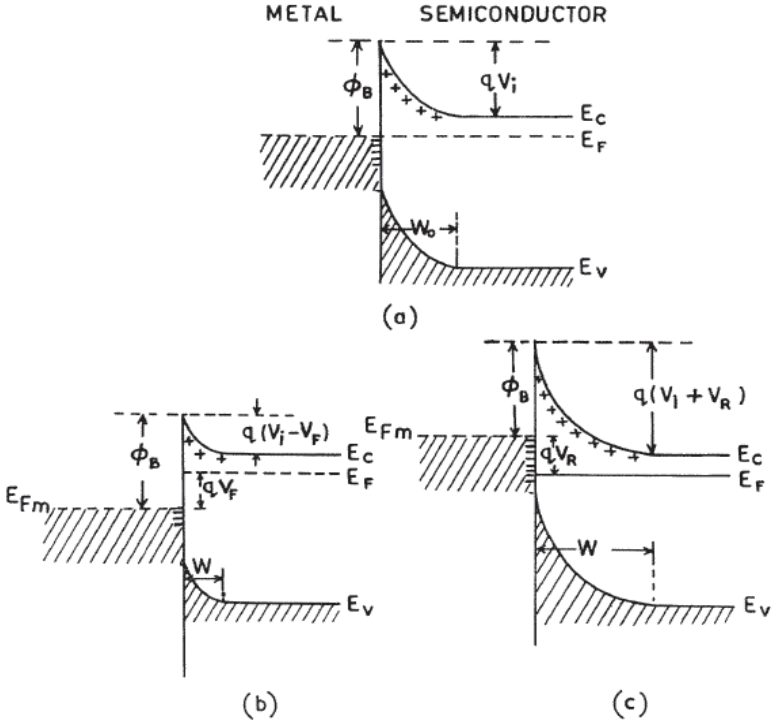

Fig. 2.4: Energy band diagrams of the rectifying contact with a metal and a n-type semiconductor. (a) the thermal equilibrium, (b) the forward bias and (c) the reverse bias condition.

The energy band diagram of the MS contact at thermal equilibrium is depicted in Fig. 2.4. In this state, the rate at which electrons traverse the barrier from the semiconductor to the metal is counterbalanced by the rate at which they travel across the barrier from the metal to the semiconductor, resulting in no net current flow. The semiconductor becomes negatively biased relative to the metal by a voltage $V=V_F$, causing

the width of the depletion region to decrease. Consequently, the voltage across this region reduces from V_i to (V_i-V_F), as displayed in Fig. 2.4(b). Electrons in the semiconductor region encounter a reduced barrier, leading to an increased electron flow from the semiconductor towards the metal compared to the thermal equilibrium value. However, ϕ_B remains unaffected by the bias voltage. Consequently, the electron flux from the metal to the semiconductor does not change from equilibrium. Therefore, when a negative bias is applied to the semiconductor, there is a net movement of electrons from the semiconductor to the metal, resulting in a current in the direction from the metal to the semiconductor. This polarity causes the junction to be forward-biased and the current rises exponentially with the applied voltage V_F. Fig. 2.4(c) illustrates the energy band diagram for a reverse-biased contact. Further, when a positive bias is applied to the semiconductor relative to the metal ($V= -V_R$), the potential drop over the depletion region increases to ($V_i + V_R$). As a result, the electron flow from the semiconductor to the metal decreases below the equilibrium value, while the flow from the metal region remains unaltered. This causes a current flow in the opposite direction (i.e., from the semiconductor to the metal) which is typically smaller than the forward current and thus, the metal-semiconductor (MS) contact behaves as a rectifying junction.

The preceding description pertains exclusively to n-type semiconductors, where $\phi_s<\phi_m$. The energy band diagrams for an n-type semiconductor with $\phi_m<\phi_s$ are illustrated in Fig. 2.5. In Fig. 2.5(a), the energy bands illustrate the state of the materials when they are separated. Following the contact, electrons migrate from the metal into the CB of the semiconductor, resulting in a positive charge on the metal and electrons accumulate in the semiconductor region at the interface. Upon reaching equilibrium, the Fermi level in the semiconductor rises by (ϕ_s-ϕ_m) as depicted in Fig. 2.5(b). The charge in the accumulated region of the semiconductor is localized within the thickness approximately equivalent to the Debye length, effectively forming a surface charge.

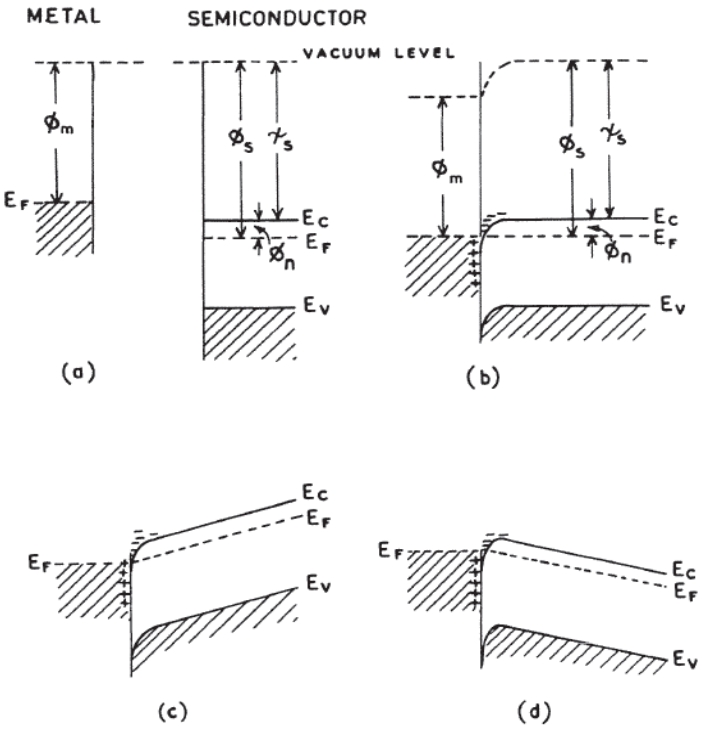

Fig. 2.5: Energy band diagrams for metal contact on an n-type semiconductor where $\phi_m<\phi_s$: (a) Neutral materials when they are separate from one another; (b) Contact at thermal equilibrium; (c) Negative bias and (d) Positive bias on the semiconductor.

Due to the high concentration of electrons in the metal, the positive charge on the metal region also constitutes a surface charge within a small distance (~0.5 Å) at the MS interface. Thus, there is neither a depletion region nor a potential barrier to prevent electrons from migrating from the semiconductor towards the metal or vice versa.

The electron concentration in the vicinity of the interface increases, and the bulk semiconductor region attains the highest resistance in the system. Almost all of the externally applied voltage is distributed across the bulk region, as depicted in Fig. 2.5(c) and Fig. 2.5(d) for the two current flowing directions. It is evident that the current is governed by the bulk-region resistance and remains unaffected by the direction of the applied bias. This type of non-rectifying contact is commonly known as an Ohmic contact.

For n-type semiconductors, an MS contact is known to be rectifying if $\phi_m>\phi_s$ and is non-rectifying if $\phi_m<\phi_s$. Conversely, for a metal-p-type semiconductor contact, the opposite phenomena occur. When $\phi_m<\phi_s$, the energy band diagrams for separate materials are depicted in Fig. 2.6(a). After the contact, electrons flow from the metal into

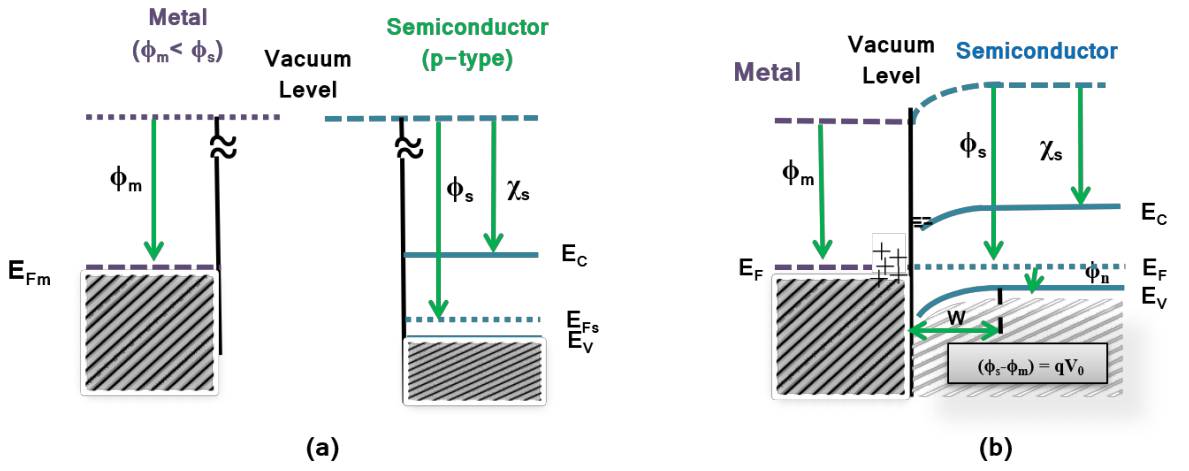

Fig. 2.6: Electron energy band diagrams of metal contact on p-type semiconductor with $\phi_m<\phi_s$ (a) Neutral and separated materials and (b) at thermal equilibrium after the contact has been formed.

the semiconductor until the Fermi levels on both sides align. These electrons, being minority carriers in the p-type semiconductor, subsequently recombine with holes, forming a space-charge layer of ionized acceptors, as illustrated in Fig. 2.6(b). The hole concentration in the space-charge region is significantly smaller in comparison with the acceptor concentration, resulting in the space-charge region on the semiconductor region consisting of a depleted region whose thickness (W_0) depends on the concentration of ionized acceptor atoms.

For p-type semiconductors, barriers for holes in the band diagram must be considered. The barrier height for holes is determined by the following relation:

$$\phi_{B'} = \chi_s + E_g - \phi_m \qquad (2.12)$$

where E_g is the band gap of the semiconductor. From equations (2.9) and (2.10), it follows that,

$$\phi_B + \phi_{B'} = E_g \qquad (2.13)$$

Similar to the discussion for n-type semiconductors, it can be shown that a contact formed by a metal and a p-type semiconductor is non-rectifying if $\phi_m>\phi_s$. However, it is observed that Schottky barriers with p-type semiconductors typically exhibit smaller barrier heights and are infrequently utilized in practical devices.

2.3.2. Modifications of Schottky Theory

Metal-semiconductor contacts in practical scenarios often deviate from the guidelines outlined above. Specifically, eq. (2.9) indicates that the barrier height (ϕ_B) varies linearly with the metal work function (ϕ_m). This strong dependence on ϕ_m is prominent in predominantly ionic semiconductors. However, in many covalent semiconductors, the barrier height exhibits less sensitivity to ϕ_m, and in some cases, it is nearly independent of ϕ_m.

Bardeen was the first to elucidate that the barrier height in covalently bonded semiconductors is insensitive to the metal work function. He highlighted the significance of localized surface states in determining the barrier height. At the semiconductor's surface, the periodicity of the crystal lattice comes to an end. In a covalent crystal, surface atoms only have neighbours on the semiconductor region, and on the vacuum region, there are no neighbours available for covalent bonds. Consequently, each surface atom has a broken covalent bond with one electron present and the other missing, known as a dangling bond. These dangling bonds create localized energy states at the semiconductor's surface, with energy levels situated within the forbidden gap.

These surface states generally form a continuous distribution in the band gap, characterized by a neutral level (ϕ_0). The position of the ϕ_0 is such that, in the absence of band bending in the semiconductor, the states are filled by electrons up to ϕ_0, rendering the surface electrically neutral. When states below ϕ_0 are occupied or empty, they behave like donors or positive, and when they are unoccupied, they function like acceptors. The density of surface states on covalent semiconductor surfaces can substantially decrease the presence of adsorbed layers of foreign atoms, which can complete the broken covalent bonds.

The presence of surface states has a notable impact on the charge distribution in the depletion region, influencing the barrier height. In Fig. 2.7(a), the energy band diagram of an n-type semiconductor with flat-band conditions is depicted. This state is characterized by non-equilibrium conditions, transitioning to equilibrium when electrons from the semiconductor near the surface occupy states above ϕ_0, aligning the Fermi level at the surface with that in the bulk. This leads to a negatively charged surface and the creation of a depletion region comprising ionized donors on the semiconductor side near the surface. Due to this dipole, a potential barrier is established in the direction

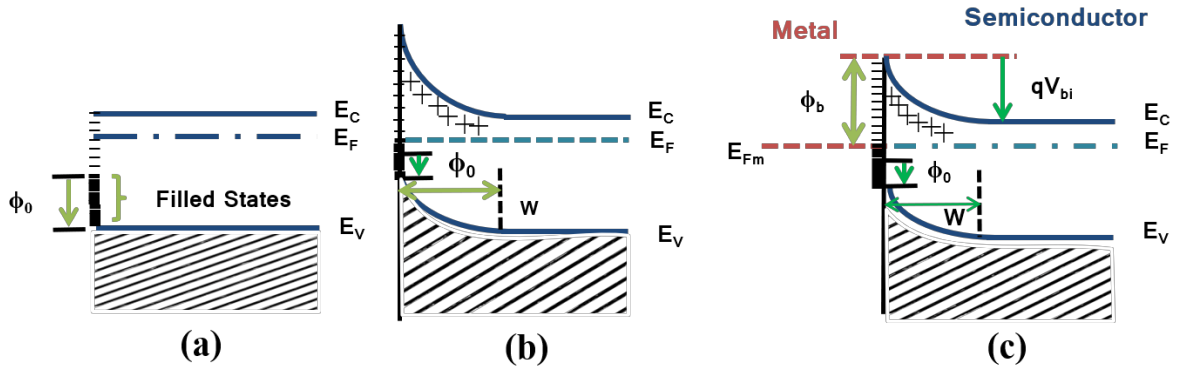

Fig. 2.7: Energy band diagrams of n-type semiconductors incorporating surface states. The diagrams depict (a) a flat-band at the surface, (b) a surface in thermal equilibrium with the bulk, and (c) a semiconductor in contact with a metal.

from the surface to the semiconductor, even when there is no metal contact, as displayed in Fig. 2.7(b).

Upon introducing a metal into contact with the semiconductor and reaching equilibrium, the Fermi level in the semiconductor changes, exchanging charge with the metal. If the density of surface states at the semiconductor surface is substantial, the charge exchange predominantly occurs between the metal and the surface states, with minimal impact on the space charge in the semiconductor. Consequently, the barrier height in Fig. 2.7(c) becomes independent of the metal work function and is determined by the expression:

$$\phi_B = (E_g - \phi_0) \qquad (2.14)$$

In this scenario, the barrier height is termed "pinned" by surface states, and eq. (2.13) is denoted as the Bardeen limit.

2.4. Classification of Metal-Semiconductor Interfaces

The interfaces between metals and non-metals can be systematically classified into four primary types based on the resulting atomic configuration at the interface. These categories are as follows:

Type I: This category involves non-metal acting as an insulator or semiconductor, where the metal is physiosorbed onto its surface. This type of interface exhibits ideal Schottky barrier contact, where the barrier height directly varies with the metal work function.

Type II: In this type, the non-metal is a highly polarizable semiconductor, such as silicon, with a dielectric constant (ε_r) greater than 7. The metal forms a weak chemical bond with the semiconductor surface, without reacting to create a bulk compound. They resemble a "Bardeen barrier," assuming that surface states are spread over the space in the semiconductor, allowing for a potential drop across this region. The barrier height in decent contacts of this type is expected to exhibit a weak dependence on ϕ_m.

Type III: In Type III interfaces, the highly polarizable semiconductor undergoes a chemical reaction with the metal, leading to the formation of one or more chemical compounds. They represent a scenario of strong chemical bonding between the metal and the semiconductor. The barrier height is expected to be influenced by factors related to chemical or metallurgical reactions occurring at the interface.

Type IV: This type involves the formation of a thin film of native oxide during the surface preparation of a highly polarizable semiconductor. This film acts as an interfacial layer, hindering intimate contact between the metal and the semiconductor. This type of interface is frequently encountered in practical metal-semiconductor devices; this case involves a brief discussion in the subsequent section.

2.5. Contacts with Surface States and an Insulating Interfacial Layer

In the majority of metal-semiconductor contacts, the semiconductor surface, before metal deposition, undergoes chemical cleaning, resulting in the presence of a thin insulating oxide layer on its surface. The thickness of this interfacial layer is contingent upon the surface preparation method and, for optimal Schottky contacts, should be maintained

below approximately 20 Å. The energy band diagram illustrating a contact with an interfacial oxide layer is depicted in Fig. 2.8.

As previously elucidated, the Fermi level remains uniform throughout the system,

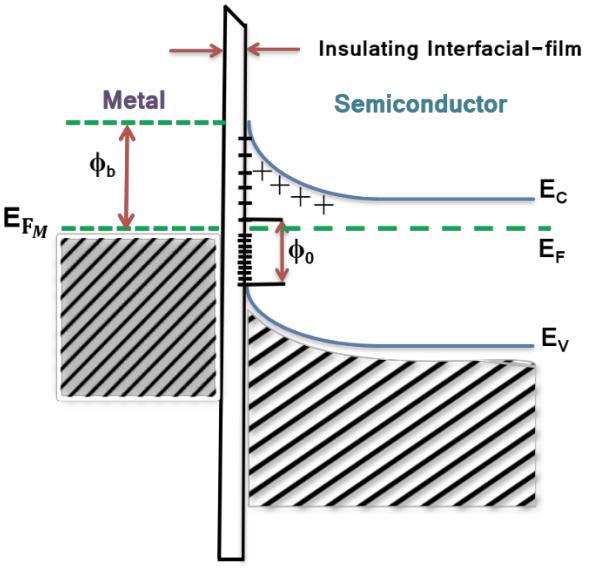

Fig. 2.8: Energy band diagram of a metal-semiconductor contacts with surface states and interfacial layer.

and the vacuum level exhibits continuity along the interface. The potential linearly drops across the interfacial oxide layer (Fig. 2.8), assuming it to be an ideal insulator with no charge. Furthermore, it is presumed that the lower edge of the CB in the insulator lies beneath the vacuum level. In instances where the interfacial layer is sufficiently narrow (i.e. <20 Å), the potential drop along it is insignificantly small in comparison to that in the semiconductor depletion region. This thin region is electron-transparent, allowing electrons to tunnel through it bi-directionally. Consequently, the ϕ_B and V_i remain largely unchanged by the presence of this thin interfacial layer.

Contacts featuring a thin insulating layer between the metal and semiconductor prove more amenable to theoretical understanding and analysis than their decent and strong counterparts. This is attributed to the insulating layer acting as a separator, enabling the treatment of the metal and semiconductor as distinct systems. Consequently, one can consider interface states as a characteristic of the specific semiconductor-insulator combination, disregarding any alterations in the surface dipole contributions to the work functions of the metal and semiconductor. Such simplifications are not applicable when dealing with clean contacts.

2.6. Fabrication Process of Schottky Diodes

Material Selection: In the fabrication of Schottky diodes, metal choice is crucial and is determined by the semiconductor type. Aluminium (Al) or platinum (Pt) is commonly preferred for n-type semiconductors to establish a rectifying contact. Despite silver's (Ag) excellent electrical conductivity, its susceptibility to oxidation limits its use in metal-semiconductor junctions. In thin film applications, indium tin oxide (ITO) on a glass substrate is utilized for its resilience at elevated temperatures. Silicon wafers with specific orientation, thickness, and resistivity are selected for silicon-based Schottky diodes.

Cleaning: To ensure an uncontaminated surface, ITO/wafers undergo meticulous cleaning with trichloroethylene, acetone, and methanol solvents. The final cleaning step involves using a 30-40% HF etching solution[11].

Rinsing: Wafers are rinsed in deionized (DI) water repeatedly before subsequent deposition procedures.

Deposition of Semiconducting Materials: The materials to be used as the semiconducting layer are deposited onto the ITO glass substrate with the help of Spin coating units with a rotation of a certain rpm. Any other PVD methods, such as evaporation by electron beam can also be used to deposit the films of the semiconducting materials.

Ohmic Contact Formation: Ohmic contacts on the back side of silicon wafers are established for efficient electrical connections to semiconductor regions. High-purity aluminium or the chosen metal is deposited using vacuum coating units, maintaining a constant low pressure for uniformity up to a few tens of nanometers. Annealing optimizes temperature, duration, and pressure, facilitating inter-diffusion and forming well-defined Ohmic contacts.

Schottky Contacts: Before metal deposition, silicon wafers are cleaned and etched in a 40% HF solution to remove the native oxide layer. A thin layer of the chosen metal is then applied to the semiconductor surface using deposition techniques such as sputtering or evaporation, with thickness controlled for desired electrical characteristics. A few optional steps are:

Photolithography: Photolithography defines the Schottky contact area by applying photoresist, exposing it to UV light through a mask, and developing the pattern through chemical processing.

Etching: Precision etchants selectively remove metal in exposed regions, defining the final geometry of the Schottky diode.

Passivation: Optionally, a passivation layer is deposited over the Schottky diode to enhance long-term stability and shield it from environmental factors.

2.6.1. Aluminium in Device Fabrication

Aluminium, the Earth's most abundant metal, stands out for its exceptional malleability, ductility, and lightweight characteristics. Compared to numerous other metals, it exhibits a relatively soft nature. Beyond its mechanical attributes, aluminium demonstrates commendable electrical and thermal conductivity while maintaining reasonable resistance to corrosion. Remarkably environmentally friendly, it can be recycled without compromising any of its intrinsic properties. In contrast, platinum, a more expensive and heavier metal, has a higher work function of 5.65 eV, in stark contrast to aluminium's lower work function of 4.2 eV.

2.6.2. Glass Substrate Coated with Indium Tin Oxide (ITO)

Indium Tin Oxide (ITO) is a compound consisting of indium (In), tin (Sn), and oxygen (O), with a composition of 74% In, 18% Sn, and 8% O. Widely recognized for its combination of electrical conductivity, optical transparency, ease of deposition as a thin layer, and moisture resistance, ITO stands out as one of the most commonly employed transparent conducting oxides. Typically, thin films of indium tin oxide are deposited onto glass surfaces using physical vapour deposition techniques. These films exhibit an optical transmittance exceeding 80% for thin layers, accompanied by a low electrical resistivity of only 10^{-4} Ω-cm[12].

2.6.3. Metal Deposition

The fabrication of metal-semiconductor junctions follows a vertical sandwich configuration, specifically Al/synthesized material/ITO, chosen for its simplicity in junction fabrication. Initial to this process is the meticulous cleaning of the ITO, necessitating a thorough cleaning procedure. The ITO-coated glass substrates undergo a

sequential cleaning process involving ultra-sonication with a mild basic water solution (containing a small amount of purified sodium hydroxide in distilled water), followed by rinsing with acetone, ethanol, and distilled water. Subsequently, the synthesized material is dispersed/dissolved in a suitable medium under ultra-sonication and is spin-coated on the pre-cleaned ITO substrate at a specified rpm for multiple cycles. The resulting films are then dried in a vacuum chamber for several hours.

The next step involves the deposition of aluminium metal on the thin film of the material through thermal evaporation. This process employs an electron gun within the vacuum coating unit, maintaining a low pressure, generally at 10^{-6} mbar. To define the metal-semiconductor interface precisely, a shadow mask is employed during metal deposition, ensuring an effective junctional area of 7.065×10^{-6} m^2. The schematic structure of the fabricated Schottky diode is provided in the following Fig. 2.9.

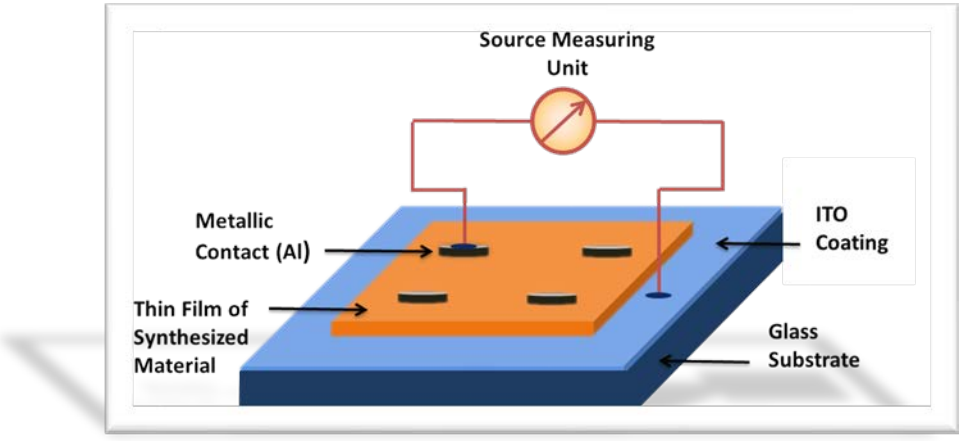

Fig. 2.9: Schematic diagram of fabricated MS junction Schottky diode.

2.7. Electrical Studies of Schottky Barrier Diodes

There are different ways to measure the important Schottky diode parameters (e.g. ideality factor, barrier height and series resistance) and charge transport parameters (e.g. mobility and transit time). They are described shortly in the following section.

2.7.1. Evaluation of Ideality Factor, Barrier Height and Series Resistance

In Schottky barrier diodes constructed on high mobility semiconductors like Si and GaAs, the current is attributed to the thermionic emission of electrons across the barrier and its dependence on the applied bias V is expressed by the relationship:

$$I = I_0 \left[exp\left(\frac{qV}{\eta kT}\right) - 1 \right] \quad (2.15)$$

where,

$$I_0 = A_{eff} A^* T^2 \, exp\left(\frac{-\phi_B}{kT}\right) \quad (2.16)$$

Here, η represents the diode ideality factor, and A^* denotes the modified Richardson constant for the semiconductor. For forward bias values of V exceeding 3kT/q, the ln (I) vs. V plot yields a linear relationship. By extrapolating this line to V = 0, I_0 can be determined. Utilizing I_0, A^*, the diode cross-sectional area A_{eff}, and the temperature T, the zero bias barrier height (ϕ_B) is computed, accounting for the image force barrier lowering distance ($\Delta\phi_B$).

In situations where A^* is unknown, the barrier height can still be deduced. Forward I-V characteristics of the diode are acquired at various temperatures, and I_0 is determined for each temperature. The $\ln(I_0/T^2)$ versus 1/T plot results in a straight line, with the slope offering the barrier height ϕ_B, and the intercept on the I_0/T^2 axis providing the value of A^*.

$$ln\left(\frac{I_0}{T^2}\right) = ln\left(A_{eff} A^*\right) - \frac{\phi_B}{kT} \quad (2.17)$$

The method yields the barrier height at 0K, marginally higher than the room-temperature barrier height. Real devices often exhibit deviations from ideal behaviour, with the emergence of a significant series resistance R_s at higher currents, encompassing the series resistance of the semiconductor, metal, and contacts. Thus,

$$V_{eff} = V - IR_S \quad (2.18)$$

Now, equation (2.15) can be rearranged as,

$$I = I_0 \left[exp\left\{\frac{q(V - IR_S)}{\eta kT}\right\} - 1 \right] \quad (2.19)$$

In forward bias, for V >kT/q and V >> IR_S, it can be derived from the diode equation that:

$$\frac{dV}{d(ln\, I)} = \left(\frac{\eta kT}{q}\right) + IR_S \quad (2.20)$$

The value of η and R_s can be estimated from the intercept and the slope of the straight line of the dV/d(ln I) vs. I plot.

2.7.2. Estimation of Mobility and Transit Time

The I-V characteristics can further be analysed by interpreting the charge carrier's mobility (μ_{eff}) and lifetime (τ) using the space-charge limited current (SCLC) theory to elucidate the charge transport mechanism for various photo-induced applications[13]. Plotting log (I) against log (V) for positive voltages reveals distinct linear regions indicative of different conduction mechanisms. In metal-semiconductor junctions, interfacial trap states significantly influence charge carrier conduction, thereby altering I-V characteristic curves. At low bias, Ohmic behaviour ($I \alpha V$) with a slope near unity is observed, indicating predominant conduction by intrinsic charge carriers[14]. Subsequently, as the slope increases (typically reaching 2), injected carriers from the contacts begin to dominate over intrinsic carriers for intermediate potential values, establishing a spatially distributed charge field. Mobility primarily governs quadratic current ($I \alpha V^2$) in this region[13,15]. Eventually, at higher applied voltages, the device surpasses the trap-filled limit, resulting in conduction primarily through 'trap-free space-charge limited current' characterized by power-law behaviour ($I \alpha V^n$, where $n > 2$), corresponding to region III[15].

The mobility of electrons is estimated from the slope of the I vs. V^2 plot, according to the Mott-Gurney equation[15]:

$$I = \frac{9\mu_{eff}\varepsilon_0\varepsilon_r A_{eff}}{8}\left(\frac{V^2}{d^3}\right) \qquad (2.21)$$

where, A_{eff}, ε_0, ε_r and d stand for the effective diode area, the free space permittivity, the dielectric constant of materials and the thickness of the diode, respectively.

Here, the dielectric constant (ε_r) of the synthesized materials could be estimated from the capacitance (C) vs. frequency (f) plot, obtained from the measurement by an impedance analyser.

$$\varepsilon_r = \frac{C_0 d}{\varepsilon_0 A_{eff}} \qquad (2.22)$$

where, C_0 is the saturated capacitance[16].

Also, the lifetime or transient time (τ) of the charge carriers could be deduced by employing the following equation[17]:

$$\tau = \frac{9\varepsilon_0 \varepsilon_r A_{eff}}{8d}\left(\frac{V}{I}\right) \quad (2.23)$$

2.7.3. Capacitance-Voltage Measurement

In the capacitance-voltage measurement approach, the diode capacitance is evaluated concerning the applied reverse bias. When subjecting a reverse-biased diode to a small AC voltage of a few millivolts, the depletion region capacitance C is defined by the equation:

$$C = A_{eff}\left[\frac{\varepsilon_S q N_d}{2\left(V_i + V_R - \frac{kT}{q}\right)}\right]^{\frac{1}{2}} \quad (2.24)$$

where A_{eff} represents the cross-sectional area of the diode, ε_S the permittivity of the semiconducting material used, V_R is the applied reverse voltage, and all other symbols maintain their conventional meanings. This formulation assumes the absence of a significant interfacial oxide layer in the diode and uniform donor concentration N_d in the n-type semiconductor. Notably, a plot of $1/C^2$ versus V_R yields a linear relationship with a slope of $(2/A_{eff}^2 \varepsilon_S q N_d)$ and an intercept on the voltage axis $V_0=(V_i-kT/q)$. The slope enables the determination of the dopant concentration N_d, and as $qV_i = (\phi_B - \phi_n)$, the barrier height ϕ_B is derived as:

$$\phi_B = qV_0 + \phi_n + kT \quad (2.25)$$

Here, the kT factor accounts for the contribution of the majority carriers to the space charge, and eq. (2.17) excludes the image force barrier lowering.

2.7.4. Photoelectric Measurement

The photo-electric measurement stands out as the direct and most accurate approach for estimating the barrier height (ϕ_B). In this method, a monochromatic light is directed onto a metal in contact with a semiconductor. If the photon energy ($h\nu$) exceeds the barrier height (ϕ_B) but is less than the band gap of the semiconductor, the incident photons cause electron excitation from the metal over the barrier. The resulting photocurrent (I_{ph}) for $(h\nu - \phi_B) \gg 3kT$ is described by the Fowler theory as:

(2.26)

where B represents the proportionality constant. When I_{ph} is plotted against hν, a straight line is generated and the intercept of the hν axis provides the value of ϕ_B.

2.7.5. Application of Schottky Diodes

Schottky diodes exhibit a superior current drive capability compared to typical p-n junctions and, contingent on the Schottky barrier height (SBH), manifest a larger saturation current. Consequently, in circuit applications necessitating high current and low voltage, Schottky diodes emerge as the favoured rectifying devices. Moreover, Schottky diodes avoid issues associated with minority carriers, as they do not face the limitations tied to minority carrier recombination time that are inherent in a p-n junction. This characteristic makes Schottky diodes notably faster, which makes them suitable for use in digital logic circuits as rapid switches. High-speed Schottky photodiodes find applications in optical measurements and communication technologies. Schottky junctions also serve as cost-effective photovoltaic cells. Additionally, metal-semiconductor contacts play a pivotal role as gate electrodes in field-effect transistors, the drain and source contacts in MOSFETs, the electrodes for high-power IMPATT oscillators, and the third terminal in a transferred-electron device.

2.8. Impedance Spectroscopy (IS)

In the late nineteenth century, Oliver Heaviside introduced the non-destructive technique of Impedance Spectroscopy, which later evolved based on complex mathematical transforms. He contributed terminologies such as Impedance, Admittance, and Conductance. A. E. Kennelly and C. P. Steinmetz further developed this approach[18], representing it through vector diagrams and complex illustrations. Impedance spectroscopy is a potent method for characterizing the electrical properties of materials and interfaces between materials and electrodes. It is applicable for analysing the dynamics of bound and mobile charges in the bulk and interfacial regions of various materials, including ionic, semiconducting, mixed electronic-ionic, and insulators (dielectrics). A significant benefit of impedance spectroscopy for studying the electrical and electrochemical properties of materials and systems is the direct correspondence often seen between the behaviour of a real system and that of an equivalent model circuit made up of distinct electrical components. Researchers often analyze or fit impedance

data to an equivalent circuit that represents the physical processes occurring in the material and at the interfaces.

2.8.1. Associated Functions in Impedance Spectroscopy

Impedance, a more comprehensive concept than resistance, incorporates phase variations, making it a fundamental idea in electrical engineering. Impedance spectroscopy is characterized by the measurement and analysis of the four impedance-related functions: Z, Y, M, and ε. The visualization of these functions in the complex plane, as we will investigate, is very advantageous for interpreting the small signal AC response of the electrode material system being studied. The utilization of Z and Y in analysing the response of electrical circuits composed of lumped (ideal) components (R, L, and C) dates back to the early stages of electrical engineering. A significant achievement in the analysis of real systems, particularly those distributed in space, was made by Cole and Cole [1941] through the plotting of ε' and ε" for dielectric systems in the complex plane, now known as a Cole-Cole plot. Moreover, Z and/or Y have found extensive application in the theoretical treatment of semiconductor and ionic systems. Complex plane plots are sometimes referred to as Nyquist plots.

Impedance, defined as a complex quantity, is real when θ=0, representing purely resistive conductance, when $Z(\omega) = Z'(\omega)$. In this situation, the impedance remains constant regardless of frequency. However, when Z' is recognized as a frequency-dependent characteristic, the Kronig-Kramers (Hilbert integral transform) and Macdonald, Brachman [1956] approach to integrate the real and imaginary components to ensure that Z'' cannot be zero across all frequencies but should vary with frequency.

Impedance is expressed as $Z^*(\omega) = Z'(\omega) - jZ''(\omega)$; where $Z'(\omega)\{=|Z|\cos\theta\}$ and $Z''(\omega)\{=|Z|\sin\theta\}$ are real and imaginary parts of the total impedance. In impedance spectroscopy, various measured or derived quantities associated with impedance play pivotal roles. The admittance is represented as, $Y = Z^{-1} = Y' + jY''$. In the complex plane, we can express v=Zi or i=Yv, where v, i, and Z are treated as complex. It is additionally standard in impedance spectroscopy to denote Z and Y as far as resistive and capacitance parts as $Z = R_S(\omega) - jX_S(\omega)$ and $Y = G_P(\omega) + jB_P(\omega)$, where the expressions signify as reactance, $X_S = \{\omega C_S(\omega)\}^{-1}$ and the susceptance, $B_P = \{\omega C_P(\omega)\}$. Here the subscripts s

and p mean "Series" and "Parallel", respectively. The other two quantities are normally characterized as the modulus function $M = j\omega C_0 Z = M' + jM''$ and the complex dielectric constant or dielectric permittivity is denoted as $\varepsilon = M^{-1} = Y/(j\omega C_0) = \varepsilon' - j\varepsilon''$. In the above equations, $C_0 = \varepsilon_0 A/l$ C_0 is the capacitance of the empty measuring cell, where A, l and ε_0 denotes the electrode area, separation length and the dielectric permittivity of free space, respectively. The relations among the four impedance functions are presented in Table 2.1.

Table. 2.1: *Relation between the four Impedance functions*[18]*.*

	Z	**Y**	**M**	**ε**
Z(=Z′-jZ″)	Z	Y^{-1}	$M/j\omega C_0$	$1/j\omega C_0\varepsilon$
Y(=Y′+jY″)	Z^{-1}	Y	$j\omega C_0/M$	$j\omega C_0\varepsilon$
M(=M′+jM″)	$j\omega C_0 Z$	$j\omega C_0/Y$	M	ε^{-1}
ε (=ε′-jε″)	$1/j\omega C_0 Z$	$Y/j\omega C_0$	M^{-1}	ε

2.8.2. Nyquist and Bode plot: Conduction of Carriers

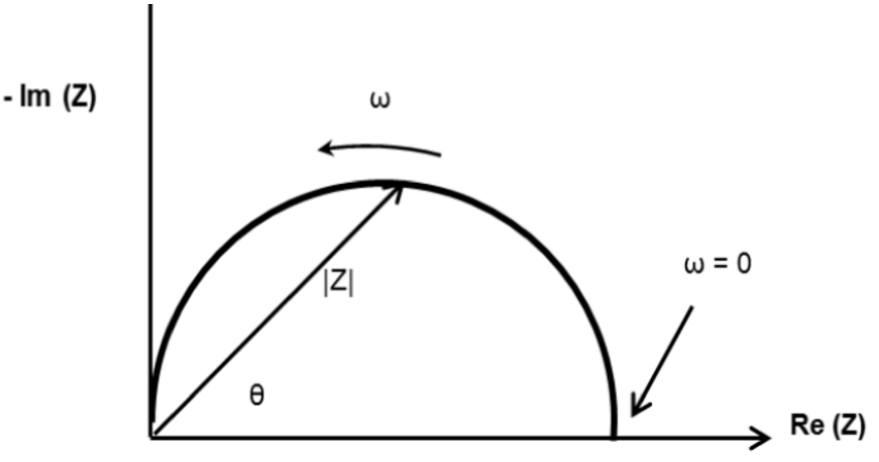

Fig. 2.10: Schematic Nyquist plot

The Nyquist diagram (Fig. 2.10), sheds light on the conduction mechanism of the materials and the material-electrode interface. It is the plot between the real and

imaginary parts of the impedance. In an ideal scenario, the Nyquist plot shows one or more perfect or depressed semicircles, which provide insight into the quantity and kind of relaxations occurring within the conduction mechanism. Occasionally, the instrument's limitations prevent the semicircles from being completed. The materials and experiment type affect the frequency range. In Nyquist plot, the frequency increases from right to left of Z′ axis. In Impedance Spectroscopy, the Bode plot is yet another crucial presentation. For the applied frequency (logarithm), it shows the fluctuation in phase angle and the logarithm of the impedance magnitude. The information about the change in impedance nature from low frequency to high frequency can be found in the Bode plot. Additionally, it offers a fundamental understanding of the time constant and corresponding resonance frequency for any material electrode system or device.

2.8.3. Equivalent Circuit Model

Impedance data, often represented in graphical plots showing impedance, dielectric properties, or modulus, is typically analyzed by fitting it to an equivalent electrical circuit model. Various basic electrical circuits, comprising combinations of ideal resistors and capacitors, are used to create representative impedance data plots. In practical settings, the impedance of an unknown system is first measured, generating impedance data plots. These plots are then compared with those of established equivalent circuits, leading to an initial selection of a circuit that best matches the experimentally obtained impedance data and offers a plausible explanation of the observed phenomenon. The choice of equivalent circuits should be guided by an intuitive understanding of the electrochemical system, relying on the chemical and physical properties of the system rather than randomly selected circuit elements[19]. Most circuit components in the model are fundamental electrical elements, such as resistors, capacitors, and inductors. It is essential to recognize that impedance analysis is an intricate endeavour, encompassing physical, chemical, electrical, and mechanical components translated into electrical terms. Impedance data is often fitted with an equivalent circuit that includes circuit elements corresponding to the physical processes occurring within the investigated device. While ideal circuit components like resistors and capacitors can often be applied, real systems may exhibit deviations from ideal behaviour. Generally, a combination of distributed circuit components, such as the constant phase element (CPE) and the

Warburg diffusion impedance, is required to adequately describe the impedance response of real systems, acknowledging their non-ideal nature (Table 2.2)[18,20].

Table. 2.2*: The circuit components utilized in the Equivalent circuit (EC) model*[18]*.*

Components	Units	Equivalent Element	Impedance
Resistor	Ohm	R	R
Capacitor	F or Ohm^{-1} S	C	$\frac{1}{j\omega C}$
Inductor	H or Ohm S	L	$j\omega L$
Infinite Diffusion	Ohm	Z_W	$\frac{R_W}{\sqrt{(j\omega)}}$
Finite Diffusion	Ohm	Z_0	$\frac{R_0 \tanh\left(\sqrt{\frac{j\omega L_0^{'}}{D}}\right)}{\sqrt{\frac{j\omega L_0^{2}}{D}}}$
Constant Phase Element	Ohm^{-1} S^{α}	Q	$\frac{1}{Q(j\omega)^{\alpha}}$

***

References

1. A. W. Burton, K. Ong, T. Rea and I. Y. Chan, Microporous and Mesoporous Materials, 2009, **117**, 75-90.

2. G. Williamson and W. Hall, Acta metallurgica, 1953, **1**, 22-31.

3. S. K. Suram, P. F. Newhouse and J. M. Gregoire, ACS combinatorial science, 2016, **18**, 673-681.

4. F. Reicha, M. Ishra and M. M. Gabr, Journal of Physics and Chemistry of Solids, 2003, **64**, 1157-1161.

5. F. Braun, Ann. Phys, 1875, **229**, 556.

6. S. M. Sze, Y. Li, and K. K. Ng, *Physics of Semiconductor Devices*, John wiley & sons, 2021.

7. W. Schottky, R. Stormer, and F. Waibel, Z. Hoch Freq, 1931, **37**, 162.

8. W. Schottky, Naturwissenschaften, 1938, **26**, 843.

9. N. F. Mott, Math. Proc. Cambridge Philos. Soc, 1938, **34**, 568.

10. B. L. Sharma, *Metal-Semiconductor Schottky Barrier Junctions and Their Applications*, Springer Science & Business Media, 2013.

11. R. Kumar and S. Chand, Solid State Sci, 2016, **58**, 115.

12. J. Hass, R. Feng, T. Li, X. Li, Z. Zong, W. A. De Heer, P. N. First, E. H. Conrad, C. A. Jeffrey, and C. Berger, Appl. Phys. Lett, 2006, **89**, 143106.

13. I. Ullah, M. Shah, M. Khan, and F. Wahab, J. Electron. Mater, 2016, **45**, 1175.

14. İ. Taşçıoğlu, U. Aydemir, and Ş. Altındal, J. Appl. Phys, 2010, **108**, 064506.

15. M. Soylu and B. Abay, Phys. E Low-Dimensional Syst. Nanostructures, 2010, **43**, 534.

16. K. C. Kao, *Dielectric Phenomena in Solids*, Elsevier, 2004.

17. S. Sil, A. Dey, J. Datta, M. Das, R. Jana, S. Halder, J. Dhar, D. Sanyal, and P. P. Ray, Mater. Res. Bull, 2018, **106**, 337.

18. E. Barsoukov and J. R. Macdonald, *Impedance Spectroscopy: Theory, Experiment, and Applications*, John Wiley & Sons, 2018.

19. In *Impedance Spectrosc,* 2012, 1–21.

20. J. R. Macdonald and W. B. Johnson, in *Impedance Spectrosc,* 2005, 1–26.

***

Investigation of particle size-dependent charge transport phenomena in copper sulphide (CuS) synthesized via solvothermal and co-precipitation methods

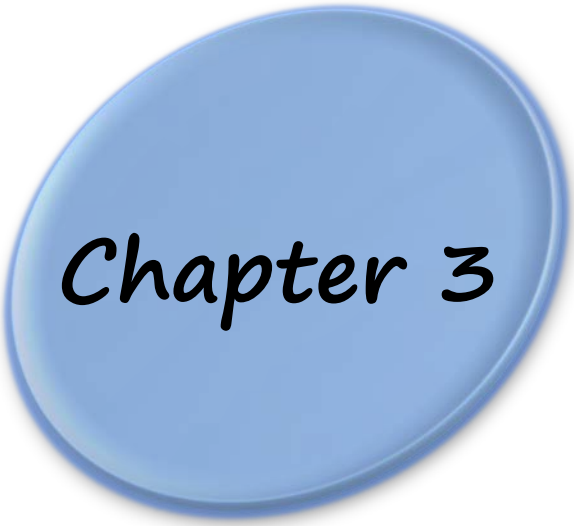

3.1. Introduction

Transition metal chalcogenides have garnered significant attention as electrode materials due to their exceptional chemical and physical properties. Notably, compounds such as CoS, MnS, NiS, and MoS_2 have been explored for their application in supercapacitors[1-4] and other electronic devices. Among these, copper sulfide (CuS), commonly known as 'covellite' stands out as a promising candidate owing to its low cost, abundance, and environmental friendliness[5]. CuS has demonstrated metal-like electronic conductivity and high theoretical capacity and finds utility in various optoelectronic devices and supercapacitors[6]. In recent years, copper sulfide (CuS) has emerged as an earth-abundant transition metal sulfide with several advantageous properties such as non-toxicity, high chemical stability, ease of regeneration, biocompatibility, and a unique optical property which encourages the preparation and study of CuS materials. CuS has a bandgap ranging from 1.3 eV to 2.4 eV[7] and is commonly utilized as a semiconducting material that exhibits a broad variety of application possibilities, including solar cells[8], gas sensors[9], supercapacitors[10], catalysts[11], field-effect transistors[12], memristors[13], and biosensors[14].

Numerous studies, including the reflux method[15], solvothermal[16], sol-gel[17], hydrothermal[18], sonochemical method[19], co-precipitation[20], and microwave-assisted method[21], have investigated the synthesis of this metal chalcogenide (CuS), and its applications in optoelectronic devices. For instance, Dutrizac et al. described a direct metal sulfurization technique involving the heating of copper and sulfur under vacuum at 450 °C[22]. Additionally, Y. Ni et al. utilized microwave irradiation to efficiently synthesize CuS nanoparticles (NPs) using $CuCl_2$ and Na_2S[23]. Armelao et al. introduced a novel method for CuS nanoparticle synthesis based on the fast nucleation of the sulfide by reacting thioacetic acid with water and copper carboxylates[24]. Other synthesis routes include thermolysis[25], physical vapor deposition[26], and template-assisted growth[27]. Despite the success of these methods in producing CuS materials with diverse morphologies, they often involve complex procedures and most of them are not energy-efficient, requiring high temperatures, vacuum environments, multiple reactants, and specialized experimental setups.

In this study, we explore two simpler methods: solvothermal and co-precipitation methods to synthesize CuS nanoparticles and investigate potential changes in their electrical properties by fabricating Metal-Semiconductor (MS) junction Schottky diodes.

The MS junction Schottky barrier diode (SBD) structures have been widely used in electrical and optoelectronic applications in recent days[28]. The development of this type of junction has a significant influence on the performance and quality of the devices[29,30]. MS junctions have numerous potential uses in the electrical as well as electronic industry[31]. The junctions also play a significant role in the characterization of semiconductor materials. At present, significant attempts have been made to improve the optical and electrical characteristics of CuS by modifying its synthesis method. To date, the synthesis process of the semiconducting sulfide has received significant attention from technological viewpoints, as the properties of synthesized materials can be affected by different synthesis processes. In our present work, we demonstrated the synthesis of CuS NPs with flake and hexagonal-like morphologies using co-precipitation and solvothermal methods. Our approach utilizes elemental sources directly in the reaction, offering a cost-effective synthesis route with minimal by-products. This single-step synthesis produces CuS in large quantities, suitable for various applications, and opens avenues for synthesizing other metal sulfides using similar strategies. The electrical properties of the materials were examined immediately following their synthesis by fabricating the SBDs with Al/CuS/ITO configuration. Furthermore, the electrical as well as charge transfer properties of the as-synthesized materials were investigated using the space charge limited current (SCLC) of thermionic emission theory, as discussed later.

3.2. Experimental Section

3.2.1. Synthesis of CuS nanoparticles

The CuS NPs were synthesized via two different techniques: co-precipitation and solvothermal methods. For the synthesis of CuS nanoparticles by co-precipitation method, 0.9664 g (4 mmol) of Copper (II) nitrate trihydrate $Cu(NO_3)_2.3H_2O$ was mixed with 30 mL of ethylene glycol and stirred for 30 minutes (solution A). Then 0.9604 g (4 mmol) of sodium sulphide $Na_2S.9H_2O$ was dissolved in 20 mL of ethylene glycol solution with a magnetic stirrer for 30 minutes (solution B). Finally, solution B was slowly added dropwise into solution A, and the resulting mixture was stirred for 12 hours at 30 °C. The precipitate was then centrifuged and rinsed multiple times with water and subsequently with ethanol. The final sample was collected and dried at 60 °C for 12 hours.

For the synthesis of CuS NPs by solvothermal method, 0.9664 g (4 mmol) of Copper (II) nitrate trihydrate $Cu(NO_3)_2.3H_2O$ was mixed with 30 mL of ethylene glycol and stirred

for 30 minutes (solution A). Then 0.9604 g (4 mmol) of sodium sulphide $Na_2S.9H_2O$ was mixed in 20 mL of ethylene glycol using a magnetic stirrer for 30 minutes (solution B). Finally, solution B was added dropwise into solution A. The resulting mixture was stirred for 2 hours at 30 °C. Then the homogenous solution mixture was transferred to a teflon-lined 100 mL autoclave. The autoclave was then placed in a vacuum oven maintaining a temperature of 150 °C for 12 hours. Next, the precipitate was centrifuged and rinsed several times with water and ethanol. Finally, the collected sample was dried at 60 °C for 12 hours.

3.2.2. Fabrication of Schottky Devices

The proposed Schottky diode based on CuS NPs was fabricated using sandwich configurations of ITO/CuS(solv)/Al and ITO/CuS(co-pr)/Al. For this, two glass substrates with Indium Tin Oxide (ITO) coatings were consecutively cleaned with the help of ultrasonication using a soap solution, pure deionized water, alcohol and acetone for 10 minutes each. CuS(solv) and CuS(co-pr) samples were dissolved into N, N-dimethyl methanamide (DMF) to make a well-dispersed solution and then these solutions were spread on the ITO-coated glasses using the spin coating unit at 800 rpm. The films were then dried at room temperature. The surface profiler estimated that the film thickness was nearly 1μm. Aluminum (Al) has been used as a metal electrode and deposited on the films. The shadow mask was used at the time of deposition on the films to fabricate a MS junction using the electron beam evaporation process. The effective area of the diodes was calculated as 7.065×10^{-6} m^2.

3.3. Materials Characterization Techniques

The crystalline size and phase structure of the synthesized CuS NPs were investigated using a powder X-ray diffractometer (PXRD) of Bruker D8 advance, with Cu-K_α (λ = 1.5418 Å) at 35 kV. A field emission scanning electron microscope (FESEM) of Inspect F50 with and a transmission electron microscope (TEM) of JEOL JEM-2010 were used for the morphological studies. The FTIR spectra of the materials were obtained to understand the bonding mechanisms in solids and on the surfaces using a Shimadzu FTIR Spectrophotometer (Model - 8400S). We used a thermo gravimetric analysis (TGA) of METTLER TOLEDO TGA/SDTA-851-e in the temperature range of 25 to 800 °C with an increment of heat rate of 10 °C/min in N_2 environment to study the thermal stability of

the CuS nanoparticles (NPs). Using a Perkin Elmer lambda 365 UV-vis spectrophotometer, the absorption spectra of the synthesized CuS NPs were recorded. The Agilent Technologies Cary Eclipse Fluorescence Spectrometer was used to record the photoluminescence spectra. The surface roughness of the films was measured using a Bruker Multimode 8 atomic force microscope (AFM). The Keithley 2635B was used as a source meter for current-voltage (I-V) measurement with the use of a computer interface. Under AM 1.5 G radiation illumination, the photo response of the materials was measured by a solar simulator [Model 10500, Abet Technologies]. The 4294A, Agilent impedance analyzer was used to record the impedance spectroscopy measurement.

3.4. Results and Discussion

3.4.1. Structural Properties

➲ ***XRD Analysis***

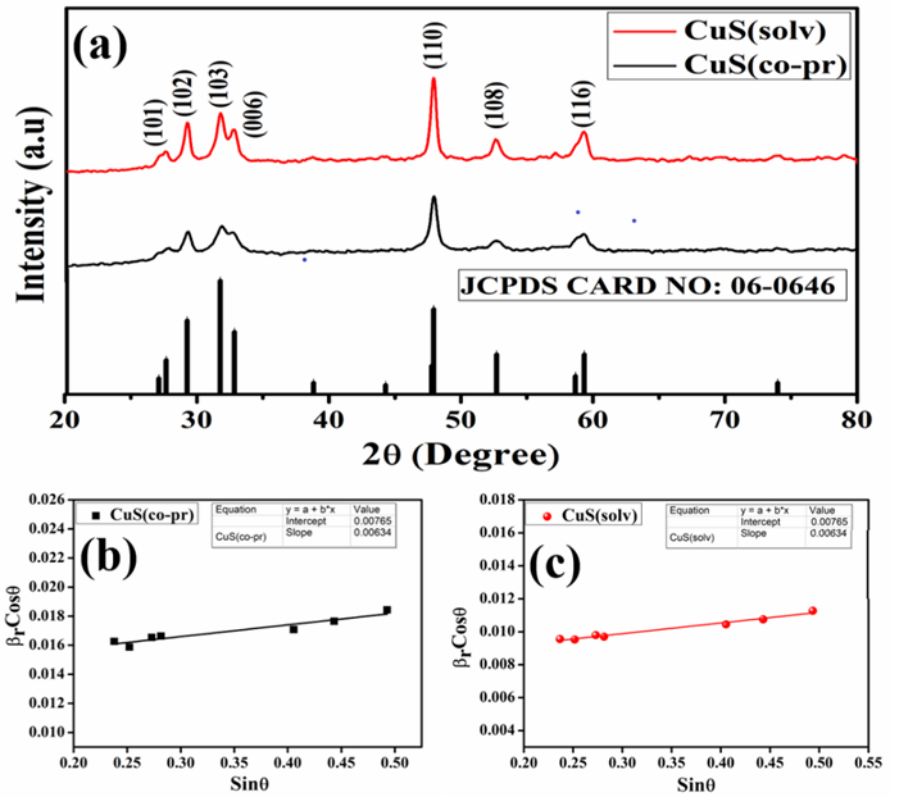

Fig. 3.1: (a) PXRD pattern of CuS synthesized by solvothermal and co-precipitation methods. Williamson Hall plot of (b) CuS(co-pr) and (c) CuS(solv).

PXRD analysis was used to verify the structural properties of the synthesized copper sulfide (CuS). CuS nanoparticles (NPs) synthesized using the co-precipitation and solvothermal methods are shown in Figure 3.1 (a) with their XRD spectra. The diffraction peaks of prepared CuS were observed at 2θ position ≈ 27.68°, 29.27°, 31.78°, 32.85°, 47.94°, 52.72° and 59.34°, which were allocated to (101), (102), (103), (006), (110), (108) and (116) crystallographic planes of the copper sulfide structure without any phase impurity (JCPDS Card No: 06-0464, a= b = 6.792 Å and c =16.34 Å). The peak widths and intensities suggest that (Fig.3.1a) the temperature applied in the solvothermal treatment exhibits better crystalline growth which shows more prominent and sharp peaks in the diffraction patterns of CuS(solv) nanoparticles rather than CuS(co-pr). From the DIFFRAC.EVA software tool of Bruker, we also obtain information about the crystalline percentage of the two differently synthesized samples. The solvothermally synthesized sample showed better crystallinity than the sample prepared by the co-precipitation method [CuS(solv): crystallinity- 47.5%, amorphous- 52.5% and CuS(co-pr): crystallinity-34.4%, amorphous- 65.6%, obtained from DIFFRAC.EVA software by Bruker].

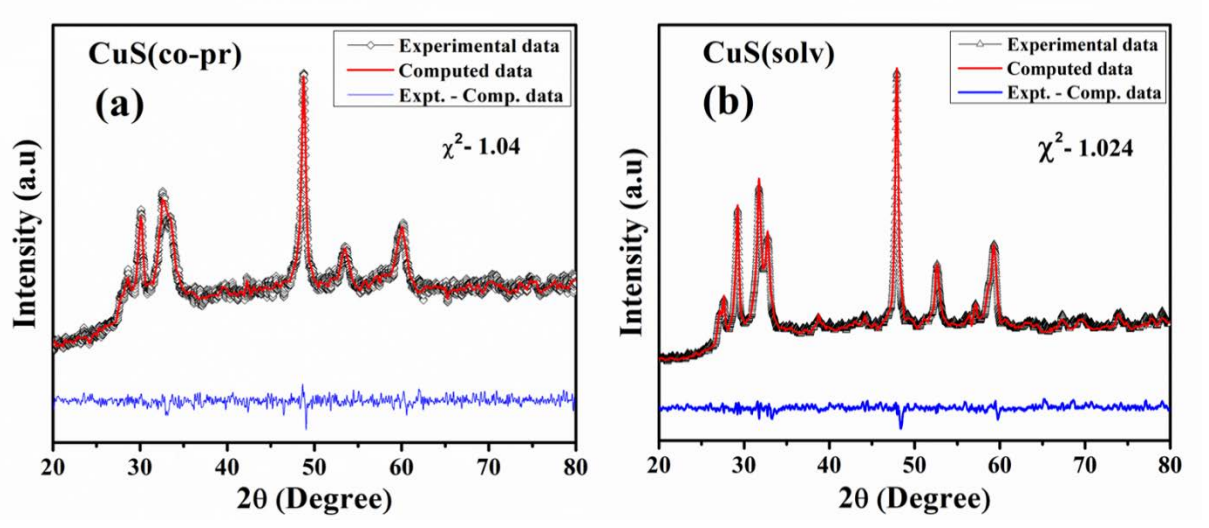

Fig. 3.2: (a, b) Profile fitting of differently synthesized CuS nanoparticles (using MAUD software). The black line with dotted symbol is the experimental data, the solid red line shows the calculated pattern, and the blue line is the difference between observed and calculated patterns.

Figure 3.2 shows the plot generated by Rietveld refinement of the CuS nanoparticles prepared via co-precipitation and solvothermal synthesis with the help of the MAUD programme. To achieve a good fit, the background factor was corrected using the cosine Fourier series with eight refinable coefficients, and the Bragg reflection profile was characterized by the Thompson-Cox-Hastings pseudo-Voigt function. Parameters such as

width dimensions, unit cell dimensions, orientation, asymmetry, structure factor, and occupancy were refined. Impurities in the nanoparticles can be ruled out since no additional peaks were found in the refinement. The goodness of fit (χ^2) is shown in the inset of Fig. 3.2. The full details of the CuS structure obtained by two different methods are provided below (Fig. 3.3 & Table 3.1).

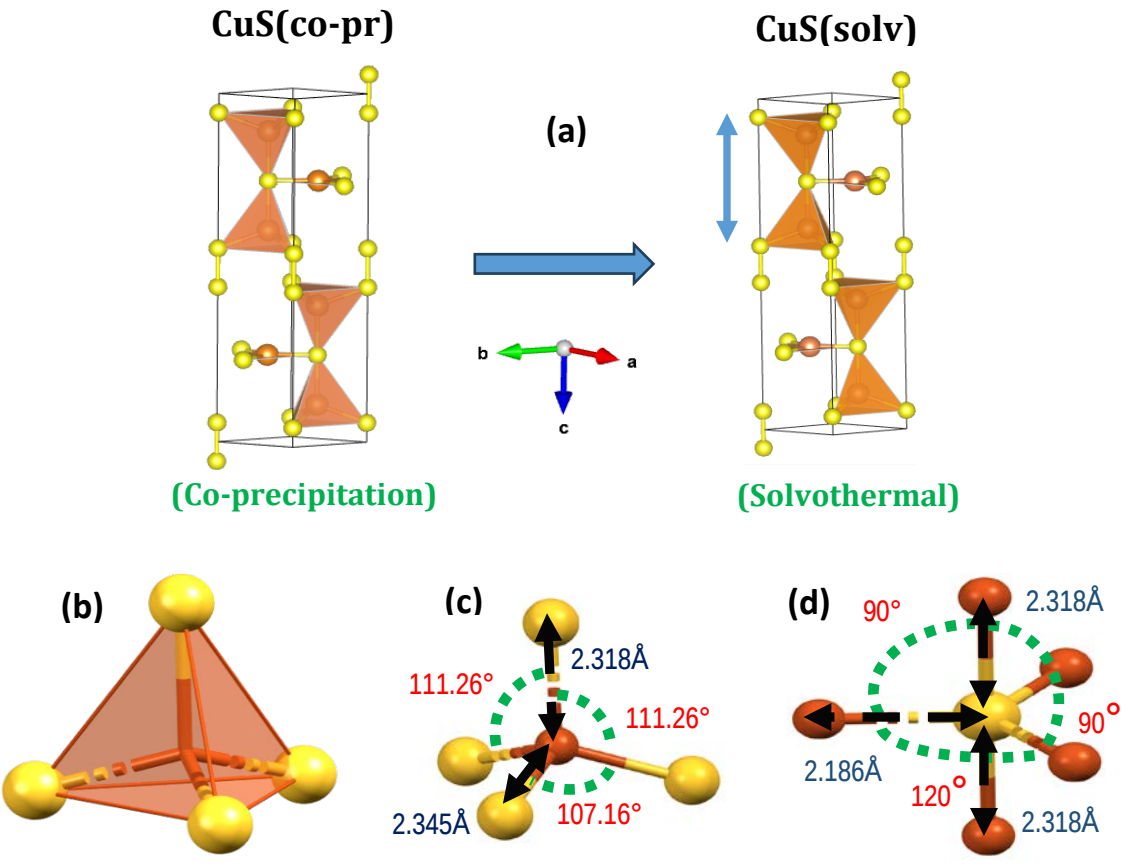

Fig. 3.3. (a) The asymmetric units of Cu-S nanocrystals prepared by two different techniques. (b) Cu adopts tetrahedral geometry by coordinating with 4 sulphur molecules in Cu-S nanocrystals. (Cu is represented by the orange and sulphur is represented by the yellow balls) (c) Some selected bond angles and bond lengths of copper tetrahedral geometry. (d) Sulphur adopted trigonal bipyramidal (TBP) by coordinating with five Cu molecules.

The crystal belongs to the hexagonal P group. We have included the crystal parameters in tabular form (Table 3.1). Our analysis of the crystal structure revealed that, in the asymmetric unit, all the Cu centers exhibit a tetrahedral geometry with 4 coordination numbers with sulphur atoms. The equatorial Cu-S bond distance is approximately 2.345 Å, while due to some distortion, the axial Cu-S bonds become slightly compressed, resulting in a bond distance of 2.318 Å. In the case of the Cu-S nanocrystal made by the

solvothermal method, there are slight differences compared to the previous technique. The crystal volume is 204 $Å^3$, slightly higher than the normal technique. The Cu-S axial bond in the tetrahedral coordination environment is also higher in the crystal obtained from the solvothermal technique. Due to the sp^3 hybridization adopted by the Cu center, all the equatorial bond angles are around 107°, but the axial S-Cu-S bond angle is around 111°. The sulphur moiety adopts the trigonal bipyramid coordination motive, with an equatorial bond angle of almost 120° and an axial bond angle of 180°. In that motif, the equatorial bond distance of Cu-S is the same, but the axial bonds are a little elongated. The two S-S bonds bind with two Cu centers, forming a six-member ring in its chair conformation. In the asymmetric unit, CuS nanocrystal S-S bond bridges by binding with Cu centers lead to the formation of the interconnected lattice, contributing to the stability of the crystal structure.

Table 3.1: *Crystal parameters of CuS synthesized by co-precipitation & solvothermal method.*

Parameters	CuS(co-pr)	CuS(solv)
Emp. formula	Cu6 S6	Cu6 S6
Cryst. system	hexagonal	hexagonal
space group	P 63/m m c	P 63/m m c
a/Å	3.78547	3.79640
b/Å	3.78547	3.79640
c/Å	16.27938	16.38558
α/°	90	90
β/°	90	90
γ/°	120	120
V/$Å^3$	202.0262	204.5204

The Debye-Scherrer equation which is given below, is used to obtain the average crystallite sizes of the as-synthesized CuS NPs[32].

$$B_r \cos\theta = \frac{K\lambda}{D} + \mu \sin\theta \qquad (3.1)$$

Here, B_r represents the full-width at half maxima (FWHM), K is a constant (K's value was taken as 1)[33], λ is the wavelength of Cu-K_α, μ is the microstrain and D stands for the crystallite size. The slope and intercept of the figure indicate the microstrain and crystallite size of the synthesized material. The crystallite sizes shown by CuS(solv) and CuS(co-pr) were 20 nm and 11 nm, respectively, as determined using the Debye-Scherrer equation. The size of the crystallites depends on the rate of crystalline nucleation and crystalline growth. When the nucleation rate is higher than the growth rate, smaller particles with low aggregation are formed. Conversely, when the growth rate is high, larger particles are formed. Therefore, it is expected that the long-time stirring during the co-precipitation method could affect the nucleation rate. As a result, CuS(co-pr) has smaller crystallites compared to CuS(solv). Additionally, the solvothermal method enhanced significant crystalline growth, resulting in larger crystallite sizes. CuS(solv) has reduced microstrain because it is inversely related to crystallite size[34]. The measured micro-strain values for the CuS(solv) and CuS(co-pr) nanostructures were 6.34×10^{-3} and 7.57×10^{-3}, respectively. The equation used to calculate the dislocation density of the CuS nanostructure is as follows[35,36]:

$$\delta = \frac{1}{D^2} \qquad (3.2)$$

here δ denotes the dislocation density and D represents crystallite size. The dislocation density of the CuS(solv) and CuS(co-pr) nanoparticles was determined to be 2.50×10^{-3} lines/m^2 and 8.26×10^{-3} lines/m^2 respectively, which shows the CuS(solv) to have a lower defect than CuS(co-pr).

➲ *FESEM and EDX Analysis*

Here in Fig. 3.4(a, b), the FESEM images of the CuS(co-pr) and CuS(solv) nanoparticles are displayed. The morphology from the SEM images suggests that the CuS(co-pr) and CuS(solv) samples to exhibit almost hexagonal-shaped and flake-like nanostructure, respectively. CuS(solv) shows clearer morphology than CuS(co-pr). For both the CuS NPs, agglomerated or distorted patterns were seen in Fig. 3.4(a, d).

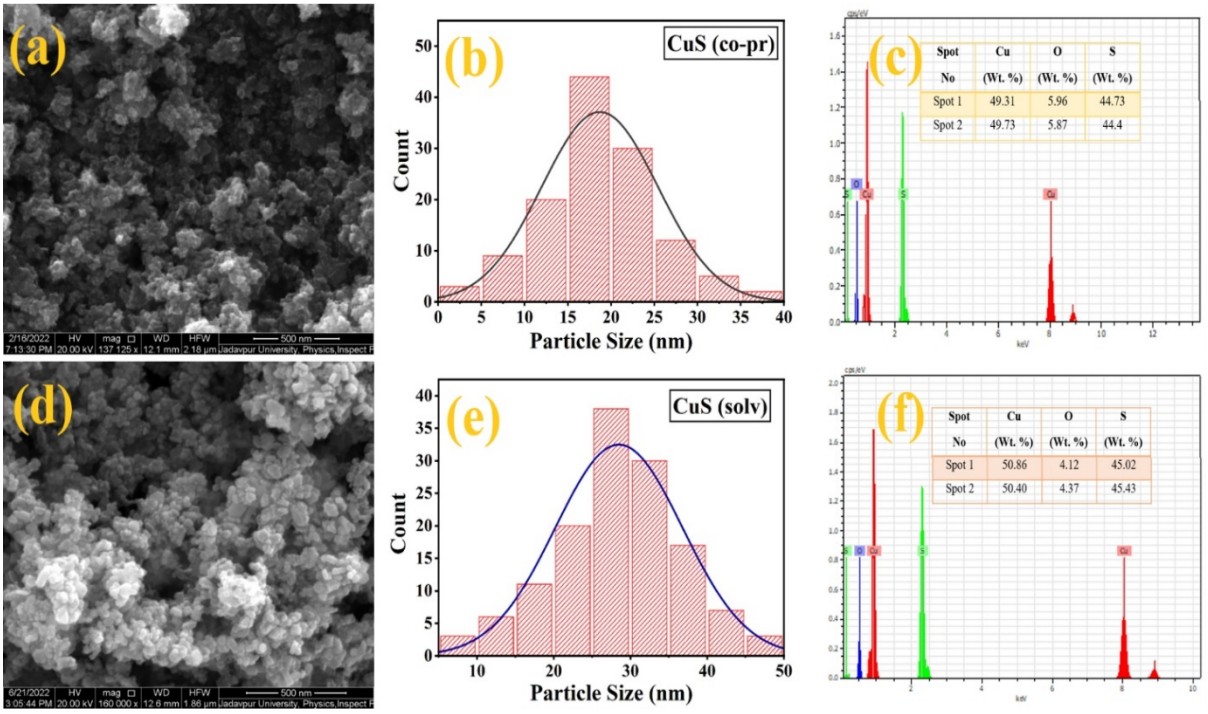

Fig. 3.4: The morphology of CuS nanoparticles is potrayed in: (a) CuS(co-pr) and (d) CuS(solv). The particle size distribution with Gaussian is shown in 3(b) CuS(co-pr) and 3(e) CuS(solv). The EDX spectra is represented in: (c) CuS(co-pr) and (f) CuS(solv).

However, CuS(co-pr) NPs exhibited more aggregation in a pattern related to other CuS samples. From the Gaussian fitted particle distribution (Fig. 3.4b and 3.4e), it is shown that the average particle size of CuS(co-pr) and CuS(solv) is 18.70 nm and 28.49 nm, respectively. This demonstrates that the shape or the morphology of the synthesized CuS NPs is highly influenced by the synthesis method and proves that the solvothermal method modifies the particle size and its crystallinity. The solvothermal method is an approach where the mixed solution is poured into a sealed reactor. The utilization of the relatively high temperature in the reactor and the high-pressure growth environment promotes the dissolution and recrystallization of moderately soluble samples. During the solvothermal process, the crystal grows to its largest possible size under non-restricted conditions and its characteristics like various shapes, high degree of crystallinity, uniform distribution, lighter particle agglomeration, etc. The EDX spectra (Fig. 3.4c and 3.4f) clarifies that the constituent elements copper, sulphur and oxygen (Cu, S, and O) were noted precisely in the nanoparticles. The molar ratio of Cu to S was close to one, indicating the stoichiometric formation of CuS NPs.

➲ ***TEM Analysis***

To study the size and shape along with the phase structure of the synthesized samples, we have examined the TEM images. Fig. 3.5 (a) and (b) illustrate the TEM images of CuS(co-pr) and CuS(solv), respectively. It shows that the solvothermally synthesised particles are more crystalline than those synthesized via co-precipitation method and also the hexagonal shape of the particles is more prominent in the solvothermal synthesis than in the co-precipitation method.

Fig. 3.5 (c) and (d) displayed the selected area electron diffraction (SAED) pattern of the CuS(co-pr) and CuS(solv), respectively. Due to the superimposition of the bright spot, Debye ring patterns are observed for both compounds. These patterns indicate the polycrystalline nature of the compounds. Among them, CuS(solv) demonstrates clearer ring patterns than CuS(co-pr). Therefore, the solvothermal technique, effectively modifies the size of the nanoparticles and improves their crystallinity.

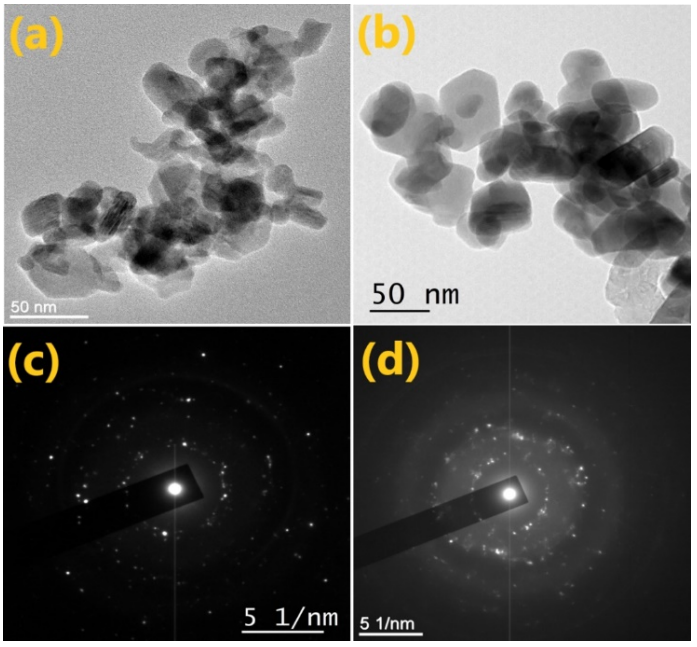

Fig. 3.5: TEM images of (a) CuS(co-pr) and (b) CuS(solv). SAED pattern of (c) CuS(co-pr) and (d) CuS(solv).

3.4.2. Optical Properties

➲ ***UV-vis absorbance study***

The optical characteristics of the CuS NPs were studied at room temperature using UV-vis absorption spectroscopy. The absorption spectra of differently synthesized copper sulfide thin films were noted between the wavelengths of 350 and 800 nm. Fig. 3.6(a)

displays the UV-vis absorption spectra of CuS(solv) and CuS(co-pr). The obtained spectra shows that the absorption of CuS(solv) is higher than that of CuS(co-pr). The increase in grain size may be responsible for shifting of the optical absorption edge of CuS(solv) towards the longer wavelength side compared to CuS(co-pr)[37].

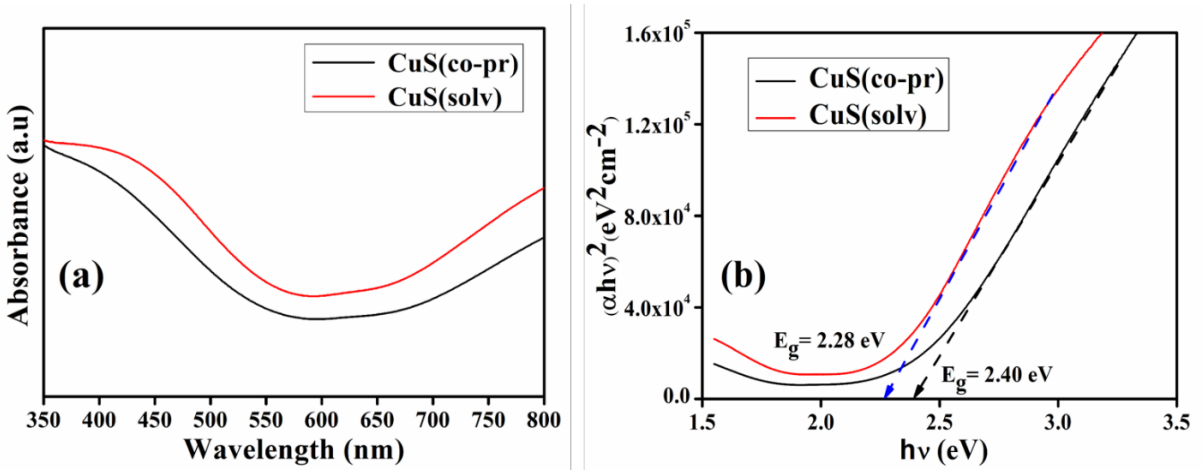

Fig. 3.6: (a) Absorbance spectra of CuS(co-pr) and CuS(solv) NPs. (b) Tauc's plot to determine the band gap of both the CuS nanoparticles.

The Tauc's plot for CuS(solv) and CuS(co-pr) is shown in Fig. 3.6(b). The optical bandgap (E_g) of the synthesized NPs was estimated using Tauc's equation (See Supplementary Information). The calculated values of the bandgap for CuS(co-pr) and CuS(solv) were approximately 2.40 eV and 2.28 eV, respectively[38]. Therefore, when the particle size is reduced, there is an enhancement in the energy band gap between the valence and conduction bands. CuS(co-pr) has a greater optical band gap than CuS(solv), indicating that its particles are smaller than CuS(solv). The optical bandgap tends to shrink as the particle size increases due to the quantum confinement effect in semiconductors[39].

➲ *FT-IR Analysis*

FTIR spectra are a useful tool to get information about the chemical bonds and its nature present in nanoparticles. Fig. 3.7 shows the FTIR spectra of the prepared CuS(solv) and CuS(co-pr) in the wave number range between 500-3500 cm^{-1} at ambient temperature. The vibrational peaks at 520 cm^{-1}, 608 cm^{-1}, and 1038 cm^{-1} are assigned to S-S bonds, Cu-S stretching, and C-O stretching alcohol, respectively. This indicates the presence of disulfide and metal-sulfide bonds[40,41].

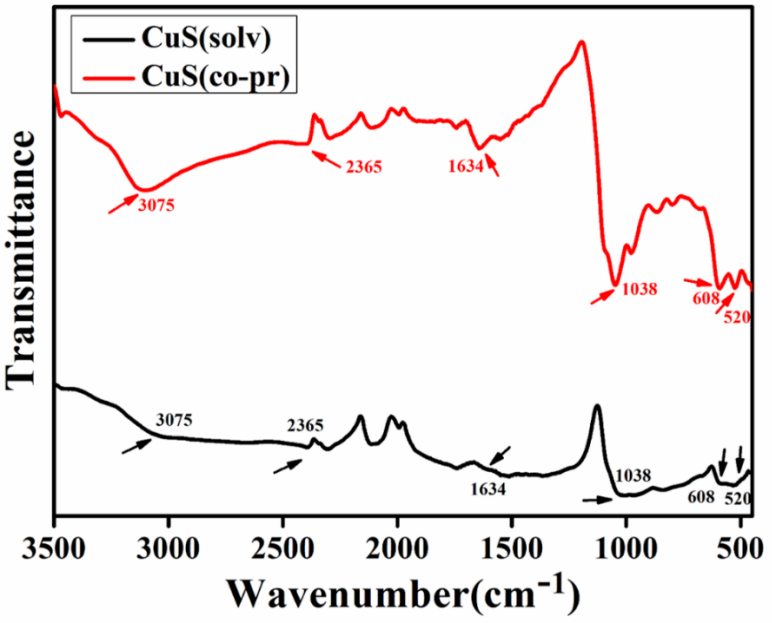

Fig. 3.7: FTIR spectra of CuS(solv) and CuS(co-pr) from wavenumber 500 cm^{-1} to 3500 cm^{-1}.

The peak around 1634 cm^{-1} is attributed to -OH bending vibration with Cu atoms[42]. The 2365 cm^{-1} vibration is assigned to the O-H bending of water molecules. As the water evaporates from the surface of the nanoparticles, the O-H stretching band of CuS(solv) is weaker compared to its counterpart in CuS(co-pr)[43]. The vibration at 3000-3100 cm^{-1} is assigned to C-H stretching.

3.4.3. Atomic Force Microscopy (AFM) Studies

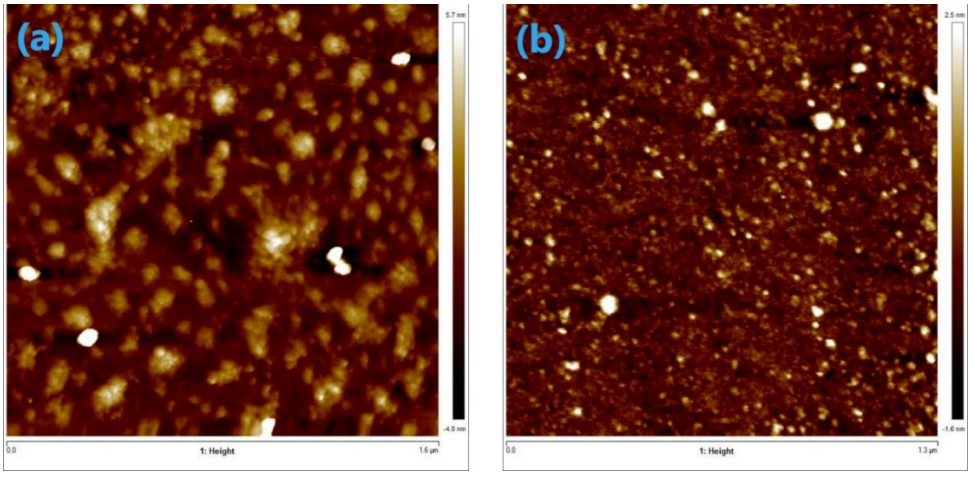

Fig. 3.8: AFM images of (a) CuS(co-pr) and (b) CuS(solv) nanoparticles-based films.

The roughness of the surfaces of as-synthesized CuS nanoparticles-based thin films was investigated using an atomic force microscope. Two separate dispersed solutions of CuS(co-pr) and CuS(solv) were dropped on two separate cleaned ITO-coated glasses at the same spinning speed. The films were dried at ambient temperature. Fig. 3.8 depicts the AFM images of the corresponding CuS(solv) and CuS(co-pr) based thin films. The roughness of the CuS(co-pr) films was found to be larger than that of the CuS(solv) films. CuS(solv) and CuS(co-pr) based thin films had r.m.s roughness values (R_q) of 1.39 nm and 3.74 nm, respectively. Smoother surfaces, which means lesser surface roughness, have a possibility of fewer number of traps. This is preferable for smoother charge transfer which increases the quality of the MS junction and improves device performance based on CuS(solv) rather than CuS(co-pr).

3.4.4. Thermal stability study

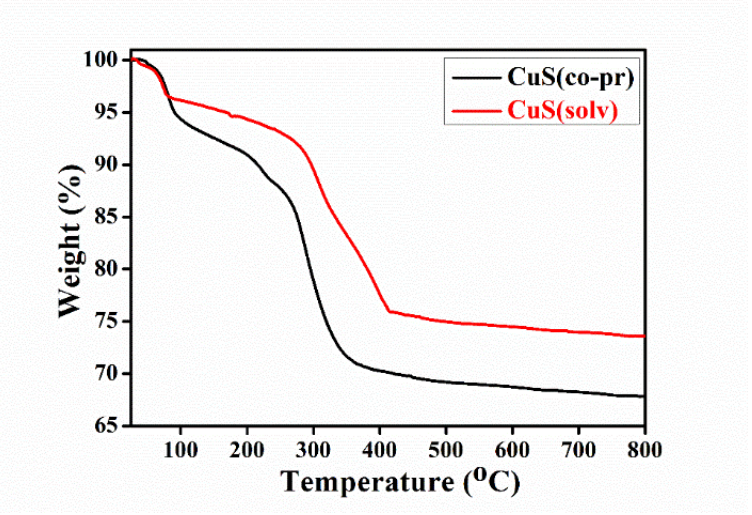

Fig. 3.9: Thermal stability graph of the CuS(solv) and CuS(co-pr) nanoparticles.

The thermal stability and weight losses of the synthesized CuS nanoparticles were investigated using thermo gravimetric analysis (TGA). Fig. 8 depicts the weight loss % of CuS(co-pr) and CuS(solv) while heated up to 800 °C at a temperature rise of 10 °C/min in an N_2 environment. The differently prepared CuS NPs exhibit a different decomposition pattern. CuS(co-pr) NPs showed weight loss and almost 68% remained up to 800 °C whereas CuS(solv) NPs remained almost 75% up to the same temperature. The initial weight loss is shown between 100-300 °C which indicates solvent desorption and moisture absorption. In the second part, that is 300-400 °C, the phase conversion of CuS occurs[44]. This result indicates that CuS(solv) is more stable than CuS(co-pr). TGA serves

a critical role in our investigation by evaluating the thermal stability of the synthesized particles. Understanding their ability to withstand heat is essential for their potential use in manufacturing optoelectronic devices. Our focus on light incidence and photo response makes it pertinent to examine how mass changes with thermal fluctuations. This analysis helps anticipate and comprehend mass variations due to thermal energy, providing a comprehensive understanding of the material's behavior under relevant operational conditions.

3.4.5. Current-Voltage (I-V) characteristics

CuS NPs' current-voltage characteristics are given in Fig. 3.10 (a, b) under both the absence and presence of light. The logarithmic I vs. V graph for each condition is provided in the inset. All electrical characterizations were carried out under ambient conditions. The Al/CuS(co-pr)/ITO, as well as the Al/CuS(solv)/ITO Schottky devices were fabricated to demonstrate the current-voltage behaviour, using the Keithley 2635B sourcemeter with a bias voltage range of -1V to +1V. The behavior of the curve observed to follow a Schottky diode, as clearly shown in Fig. 3.10 (a, b) with a non-linear and rectifying nature for both the I-V graphs. We have applied the thermionic emission theory, along with the diode equation, to derive various diode parameters such as on/off ratio, conductivity, ideality factor, series resistances etc. The related expressions are provided in the previous chapter (§ 2.7.1).

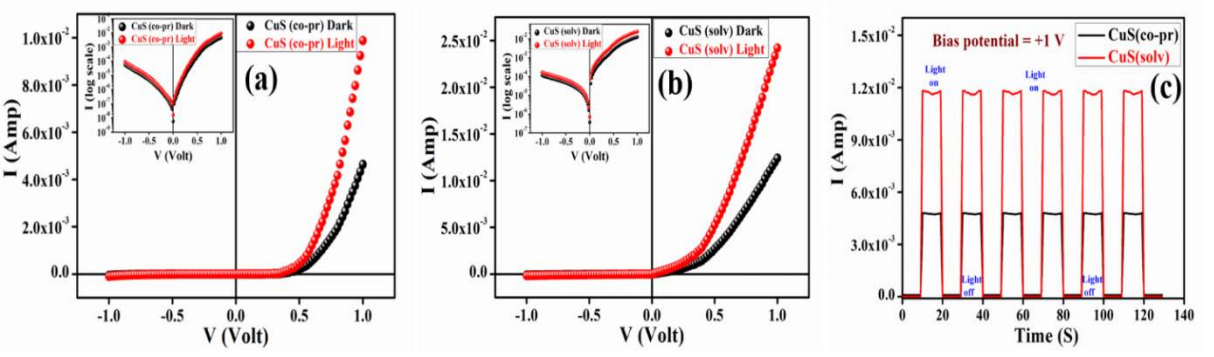

Fig. 3.10: Current-Voltage characteristics graph and (log I) vs. V graph (in the inset) for (a) CuS(co-pr) and (b) CuS(solv) under dark and illumination conditions, (c) photo-current vs. time graph of ITO/CuS/Al-based devices.

For CuS(co-pr) based devices, the measured on/off ratio was 83 and 98, whereas, for CuS(solv) based devices, it was 107 and 145 in the absence (dark) and presence of light, respectively. CuS(solv) has far better rectifying properties than the other one, as

demonstrated by an enhancement of the on/off ratio in CuS(solv)-based devices. It's interesting to note that the current measured in dark conditions for the Al/CuS(solv)/ITO device showed a significantly higher value than the Al/CuS(co-pr)/ITO device. The dc conductivity was calculated using the I vs. V curve. CuS(co-pr) has a measured dc conductivity of 6.49×10^{-6} Sm^{-1} and 1.12×10^{-5} Sm^{-1} in both dark and light conditions, but CuS(solv) had values of 3.60×10^{-4} Sm^{-1} and 6.99×10^{-4} Sm^{-1}, respectively, indicating higher conductivity. To understand the temperature dependency of conductivity, I-V characteristics were also performed at various temperatures. The results show that the conductivity of our material increases with the experimental temperature, which is a characteristic of a semiconductor material. The conductivity values are depicted in Table 3.2.

Table 3.2: *Temperature vs. Conductivity*

Temperature (K)	**Conductivity (sm^{-1})** **CuS(co-pr)**	**Conductivity (sm^{-1})** **CuS(solv)**
300	6.49×10^{-6}	3.60×10^{-4}
315	6.85×10^{-6}	3.83×10^{-4}
330	7.28×10^{-6}	4.16×10^{-4}
345	7.60×10^{-6}	4.53×10^{-4}

The increase in dc conductivity suggests that a CuS(solv)-based device has a higher electrical charge transfer capacity compared to a CuS(co-pr)-based device. Under an illumination of AM 1.5 G, Fig. 3.10 (c) depicts the time vs. photocurrent of the devices at a bias voltage of 1 volt. Here, dark current values were subtracted to compare the photo-response. The figure also demonstrates that CuS(solv) has a better photo response than the other candidate. Therefore, CuS(solv) may be a better material for use in electronic switching[45]. The following equation[46] has been used to evaluate the photosensitivity (S) of the Al/CuS structure (Table 3.3):

$$S = \frac{I_{light} - I_{dark}}{I_{dark}} \qquad (3.3)$$

The photosensitivity of a CuS(co-pr)-based diode was determined to be 0.95. This value increased to 1.09 for the CuS(solv)-based diode, which was over 15% higher than the CuS(co-pr)-based diode. This increase in value can be attributed to the greater absorption of light by CuS(solv). The photo responsivity (R) of the SBD, which is defined as the ratio of the photo-induced current density to the incoming intensity of light, was estimated using the equation[47,48]:

$$R = \frac{I_{light} - I_{dark}}{I_{\lambda} \cdot A} \quad (3.4)$$

Here, I_{light} and I_{dark} represent the currents at +1V in the light and dark conditions, respectively. I_{λ} represent the incident intensity of light falling on the device, and A is the device's effective area. The photoresponsivity values of CuS(co-pr) and CuS(solv) were 6.30 AW^{-1} and 16.68 AW^{-1}, respectively, and it was discovered that the photoresponsivity of CuS(solv) rose by 164% when compared to others. Furthermore, one of the crucial detector metrics is specific detectivity (D*), which may be represented as[49]:

$$D^{*} = \frac{R}{\sqrt{2qI_d}} \quad (3.5)$$

where q represents the electron charge, I_d represents the current in dark conditions at +1V. CuS(co-pr) and CuS(solv) specific detectivities were measured to be 0.778 x 10^{10} Jones and 1.72 x 10^{10} Jones, respectively. The CuS(solv)-based diode had a specific detectivity that is approximately 2.21 times greater than the CuS(co-pr)-based diode. These findings show that the CuS(solv)-based device is far better and has a significant possibility for usage in photodetectors. Table 3.3 displays all of the determined photosensitivity, photoresponsivity, and detectivity values.

Table 3.3: *Important parameter for Schottky diodes*

Sample Name	Photosensitivity(S)	Photo responsivity(R) (A/W)	Detectivity(D*) (Jones)
CuS(solv)	1.09	16.68	1.720×10^{10}
CuS(co-pr)	0.95	6.30	0.778×10^{10}

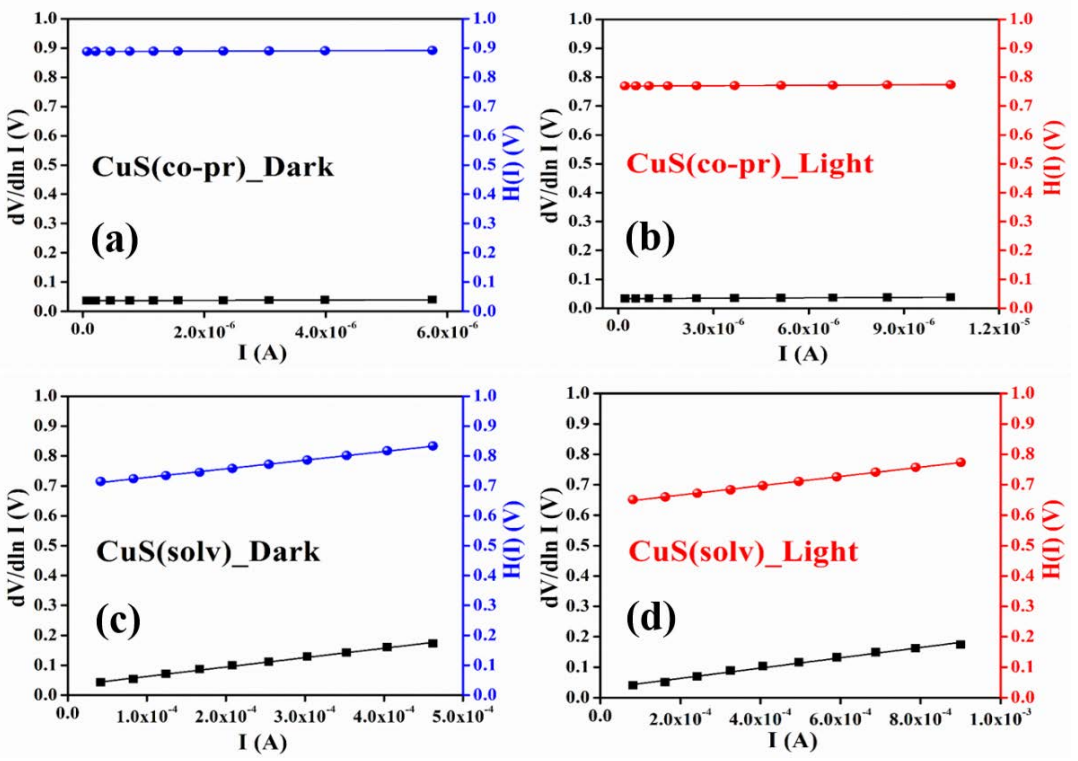

Fig. 3.11: dV/dlnI vs. I and H(I) vs. I plot of CuS(co-pr) (a, b) and CuS(solv) (c, d) for dark and light conditions, respectively to determine the diode parameters like series resistance, barrier height and ideality factors.

The dV/dlnI vs. I curve, as well as the H (I) vs. I curve, of the Al/CuS(solv)/ITO and Al/CuS(co-pr)/ITO structures were shown in Fig. 3.11 under dark and the light conditions. Table 3.4 displays the series resistance (R_s) and ideality factor (η) of the devices. The ideality factor is a quantity that measures the deviation of its quality from ideal diode behavior. From both structures, it was observed that the ideality factor deviated from unity under the specified circumstances. The existence of interface states, the structure's current conduction mechanism, inhomogeneity of barrier height, and the SBD structure's series resistance, all contribute to the deviation of the ideality factor from unity[50,51]. The barrier height (Φ_b) based on the slope of the H(I)-I graph was 0.62 eV and

0.59 eV for CuS(co-pr)-based devices, and 0.57 eV and 0.55 eV for CuS(solv)-based devices in the absence and presence of light, respectively (Table 3.4). The barrier height of the Al/CuS(solv) junction is lower than that of the Al/CuS(co-pr) junction. The implementation of the Schottky diode greatly benefits from a lower barrier height, as it leads to higher on-currents and improved subthreshold behavior. The R_S value obtained from the dV/dlnI versus I curve closely agrees with the resistance values obtained from the H(I) versus I plot for both diodes. The value of R_S of the CuS(solv)-based device is lower than that of the CuS(co-pr)-based device and it is quite significant.

Table 3.4: *Electrical parameters for CuS(co-pr) and CuS(solv)-based Schottky barrier diode*

Sample name	Condition	on/ off	Conductivity (Sm^{-1})	Ideality Factor(η)	R_s (Ω)		Φ_b (eV)
					dV/dlnI vs. I	H(I) vs. I	
CuS(co-pr)	Dark	83	6.49×10^{-6}	1.42	512	579	0.62
	Light	98	1.12×10^{-5}	1.29	437	449	0.59
CuS(solv)	Dark	107	3.60×10^{-4}	1.21	314	288	0.57
	Light	145	6.99×10^{-4}	1.14	169	152	0.55

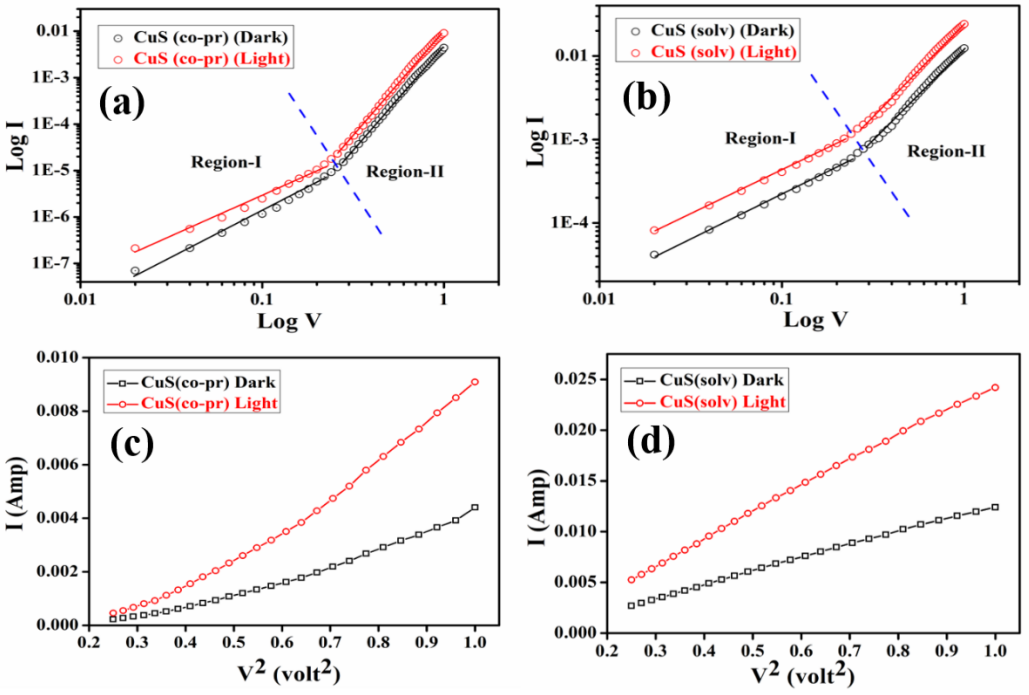

Fig. 3.12: Log I-Log V graph and I-V^2graph of (a, c) CuS(co-pr) and (b, d) CuS(solv) -based device under dark and light conditions to determine charge transport parameters like mobility and transit time.

SCLC theory was presented in the metal-semiconductor junction to clarify the charge transport features of these two NP materials. Figure 3.12 (a, b) depicts double logarithmic graphs of I-V characteristics for CuS(solv) and CuS(co-pr)-based devices in dark and light conditions. The diagram displays two unique sections of the current conduction process. The possibility of traps at the interface, as well as changes in the charge transport profile, affect the slope of the current-voltage characteristics[52]. The power law ($I \alpha V^r$)[53] governs the current conduction process, where r denotes the slope of the I-V curve. The I vs. V curves have an ohmic character at an extremely low bias (region I), where the free carrier concentration is larger than the injected carrier concentration under equilibrium. In regime I, charge carrier injection from electrode to semiconductor is lower due to the small bias voltage[53]. The space charge limited current (SCLC) zone exists in regime II, where the current correlates to the square of the voltage. Furthermore, the existence of traps in the CuS band gap governs the space charge limited current[54], and the concentration of the free charge carrier is equivalent to the injected charge carrier concentration[52,55].

The Mott-Gurney equation was proposed for the SCLC regime[56,57] to evaluate the effective carrier mobility of the charge carrier (μ_{eff}).

$$I = \frac{9\mu_{eff}\ \varepsilon_0\varepsilon_r A}{8}\left(\frac{V^2}{d^3}\right) \qquad (3.6)$$

where (μ_{eff}) is the effective carrier mobility, ε_0 is the free space permittivity, A denotes the effective area of the diode, d is the effective thickness of the film, and ε_r represents the dielectric constant of the synthesized materials. The ε_r values for both materials were calculated using the equation[58]:

$$\varepsilon_r = \frac{1}{\varepsilon_0}.\frac{C.d}{A} \qquad (3.7)$$

where C represents the capacitance value. The calculated values of ε_r for CuS(solv) and CuS(co-pr) were 4.38 and 2.90, respectively. The transition or transit time (τ) for charge carriers was calculated using the equation below[59]:

$$\tau = \frac{9\varepsilon_0\varepsilon_r A}{8d}\left(\frac{V}{I}\right) \qquad (3.8)$$

The transition time of the charge carrier was estimated by using the slope of the I vs. V graph in the SCLC region. The diffusion length (L_D) of the charge carrier was determined using the value of relaxation time (τ) by the following equation[60]:

$$L_D = \sqrt{2D\tau} \tag{3.9}$$

Here, to calculate the diffusion coefficient D, the Einstein-Smoluchowski formula was used[61]:

$$\mu_{eff} = \frac{qD}{kT} \tag{3.10}$$

where q is the magnitude of charge, k stands for the Boltzmann constant and T is the effective temperature.

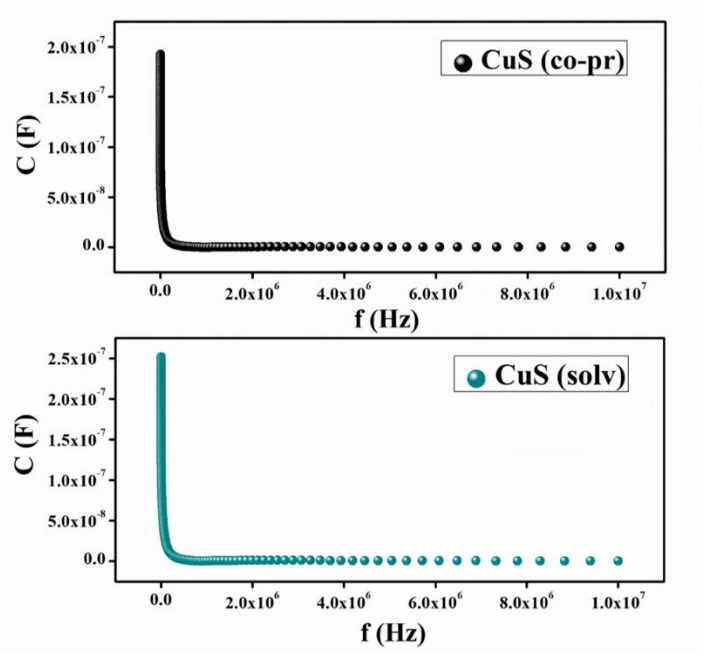

Fig. 3.13: Capacitance-frequency (C-f) plot of CuS(co-pr) and CuS(solv) films at zero bias.

Table 3.5: *Charge transport parameters of Al/CuS(co-pr)/ITO and Al/CuS(solv)/ITO structure.*

Sample	**Condition**	**μ_{eff} x10^{-5} (m^2/V. S)**	**τ (Sec)**	**D (S.I)**	**L_Dx10^{-9} (m)**
CuS(co-pr)	Dark	2.42	2.41 x10^{-8}	6.26 x10^{-7}	173
	Light	5.12	1.18 x10^{-8}	1.32 x10^{-6}	177
CuS(solv)	Dark	4.02	1.55 x10^{-8}	1.04 x10^{-6}	180
	Light	9.39	7.99 x10^{-9}	2.43 x10^{-6}	197

Table 3.5 shows the calculated values for carrier mobility, transit time, diffusion coefficient and diffusion length. As shown in Table 3.5, the carrier mobility, an important device parameter, was higher for CuS(solv) than CuS(co-pr). The enhancement in mobility of the CuS(solv) based Schottky diode can be attributed to the particle size[62]. To explain size-dependent mobility, we have explored two possibilities: (a) hopping via the nearest neighbour, and (b) trapping and thermal releasing mechanism[63]. Based on the first consideration, the transport probability of a carrier during hopping, is directly correlated to the product of the tunnelling probabilities of that pathway. This suggests that mobility increases as particle size decreases, since larger particles require fewer hops to travel a specific distance[64], which is also supported by the shorter transit time observed in the diode fabricated by CuS(solv). The trapping and releasing of charge carriers are connected to the presence of localized traps within the energy gap, giving rise to a space charge-limited current mechanism. It is assumed that smaller-sized nanocrystalline materials have a greater number of grain boundaries, where charges could be trapped, whereas larger-sized materials have fewer traps per unit volume[65]. This leads to a higher density of free carriers resulting in space charge-limited currents. It was observed from the experiment that, in the dark, the mobility of the charge carriers for CuS(solv) increased by 66%, whereas in the light, it was increased by 83%. The carrier mobility of CuS(solv) was enhanced by 134% under light, but the mobility of CuS(co-pr) increased by 111% under light. In addition, CuS(solv) has a greater increase in diffusion length following light irradiation than CuS(co-pr). Therefore, after light irradiation, the improvement in charge transport properties of CuS(solv) was much greater than that of CuS(co-pr), explaining the increased photo responsivity in CuS(solv). Another significant characteristic, the charge carrier diffusion length (L_D), was higher in CuS(solv), especially

under light conditions, resulting in improved photo response. As a result, it is evident that the performance of the device of solvothermally synthesized CuS was better than its counterpart. This signifies that, the crystallinity and particle size affect the electrical conductivity of differently synthesized CuS samples[66].

3.4.6. Impedance spectroscopy analysis

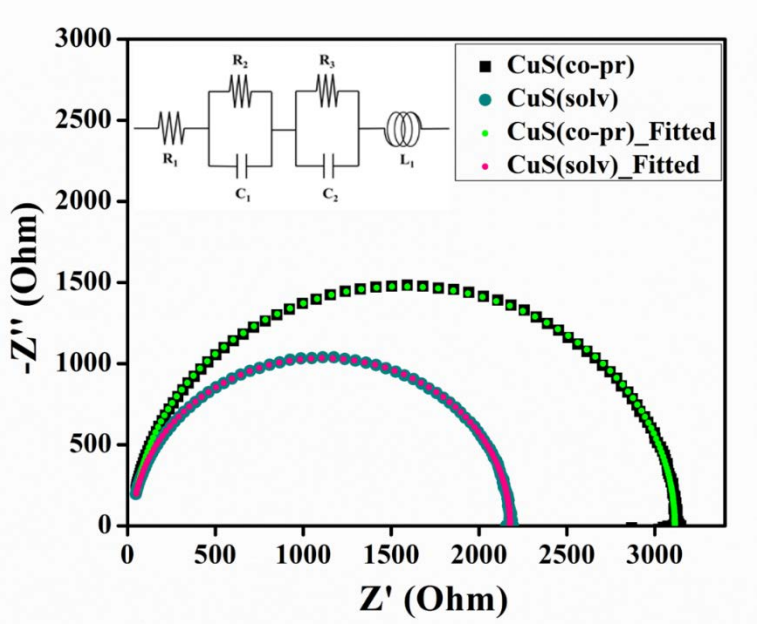

Fig. 3.14: Nyquist plot of CuS(solv) and CuS(co-pr) based films with equivalent circuit.

The impedance spectroscopy (IS) method is a valuable tool for studying the kinetics of charge transport and the recombination mechanisms[67] at the metal-semiconductor junction. IS was used to understand the kinetics of charge transfers at the metal-semiconductor junction of Al/CuS/ITO devices in the absence of light at room temperature. Figure 3.14 displays the Nyquist plot of equivalent devices with a frequency range of 40 Hz to 10 MHz. The radius of the semicircular arc of the Nyquist plots for CuS(solv) was smaller than that of CuS(co-pr). However, in the intermediate-frequency regime, the impedance for the transfer of electrons in a MS junction that is represented by a semicircle is significantly smaller for Al/CuS(solv) than for Al/CuS(co-pr). The decreasing diameter of the semicircular arc suggests a lower electron transport barrier and a slower recombination process. As a result, because of its superior conductivity, CuS(solv) promotes improved charge transfer and minimizes charge carrier recombination[68].

The semi-circular-like Nyquist plots can be designed using the equivalent circuit with RC networks. Therefore, we have designed an equivalent circuit model for analyzing of Nyquist spectra. This equivalent circuit model consists of two parallel RC network, with a series resistance (R_1) and a parasitic inductance (L_1). The R_2C_1 circuit can be attributed to the Schottky contact, while the other R_3C_2 circuit corresponds to the material/ITO interface. The values of R_1, R_2, R_3, C_1, C_2 and L_1 are presented in Table 3.6. The lower series resistance (R_1) and the value of R_2 for the CuS(solv)-based device indicate reduced blockage of charge carriers by the Schottky junction. Similar improvement also observed in the I-V characteristics.

Table 3.6: *Fitted values of R1, R2, R3, C1, C2 and L1 for Al/CuS(co-pr)/ITO and Al/CuS(solv)/ITO structure using equivalent circuit model*.

Sample	**R_1 (Ω)**	**R_2 (Ω)**	**C_1 (F)**	**R_3 (Ω)**	**C_2 (F)**	**L_1 (H)**
CuS(co-pr)	17.27	1976.80	1.19×10^{-10}	2124.9	13.70×10^{-10}	1.7776×10^{-7}
CuS(solv)	5.26	986.23	5.85×10^{-10}	1185.3	1.18×10^{-10}	3.5515×10^{-7}

3.5. Conclusion

Using solvothermal and co-precipitation techniques, we successfully synthesized pure and uniform CuS nanoparticles. Structural characterization showed that CuS(solv) has a larger particle size and better crystallinity than CuS(co-pr). CuS(solv) nanoparticles also possess greater absorption and a lower bandgap energy compared to CuS(co-pr), enhancing electron transition. Furthermore, in comparison to CuS(co-pr)-based diodes, CuS(solv)-based Schottky diodes displayed better current rectification and photosensitivity, measuring almost 1.15 times higher. CuS(solv) based SBDs showed a 146% improvement in photoresponsivity and a 121% improvement in photo-detectivity compared to CuS(co-pr) counterparts. Analysis of the charge transport mechanism using SCLC theory across the M-S junction revealed a 66% increase in charge carrier mobility under dark and an 83% increase under light illumination. CuS(solv) diodes also exhibited better charge transfer through the Al/CuS(solv)/ITO interface due to higher carrier mobility and less transit time, resulting in reduced interfacial resistance and improved charge kinetics compared to CuS(co-pr) diodes. EIS measurements further confirmed the

improved charge transfer and reduced carrier recombination of solvothermally synthesized CuS nanoparticles in Schottky diodes. Overall, our work demonstrates that the solvothermally synthesized nanoparticles have larger particle sizes and better crystallinity than the particles synthesized by the co-precipitation method. The crystalline size played a crucial factor in enhancing the charge transfer and electrical properties of CuS(solv) thin films than CuS(co-pr), making it a promising method for fabricating CuS-based Schottky devices with enhanced photo response. The solvothermally produced CuS nanoparticles hold potential for improving photovoltaic applications. Therefore, the superior charge transport mechanism of CuS(solv) was influenced by its larger particle size. To conclude, this literature highlights the charge transport of CuS-based photovoltaic devices and a better perception of the synthesis procedure-dependent conduction mechanism.

***

References

1. R. Gao, Q. Zhang, F. Soyekwo, C. Lin, R. Lv, Y. Qu, M. Chen, A. Zhu, Q. Liu, Electrochim Acta, 2014, **237**, 94–101.

2. X. Li, J. Shen, N. Li, M. Ye, J Power Sources, 2015, **282**, 194–201.

3. W. Li, S. Wang, L. Xin, M. Wu, X. Lou, J Mater Chem A Mater, 2016, **4**,7700–7709.

4. K.-J. Huang, J.-Z. Zhang, G.-W. Shi, Y.-M. Liu, Electrochim Acta, 2014, **132**, 397–403.

5. A.M. Mansour, G.M. Mahmoud, E.M. El Menyawy, International Journal of Microstructure and Materials Properties, 2019, **14**, 272.

6. K.-J. Huang, J.-Z. Zhang, Y. Liu, Y.-M. Liu, Int J Hydrogen Energy, 2015, **40**, 10158–10167.

7. S.M.H. Al-Jawad, A.A. Taha, M.M. Muhsen, J Phys Conf Ser, 2021, **1795**, 012053.

8. M.A. Adedeji, M.S.G. Hamed, G.T. Mola, Solar Energy, 2020, **203**, 83–90.

9. X. Chen, T. Wang, J. Shi, W. Lv, Y. Han, M. Zeng, J. Yang, N. Hu, Y. Su, H. Wei, Z. Zhou, Z. Yang, Y. Zhang, Nanomicro Lett, 2022, **14**, 8.

10. K. Samdhyan, P. Chand, H. Anand, S. Saini, J Energy Storage, 2022, **46**, 103886.

11. Z. Huang, L. Wang, H. Wu, H. Hu, H. Lin, L. Qin, Q. Li, Shape-controlled synthesis of CuS as a Fenton-like photocatalyst with high catalytic performance and stability, J Alloys Compd, 2022, **896**, 163045.

12. S. Pak, J. Son, T. Kim, J. Lim, J. Hong, Y. Lim, C.-J. Heo, K.-B. Park, Y.W. Jin, K.-H. Park, Y. Cho, S. Cha, Nanotechnology, 2023, **34**, 015702.

13. K. Wang, Q. Hu, B. Gao, Q. Lin, F.-W. Zhuge, D.-Y. Zhang, L. Wang, Y.-H. He, R.H. Scheicher, H. Tong, X.-S. Miao, Mater Horiz, 2021, **8**, 619–629.

14. S. Palanisamy, S. Velmurugan, T.C.K. Yang, Ultrason Sonochem, 2020, **64**, 105043.

15. K. Mageshwari, S.S. Mali, T. Hemalatha, R. Sathyamoorthy, P.S. Patil, Progress in Solid State Chemistry, 2011, **39**, 108–113.

16. J. Liu, D. Xue, Mater Res Bull, 2010, **45**, 309–313.

17. S. Riyaz, A. Parveen, A. Azam, Perspect Sci (Neth), 2016, **8**, 632–635.

18. Y. Gao, Y. Guo, Y. Zou, W. Liu, Y. Luo, B. Liu, C. Zhao, ACS Appl Energy Mater, 2023, **6**, 1340–1354.

19. A. Singh, R. Manivannan, S. Noyel Victoria, Arabian Journal of Chemistry, 2019, **12**, 2439–2447.

20. B. Pejjai, M. Reddivari, T.R.R. Kotte, Mater Chem Phys, 2020, **239**, 122030.

21. Z. Wang, S. Rafai, C. Qiao, J. Jia, Y. Zhu, X. Ma, C. Cao, ACS Appl Mater Interfaces, 2019, **11**, 7046–7054.

22. J.E. Dutrizac, R.J.C. MacDonald, Mater Res Bull, 1973, **8**, 961–971.

23. Y. Ni, H. Liu, F. Wang, G. Yin, J. Hong, X. Ma, Z. Xu, Applied Physics A, 2004, **79**, 2007–

2011.

24. L. Armelao, D. Camozzo, S. Gross, E. Tondello, J Nanosci Nanotechnol, 2006, **6**, 401–408.

25. T.H. Larsen, M. Sigman, A. Ghezelbash, R.C. Doty, B.A. Korgel, J Am Chem Soc, 2003, **125**, 5638–5639.

26. S. Siol, H. Sträter, R. Brüggemann, J. Brötz, G.H. Bauer, A. Klein, W. Jaegermann, J Phys D Appl Phys, 2013, **46**, 495112.

27. S. Jiao, L. Xu, K. Jiang, D. Xu, Advanced Materials, 2006, **18**, 1174–1177.

28. M. Cuneyt Haciismailoglu, M. Ahmetoglu, M. Haciismailoglu, M. Alper, T. Batmaz, Sens Actuators A Phys, 2022, **347**, 113931.

29. S. Çetinkaya, H.A. Çetinkara, F. Bayansal, S. Kahraman, Growth and Characterization of CuO Nanostructures on Si for the Fabrication of CuO/p-Si Schottky Diodes, The Scientific World Journal, 2013, **2013**, 1–6.

30. K. Ozel, A. Yildiz, Sens Actuators A Phys, 2021, **332**, 113141.

31. N.A. Al-Ahmadi, Mater Res Express, 2020, **7**, 032001.

32. A.A.M. Farag, A.M. Mansour, A.H. Ammar, M.A. Rafea, Characterization of electrical and optical absorption of organic based methyl orange for photovoltaic application, Synth Met, 2011, **161**, 2135–2143.

33. A.M. Mansour, A.B. Abou Hammad, A.M. El Nahrawy, Nano-Structures & Nano-Objects, 2021, **25**, 100646.

34. V. Dhanasekaran, N. Soundaram, S.-I. Kim, R. Chandramohan, S. Mantha, S. Saravanakumar, T. Mahalingam, New Journal of Chemistry, 2014, **38**, 2327.

35. J. Madhavi, SN Appl Sci, 2019, **1**, 1509.

36. I.M. El Radaf, A.M. Mansour, G.B. Sakr, Journal of Semiconductors, 2018, **39**, 124010.

37. N. Bouazizi, R. Bargougui, A. Oueslati, R. Benslama, Adv Mater Lett, 2015, **6**, 158–164.

38. M. Isik, M. Terlemezoglu, N. Gasanly, M. Parlak, Physica E Low Dimens Syst Nanostruct, 2022, **144**, 115407.

39. A. Bhattacharjee, M. Ahmaruzzaman, RSC Adv, 2016, **6**, 41348–41363.

40. I. Savarimuthu, M.J.A.M. Susairaj, ACS Omega, 2022, **7**, 4140–4149.

41. S. Rajeshkumar, J. Santhoshkumar, M. Vanaja, P. Sivaperumal, M. Ponnanikajamideen, D. Ali, K. Arunachalam, Oxid Med Cell Longev, 2022, **2022** 1–12.

42. P. Naveenkumar, G. Paruthimal Kalaignan, S. Arulmani, S. Anandan, Journal of Materials Science: Materials in Electronics, 2018, **29**, 16853–16863.

43. F. Motahari, M.R. Mozdianfard, M. Salavati-Niasari, Process Safety and Environmental Protection, 2015, 93, 282–292.

44. S. Iqbal, A. Bahadur, A. Saeed, K. Zhou, M. Shoaib, M. Waqas, J Colloid Interface Sci,

2017, **502**, 16–23.

45. X. Qian, H. Liu, N. Chen, H. Zhou, L. Sun, Y. Li, Y. Li, Inorg Chem, 2012, **51**, 6771–6775.

46. J. Gaur, H.K. Sharma, S. Tyagi, C. Tyagi, P. Vashishtha, S.K. Sharma, B.P. Singh, Nano Express, 2020, **1**, 020044.

47. C.-H. Liu, Y.-C. Chang, T.B. Norris, Z. Zhong, Nat Nanotechnol, 2014, **9**, 273–278.

48. H. Zhang, X. Zhang, C. Liu, S.-T. Lee, J. Jie, ACS Nano, 2016, **10**, 5113–5122.

49. S. Sil, A. Dey, J. Datta, M. Das, R. Jana, S. Halder, J. Dhar, D. Sanyal, P.P. Ray, Mater Res Bull, 2018, **106**, 337–345.

50. S. Laha, D. Sathapathi, M. Das, M. Das, P.P. Ray, A. Bag, B.C. Samanta, U.K. Das, T. Maity, New Journal of Chemistry, 2022, **46**, 16730–16742.

51. A.M. Mansour, M. Nasr, H.A. Saleh, G.M. Mahmoud, Applied Physics A, 2019, **125**, 625.

52. L. Rajan, C. Periasamy, V. Sahula, Perspect Sci (Neth), 2016, **8**, 66–68.

53. S. Saha, M. Das, K.S. Das, R. Datta, S. Bala, J.-L. Liu, P.P. Ray, R. Mondal, Cryst Growth Des, 2023, **23**, 1104–1118.

54. A.M. Mansour, S.A. Gad, A.M. Moustafa, G.M. Mahmoud, Silicon, 2022, **14**, 2189–2199.

55. S. Mahato, A. Mondal, M. Das, M. Joshi, P.P. Ray, A. Roy Choudhury, C.M. Reddy, B. Biswas, Dalton Transactions, 2022, **51**, 1561–1570.

56. D. Das, M. Das, S. Sil, P. Sahu, P.P. Ray, ACS Omega, 2022, **7**, 26483–26494.

57. M. Soylu, B. Abay, Physica E Low Dimens Syst Nanostruct, 2010, **43**, 534–538.

58. S. Diyali, N. Diyali, M. Das, M. Joshi, P.P. Ray, Md.S.A. Sher Shah, A. Roy Choudhury, B. Biswas, Cryst Growth Des, 2022, **22**, 7590–7602.

59. M. Das, D. Das, S. Sil, P.P. Ray, Nanoscale Adv, 2023, **5**, 3655-3663.

60. D. Das, M. Das, P. Sahu, P. Pratim Ray, Mater Today Proc, 2024, **102**, 165-170.

61. S. Majumdar, P.P. Ray, R. Sahu, A. Dey, B. Dey, Int J Biol Macromol, 2022,**195**, 287–293.

62. P. Ghosh, R.N. Bhowmik, S. Bandyopadhyay, P. Mitra, 2019, **78**, 111–120.

63. M.S. Kang, A. Sahu, D.J. Norris, C.D. Frisbie, Nano Lett, 2010, **10**, 3727–3732.

64. Y. Liu, M. Gibbs, J. Puthussery, S. Gaik, R. Ihly, H.W. Hillhouse, M. Law, Nano Lett, 2010, **10**, 1960–1969.

65. C.-W. Nan, A. Tschöpe, S. Holten, H. Kliem, R. Birringer, J. Appl. Phys, 1999, **85**, 7735–7740.

66. E.M. Kamar, M. Khairy, M.A. Mousa, Journal of Materials Research and Technology, 2023, **24**, 7381–7393.

67. W.H. Leng, Z. Zhang, J.Q. Zhang, C.N. Cao, J Phys Chem B, 2005, **109**, 15008–15023.

68. M. Das, J. Datta, R. Jana, S. Sil, S. Halder, P.P. Ray, New Journal of Chemistry, 2017, **41**, 5476–5486.

***

Investigation of charge transfer in optoelectronic devices: a study of carbon nanotube-copper sulfide nanocomposites using equivalent circuit models for metal–semiconductor interfaces

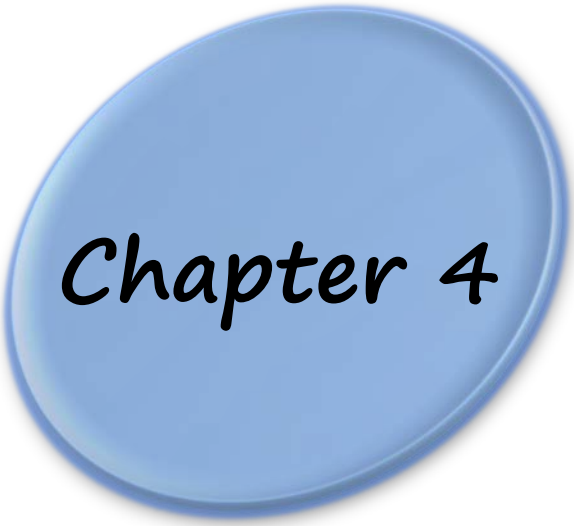

4.1. Introduction

In recent years, the usage of compound semiconductors in electronic and optoelectronic devices has witnessed a notable increase, primarily propelled by the growing demand for solar energy solutions[1] Copper metal chalcogenide semiconductors, exemplified by copper oxide (CuO), copper selenide (CuSe), and copper telluride (CuTe), have garnered attention owing to their favourable attributes, encompassing low environmental impact, cost-effectiveness, and widespread availability. Copper sulfide (CuS), exhibiting a distinctive black colour and a direct bandgap of approximately 2.29 eV, stands out due to its favourable features for optoelectronic applications[2]. These include facile processing, non-toxicity, efficient absorption of visible light and high physical and thermal stability[3]. These qualities position CuS as a desirable option for a variety of devices such as solar cells[4], light-emitting diodes (LEDs)[5], and sensors[6,7]. However, a significant drawback of CuS lies in its propensity for rapid electron-hole ($e\text{-}h^+$) recombination, resulting in limited charge transfer, primarily in optoelectronic applications. To address this issue, the synthesis of carbon-based composites has emerged as a feasible strategy after a variety of approaches have been investigated[8,9]. Carbon nanotubes (CNT) are particularly appealing due to their cost-effectiveness, ease of processability, superior conductivity and high specific surface area[10]. According to the earlier report, in comparison to pure CuS, graphene or CNT-based nanocomposite has a few advantages, namely enhanced electron-hole pair (EHP) separation and extended visible light absorption[11]. CNT increases the migration rate of photo-generated electrons, thereby pushing electrons and holes away which prevents electron (e^-)–hole (h^+) recombination. Considering these factors, some investigation on the CNT-CuS composite has been done but, an in-depth analysis of the Schottky diode parameters and charge transport properties through a metal/CNT-CuS junction has received little attention. With the recent advancement in novel Schottky barrier-based nanoelectronics, a comprehensive understanding of this interface is needed. These led to our great interest in studying the CNT-CuS nanocomposite based Schottky diode and its transport mechanism, compared to the one fabricated with pure CuS.

This investigation delves into the potential of CuS and CNT-CuS (T-CuS) in the fabrication of optoelectronic devices, utilizing an analysis of the equivalent circuit model of the interfaces and electrical charge transport parameters. The recent investigation is based on Schottky barrier diodes as a foundational assessment of the performance of the device

in terms of electronic conduction across metal-semiconductor interfaces. To be more precise, Al/CuS/ITO and Al/T-CuS/ITO Schottky barrier diodes are made by sandwiching thin layers of T-CuS and CuS between Al and ITO electrodes. Morphological properties of the CuS and T-CuS thin films are studied to optimize device performance. Furthermore, to understand various interfacial characteristics of the fabricated diodes, the research investigates frequency-dependent and bias-dependent impedance spectroscopy (IS). Measurements of current-voltage (I-V) are performed in both dark and illuminated conditions to scrutinize the photoresponsive properties and the charge transport mechanism within the Metal-Semiconductor (MS) junction of the Al/CuS and T-CuS/ITO Schottky devices.

4.2. Materials and Methods

4.2.1. Materials

The chemicals used in this study were Copper (II) nitrate trihydrate [$Cu(NO_3)_2.3H_2O$], deionized (DI) water, ethylene glycol ($HOCH_2CH_2OH$), hydrogen peroxide (H_2O_2) and absolute ethanol (C_2H_6O). These chemicals were purchased from Merck (Merck Specialities Private Limited). Sodium sulphide ($Na_2S.9H_2O$) was obtained from RANKEM Laboratory Reagent and multi-walled carbon nanotubes (MWCNT) were purchased from Sigma Aldrich.

4.2.2. Synthesis of CuS

The solvothermal method was used to synthesize CuS nanoparticles. Firstly, 0.9964 g of $Cu(NO_3)_2.3H_2O$ was mixed with 30 mL of ethylene glycol and placed on a magnetic stirrer for 30 minutes to obtain a homogeneous solution (solution 1). Then, 0.9604 g of $Na_2S.9H_2O$ was mixed with 20 mL ethylene glycol and another homogeneous solution was prepared using magnetic stirring for 30 minutes (solution 2). Solution 2 was slowly added drop by drop into solution 1. The resulting mixture was stirred for 1 hour and then transferred to a Teflon-lined solvothermal autoclave. The autoclave was placed inside an oven and kept at a temperature of 160 °C for 16 hours. The precipitate was washed four times with DI water and ethanol before being collected using centrifugation techniques. Finally, the collected CuS nanoparticles were dried at 60 °C for 16 hours.

4.2.3. Synthesis of CNT-CuS

At first, CNT was purified by acid treatment to remove the impurities. A certain amount of CNT is oxidized by a mixed solution of concentrated nitric acid and sulfuric acid, with a volume ratio of 1:3 and then sonicated for 12 hours at 40 °C. After that the acidic CNT is filtered and washed with distilled water for several times. Finally, the CNT has been dried in a vacuum and collected[12]. After that, a similar solvothermal method was used to synthesise the CNT-CuS composites (T-CuS). In this process, a certain amount (3%) of carbon nanotubes (CNTs) were dispersed in $Cu(NO_3)_2$ precursor solution and stirred for 30 minutes. Na_2S solution was then slowly added dropwise into the mixer. This resulting solution was kept under magnetic stirring for 6 hours. Next, the solution was kept in a Teflon-lined autoclave and placed in a hot air oven at a fixed temperature of 160 °C for 16 hours. The collected samples were washed multiple times with DI water and absolute ethanol and dried on a hot plate at 60° C for 12 hours. The entire synthesis process of the CNT-CuS (T-CuS) composite is collectively schemed out in Fig. 4.1.

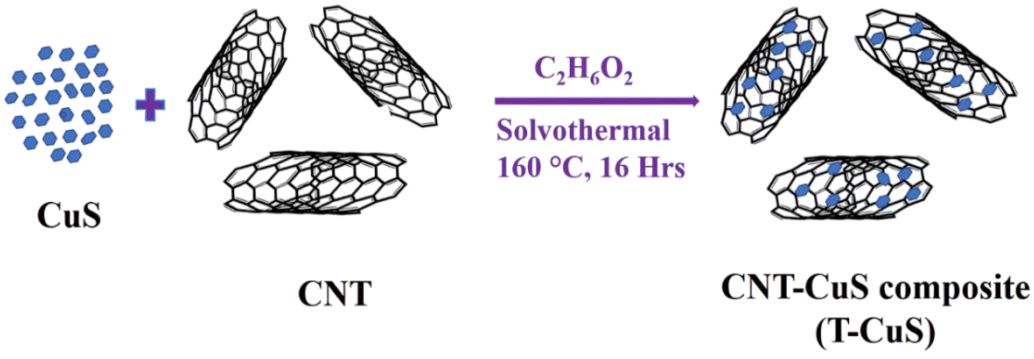

Fig. 4.1: Schematic diagram of the synthesis process of CNT-CuS nanocomposite.

4.2.4. Fabrication of Schottky Devices

In this report, the electrical characteristics were studied in CuS and T-CuS-based metal-semiconductor (MS) junction Schottky devices. First, ITO-coated glass substrates were cleaned using acetone, followed by 2-propanol and distilled water. Then, on the top of the cleaned ITO-coated substrate, the thin film of CuS and T-CuS was deposited by the effusion cell coating unit (HindHivac Coating unit 3.0) under an atmospheric pressure of 5.0×10^{-6} mbar. Subsequently, the as-prepared films were dried in a vacuum oven for 1 h. Next, as a metallic contact, Aluminium (Al) was deposited onto the coated film using a

vacuum coating unit (12A4D, HINDHIVAC) under an atmospheric pressure of 3.2 $\times 10^{-6}$ Torr. In the deposition method, a typical quad-punch-hole shadow mask was used to control the effective contact area of the Schottky devices as 7.065×10^{-6} m^{-2}. The schematic diagram of the Schottky device structure is portrayed in Fig. 4.2.

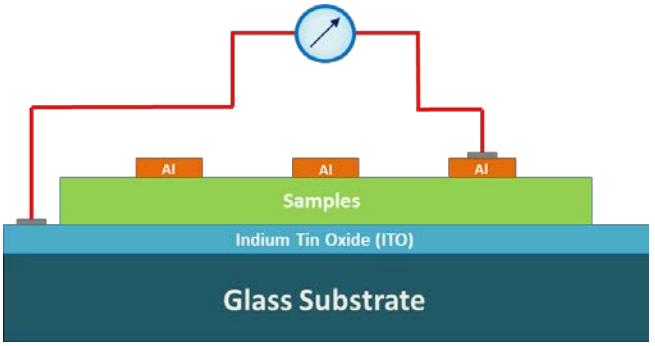

Fig. 4.2: Schematic diagram of the fabricated Schottky devices.

4.3. Material Characterizations Techniques

The constituent phases and crystal structure were analyzed by X-ray diffraction (XRD) by a Bruker D8 apparatus, having Cu-Kα radiation (λ = 1.5418 Å). The surface morphology was examined through the images of vacuum-deposited CuS and T-CuS thin films, captured by field emission scanning electron microscopy (FESEM) obtained from FEI Inspect F50. The surface topography of the fabricated Schottky diodes was evaluated using atomic force microscopy (AFM) images. Using an Agilent 4294A impedance analyzer, impedance spectroscopy (IS) of the MS junction diodes was carried out. A semi-automated source measurement equipment (Keithley 2635B) was used to measure the current-voltage (I-V) of CuS and T-CuS-based devices and the photo-responsive behaviour of the materials was measured by a solar simulator [Model 10500, Abet Technologies].

4.4. Results and Discussion

4.4.1. Structural Properties

The PXRD pattern of CuS and T-CuS nanocomposites is shown in Fig. 4.3. The diffraction peaks of the synthesised CuS were observed at specific angles, at 2θ ≈ 27.12°, 27.68°,

29.28°, 31.78°, 32.85°, 38.83°, 47.94°, 52.71°, 59.34°, 73.99°, and 79.07°. These peaks were assigned to the crystallographic planes (100), (101), (102), (103), (006), (105), (110), (108), (116), (208), and (213) of the hexagonal copper sulphide structure. The corresponding values of lattice parameters, as determined by the JCPDS Card No. 06-0464, (a = 6.792 Å and c = 16.34 Å). The narrow and sharp peaks show the crystallinity of bare CuS. The major diffraction peaks of the T-CuS composite were identical to those of bare CuS, as seen by the XRD pattern. This indicates that the CNT attachment had no effect on the preferred orientations of CuS and resulted in the formation of a new crystallographic phase. The composite showed no distinct CNT diffraction peaks. It might have happened because of the lower loading and comparatively weak diffraction peaks of CNT[13].

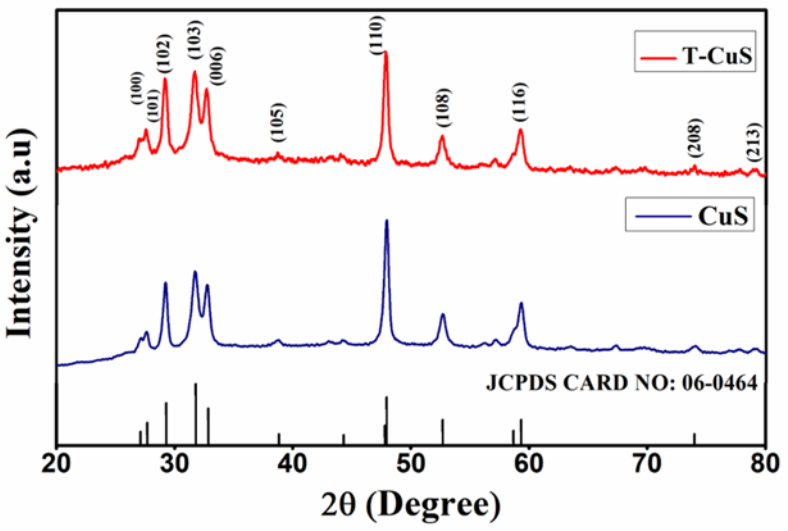

Fig. 4.3: PXRD spectra of as-synthesized CuS and T-CuS nanocomposite

4.4.2. Morphological Studies

Fig. 4.4 depicts the images of FESEM for the synthesized CuS and T-CuS nanocomposites. According to the microstructural and morphological information obtained from SEM images, the CuS and T-CuS composites are almost hexagon-shaped nanostructures (~ 50 - 60 nm) and have some aggregation in the pattern. Fig. 4.4(b) clearly shows a good attachment of CuS nanocomposites to the CNT during the solvothermal synthesis. The CNT network structure creates a certain space which assists the diffusion process and helps to aggregate the CuS materials onto the CNT with efficient suppression.

Therefore, it is expected that the electron transfer between CuS and CNT could be enhanced.

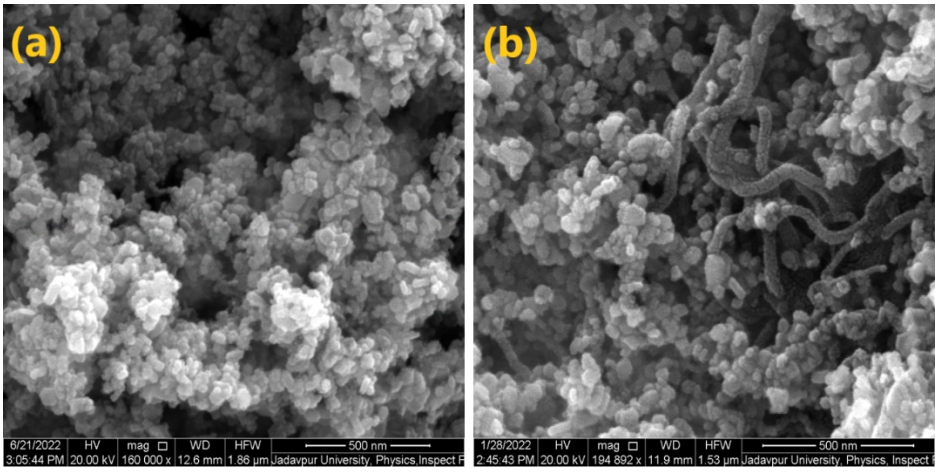

Fig. 4.4: FESEM micrographs of (a) CuS and (b) T-CuS thin films

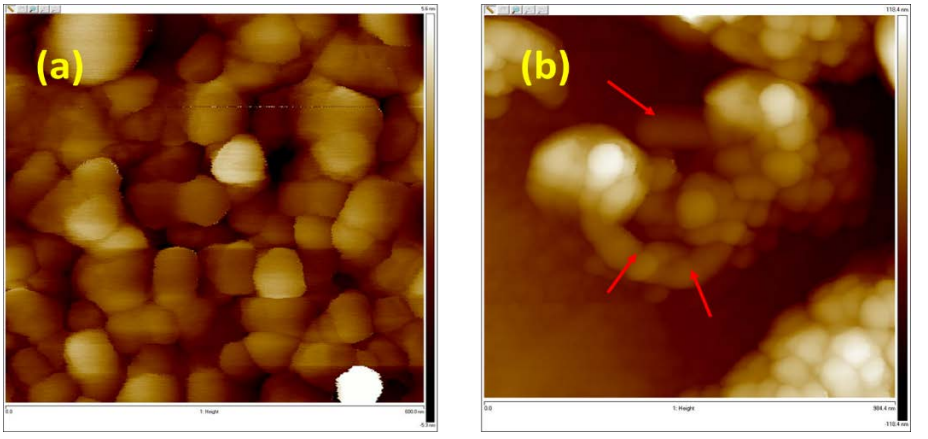

Fig.4.5: AFM images of the (a) CuS/Al and (b) T-CuS/Al Schottky contacts

AFM pictures (Fig. 4.5) provide important information on the interfacial structures and topography of the fabricated Schottky diodes. In figure 4.5a, a uniform distribution of CuS particles over the surface of indium tin oxide (ITO) is evident[14]. The AFM images, as shown in Fig. 4.5a reveal hexagonal-shaped CuS particles with sizes ranging from 50 to 60 nm, consistent with the SEM images discussed earlier. This homogenous dispersion is beneficial for producing good-quality Al/CuS Schottky contacts. For the Schottky devices based on T-CuS, the CuS particles exhibit a random scattering over the carbon nanotubes (CNTs), exposing a greater surface area to the Al contacts and promoting effective charge transfer.

While the CNTs may not be distinctly visible in the AFM micrographs compared to SEM images, their presence is acknowledged. In Fig. 4.5b, a few CNTs are discerned, surrounded by CuS particles, providing an increased surface area to the Schottky junction and facilitating smooth charge transfer. The surface roughness of both the layers on the ITO surface was measured, resulting in the root mean square (RMS) values of surface roughness as 1.39 nm and 0.81 nm for CuS and T-CuS-based devices, respectively. It is expected that fewer traps are created in the T-CuS composite due to its lesser surface roughness. In addition, lower surface roughness is preferred for the charge transfer from the electrode to the semiconducting materials. Since, during deposition, the metal penetrates less into the film layer having lower surface roughness[15]. The reduced roughness observed in CNT-CuS-based Schottky diodes signifies the formation of well-defined interfacial contacts, enhancing the capabilities of charge transfer[16].

4.4.3. Impedance Spectroscopy Analysis

Impedance spectroscopy is a useful technique for exploring the frequency-dependent characteristics of Schottky devices including MS junction. In this investigation, we scrutinized the characteristics of Al/CuS and Al/T-CuS MS junction Schottky diodes (SDs) by conducting bias-dependent impedance spectra measurements across a voltage range from -1.0 Volt to +1.0 Volt. The frequency varied from 40 Hz to 10 MHz while maintaining a consistent oscillating voltage of 100 mV. The Nyquist plots illustrated in Fig. 4.6 display distinct semicircular arcs, with the arc diameter increasing when the negative bias value decreases and decreasing with the increment of positive biases. These results demonstrate how applied voltages have a substantial impact on the impedance of the MS junction[17].

Upon application of a negative voltage to the circuit, the Fermi energy (E_F) of the semiconductor decreases relative to that of the metal, leading to an elevation in the semiconductor's potential. As a result, the depletion region is broader and at the interface, the electronic charge field is greater than the previous field. Consequently, under reverse bias voltages, a barrier arises that prevents electron movement at the metal-semiconductor (MS) contact. In contrast, under forward bias conditions, the semiconductor's Fermi energy level rises above that of the metal, reducing the potential across the semiconductor and disrupting the drift current-diffusion relationship[18].

Consequently, under forward bias voltages, the barrier is decreased, allowing more electrons to diffuse towards the metal instead of drifting into the semiconductor.

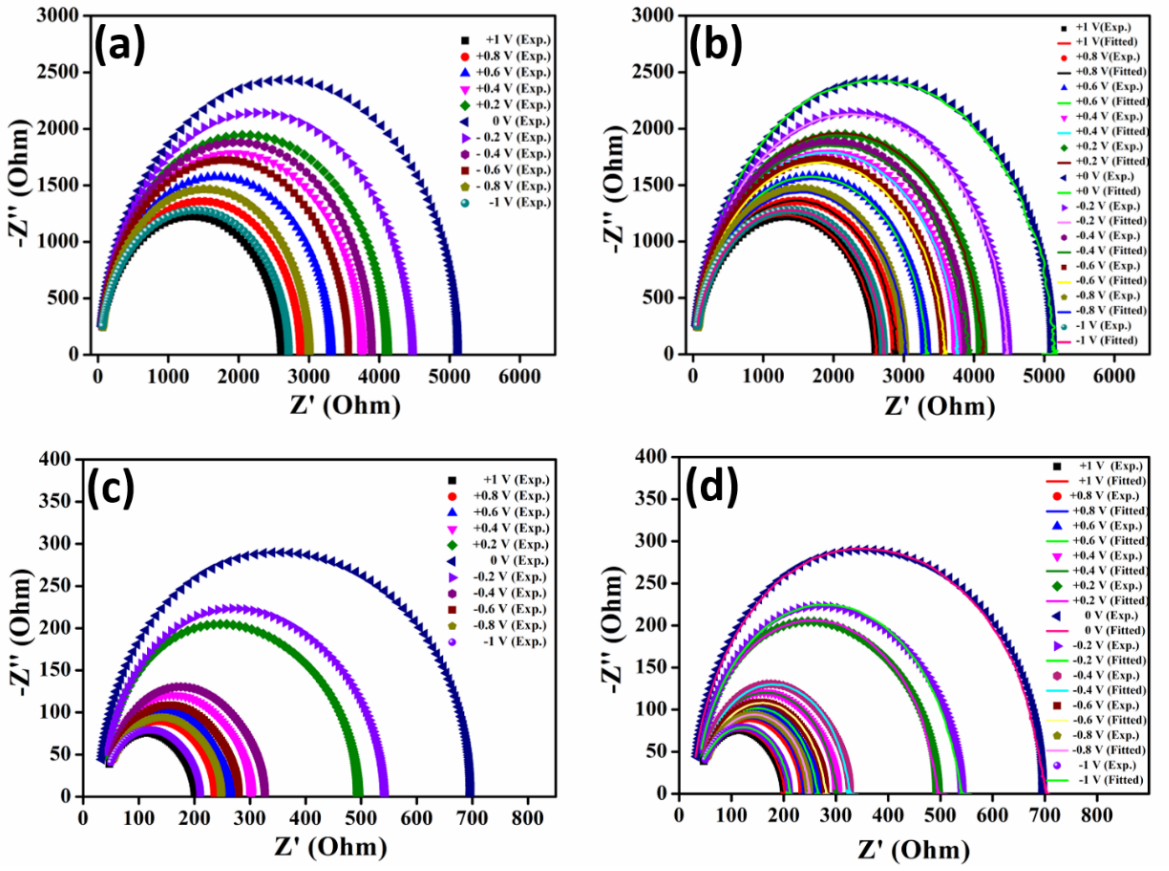

Fig. 4.6: Experimental as well as the Nyquist fitted plots for (a, b) CuS and (c, d) T-CuS-based SD under reverse and forward bias voltages

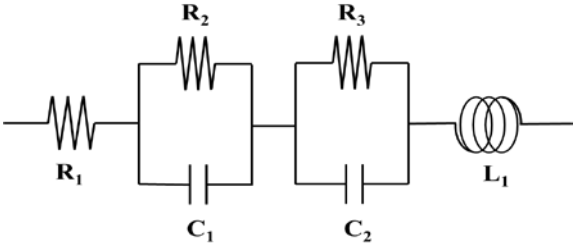

Fig. 4.7: Equivalent circuit model of the Al/CuS and Al/T-CuS based MS junction diode

An equivalent circuit made up of capacitances (C), resistances (R) and inductors (L) was employed to precisely characterize the impedance spectra recorded at different bias voltages. Fig. 4.7 depicts the equivalent circuit utilized for CuS and T-CuS-based Schottky diode (SD), featuring a series of resistances connected to two meshes of resistance and a parasitic inductance (L).

The Nyquist curves obtained for CuS and T-CuS-based Schottky diodes were fitted and presented in Fig. 4.6b and 4.6d, respectively; demonstrating a close agreement between the experimental and fitted data. Table 3.1 and Table 3.2 summarize the fitted parameters for CuS and T-CuS-based Schottky devices, respectively. Notably, the shunt resistance (R_1) remains constant across the entire DC bias range, while the other series resistances, R_2 and R_3, exhibit significant changes as the voltage shifts from reverse bias to forward bias. Specifically, R_2 assumes considerably higher values than R_3 under reverse bias voltages, indicating that the R_2C_1 component in the equivalent circuit correlates to the Schottky barrier forming at the Al/CuS or Al/T-CuS interface, restricting charge flow through the junction. On the other hand, under forward bias, R_2 sharply decreases as bias voltages increase, allowing a greater current flow due to the barrier being decreased[19]. The relatively small variations observed in R_3 across the entire DC bias range can be attributed to the ITO-CuS or ITO/T-CuS interface, where slight fluctuations may arise due to the presence of defects[20].

Table 4.1: *Parameters of CuS-based SD obtained from the fitted impedance spectra.*

Voltage (V)	R_1 (Ω)	R_2 (Ω)	C_1 (F)	R_3 (Ω)	C_2 (F)	L_1 (H)
+1	36.144	1694	1.16×10^{-10}	855.26	1.21×10^{-10}	1.75×10^{-7}
+0.8	37.798	2044.4	1.07×10^{-10}	797.35	1.39×10^{-10}	1.20×10^{-7}
+0.6	37.841	2502.7	1.47×10^{-9}	776.64	9.00×10^{-11}	1.89×10^{-7}
+0.4	37.883	2833.8	1.54×10^{-10}	886.21	9.66×10^{-11}	1.12×10^{-7}
+0.2	38.354	3133.8	1.25×10^{-10}	880.23	1.06×10^{-10}	1.37×10^{-7}
0	39.826	4211.5	2.18×10^{-9}	1236.9	9.78×10^{-10}	8.43×10^{-8}
-0.2	38.577	3471	1.78×10^{-10}	945.28	9.01×10^{-11}	8.72×10^{-8}
-0.4	37.063	3012.2	1.82×10^{-10}	902.73	8.80×10^{-11}	1.35×10^{-7}
-0.6	37.705	2677.7	1.76×10^{-10}	812.77	9.29×10^{-11}	8.45×10^{-7}
-0.8	37.447	2110	1.69×10^{-10}	842.73	9.26×10^{-11}	1.95×10^{-7}
-1	36.537	1709.9	1.15×10^{-10}	981.66	1.24×10^{-10}	1.35×10^{-7}

Table 4.2: *Parameters of T-CuS-based SD obtained from the fitted impedance spectra.*

Voltage (V)	R_1 (Ω)	R_2 (Ω)	C_1 (F)	R_3 (Ω)	C_2 (F)	L_1 (H)
+1	22.873	141.34	5.08×10^{-9}	125.314	3.07×10^{-10}	1.61×10^{-7}
+0.8	25.316	168.3	4.29×10^{-9}	130.413	2.62×10^{-10}	2.11×10^{-7}
+0.6	25.839	199.86	7.70×10^{-9}	136.691	2.52×10^{-10}	2.10×10^{-7}
+0.4	26.77	227.36	5.79×10^{-9}	141.879	2.61×10^{-10}	1.99×10^{-7}
+0.2	26.974	339.1	2.59×10^{-9}	146.12	2.85×10^{-10}	1.77×10^{-7}
0	27.881	390.29	1.56×10^{-9}	180.13	3.64×10^{-10}	1.43×10^{-7}
-0.2	27.088	369.62	2.38×10^{-9}	151.29	2.61×10^{-10}	1.93×10^{-7}
-0.4	26.647	245.82	5.35×10^{-9}	142.279	2.41×10^{-10}	2.15×10^{-7}
-0.6	25.944	211.93	7.26×10^{-9}	139.485	2.38×10^{-10}	2.23×10^{-7}
-0.8	25.565	176.48	4.09×10^{-9}	136.086	2.51×10^{-10}	2.21×10^{-7}
-1	23.366	148.41	4.84×10^{-9}	130.779	2.92×10^{-10}	1.69×10^{-7}

4.4.4. Current-Voltage (I-V) Measurement

We investigated the electrical properties of CuS and T-CuS-based MS junction thin-film devices in more detail by impedance spectroscopy analysis. Subsequently, the current-voltage (I-V) properties of CuS and T-CuS-based Schottky devices were analyzed in the dark and light conditions both, within a bias voltage of ±1 V. The I-V characteristics of the Al/CuS/ITO and Al/T-CuS/ITO configurations show the rectifying nonlinear behaviour of a Schottky diode (SD) as displayed in Fig. 4.8[21]. The CuS-based SD's on/off ratio was calculated and the results showed that it was 15.69 in the dark and 21.80 in the light condition. In contrast, the T-CuS-based SDs showed values of 16.27 and 25.10 in the dark and light, respectively. The significantly greater current seen in the presence of light suggests that the device is photoresponsive. Additionally, the conductivities of the CuS and T-CuS-based SDs were measured in dark and light conditions and the conductivities of both types of SDs significantly increased after photo-irradiation shown in Table 4.3.

This indicates a notable improvement in the carbon nanotube composites' conductivity over the pure CuS-based devices[22,23].

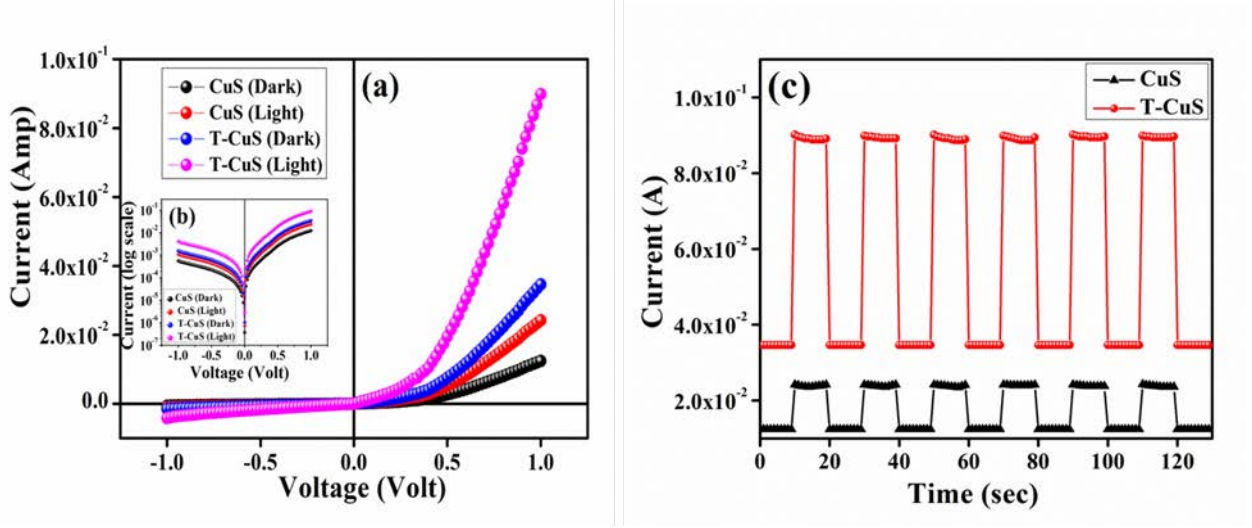

Fig. 4.8: I-V characteristics curve for the (a) CuS and T-CuS-based Schottky devices (b) log scale current-voltage curve (inset) and (c) Transient photocurrent response of CuS and T-CuS composite.

The current-voltage (I-V) characteristics of the CuS and T-CuS-based Schottky diodes (SDs) were further investigated with the thermionic emission (TE) theory discussed in the preceding chapter (§ 2.7.1)[24,25]. Cheung equations were used to obtain different diode parameters[26,27]. For a quantitative analysis of the I-V curves, the following standard equations were taken into consideration:

$$I = I_0 \left[exp\left(\frac{qV}{\eta kT}\right) - 1 \right] \quad (4.1)$$

where I_0 represent the saturation current and is given by:

$$I_0 = AA^*T^2 \, exp\left(\frac{-q\phi_B}{kT}\right) \quad (4.2)$$

Here, the symbols represent as follows:

q – charge of the electron, k - Boltzmann constant, T – temperature value in Kelvin scale, V_D - voltage across the diode, A_{eff} – effective area of diode, η - ideality factor, ϕ_B - barrier height and A* - Richardson constant, correspondingly. Eq. 1 can also be represented with the series resistance taken into consideration as:

$$I = I_0 \, exp\left[\frac{q(V - IR_S)}{\eta kT}\right] \quad (4.3)$$

In this equation, the voltage drops across the series resistance are represented by the IR_S term. The ideality factor and series resistance have a relationship that may be described as follows by using the Cheung and Cheung analysis[26], which can be expressed as:

$$\frac{dV}{d(\ln I)} = \left(\frac{\eta kT}{q}\right) + IR_S \qquad (4.4)$$

Moreover, the following equation can be used to calculate the effective barrier height of the SBD as follows:

$$H(I) = V - \left(\frac{\eta kT}{q}\right) ln\left(\frac{I}{AA*T^2}\right) \qquad (4.5)$$

Eq. 4.5 can be expressed as:

$$H(I) = IR_S + \eta\phi_B \qquad (4.6)$$

A graphical representation of dV/d(lnI) vs. I and H vs. I for the samples in both the dark and the light is shown in Figure 4.9. Important parameters like ideality factor (η) and series resistance (R_S), were found by analyzing the linear plot of dV/dlnI vs. I and its intercept and slope, respectively. In addition, the intercept of the H vs. I plot was used to determine the barrier height (BH). The results, represented in Table 4.4, show that the devices' ideality factor deviated from ideal behaviour mainly because of the existence of interfacial states and the inhomogeneity of Schottky contacts[28].

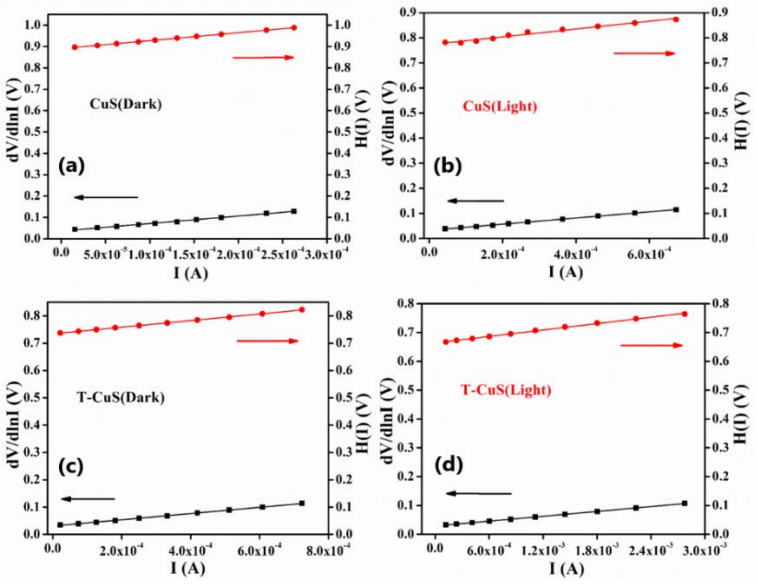

Fig. 4.9: (a) dV/dlnI vs. I and H (V) vs. I plot of CuS[(a) dark and (b) light] and T-CuS[(c)dark and (d)light] based Schottky devices.

On the other hand, light exposure produced an improved ideality factor (IF) that was approaching 1, suggesting a more ideal device. This improvement is explained by

decreased carrier recombination and increased homogeneity of Schottky connections under photo irradiance conditions. Moreover, the calculated barrier height (BH) values indicate a somewhat reduced turn-on voltage when lighted. The decreased barrier height may be responsible for the greater rectification ratio that was seen under light irradiance[29]. Interestingly, in the presence of light, the series resistance of CuS and T-CuS significantly decreased, which resulted in a large rise in the photocurrent. The devices' enhanced performance after being exposed to light is highlighted by the summarized values of IF, BH, and series resistance in Table 4.4.

Transient photo-response spectra were performed to investigate the optoelectronic response of the fabricated devices and are shown in Figure 4.8c. The photocurrent intensity of the T-CuS composite was found to be significantly higher (Figure 4.8c) than that of the pure CuS, as expected. This result suggests that incorporating CNT into the CuS nanoparticles could facilitate the separation of photo-generated electrons and holes and their swift transfer through the complex network. These results demonstrate CuS and T-CuS's enormous potential in a variety of optoelectronic devices, highlighting their importance in the field.

Table 4.3: *Charge transport parameters.*

Sample	**Conductivity (σ) ($S.m^{-1}$)**		**Photo-sensitivity**	**Rectification Ratio**	
	Dark	**Light**	**-**	**Dark**	**Light**
CuS	3.42×10^{-4}	6.71×10^{-4}	1.01	15.69	21.80
T-CuS	9.57×10^{-4}	2.48×10^{-3}	2.05	16.27	25.10

Table 4.4: *Schottky diode parameters.*

Sample	**Ideality factor (η)**		**Barrier height (ϕ_B) (eV)**		**Series Resistance (R_S) (Ω)**	
	Dark	**Light**	**Dark**	**Light**	**Dark**	**Light**
CuS	1.40	1.25	0.63	0.62	361	139
T-CuS	1.19	1.12	0.60	0.58	116.5	32.5

4.5. Conclusions

This study included a thorough examination of CuS and T-CuS-based Schottky diodes (SDs) by using DC current-voltage measurements and AC impedance spectroscopy analysis. The ac impedance spectroscopy investigation shed light on the interfacial characteristics of the CuS and T-CuS-based metal-semiconductor (MS) junction SDs at different DC bias voltages. In addition, an AC equivalent circuit model was built to expand our understanding of the circuit components regulating the interfaces inside the fabricated SDs. Through the utilization of AC impedance spectroscopy, a comprehensive examination of different interfaces and their electrical charge transport characteristics was accomplished. This approach allowed us to analyze these features at a level depth that cannot be achieved just via dc analysis. The CNT-CuS-based SDs with their enhanced photosensitivity and greater rectification ratio showed great promise for use in the application of opto-electronic devices and rectification processes.

***

References

1. E. Shalaan, E. Ibrahim, F. Al-Marzouki and M. Al-Dossari, *Applied Physics A*, 2020, **126**, 852.

2. M. Isik, M. Terlemezoglu, N. Gasanly and M. Parlak, *Physica E Low Dimens Syst Nanostruct*, 2022, **144**, 115407.

3. S. Sun, P. Li, S. Liang and Z. Yang, *Nanoscale*, 2017, **9**, 11357–11404.

4. F. Ghribi, A. Alyamani, Z. Ben Ayadi, K. Djessas and L. EL Mir, *Energy Procedia*, 2015, **84**, 197–203.

5. H. Wang, Q. Liu, W. Li, L. Wen, D. Zheng, Z. Bo and L. Jiang, *ACS Nano*, 2016, **10**, 3606–361.

6. D. Wang, M. Sun, G. Feng and C. Song, *J Mater Eng Perform*, 2019, **28**, 6649–6655.

7. N. ul Ain, J. Abdul Nasir, Z. Khan, I. S. Butler and Z. Rehman, *RSC Adv*, 2022, **12**, 7550–7567.

8. X. Meng, L. Shi, L. Cui, L. Yao and Y. Zhang, *Mater Res Bull*, 2021, **135**, 111156.

9. K. Thakur and B. Kandasubramanian, *J Chem Eng Data*, 2019, **64**, 833–867.

10. N. Anzar, R. Hasan, M. Tyagi, N. Yadav and J. Narang, *Sensors International*, 2020, **1**, 100003.

11. M. F. Abou Taleb, N. Shaheen, F. I. A. El Fadl, H. A. Albalwi, M. M. Ibrahim, and M. F. Warsi, J Alloys Compd, 2023, **958**, 170468.

12. M. Kolahdouz, B. Xu, A. F. Nasiri, M. Fathollahzadeh, M. Manian, H. Aghababa, Y. Wu, and H. H. Radamson, Micromachines (Basel), 2022, **13**, 1257.

13. Y.-L. Chen, Z.-A. Hu, Y.-Q. Chang, H.-W. Wang, Z.-Y. Zhang, Y.-Y. Yang and H.-Y. Wu, *The Journal of Physical Chemistry C*, 2011, **115**, 2563–2571.

14. A. Chowdhury, B. Biswas, M. Majumder, M. K. Sanyal and B. Mallik, *Thin Solid Films*, 2012, **520**, 6695–6704.

15. H. H. Radamson, A. Hallén, I. Sychugov, and A. Azarov, *Analytical Methods and Instruments for Micro- and Nanomaterials*, Springer International Publishing, Cham, 2023.

16. A. Fernández-Pérez, C. Navarrete, R. Muñoz, E. Baradit, M. Saavedra, G. Cabello-Guzmán and W. Gacitúa, *Mater Res Express*, 2021, **8**, 016408.

17. C. Yim, N. McEvoy and G. S. Duesberg, *Appl Phys Lett*, 2013, **103**, 193106.

18. Z. Benamara, B. Akkal, A. Talbi and B. Gruzza, *Materials Science and Engineering: C*, 2006, **26**, 519–522.

19. D. Das, M. Das, A. Biswas, P. Sahu and P. P. Ray, *Journal of Materials Science: Materials in Electronics*, 2023, **34**, 1574.

20. H. Kim, M. J. Jung and B. J. Choi, *Solid State Commun*, 2022, **344**, 114685.

21. M. Shah, M. H. Sayyad, Kh. S. Karimov and M. Maroof-Tahir, *Physica B Condens Matter*, 2010, **405**, 1188–1192.

22. D. Das, M. Das, S. Sil, P. Sahu and P. P. Ray, *ACS Omega*, 2022, **7**, 26483–26494.

23. M. Das, D. Das, S. Sil and P. P. Ray, *Nanoscale Adv*, 2023, **5**, 3655–3663.

24. S. M. Sze and K. K. Ng, *Physics of Semiconductor Devices*, Wiley, 2006.

25. S. S. Li, in *Semiconductor Physical Electronics*, Springer New York, New York, NY, pp. 284–333.

26. S. K. Cheung and N. W. Cheung, *Appl Phys Lett*, 1986, **49**, 85–87.

27. D. Das, M. Das, P. Sahu and P. Pratim Ray, *Mater Today Proc*, 2023.

28. İ. Taşçıoğlu, U. Aydemir and Ş. Altındal, *J Appl Phys*, 2010, **108**, 064506.

29. I. Ullah, M. Shah, M. Khan and F. Wahab, *J Electron Mater*, 2016, **45**, 1175–1183.

***

Development of hierarchical copper sulfide-carbon nanotube (CuS-CNT) composites and utilization of its superior carrier mobility in efficient charge transport towards photodegradation of Rhodamine B under visible light

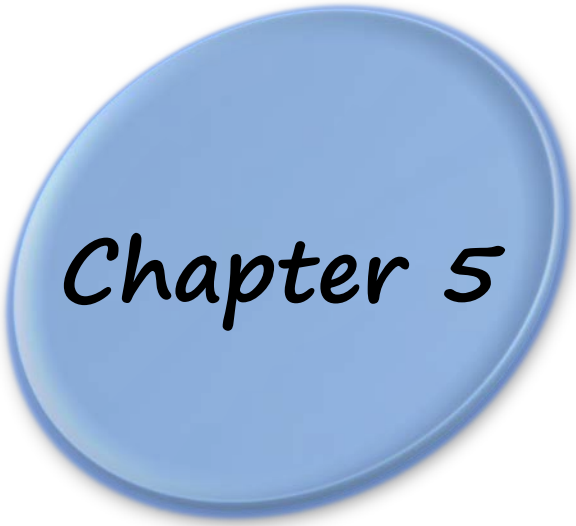

5.1. Introduction

Organic dyes and pigments discharged into water sources, mostly by the paint and textile industries, are causing serious environmental issues and harming the ecosystem in other ways[1]. Over the last few decades, various biological and physicochemical experiments based on physical as well as chemical adsorption approaches have been conducted to decompose these industrial pollutants. However, these processes often produce secondary pollutants and are not cost-effective from the economic viewpoint[2]. The photocatalytic approach based on semiconductor materials has demonstrated significant efficiency in wastewater purification among all advanced oxidation techniques known to exist[3]. There are some well-known semiconducting photocatalysts, namely TiO_2 and ZnO, which have been widely used to decompose organic pollutants, but their use is hindered due to their wide range bandgaps, which are 3.2 eV and 3.37 eV for TiO_2 and ZnO, respectively, limiting their light absorption mainly in the ultraviolet (UV) region of the solar spectrum[4,5]. This reduces the redox reactions with the impurities and significantly affects the rate of degradation[6].

On the other hand, copper (II) sulfide (CuS) has a narrow direct bandgap of 2.29 eV, due to which it can efficiently capture visible light from the solar spectrum, making it practically function as a 'visible-light-driven photocatalyst'. It also has excellent optical and electronic properties which show great potential in many fields like solar cells[7], energy storage[8], gas sensors[9], biosensors[10] and photocatalysis[11]. Copper sulfide has some excellent features, such as its environmentally friendly and non-toxic nature, low cost, biocompatibility, higher physical and chemical stability and ease of recyclability which enhances its effectiveness as a prospective photocatalyst. On the other hand, CuS nanomaterials also have an intrinsic drawback of having poor photocatalytic performance, especially when exposed to visible light, due to the quick electron (e^-)–hole (h^+) recombination. There have been several attempts to enhance the electron transfer during the photocatalytic process by reducing the electron–hole recombination in these materials. Carbon nanomaterials are eco-friendly, cost-effective and good electron acceptors, so they can suppress electron–hole recombination effectively[12]. Among them, carbon nanotubes (CNTs) are unique in terms of their morphological, structural, and electrical characteristics, such as their organised structure with a high surface to volume ratio, light weight, and high electrical conductivity. CNT increases the migration rate of photogenerated electrons, thereby pushing electrons and holes away which prohibits

electron (e^-)–hole (h^+) recombination. Absorption of light also induces electrons into the CNTs and enhances the participation of electrons in the photocatalytic reaction[13,14]. For higher photocatalytic performances, the electrons are expected to swiftly transfer and their subsequent recombination should be as slow as possible[15]. Further, the fast electron transfer depends on the mobility of the carriers. To enhance the mobility and the associated charge carrier transport properties, CNT is incorporated with bare CuS in this work. This enhanced mobility of the charge carriers in the T-CuS composite reflects in better photocatalytic performances than for bare CuS. This report describes the synthesis of a carbon nanotubes–copper sulfide (T-CuS) composite and demonstrates its capability to decompose the organic dye Rhodamine B in the presence of visible light.

5.2. Materials and Methods

The synthesis procedure of the CuS and CNT-CuS nanocomposites and the fabrication of the Schottky diodes were discussed in detail in the previous chapter (§ 4.2.3).

5.3. Material Characterization Techniques

The crystallographic structure and phase purity of the synthesized materials (CuS and T-CuS) were analysed using a powder X-ray diffractometer (Bruker D8 Advance) having Cu-K_α (λ = 1.5418 Å) radiation, operated at a scan rate of 0.02 ° s^{-1}. The surface morphology was studied with the help of a scanning electron microscope (FEI Inspect F50) and the elemental combination was determined using an EDX (Energy Dispersive X-ray) analyser. Information regarding the microstructure of the synthesised materials was analysed with the help of a transmission electron microscope (JEOL JEM 2100 F). XPS (X-ray Photoelectron Spectroscopy; Omicron Nanotechnology) with Al- K_α radiation (E = 1486.7 eV) was utilised to examine the electronic states of the elements present on the surface of the samples. The absorption spectra and the photocatalytic behaviour of the synthesized materials were recorded using a UV-Vis (PerkinElmer, Lambda 365) spectrophotometer and a solar simulator [Model 10500, Abet Technologies], respectively. The photoluminescence (PL) spectra were collected using a spectro-fluorimeter (Cary Eclipse fluorescence spectrometer, Agilent Technologies). The thermal stability of both of the materials was investigated using a thermogravimetric analyser (DTG-60H, Shimadzu) within the temperature range from 30 °C to 800 °C in a N_2 atmosphere. The estimation of the Brunauer–Emmett–Teller (BET) surface area of the

synthesised materials by N_2 adsorption–desorption was done using an Autosorb iQ2 (Quantachrome, USA) at 77 K. The measurements of current–voltage (I–V) characteristics were performed with a source measurement unit (Keithley 2635B).

5.4. Results and Discussion

5.4.1. Structural Properties

➲ *XRD Analysis*

Fig. 5.1 displays the PXRD pattern of CuS and T-CuS nanocomposites. The diffraction peaks of prepared CuS were observed at 2θ ≈ 27.12°, 27.68°, 29.28°, 31.78°, 32.85°, 38.83°, 47.94°, 52.71°, 59.34°, 73.99° and 79.07° were assigned to (100), (101), (102), (103), (006), (105), (110), (108), (116), (208) and (213) crystallographic planes of the hexagonal copper sulfide structure (JCPDS Card No. 06-00464, *a* = 6.792 Å and c=16.34 Å). The narrow, sharp peaks indicate the crystallinity of the bare CuS. The peaks at 25.89° and 43.56° were assigned to (002) and (101) planes of the CNTs respectively[16]. This XRD pattern showed that the major diffraction peaks of the T-CuS composite were similar to those of bare CuS, which explains that the attachment of CNT did not affect the preferred orientations of CuS and result in to grow a new crystallographic phase. Also, very small diffraction peaks of CNT were observed in the composite. It might have occurred due to the less amount of loading and relatively weak diffraction peaks of CNT[17].

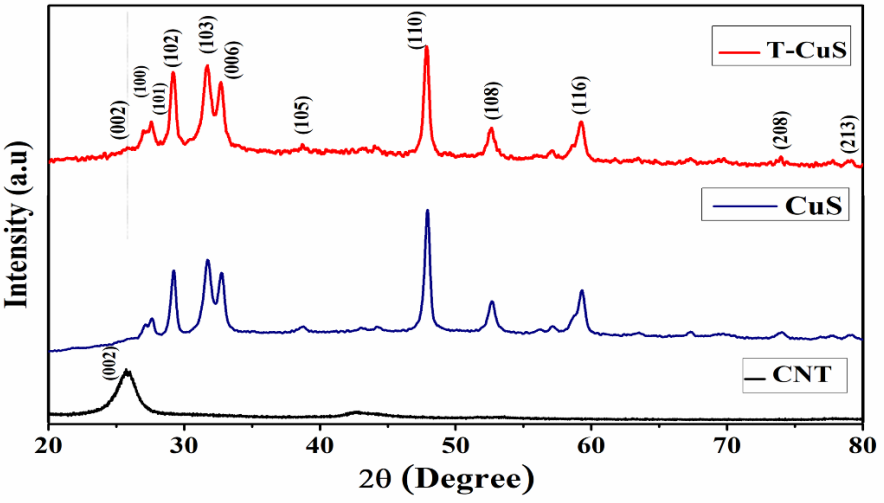

Fig. 5.1: XRD pattern of synthesized CuS and T-CuS nanocomposite.

➲ ***FESEM Study***

The FESEM images of synthesized CuS and T-CuS nanocomposite were displayed in Fig. 5.2. The microstructural and morphological information from SEM images suggests that the CuS and T-CuS composite consists of nearly hexagonal-shaped nanostructures, which contains some agglomeration in the pattern. It is clear in Fig. 5.2(b) that CuS nanocomposites were properly attached to the CNT during the hydrothermal synthesis. From the EDAX spectra (Fig. 5.2c), the appearance of constituting elements (C, O, Cu and S) in the composite was precisely noted. Further, the quantitative interpretation of the EDAX exhibited that in the synthesized material, the molar ratio of Cu to S was close to one, indicating the stoichiometric formation of CuS NPs.

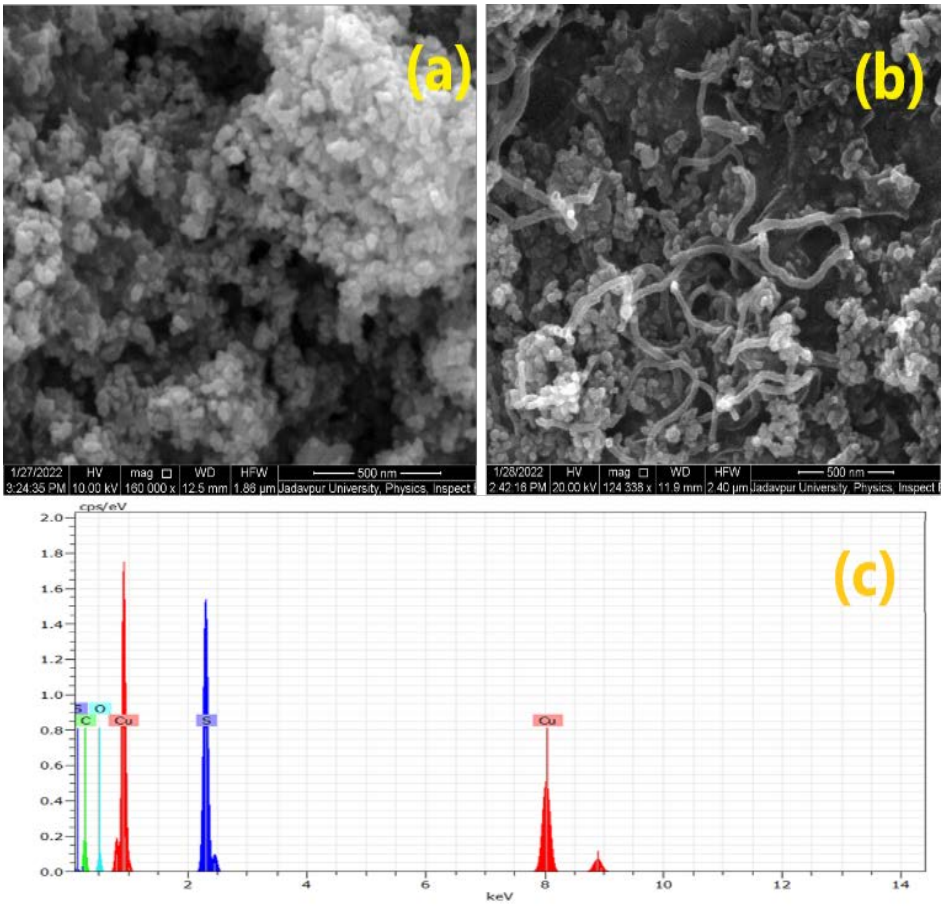

Fig. 5.2: (a) FE-SEM image of (a) CuS and (b) T-CuS and (c) EDAX spectra of the T-CuS nanocomposite.

➲ ***TEM Study***

The TEM images (Fig. 5.3a and 5.3b) further revealed that the hexagonal-like CuS NPs were uniformly attached to the carbon nanotubes, suggesting the formation of a strong interface with nominal aggregation of particles. The finer attachment between the CuS

NPs and CNT (Fig. 5.3b) by this familiar bonding could assist the transfer of charge carriers; and thus, suppress e^--h^+ recombination- which is advantageous for better photocatalytic response that will be discussed in the following paragraph. Fig. 5.3d shows the SAED pattern of T-CuS NPs with various concentric diffraction rings, suggesting the polycrystalline nature of the materials.

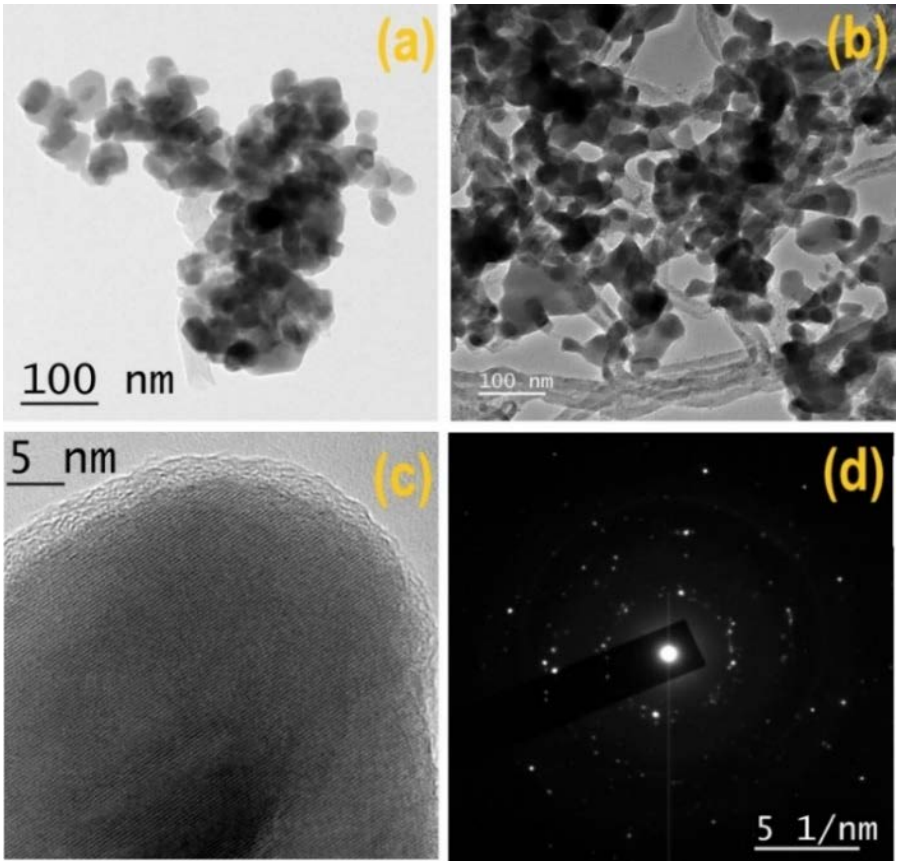

Fig. 5.3: (a) TEM image of (a) CuS and (b) T-CuS composite (c) HRTEM and (d) The SAED pattern of CuS NPs attached with CNT.

➲ ***XPS Study***

X-ray Photoelectron Spectroscopy (XPS) of T-CuS nanostructures was measured to examine the elemental composition and identify the chemical bond type as well as the oxidation states. The existence of the C, Cu, S, and O in the T-CuS composite was verified by the XPS survey spectrum scan (0-1200 eV) (Fig. 5.4a) confirming the presence of elemental Cu and S in the nanocomposite. The core level XPS spectrum of C-1s, Cu-2p and S-2p are shown in Fig. 5.4(b-d) subsequently. XPS peak for C-1s of the composite was deconvoluted into four distinct peaks centred at the corresponding binding energies (B.E.) of 284.40, 285.10, 287.60 and 290 eV, that could be ascribed to C=C, C-C, C=O and π-π* shake-up features respectively (Fig. 5.4b)[18]. This suggests the probable existence of

graphitic layers which prefer fast electron transfer and the O_2-containing group establishes strong interaction in between the aqueous solution and the nanocomposite at the time of photocatalytic decomposition, which will be discussed in the following.

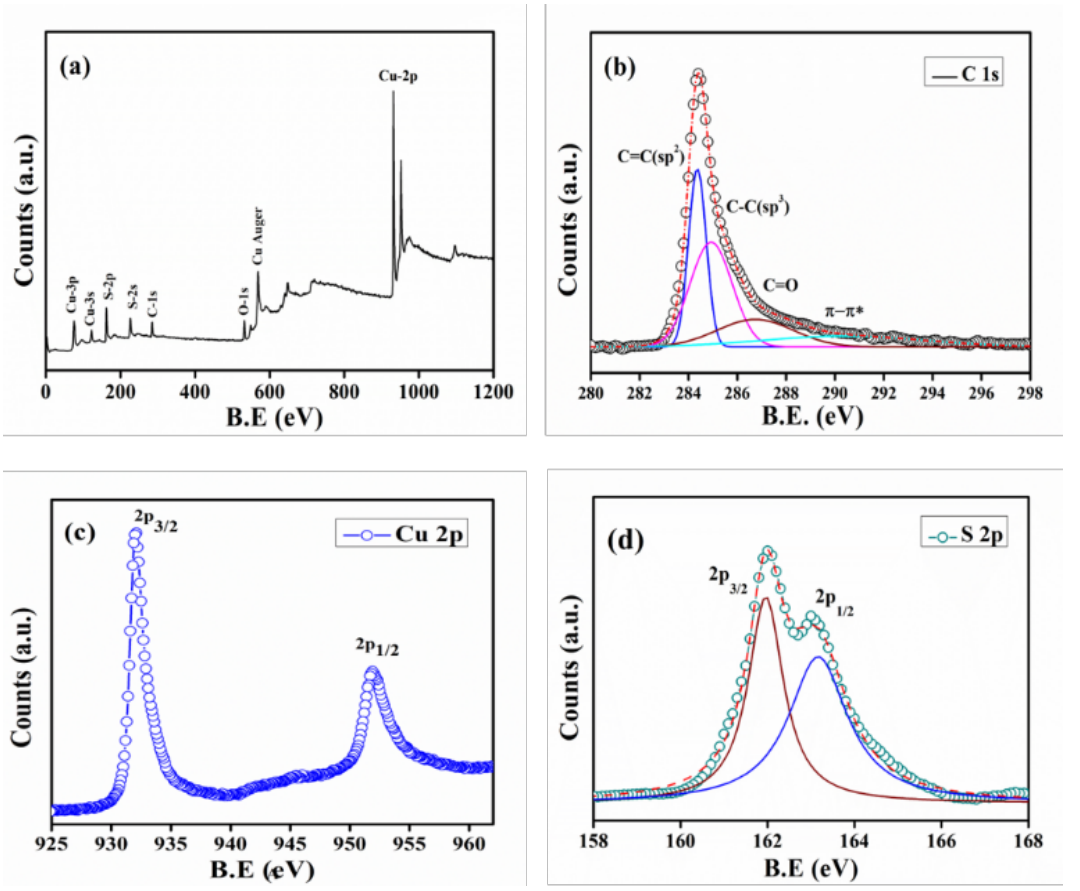

Fig. 5.4: XPS Analysis (a) full scan spectrum of T-CuS (b) spectrum C 1s for T-CuS composite. Narrow scan of (c) Cu-2p and (d) S-2p states.

The higher resolution XPS of Cu-2p which is represented in Fig. 5.4c displays two distinct peaks at 932.4 eV and 952.3 eV. The difference between these states is 19.9 eV, which is consistent with the previously reported data for Cu $2p_{3/2}$ and Cu $2p_{1/2}$ states[19].These peaks can be assigned to the Cu^{2+} state in CuS nanostructures. The higher resolution XPS spectrum of S-2p (Fig. 5.4d) represents the existence of two peaks at B.E. values of 161.9 eV and 163.3 eV, which could suggest to S $2p_{3/2}$ and S $2p_{1/2}$ states, sequentially[20]. S^{2-} species are responsible for the detection of these two peaks.

5.4.2. Optical Properties

➲ ***UV-visible Spectroscopy***

UV-vis absorbance spectra of the synthesized CuS and T-CuS nano-composite were recorded in the 300-750 nm wavelength range (Fig. 6a) to study their optical properties.

The optical band gaps (E_g) of the catalysts were deduced followed by Tauc's equation Eq. 5.1[21]. According to Tauc's equation:

$$(\alpha h\nu)^n = A(h\nu - E_g) \quad (5.1)$$

where α is the absorption coefficient, E_g is the bandgap, h is Planck's constant, ν is frequency, A is a constant, and n=2 and ½ is corresponding to the allowed direct and indirect optical transition respectively.

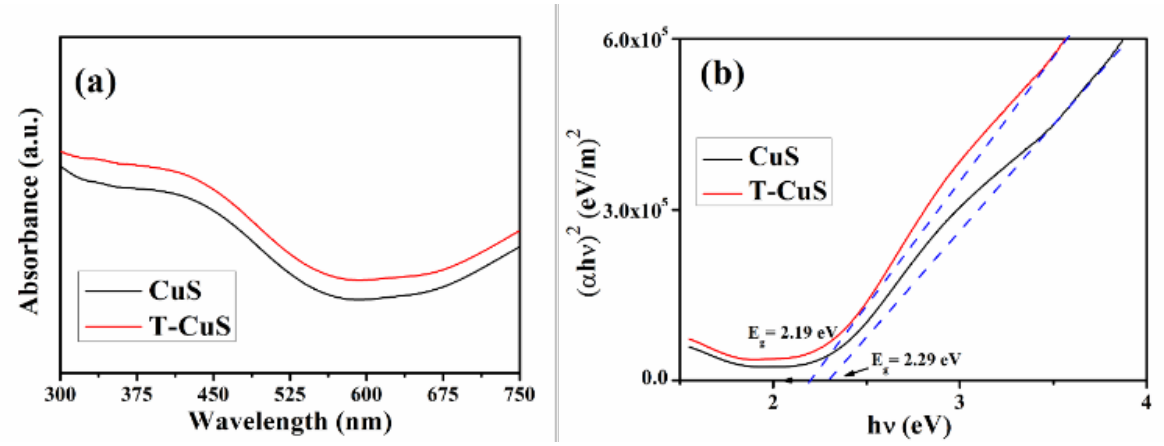

Fig. 5.5: (a) Absorption (optical) graph of bare CuS and T-CuS composite (b) Tauc's plot to obtain direct band gap of CuS and T-CuS.

The estimated value of the bandgaps of the synthesised CuS and T-CuS from Tauc's plot (Fig. 5.5b) was 2.29 eV and 2.19 eV respectively, close to the previously reported value[22]. The broadness of the absorption band and the reduced bandgap of the CNT-attached material compared to bare NPs suggests the improvement in photon absorption and more e^--h^+ pair generation for the photocatalytic experiment. The more generated e^--h^+ pairs participating in the degradation process should enhance the deterioration rate for T-CuS than bare CuS.

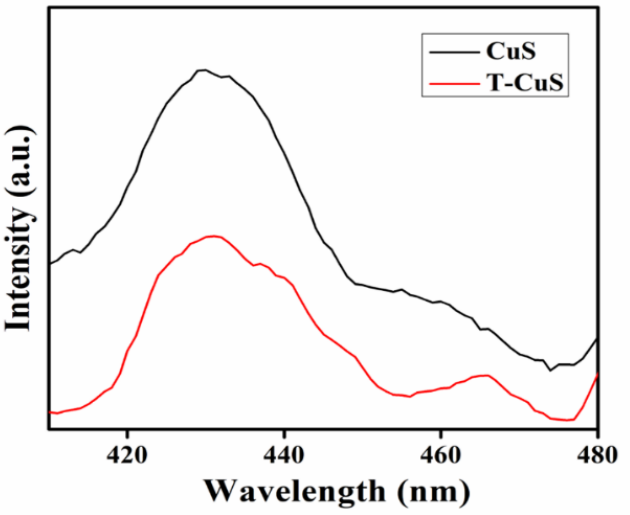

Fig. 5.6: Photoluminescence spectra of CuS and T-CuS nanocomposite.

➲ ***Photoluminescence (PL) Spectroscopy***

PL was used to study the interaction among the holes and electrons, originating from the excitation of photons in synthesized catalysts. Fig. 5.6 represents the PL spectra of CuS and T-CuS composite at 370 nm excitation. The bare CuS exhibit an eminent emission centred at 425 nm, which was sufficiently weakened after loading CNT[23,24]. This is because, there exists an effective interfacial linkage in the composite materials, so that, electrons and holes acquire a dedicated pathway to interact between CuS and CNT layers. The high electrical conductivity and sp^2 hybridization of carbon atoms show high mobility of photo-induced holes and electrons. The electrons could easily transfer from the excited CuS to the carbon nanotube through the π-conjugated carbon network and the 'quenching' of fluorescence occurs. The CNT composites are efficient to suppress the recombination rate of electrons and holes by fast electron transfer. This kind of extended separation of photo-induced charge carriers and their immediate processes is advantageous for catalytic degradation, which will be discussed in the following[24,25].

5.4.3. Thermal Stability Study

Thermal stability of the as-synthesized CuS and T-CuS composite was examined by the thermo-gravimetric analysis (TGA), executed with a gradual increase in temperature (10 °C /min) ranging from 25 °C to 800 °C in N_2 atmosphere. Fig. 5.7 represents the TGA graph

of the T-CuS composite, showing two definite stages of weight loss where 78% of weight remained up to 800 °C temperature.

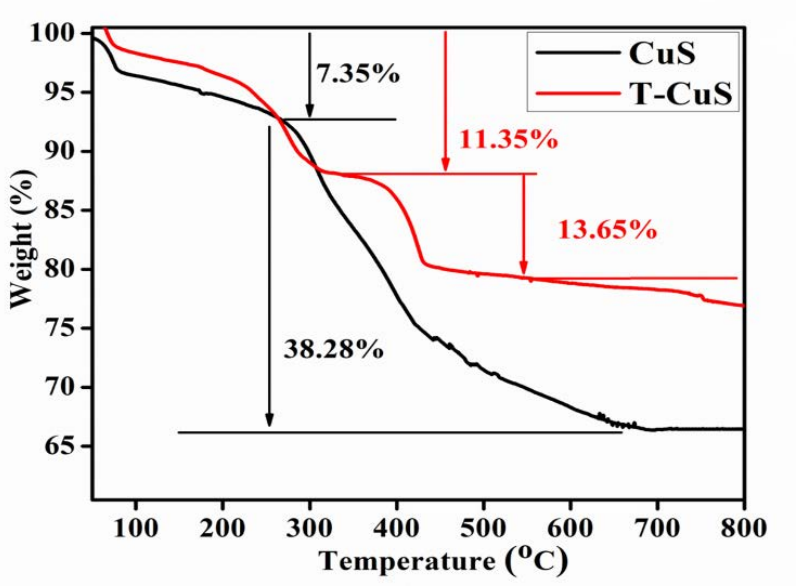

Fig. 5.7: TGA curves of bare CuS and T-CuS composite.

The initial weight loss (7.35%) for bare CuS was observed between 100-300 °C which indicates the solvent desorption and moisture absorption. Additionally, the bare CuS undertook a rapid weight loss (38.28%) around 300-650 °C due to the decomposition of CuS into Cu_2S and phase transition of sulfur elements, leaving 67 % residue[26].The first weight loss (11.35%) of T-CuS around 100-300 °C is observed due to removal of solvent and the residual organic molecular absorbed on the samples. In the second stage (300-450 °C), the weight loss (13.65%) for T-CuS was observed due to the oxidation of CNT and phase conversion of CuS. This result indicates that the CNT composite (T-CuS) is thermally more stable than bare CuS.

5.4.4. BET Surface Area Studies

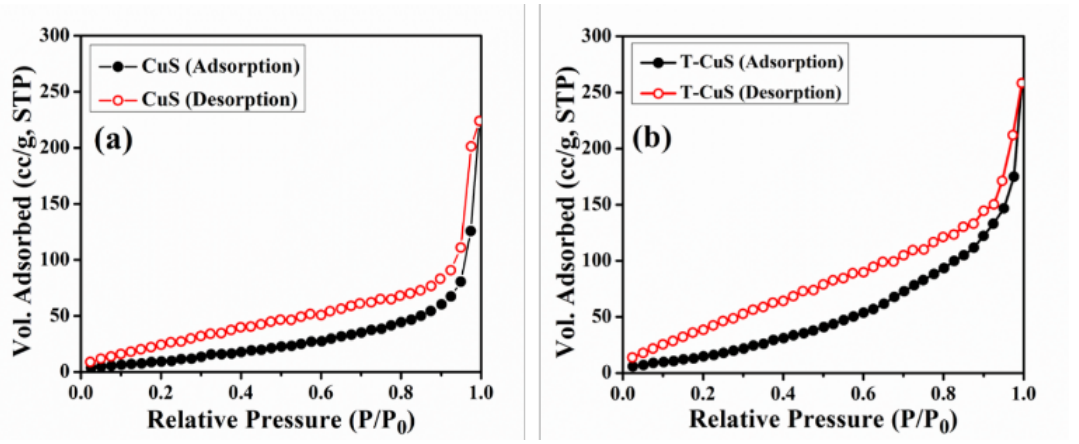

Fig. 5.8: N_2 adsorption/desorption isotherm of (a) CuS and (b) T-CuS composites.

N_2 adsorption/desorption isotherms (Fig. 5.8) were also performed at 77 K to collect more information about Brunauer-Emmett-Teller (BET) specific surfaces for the bare CuS and T-CuS nano-composite[27]. According to the BET analysis, the bare CuS and T-CuS composite displayed specific surface areas of 50.67 m^2g^{-1} and 86.83 m^2g^{-1}, respectively, showing that the CNT-based composite had a greater surface area as expected[28]. The rate of photo-absorption and effective molecular diffusion will increase with larger surface area. Generally, a greater absorbance cross-section is preferred in photocatalytic processes, and it is expected that the CNT-based composite will meet these requirements as shown in the later part. The larger surface area of CNT provides adequate interfacial contact with CuS nanoparticles which suppresses the recombination of e^--h^+ and enhances the charge transport facility for T-CuS than CuS.

5.4.5. Electrical Properties

➲ *Current-Voltage (I-V) Measurements*

To understand electronic charge, transfer characteristics of the above-discussed materials, current-voltage (I–V) measurements of the Schottky diodes fabricated as-(Al/CuS/ITO) & (Al/T-CuS/ITO) structure in the previous Chapter (§ 4.2.4), were investigated using a bias voltage range of ±1 Volt in dark and light (~ 1000 W/m^2) conditions at 300K temperature. The measurement of charge flow, known as dc conductivity (σ), was evaluated from the ohmic (linear) region of the characteristic curves (Fig. 5.9a) of both devices under dark and illumination/light conditions (Table 5.1). A notable increment of current in illumination conditions reflects the photosensitivity of the synthesized materials. The definition of photosensitivity (S), like,

$S = I_v / I_d$, (here $I_v = I_l - I_d$ is denoted as light-induced current, on the other hand, I_d denotes the current in dark conditions) was derived for two different devices[29]. The CNT-based device with greater absorption capacity has better sensitivity than bare CuS (Table 5.1). In addition, the higher conductivity of the composite material means efficient charge transport with excellent mobility. For any semiconductor material, carrier mobility determines how fast a carrier, i.e., e^- or h^+, can move through its complex network and reach active sites before recombination. Since CNT provides higher electronic mobility ($\sim 10^5$ cm^2/Vs at 300 K), it is expected the enhancement of electron transport and e^--h^+ pair separation through its high-quality complex network[30].

To observe the overall effect of CNT in the photo-degradation process and to better understand the charge transfer mechanism, the current-voltage (I-V) mechanism was further analyzed by introducing the transit time (τ) and carrier mobility (μ_{eff}). For this purpose, log I vs. log V graphs are plotted for the positive voltages as shown in Fig. 5.9b, which represents two distinct linear regions, suggesting different conduction mechanisms.

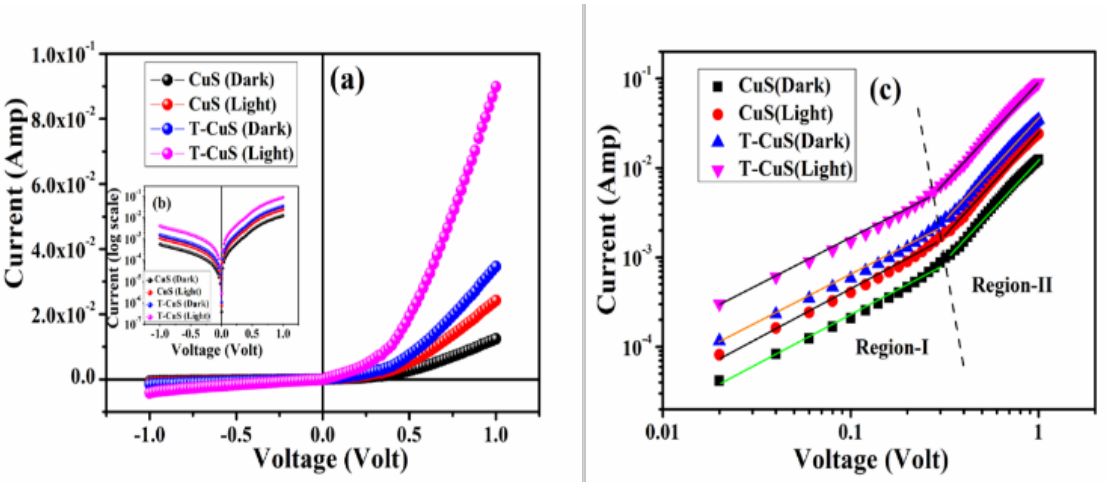

Fig. 5.9: (a) current-voltage (I-V) plots (b) Log Scale I vs. V curve and (c) Log I-Log V plot of the bare CuS and T-CuS composite-based Schottky diodes under dark and illumination conditions.

Interfacial trap states at the metal-semiconductor junction modify the conduction mechanism of charge carriers which revised the I-V characteristics. In small bias (Region-I), current shows ohmic (I α V) behaviour with the slope value approximately to one. At this region, the current is guided by the intrinsic charge carriers of the material[31]. The carriers injected from the junction spread over the space at the intermediate potential difference (Region II) and create a spatially distributed field of charge. This field

dominates the charge carriers and their "mobility" becomes a key factor for the quadratic current ($I \alpha V^2$)[32,33].

➲ *Estimation of the Charge Transport Parameters*

To obtain a better understanding of the charge transport mechanism, the I-V characteristics were further analysed by deciphering the effective carrier's mobility (μ_{eff}) and lifetime (τ) from region II [Fig. 5.9b] based on the space-charge limited current (SCLC) theory. The electron mobility was evaluated from the slope of the I-V^2 plot (Fig. 5.10a and 5.10b). The dielectric constant of the synthesized materials (ε_r), the mobility (μ_{eff}), and the lifetime or transient time (τ) of the charge carriers were estimated employing the following equations[34]:

$$\boldsymbol{\varepsilon_r = \frac{C_0 d}{\varepsilon_0 A_{eff}}} \qquad (5.2)$$

$$I = \frac{9\mu_{eff}\varepsilon_0\varepsilon_r A_{eff}}{8}\left(\frac{V^2}{d^3}\right) \qquad (5.3)$$

$$\tau = \frac{9\varepsilon_0\varepsilon_r A_{eff}}{8d}\left(\frac{V}{I}\right) \qquad (5.4)$$

The detailed elucidation of all the symbols used in the above-mentioned equations was provided in Chapter 2 (§ 2.7.2). Also, the plot illustrating the capacitance (C) vs. frequency (f) characteristics for both CuS and T-CuS films is presented in Fig. 5.11.

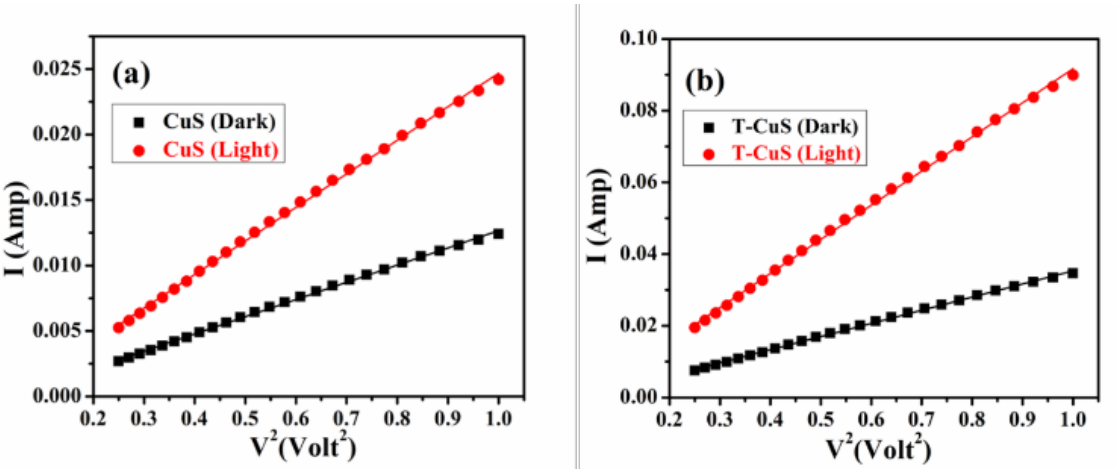

Fig. 5.10: The I vs. V^2 plot for the SCLC region of (a) CuS and (b) T-CuS nanocomposite.

The calculated values of μ_{eff} and τ are given below in Table-5.1. Our results reflected higher mobility for the carbon nanotube and its effective contribution to the

transfer of charge carriers smoothly. The CNT-based composite showed greater mobility & transit time than the bare CuS NPs. The result shows compatibility with previously reported data of a carbon-based (rGO) composite[35,36]. Both in dark and in the illumination, the mobility of carriers increased remarkably up to 4-5 times. The enrichment of mobility & transition time can increase the efficiency of charge transfer and thus the photocatalytic activity.

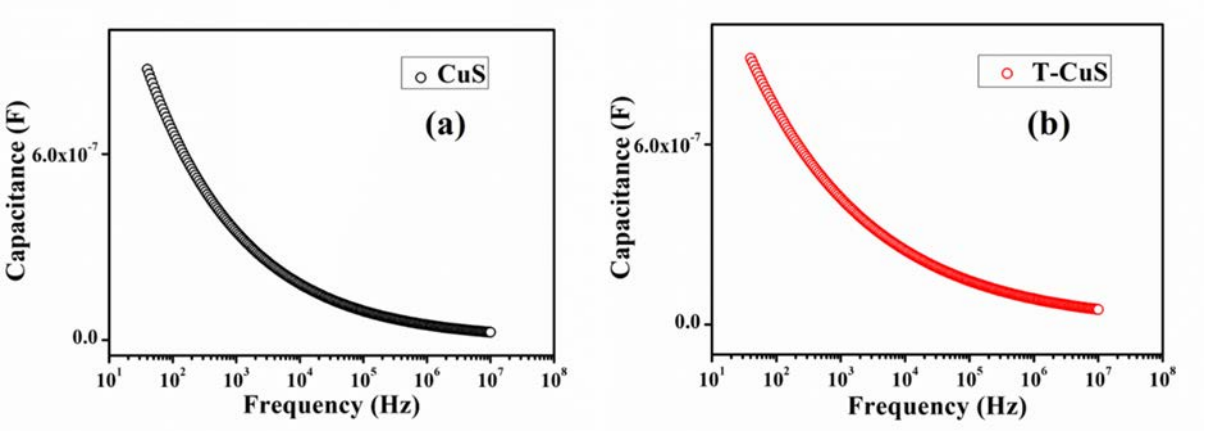

Fig. 5.11: Capacitance vs. frequency plot for the CuS and CNT-CuS thin film.

Table 5.1: *Charge transport parameters.*

Sample	Photo-sensitivity (S)	Conductivity (σ) (Sm^{-1})		Mobility (μ_{eff}) ($m^2V^{-1}s^{-1}$)		Transition time (τ) (s)	
Condition		**Dark**	**Light**	**Dark**	**Light**	**Dark**	**Light**
CuS	1.01	3.42×10^{-4}	6.71×10^{-4}	2.32×10^{-5}	5.39×10^{-5}	1.54×10^{-8}	8.32×10^{-9}
T-CuS	2.05	9.57×10^{-4}	2.48×10^{-3}	7.98×10^{-5}	2.67×10^{-4}	7.92×10^{-9}	3.20×10^{-9}

➲ *Transient Photocurrent Measurements and Nyquist Plots*

Transient photo-response spectra and electrochemical impedance spectroscopy (EIS) were performed to investigate the photo-electrochemical characteristics of the as-prepared catalysts, and are shown in Fig. 5.12a and 5.12b respectively. The photocurrent intensity of the T-CuS composite was found to be significantly higher (Fig. 5.12a) than that of the pure CuS, as expected. This result suggests that incorporating CNT into the CuS nanoparticles could facilitate the separation of photo-generated electrons and holes and their swift transfer through the complex network. Furthermore, the EIS Nyquist spectra, which is an effective tool for investigating the conductance and charge transfer facility,

revealed that the diameter of the semi-circular arc for the T-CuS composite was significantly smaller than for the pure CuS (Fig. 5.12b). This finding affirms that the addition of CNT significantly reduced the charge transfer resistance in the composite material, allowing electrons and holes to migrate to active sites during the degradation process, as discussed further below.

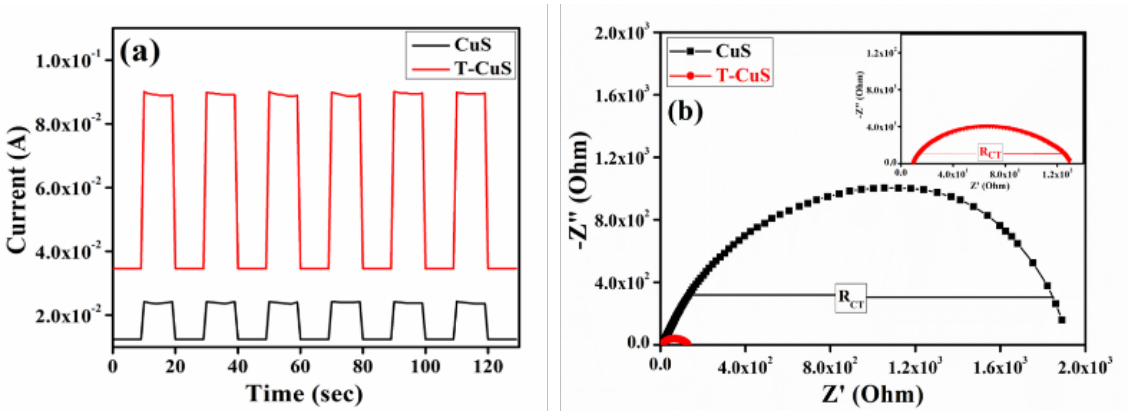

Fig. 5.12: (a) Transient photocurrent response and (b) EIS Nyquist plot of CuS and T-CuS composite.

➲ ***Charge Transfer Characteristics of CNT***

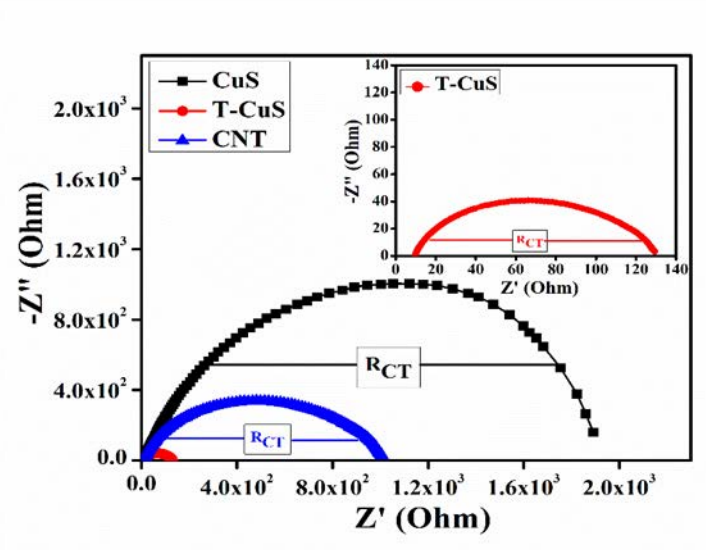

Figure 5.13: Nyquist Plot for CuS, CNT and T-CuS Composite.

The EIS Nyquist plot is an effective tool to investigate the conductance and charge transfer characteristics of the materials. Fig. 5.13 revealed that the diameter of the semi-circular arc for the T-CuS composite was significantly smaller than for the pure CuS and the diameter of the semi-circular arc for pure CNT is lies between pure CuS and the T-CuS composite. So, it can be concluded that the charge transfer for CNT is higher than pure CuS but lower than T-CuS composite.

5.4.6. Photocatalytic Activity

➲ ***Photo-degradation Process***

The photocatalytic performance of the as-prepared samples was evaluated by photocatalytic degradation of Rh B under UV light irradiation. In the experiment, 30 mg of the samples and 1 mL H_2O_2 were dispersed in 100 mL of Rh B aqueous solution (100 ppm). The mixed suspensions were magnetically stirred for 30 mins in the dark to attain an adsorption-desorption equilibrium. Under ambient conditions and stirring, the mixed suspensions were exposed to visible light produced by a solar simulator (Abet Technologies, Model 10500). At regular time intervals, 3 mL of the examined suspensions were extracted and centrifuged to remove the suspended impurities. The absorption of Rh B in the filtrate centred at 553.5 nm was then examined using a UV-Vis spectrometer and the degradation process was analysed.

For the recyclability test, the catalyst was extracted after the degradation cycle by centrifugation and washed with isopropyl alcohol followed by Millipore water and reused in the next cycle. In this study, all the experiments have been repeated three times and displayed almost similar activity.

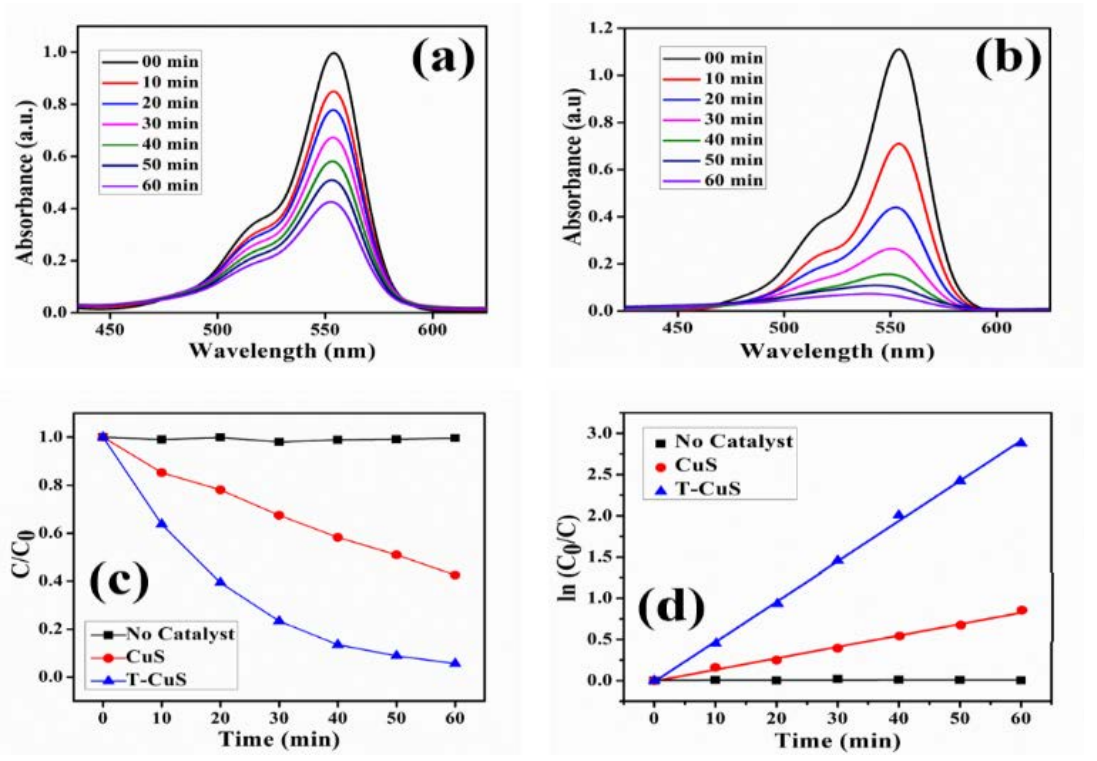

Fig. 5.14: Absorbance spectra of aqueous Rh. B solution at different intervals of time in the presence of (a) CuS and (b) T-CuS nanocomposite under solar irradiations. (c) Photocatalytic degradation behaviour of Rh. B solution (d) ln (C_0/C) vs. Time plot for RhB solution in presence of CuS and T-CuS catalysts.

➲ *Photo-degradation Behaviour and Performances*

Photocatalytic decomposition of RhB under a solar simulator is used to investigate the photocatalytic behaviour of bare CuS and T-CuS nanocomposites. The degradation procedure was recorded by monitoring the major absorption peaks of aqueous RhB solution centred at 553.5 nm using a UV-Vis spectrometer (Fig. 5.14a and 5.14b) and the decomposition process was determined by the following Equation:

$$Degradation = \left(\frac{C_0 - C_t}{C_0} \times 100\right) \% \qquad (5.5)$$

where C_0 and C_t represent the RhB concentration at the time t=0 & t= time after its initial condition, respectively[37]. The linear behaviour of ln(C_0/C) vs. exposure time (min) graph of both bare CuS and T-CuS composites (Fig. 5.14d) indicates the presence of pseudo-first-order decomposition kinetics[38]. No significant change in RhB concentration was observed in the catalyst-free suspension after exposed to solar-simulated light for 60 minutes. It was found that the addition of bare CuS catalyst bleached the RhB solution to 58% from its initial concentration. Furthermore, the T-CuS nanocomposites enhanced the degradation by up to 94% due to the synergistic effect of CuS-NPs and CNTs (Fig. 5.14c).

Recycling test in Fig 5.15 demonstrated that the decomposition efficiency of T-CuS catalyst did not change significantly after repeated use of three cycles.

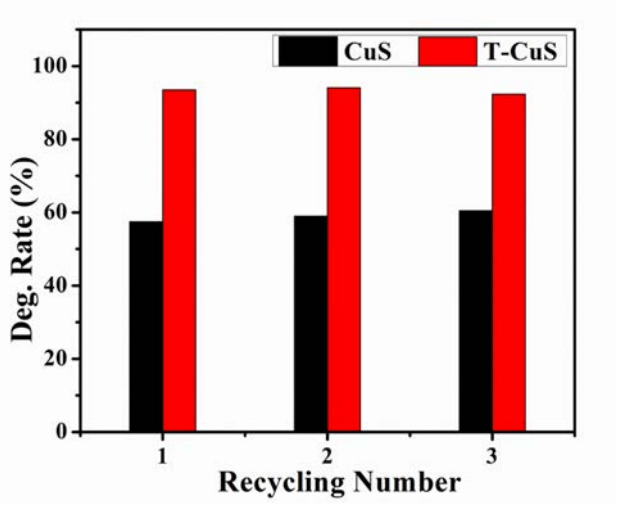

Fig. 5.15: Recycle performance of CuS and T-CuS catalyst for Rh. B decomposition.

➲ ***Adsorption of RhB by the Photocatalysts***

The adsorption of RhB on the photocatalysts were measured since the pre-adsorption of the dyes aids the migration of the charge carriers. The adsorption experiments were performed by continuous stirring 100 mL of aqueous RhB solution with 30 mg of each catalyst (CuS and T-CuS) for 30 min in the dark condition. Figure 5.16 displays the adsorption profiles of aqueous RhB solution as a function of time in the dark on the pure CuS and the T-CuS composite, respectively. The pure CuS demonstrated no adsorption in the dark, as the concentration of the RhB solution remained almost unchanged. In addition, the T-CuS composite also showed negligible adsorption behaviour to RhB, which was less than 1% for 30 min of stirring. These results indicate that the adsorption experiments did not show a significant effect on RhB removal and, the pre-adsorption was displayed in the following.

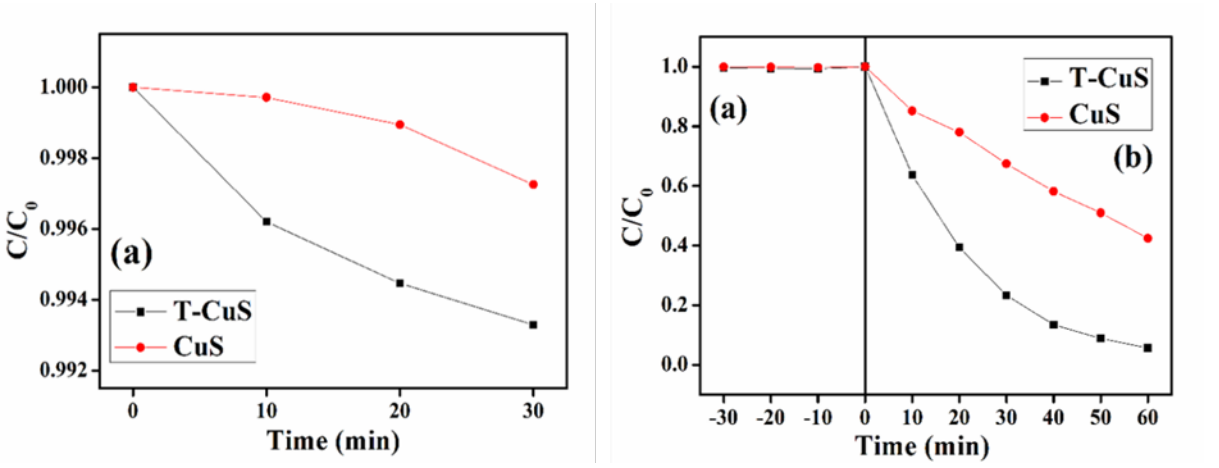

Fig. 5.16: The adsorption profiles of aqueous RhB solution on pure CuS and the T-CuS composite, as a function of time in the dark.

➲ *Identifications of Reactive Species*

The reactive species trapping experiments were carried out to determine the active species in the 3% T-CuS photocatalytic system. First, 0.1 mmol of methyl alcohol (MeOH), a scavenger of photogenerated h^+, 0.1 mmol of iso-propyl alcohol (IPA), a scavenger of hydroxyl •OH and 0.1 mmol of benzoquinone (BQ), a scavenger of superoxide $\bullet O_2^-$ were separately added in the photodegradation system. Then, the photodegradation experiment was performed under the same procedure without adding scavengers. The absorption plots of degraded RhB by T-CuS in presence of different scavengers are shown in Fig. 5.17. Figure 5.18 shows the effect of the scavengers on the degradation percentage of RhB with 60 min irradiation time.

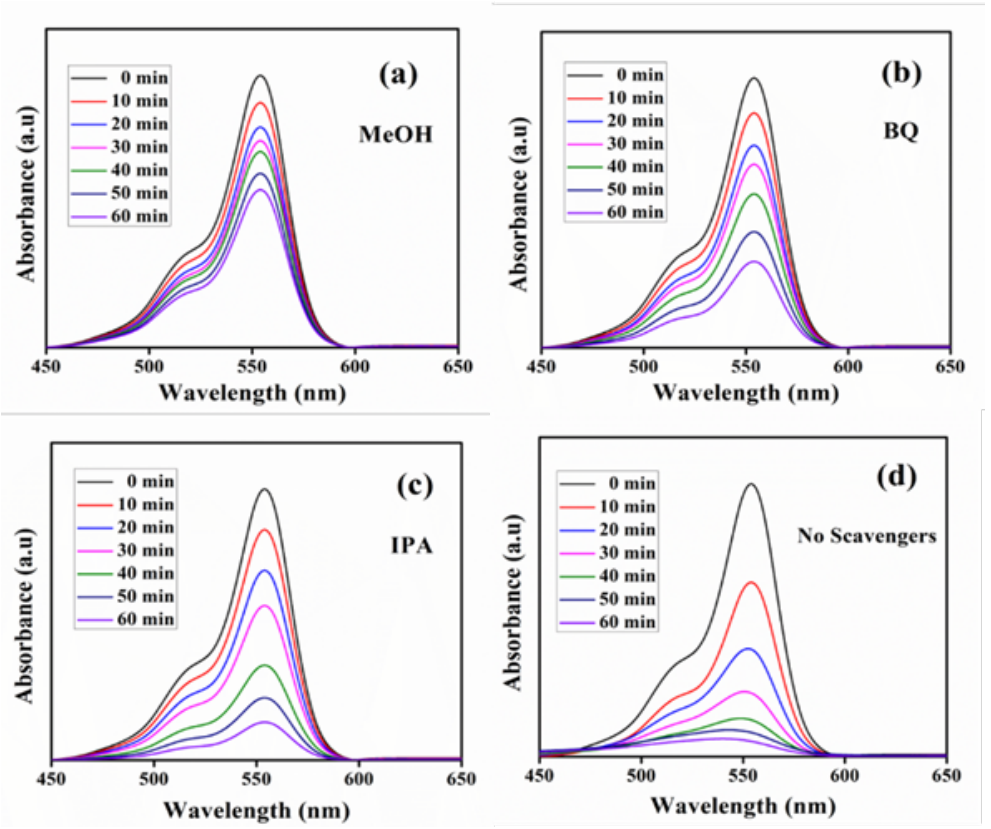

Fig. 5.17: Absorbance spectra of degraded RhB aqueous solution by T-CuS in presence of (a) methyl alcohol (b) benzoquinone (c) iso-propyl alcohol and (d) No scavengers.

As seen in figure 5.18, the RhB solution degraded up to 86% of its initial concentration which demonstrates that the decomposition of RhB was slightly suppressed in the presence of IPA, as compared to 94% in the absence of scavengers. This finding indicates that •OH has a minor impact on degradation of RhB using T-CuS catalyst. In case of MeOH, the value of (C/C_0) was not reduced below 42%, indicating that holes (h^+) play a significant role in RhB degradation. However, when BQ was present during the reaction, the concentration of (C/C_0) was somewhat reduced by up to 68%. This suggests that $\bullet O_2^-$ radical is also markedly responsible for photocatalytic degradation of RhB. Here, RhB degradation was observed to be obviously inhibited on the addition of BQ and MeOH; in contrast, IPA had a very small effect on the dye degradation. This implies that the photogenerated holes (h^+) and $\bullet O_2^-$ radicals plays the main role in removal process of the dye, whereas •OH plays a minor role in the dye degradation.

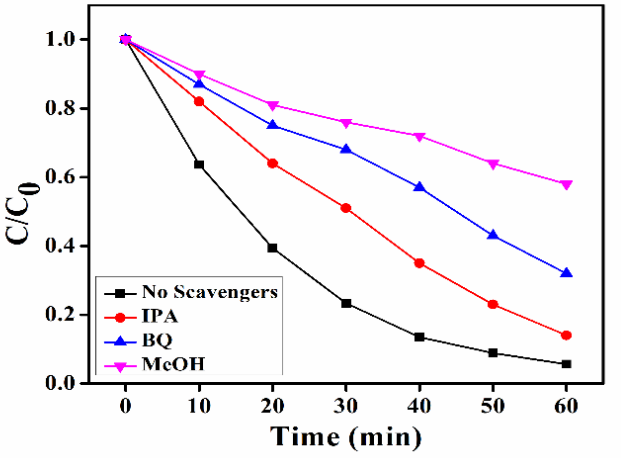

Fig. 5.18: Photocatalytic degradation of RhB aqueous solution by T-CuS in presence of IPA, BQ, MeOH and no scavengers.

➲ ***Optimization of the composite material with different CNT content***

To determine the optimum composite photocatalyst for achieving the highest photocatalytic activity, the T-CuS composites with different CNT content were prepared and they were labelled as "T (x%)-CuS", where x stands for the weight % of the CNT (0%, 2%, 3% and 4%). Fig. 5.19 shows the variation of RhB concentration (C/C_0) with time in the presence of different catalysts under visible-light irradiation for 60 min irradiation. It was seen that no considerable change in the RhB concentration was observed for catalyst-free suspensions. After adding the pristine CuS catalyst, the RhB solution was found to be bleached up to 58% of its initial concentration. On the other hand, the RhB solution was degraded up to 82%, 94% and 89% with the T (2%)-CuS, T (3%)-CuS, T (4%)-CuS, respectively. The result demonstrates that the photocatalytic activity of T-CuS composites was first enhanced and then diminished with the increasing amount of CNT. Among the prepared samples, the composite with 3% CNT content showed the highest photocatalytic activity (94%).

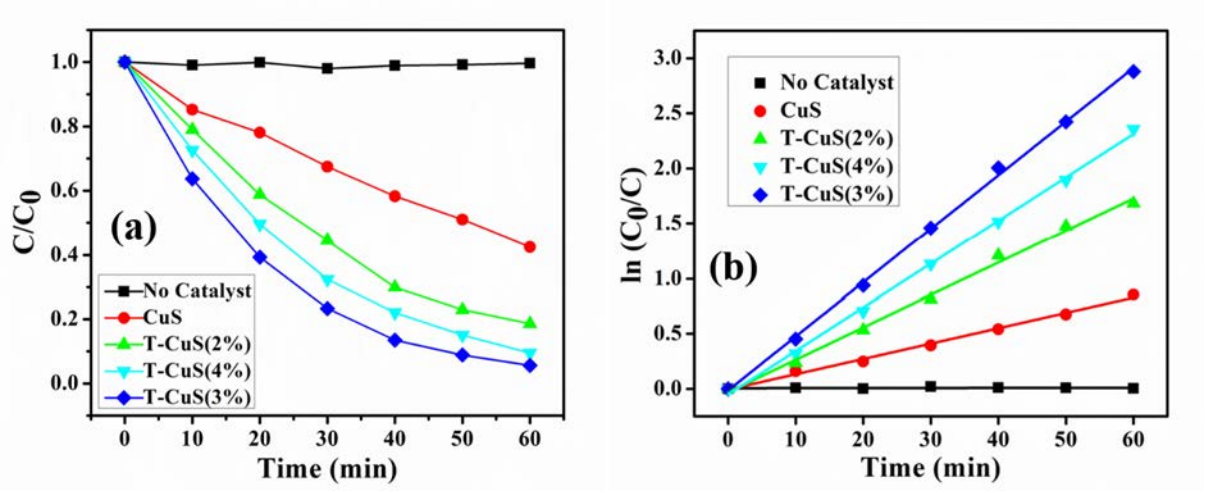

Fig. 5.19: (a) Changes in concentration vs. time and (b) ln (C_0/C) vs. time plot in the presence of different catalysts under visible-light irradiation.

➲ *Weight (%) test of CNT*

Here we have tested the CNT (wt.%) content with the help of EDX analysis in three different spots and take an average value and also, we have performed EDX Mapping (Fig. 5.20) of the composite. Here from the different spot, we get an average wt. % of CNT in the composite is around 2.80% which is close to 3%.

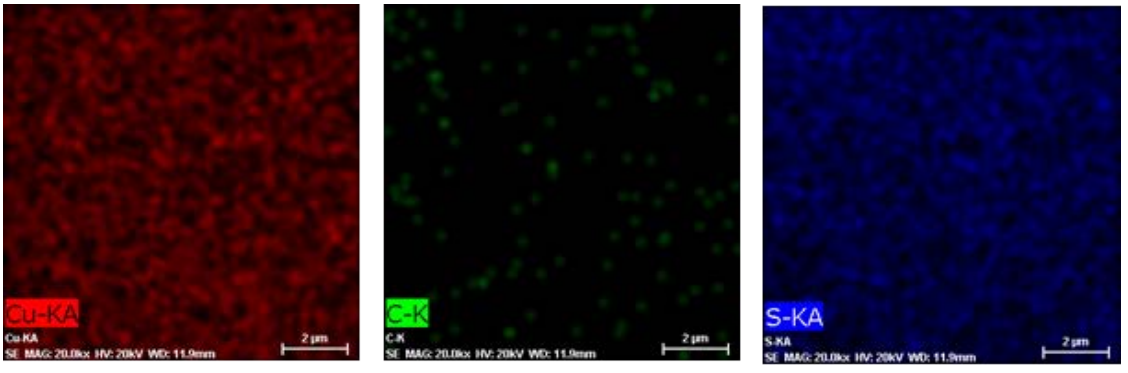

Fig. 5.20: EDX Mapping of the sample T-CuS (3%)

Table 5.2: *Weight (%) of CNT in the T-CuS nanocomposite*

Spot No	Cu (Wt.%)	C (Wt.%)	S (Wt.%)
Spot 1	51.31	2.72	45.97
Spot 2	51.78	2.87	45.35
Spot 3	51.96	2.81	45.23
Average	51.68	2.80	45.52

➲ *Photocatalytic activity of a non-azo dye*

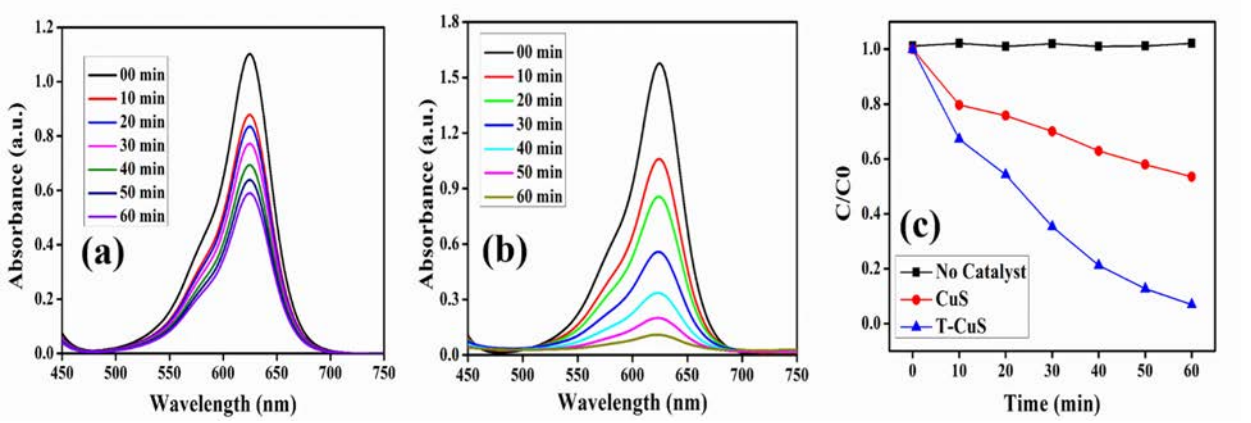

Fig. 5.21: Changes in concentration vs. time (a) CuS (b) T-CuS and (c) ln (C_0/C) vs. time plot in the presence of different catalysts under visible-light irradiation.

Here, we conducted the catalytic experiment with the bare CuS (Fig. 5.21a) and CuS-CNT (3%) (Fig. 5.21b) to degrade the Brilliant Green (BG) dye, which belongs to the non-azo groups, and we observed the almost similar results as we obtained in the case of RhB. It was found that the addition of bare CuS catalyst bleached the BG solution to 47% from its initial concentration. Furthermore, the T-CuS nanocomposites enhanced the degradation by up to 93%.

➲ *Photo-degradation Mechanism*

To explain the synergistic effect of CNTs and CuS in the composite, we analysed the photocatalytic degradation process. In presence of visible light illumination, excitons of interfaces are generated on the surface of CuS NPs and segregated into free holes in the valence band & free electrons in the conduction band. Though, this photogenerated h^+ and e^- tending recombination before the appearance of the active site resulting in a poor photocatalytic response. When the CuS NPs bind with CNTs, the photo-induced e^- in the conduction band of CuS can be separated effectively at the carbon nanotube interfaces, leaving h^+ in the valence band of CuS due to its favourable energy level (Fig. 5.22)[39,40]. Therefore, photo-generated electrons in CuS can reach effortlessly to the active site through the CNT network and reduce the dissolved O_2 present in the aqueous medium, into the hugely reactive superoxide anion (O^{2-}) and react further with H_2O to form hydroxyl (OH*) radicals[41]. Furthermore, photo-induced h^+ can react also with H_2O or OH^- to oxidize them to $OH^{\bullet}$ [42]. The $O_2^{\bullet-}$, $OH^{\bullet}$ and the photo-generated h^+ are jointly involved

in the decomposition process of RhB solutions[43,44]. Fig. 5.22 shows a pictorial view of the photocatalytic activity of the T-CuS photo-catalyst.

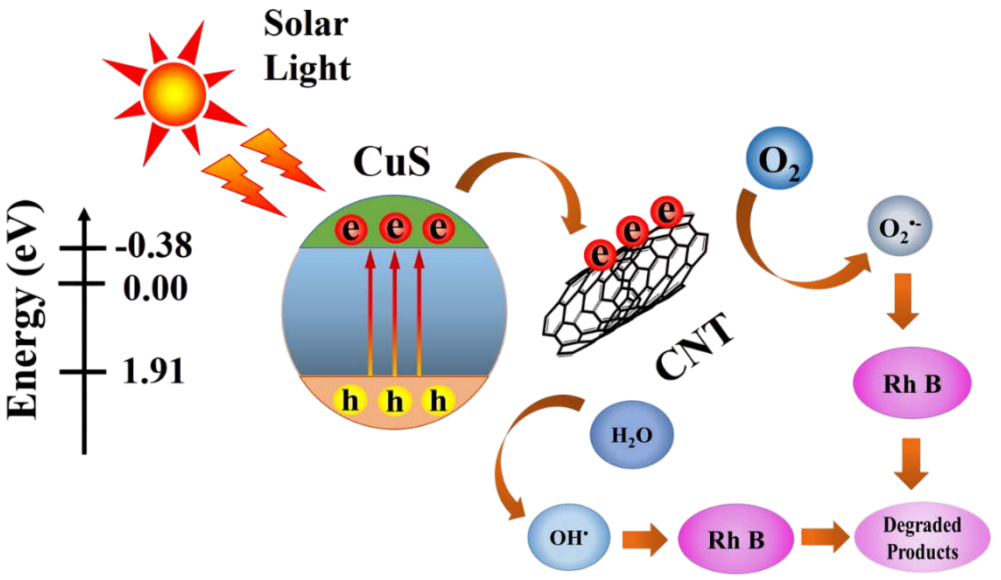

Fig. 5.22: Pictorial representation of photocatalytic degradation of RhB in the presence of T-CuS nanocatalyst under solar simulator.

5.5. Conclusion

The CuS NPs were synthesized successfully and the CNT incorporation with CuS was assisted by PXRD, FESEM, FEG-TEM, XPS, UV-Vis and PL data. The importance of charge transport kinetics and higher charge carrier mobility of the photo-catalysts for RhB decomposition was reported. It was seen that in presence of visible light, the T-CuS exhibited higher photocatalytic activity than the bare CuS. The higher mobility of the composites helped the photo-induced charges to quickly transfer between the active site and the target molecules at the time of the degradation process. Strong interfacial contacts, higher absorption of visible light and reduced recombination of e^--h^+ pairs are the additional crucial key factors for enhancing the photocatalytic performance of the composites. Overall, addressing the challenge of visible light-induced photocatalysis, the superiority of CNT composites over as-synthesized bare CuS catalysts was demonstrated in this study. Finally, our results shed light on design of carbon-based semiconductor (T-CuS) composites and established them as promising photo-catalysts for various potential applications in wastewater treatment.

***

References

1. R. Al-Tohamy, S. S. Ali, F. Li, K. M. Okasha, Y. A. G. Mahmoud, T. Elsamahy, H. Jiao, Y. Fu and J. Sun, *Ecotoxicol Environ Saf*, 2022, 231.
2. V. Selvaraj, T. Swarna Karthika, C. Mansiya and M. Alagar, *J Mol Struct*, 2021, **1224**, 129195.
3. M. A. Al-Nuaim, A. A. Alwasiti and Z. Y. Shnain, *Chemical Papers*, 2022.
4. S.-Y. Wang, J.-Y. Ma, Z.-J. Li, H. Q. Su, N. R. Alkurd, W.-L. Zhou, L. Wang, B. Du, Y.-L. Tang, D.-Y. Ao, S.-C. Zhang, Q. K. Yu and X.-T. Zu, *J Hazard Mater*, 2015, **285**, 368–374.
5. O. Elbanna, M. Zhu, M. Fujitsuka and T. Majima, *ACS Catal*, 2019, **9**, 3618–3626.
6. T. Aarthi and G. Madras, *Ind Eng Chem Res*, 2007, **46**, 7–14.
7. F. Ghribi, A. Alyamani, Z. ben Ayadi, K. Djessas and L. el Mir, in *Energy Procedia*, Elsevier Ltd, 2015, vol. **84**, 197–203.
8. T. Kajana, A. Pirashanthan, D. Velauthapillai, A. Yuvapragasam, S. Yohi, P. Ravirajan and M. Senthilnanthanan, RSC Adv, 2022, **12**, 18041–18062.
9. D. Wang, M. Sun, G. Feng and C. Song, J Mater Eng Perform, 2019, **28**, 6649–6655.
10. N. Ul Ain, J. A. Nasir, Z. Khan, I. S. Butler and Z. Rehman, *RSC Adv*, 2022, **12**, 7550–7567.
11. M. Baláž, E. Dutková, Z. Bujňáková, E. Tóthová, N. G. Kostova, Y. Karakirova, J. Briančin and M. Kaňuchová, J Alloys Compd, 2018, **746**, 576–582.
12. X. Meng, L. Shi, L. Cui, L. Yao and Y. Zhang, Mater Res Bull, 2021, **135**, 111156.
13. J. C. Ortiz-Herrera, H. Cruz-Martínez, O. Solorza-Feria and D. I. Medina, Int J Hydrogen Energy, 2022, **47**, 30213–30224.
14. Y. Huang, R. Li, D. Chen, X. Hu, P. Chen, Z. Chen and D. Li, Catalysts, 2018, **8**, 151.
15. R. Sarkar, M. Kar, M. Habib, G. Zhou, T. Frauenheim, P. Sarkar, S. Pal and O. v. Prezhdo, J Am Chem Soc, 2021, **143**, 6649–6656.
16. X. He, X. Xu, G. Bo and Y. Yan, *RSC Adv*, 2020, **10**, 2180–2190.
17. Y.-L. Chen, Z.-A. Hu, Y.-Q. Chang, H.-W. Wang, Z.-Y. Zhang, Y.-Y. Yang and H.-Y. Wu, The Journal of Physical Chemistry C, 2011, **115**, 2563–2571.
18. M. Varga, T. Izak, V. Vretenar, H. Kozak, J. Holovsky, A. Artemenko, M. Hulman, V. Skakalova, D. S. Lee and A. Kromka, Carbon N Y, 2017, **111**, 54–61.
19. M. Chandra, K. Bhunia and D. Pradhan, Inorg Chem, 2018, **57**, 4524–4533.

20. Y. Yan, H. Yang, Z. Yi, T. Xian, R. Li and X. Wang, Desalination Water Treat, 2019, **170**, 349–360.

21. J. Tauc, R. Grigorovici and A. Vancu, physica status solidi (b), 1966, **15**, 627–637.

22. Z. Huang, L. Wang, H. Wu, H. Hu, H. Lin, L. Qin and Q. Li, J Alloys Compd, 2022, **896**, 163045.

23. M. Tanveer, C. Cao, I. Aslam, Z. Ali, F. Idrees, M. Tahir, W. S. Khan, F. K. Butt and A. Mahmood, RSC Adv., 2014, **4**, 63447–63456.

24. P. Borthakur, P. K. Boruah, G. Darabdhara, P. Sengupta, M. R. Das, A. I. Boronin, L. S. Kibis, M. N. Kozlova and V. E. Fedorov, J Environ Chem Eng, 2016, **4**, 4600–4611.

25. Z. Chen, S. Berciaud, C. Nuckolls, T. F. Heinz and L. E. Brus, ACS Nano, 2010, **4**, 2964–2968.

26. S. Iqbal, A. Bahadur, A. Saeed, K. Zhou, M. Shoaib and M. Waqas, J Colloid Interface Sci, 2017, **502**, 16–23.

27. P. Madhusudan, J. Zhang, B. Cheng and G. Liu, CrystEngComm, 2013, **15**, 231–240.

28. Y. Quan, M. Zhang, G. Wang, L. Lu, Z. Wang, H. Xu, S. Liu and Q. Min, New Journal of Chemistry, 2019, **43**, 10906–10914.

29. Q. Yang, X. Guo, W. Wang, Y. Zhang, S. Xu, D. H. Lien and Z. L. Wang, ACS Nano, 2010, **4**, 6285–6291.

30. T. Dürkop, S. A. Getty, E. Cobas and M. S. Fuhrer, Nano Lett, 2004, **4**, 35–39.

31. İ. Taşçıoğlu, U. Aydemir and Ş. Altındal, J Appl Phys, 2010, **108**, 064506.

32. I. Ullah, M. Shah, M. Khan and F. Wahab, J Electron Mater, 2016, **45**, 1175–1183.

33. M. Soylu and B. Abay, Physica E Low Dimens Syst Nanostruct, 2010, **43**, 534–538.

34. S. Sil, A. Dey, J. Datta, M. Das, R. Jana, S. Halder, J. Dhar, D. Sanyal and P. P. Ray, Mater Res Bull, 2018, **106**, 337–345.

35. M. Das, J. Datta, A. Dey, R. Jana, A. Layek, S. Middya and P. P. Ray, RSC Adv, 2015, **5**, 101582–101592.

36. D. Das, M. Das, S. Sil, P. Sahu and P. P. Ray, ACS Omega, 2022, **7**, 26483–26494.

37. S. Khanchandani, S. Kundu, A. Patra and A. K. Ganguli, The Journal of Physical Chemistry C, 2013, **117**, 5558–5567.

38. J.-M. Herrmann, Catal Today, 1999, **53**, 115–129.

39. S. Rawalekar, S. Kaniyankandy, S. Verma and H. N. Ghosh, The Journal of Physical Chemistry C, 2011, **115**, 12335–12342.

40. D. K. Padhi and K. Parida, J. Mater. Chem. A, 2014, **2**, 10300–10312.

41. L. Huang, F. Peng, H. Yu and H. Wang, Solid State Sci, 2009, **11**, 129–138.
42. M. Wang, L. Sun, Z. Lin, J. Cai, K. Xie and C. Lin, Energy Environ Sci, 2013, **6**, 1211.
43. Y. Du, Z. Niu, T. Yan, K. Zhu, Y. Yu and Z. Jing, Front Mater Sci, 2021, **15**, 241–252.
44. Z. Zhang, S. Zhai, M. Wang, H. Ji, L. He, C. Ye, C. Wang, S. Fang and H. Zhang, J Alloys Compd, 2016, **659**, 101–111.

***

Investigation of charge transport properties of rGO-CuSe-based Schottky diode by tuning graphene content

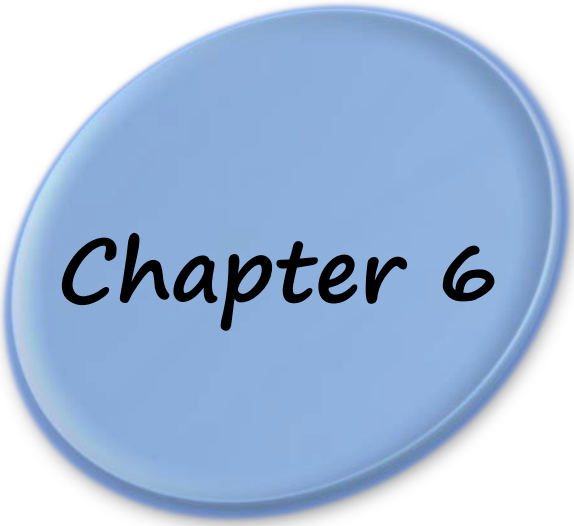

6.1. Introduction

The fabrication of Schottky barrier diodes (SBDs) at metal-semiconductor (MS) junctions and the analysis of charge transport have recently received considerable attention in modern electronics[1]. The performance of a SBD depends on some factors, like mobility of charge carriers, recombination rate, and interface quality. CuSe (CS) is a material that has several features such as non-toxicity, tunable microstructure, tunable bandgap in the semiconducting range, and low cost but CS has a high electron-hole recombination rate, which impacts device performance. However, graphene, a carbon-based material has gained attention due to its excellent conductivity, high carrier mobility, electron-hole-suppressing ability and emerged as a promising material for electronic devices[2]. Thus, combining graphene with CS holds promise to enhance charge transport kinetics, specifically by inhibiting recombination in CS. Producing pure graphene is difficult so reduced graphene oxide (rGO) has been synthesized. In this study, we have synthesized rGO-CuSe (RCS) composites with different weight ratios of rGO (0% (CS), 1% (RCS1), 3% (RCS3), 5% (RCS5) and 7% (RCS7)). Subsequently, SBDs were fabricated and the charge transport performances were analyzed by space charge limited current (SCLC) theory. We estimated some charge transport parameters and investigated the effect of rGO on the charge transport of CS.

6.2. Materials and Methods

6.2.1. Materials

The chemicals used in this study were Copper dichloride dihydrate ($CuCl_2.2H_2O$), tartaric acid ($C_4H_6O_6$), deionized (DI) water, hydrazine hydrate ($H_4N_2.H_2O$), aqueous ammonia (NH_4OH), sodium selenite ($Na_2S_2O_3$). All the chemicals were procured from Sigma-Aldrich (India) and used as received without requiring any further purification steps.

6.2.2. Synthesis of CuSe

CuSe (CS) was synthesized using hydrothermal method. 0.2 M Copper dichloride dihydrate ($CuCl_2.2H_2O$) and 0.5g of tartaric acid were dissolved in 25 mL of distilled water while stirring. 3 mL hydrazine hydrate and 3 mL aqueous ammonia were added. A separate aqueous solution of 0.2 M sodium selenite ($Na_2S_2O_3$) was prepared and added to the first mixture. After 15 minutes of stirring, the mixture was transferred to a Teflon-

lined stainless-steel autoclave and placed in an oven set at 180 °C for 12 hrs. The collected black material was washed with distilled water and ethanol and dried at 60 °C for 4 hrs.

6.2.3. Synthesis of GO

Graphene oxide (GO) was synthesized via improved Hummer's method, initially proposed by Marcano et al.[3,4]. In this procedure, a 100 mL solution of H_2SO_4/H_3PO_4 with a molar ratio of 9:1 was prepared. Next, 0.75 g of graphite flakes was dispersed in the solution through intense sonication. Following this, 4.5 g of potassium permanganate ($KMnO_4$) was gradually added to the acidic suspension, which was stirred for 12 hours at 50 °C. After the reaction, the mixture was allowed to cool to room temperature and then transferred to 100 mL of ice water. To this homogeneous mixture, 0.75 mL of a 30% aqueous hydrogen peroxide (H_2O_2) solution was slowly added, resulting in the formation of a golden-brown GO suspension. The suspension was then filtered and subjected to centrifugation at 6000 rpm for 1 hour. The resulting GO was washed multiple times with deionized (DI) water, dilute hydrochloric acid (HCl), and ethanol. Finally, the product was dried overnight at 100 °C.

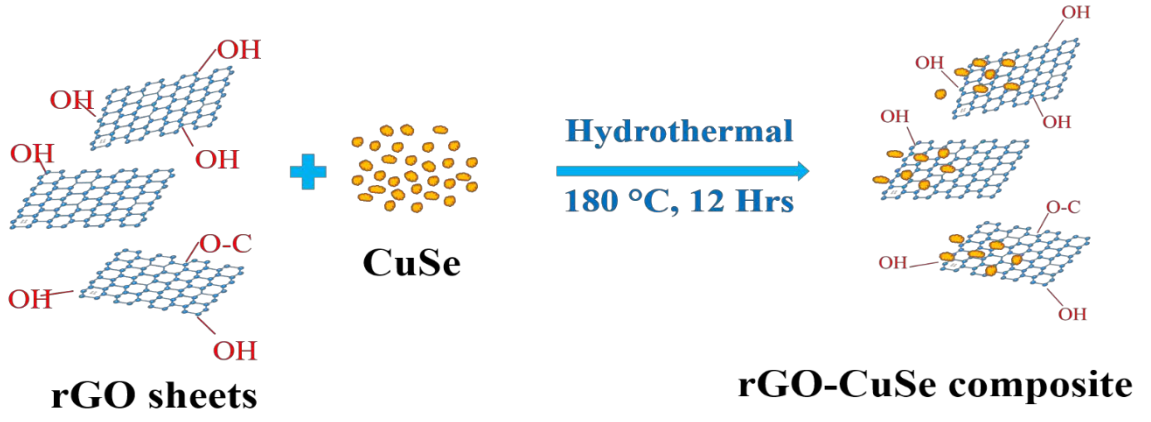

Fig. 6.1: Schematic illustration of the synthesis of the rGO-CuSe nanocomposite.

6.2.4. Synthesis of rGO-CuSe

The composite material rGO-CuSe (RCS) was synthesized using a similar alkaline hydrothermal reaction as described for CuSe synthesis. The synthesis procedure involved several steps. Firstly, 10 mg of graphene oxide (GO) was reduced to obtain 10 mg of reduced GO through hydrazine treatment, following the method described by Das et.al.[5]. Next, 5 mg of the reduced GO was dispersed in 30 mL of DI water through ultrasonication

for 1 hour, resulting in a well-dispersed and homogeneous solution. Subsequently, the synthesized CuSe nanoparticles were slowly added to the rGO suspension while maintaining stirring. The mixture was further stirred for 1 hour to ensure uniform dispersion and then transferred into a hydrothermal autoclave to synthesize the RCS nanocomposite. To produce the rGO-CuSe (RCS) composite, rGO was added to the CS in different weight ratios as rGO weight ratios of 0% (CS), 1% (RCS1), 3% (RCS3), 5% (RCS5), and 7% (RCS7) and stirred for 8 hrs. Then, a similar hydrothermal process was carried out and RCS was obtained by washing several times with deionized water and ethanol and drying at 60 °C for 4 hrs. The entire synthesis process of the rGO-CuSe composite is collectively schemed out in Fig. 6.1.

6.2.5. Fabrication of Schottky Devices

To fabricate SBDs, fluorine-doped tin oxide (FTO) coated glass was cleaned using a sequence of soap solution, acetone, ethanol, and distilled water in an ultrasonic bath. The materials were then spin-coated onto the FTO-coated glass and left to dry, resulting in thin films. The film thickness was approximately 1 µm, as determined by a surface profiler. Metal contacts of aluminium were made to the film by depositing through the thermal evaporation technique. The diode's effective area (A) was maintained at 7.065×10^{-6} m^2 using a shadow mask[6].

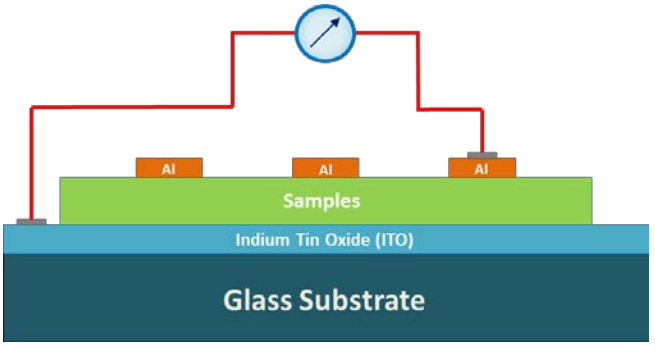

Fig. 6.2: Schematic diagram of the fabricated Schottky devices.

6.3. Material Characterizations Techniques

The morphology of the sample was assessed using a field emission scanning electron microscope (FESEM), by the FEI Inspect F50 model and the elemental combination was determined using an energy-dispersive X-ray (EDX) analyzer. To analyze the crystalline

phase, a powder X-ray diffraction (PXRD) experiment was performed using a Bruker D8 advance X-ray diffractometer, with Cu-K_α radiation (λ=1.5418 Å). Current-voltage (I-V) measurements were performed using a Keithley 2635B sourcemeter.

6.4. Results and Discussion

6.4.1. Structural Properties

The PXRD patterns of the samples are shown in Fig. 6.3. The peak (002) of rGO appeared at approximately 2θ=24°-25°. Peaks were observed at 2θ = 26.62°, 28.11°, 31.08°, 41.03°, 45.36°, 46.04°, 50.0°, 56.60° and 70.32° corresponding to the (101), (102), (006), (106), (107), (110), (108), (116) and (208) diffraction planes, respectively. This is confirmed by JCPDS card no. 34-0171 and the phase of CuSe is verified. The spectrum for RCS was similar to that of bare CS. The intensity of the rGO peak was low due to the presence of small amount of rGO in the composite.

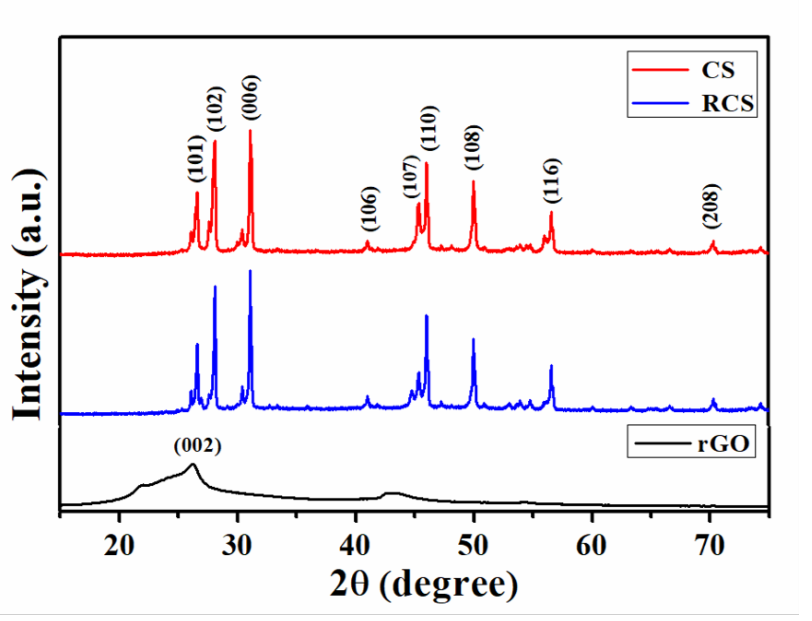

Fig. 6.3: XRD spectra of pristine CS and RCS nanocomposite and rGO.

6.4.2. Morphological and Elemental Studies

The FESEM images of the samples are shown below. Figure 6.4(a) displays hexagonal CS particles, which are approximately 200-250 nm in size. The nice decoration of CS nanoparticles on the rGO sheets is shown in Fig. 6.4(b). Figure 6.4(c) represents the EDX spectra of RCS, satisfying the presence of elements (Cu, Se, C) in the composite indicating the successful synthesis of the composite.

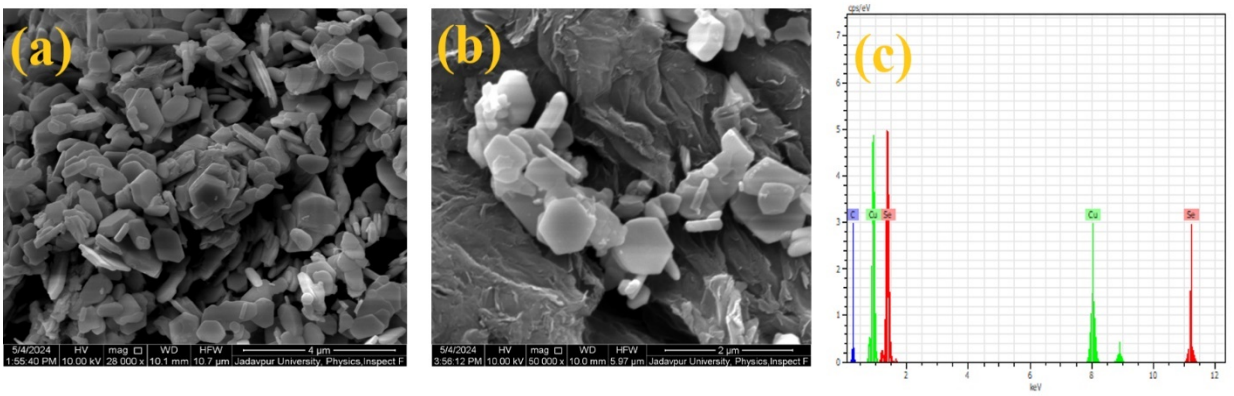

Fig. 6.4: FESEM image of (a) CS and (b) RCS (c) EDX spectra of RCS composite.

6.4.3. Current-Voltage (I-V) Measurement

The I-V characteristics of the devices were measured within a bias voltage range of ±1 V and shown in Fig. 6.5(a). The devices exhibited excellent rectifying behaviour, indicating Schottky nature. The RCS5-based device demonstrated the highest current. Furthermore, all the RCS7, RCS5, RCS3, and RCS1 devices had higher on/off current ratio, indicating greater rectification compared to CS. The enhanced current in the RCS-based diodes can be attributed to the high conductivity of graphene. The diodes were analyzed by the thermionic emission theory and the I-V dependence can be represented by the equation

$$I = I_0 \exp\left(\frac{qV}{\eta kT}\right)\left[1 - \exp\left(-\frac{qV}{\eta kT}\right)\right] \qquad (6.1)$$

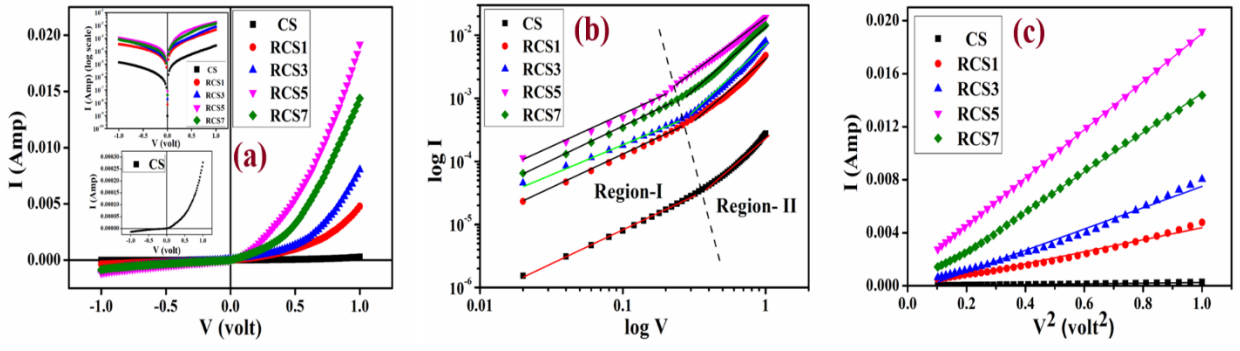

Fig. 6.5: (a) I-V plot of CS and RCS-based SBDs. (b) log I-log V plot and (c) I-V² plot for the SCLC region.

To gain a deeper understanding of charge transport, we examined the forward current region using the SCLC theory[7]. In Fig. 6.5(b), we present the log I vs log V graph, divided into two different regions. The SCLC region (Region-II), where the current follows the relation $I \alpha V^2$, is depicted in Fig. 6.5(b). From the I vs V^2 graph Fig. 6.5(c), we estimated the effective carrier mobility using the Mott-Gurney equation[8].

$$I = \frac{9\mu_{eff}\ \varepsilon_0\varepsilon_r A}{8}\left(\frac{V^2}{d^3}\right) \quad (6.2)$$

where ε_0 - permittivity of vacuum, ε_r - dielectric const. of material, μ_{eff} - electron mobility, and *d* - thickness of film. The transit time (τ) was determined from the I vs V graph using equation (3), and the diffusion lengths (L_D) of the charge carriers were extracted using equation (4).

$$\tau = \frac{9\varepsilon_0\varepsilon_r A}{8d}\left(\frac{V}{I}\right) \quad (6.3)$$

$$L_D = \sqrt{2D\tau} \quad (6.4)$$

where, *D* is denoted the diffusion coefficient, calculated from the Einstein-Smoluchowski equation[9]:

$$\mu_{eff} = \frac{qD}{kT} \quad (6.5)$$

Table 6.1: *Charge transport parameters*

Sample	On/Off	μeff ($m^2V^{-1}s^{-1}$)	τ (ns)	L_D (nm)
CS	20	2.26×10^{-6}	329	199
RCS1	26	2.86×10^{-5}	29.9	210
RCS3	38	3.60×10^{-5}	26.0	220
RCS5	52	8.60×10^{-5}	15.2	260
RCS7	44	6.34×10^{-5}	18.5	246

The above tabulated data shows that there is a continuous improvement in charge transport kinetics after incorporating rGO. The mobility of the charge carriers increases with increase in rGO amount and decreases after a certain amount of rGO loading. In comparison to the bare CS, RCS5 showed the best result with highest carrier mobility of 8.60×10^{-5} $m^2V^{-1}s^{-1}$, a huge 38-fold increase in value. The transit time obtained was 15.2 ns that was improved by 22 times and the diffusion length as calculated was 260 nm where it was also increased by 30%. This study shows that, the rGO incorporated CuSe can be beneficial for several device applications.

6.5. Conclusions

In conclusion, CS and RCS nanocomposites with incorporation of different amounts of rGO have been synthesized by hydrothermal method and SBDs have been fabricated with the samples. The I-V characteristics indicated that mobility of the charge carriers greatly depends on the rGO content present in the samples. All rGO-based devices performed better than the CS-based SBDs, where the best performance was observed in Al/RCS5/ITO SBD. This device exhibited a significant 38 times increase in carrier mobility compared to CS. The transit time was improved and diffusion length of the carriers also increased substantially. Therefore, the result suggests a better understanding and further improvement in charge transport of MS devices.

***

References

1. N.A. Al-Ahmadi, Mater Res Express, 2020, **7**(3), 032001.

2. Z.-Y. Feng, J.-C. Jiang, and L.-Y. Meng, Dalton Transactions, 2024, **53**(27), 11192–11215.

3. W. S. J. Hummers and R. E. Offeman, J. Am. Chem. Soc, 1958, **80**, 1339.

4. D. C. Marcano, D. V Kosynkin, J. M. Berlin, A. Sinitskii, Z. Sun, A. Slesarev, L. B. Alemany, W. Lu, and J. M. Tour, ACS Nano, 2010, **4**, 4806.

5. M. Das, J. Datta, A. Dey, R. Jana, A. Layek, S. Middya, and P. P. Ray, RSC Adv, 2015, **5**, 101582.

6. R. Sk, A. Biswas, A. Layek, P. P. Ray, Chemical Physics, 2024, **580,** 112233.

7. K.S. Das, M. Das, S. Saha, A. Adhikary, S. Bala, P.P. Ray, R. Mondal, Mater Adv, 2023, **4**(23), 6367–6380.

8. P. Das, M. Das, P.P. Ray, and S.K. Seth, ChemistrySelect, 2024, **9**(6), e202303361.

9. M.A. Islam, Phys Scr, 2004, **70**(2–3), 120–125.

***

Effect of enhanced carrier mobility of reduced graphene oxide-copper selenide (rGO-CuSe) nanocomposite towards efficient charge transfer in the visible light driven photodegradation of Methylene Blue dye

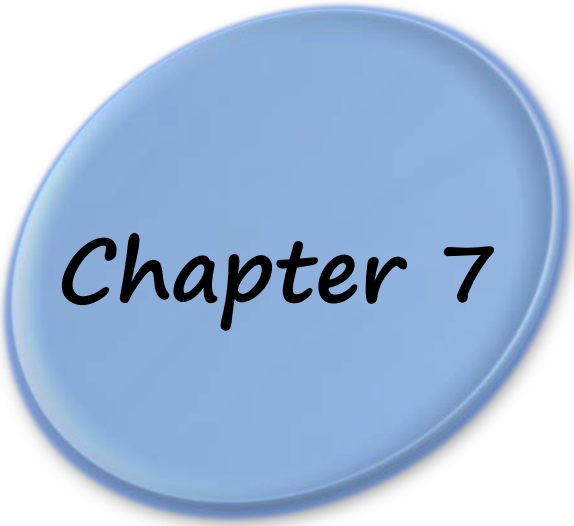

7.1. Introduction

Dye wastewater released into water bodies, predominantly by textile industries, has emerged as a significant environmental concern, resulting in various ecological issues[1]. Over the past few decades, numerous physicochemical and biological strategies, employing chemical and physical adsorption techniques, have been developed to degrade these industrial effluents; however, these methods often lack cost-effectiveness and can produce secondary pollutants[2]. Among the advanced oxidation processes currently available, the photocatalytic approach utilizing semiconducting materials has demonstrated considerable efficacy in wastewater decontamination[3]. A substantial number of compound semiconductors have been explored for the decomposition of organic dyes, owing to their superior absorbance cross-section and enhanced environmental stability[4,5]. Despite the promising potential of semiconductor materials for the decolorization of organic dyes, they are hindered by limitations such as wide bandgaps and relatively short exciton lifespans, which restrict their practical applications[6]. For instance, titanium dioxide (TiO_2), recognized as one of the most effective materials for the degradation of various organic pollutants, is responsive primarily within the ultraviolet region of the electromagnetic spectrum, a limitation attributed to its wide bandgap 3.2 eV[7,8]. This characteristic results in fewer redox reactions with pollutants, adversely affecting its degradation efficiency[9].

On the other hand, copper selenide (CuSe), an important copper chalcogenide semiconductor with a direct bandgap of approximately 2.60 eV, has demonstrated significant potential across a wide range of applications, including solar cells[10], light-emitting diodes (LEDs)[11], optoelectronic devices[12], carbon dioxide reduction[13], and wastewater treatment[14,15]. Solution-processed CuSe nanostructures exhibit several advantageous characteristics, including low production costs, large surface area, good environmental stability, excellent reusability, and notable visible-light absorption, which position them as promising photocatalysts. However, a significant limitation of these materials is the rapid recombination of photo-generated electron-hole pairs (e^- and h^+) in CuSe nanomaterials, which adversely affects their photocatalytic performance, particularly under visible light irradiation. Numerous strategies have been explored to mitigate electron-hole recombination and thereby enhance electron transfer during the photocatalytic process. Among these strategies, the synthesis of graphene-based composites has emerged as one of the most effective approaches[16,17]. In this context,

easily processed, cost-effective graphene oxide (GO) and/or reduced graphene oxide (rGO) exhibit a high specific surface area and demonstrate superior electrical conductivity[18,19]. The presence of various functional groups facilitates the easy exfoliation of GO sheets in water, leading to the formation of stable dispersions. These exfoliated GO sheets, characterized by their large surface area, also provide substantial interfacial contact with nanoparticles, which in turn suppresses the recombination of photo-generated electron-hole pairs and enhances charge transfer efficiency[20]. The present study details the synthesis of a reduced graphene oxide-copper selenide (rGO-CuSe) nanocomposite and assesses its efficacy in the degradation of organic dye (Methylene Blue) under visible-light irradiation. The associated improvements in the transport properties of charge carriers and the implications of their mobility in dye degradation are discussed in detail in this report.

7.2. Materials and Methods

The synthesis procedure of the CuSe and rGO-CuSe nanocomposites and the fabrication of the Schottky diodes were discussed in detail in the previous chapter (§ 6.2).

7.3. Material Characterization Techniques

The material characterization techniques employed in the preceding chapter (§ 6.3) have been consistently applied in this chapter. Additional techniques include:

The surface morphology and elemental composition were examined using the FEI Inspect F50 field emission scanning electron microscope (FESEM) in conjunction with an integrated energy dispersive X-ray (EDX) analyzer. Microstructural information regarding the nanocomposite was analyzed utilizing the JEOL JEM 2100F field emission gun (FEG) transmission electron microscope (TEM). The X-ray photoelectron spectroscopy (XPS) technique (Omicron Nanotechnology), employing Al-Kα radiation (E = 1486.7 eV), was applied to investigate the surface electronic states of the constituent elements and the reduction state of graphene oxide (GO). The absorption spectra of the synthesized materials and their photocatalytic behavior were assessed using a UV-Vis spectrophotometer (Perkin Elmer, Lambda 365) and a low-cost solar simulator (Abet Technologies, Model 10500), respectively. Photoluminescence spectra of the samples were obtained with a spectrofluorimeter (PerkinElmer LS55). To interpret the Brunauer-Emmett-Teller (BET) specific surface area of the nanomaterials, nitrogen adsorption-

desorption measurements were conducted at 77K using an Autosorb iQ2 (Quantachrome Instruments, USA).

7.4. Results and Discussion

7.4.1. Structural Properties

➲ *XRD Analysis*

The PXRD patterns of the samples are presented in Fig. 7.1. The peaks were identified at 2θ = 26.62°, 28.11°, 31.08°, 41.03°, 45.36°, 46.04°, 50.0°, 56.60°, and 70.32°, corresponding to the (101), (102), (006), (106), (107), (110), (108), (116), and (208) diffraction planes, respectively. This observation is corroborated by JCPDS card no. 34-0171, thereby confirming the presence of the CuSe phase.

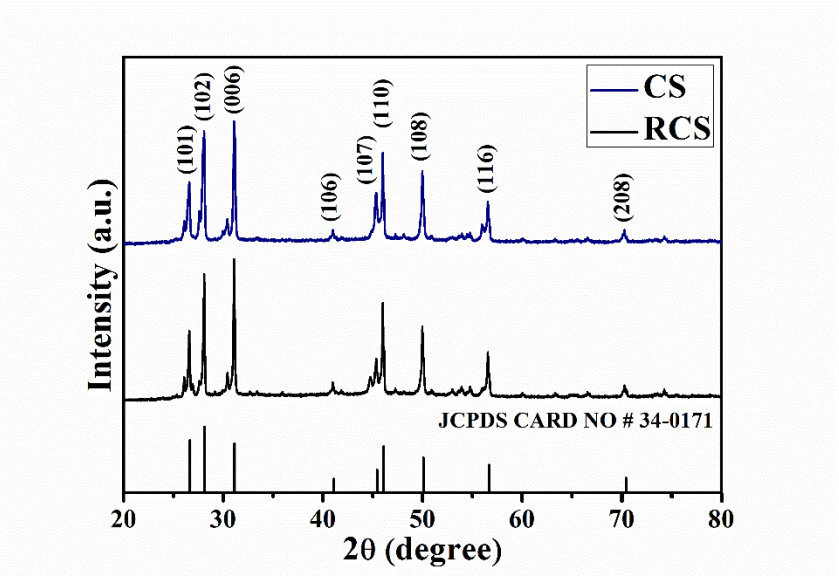

Fig. 7.1: XRD spectra of as-synthesized CS and RCS nanocomposite.

A further observation from Fig. 7.1 is that the addition of rGO did not affect the relative intensities and positions of the Bragg reflections in CS and RCS which could result in the growth of new crystallographic phases. Also, no characteristic diffraction peaks for rGO were noticed in the composite, which is attributed to the low level of loading and comparatively weaker diffraction peaks of GO[21]. Moreover, the X-ray diffraction was performed for the synthesized Graphene oxide (GO) and reduced graphene oxide (rGO). The signature peak of the graphene oxide was found at 10.9° in the XRD pattern in Fig. 7.2(a). This authenticates the successful formation of GO from the graphite powder. After hydrazine treatment, the peak at 10.9° was almost diminished and a new and wide peak at 24.7° is observed in Fig. 7.2(b), indicating the reduction of GO[22].

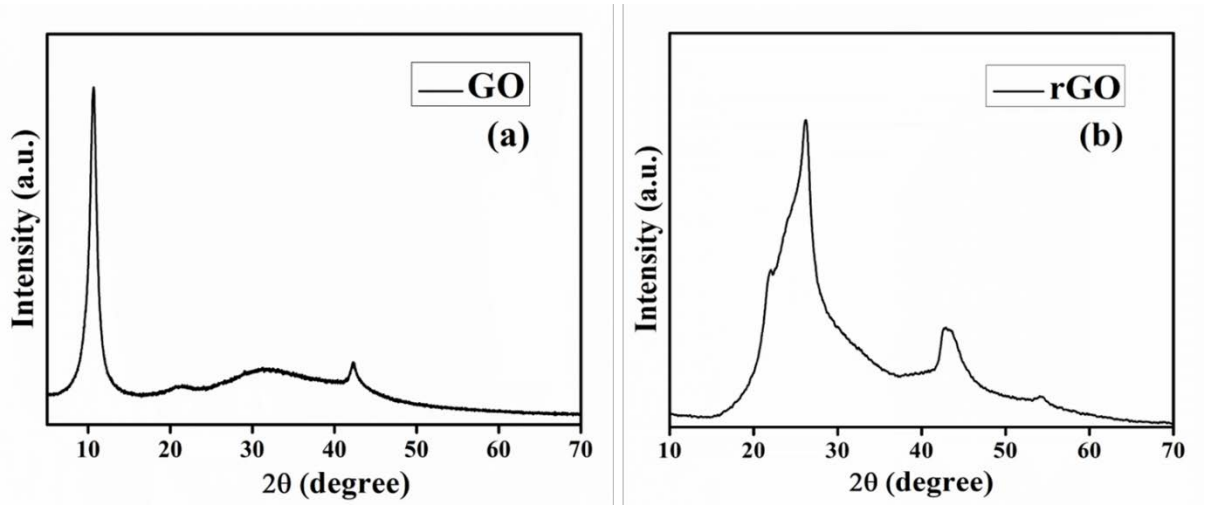

Fig. 7.2: XRD spectra of (a) GO and (b) rGO.

➲ *FESEM Study*

The morphology and microstructural characteristics of the synthesized materials were corroborated through electron microscopy studies. Firstly, the field emission scanning electron microscopy (FESEM) image presented in Fig. 7.3(a) illustrates hexagonal copper selenide (CS) nanoparticles. Figure 7.3(b) depicts the distribution of CS nanoparticles across the graphene layers within the reduced graphene oxide-copper selenide (RCS) composite. Additionally, some random agglomeration of CS nanoparticles is observed, which may result from the aggregation tendency of the graphene layers due to van der Waals interactions[22]. The accompanying energy dispersive X-ray (EDX) spectra provided in Fig. 7.3(c) confirm the presence of the constituent elements (Cu, Se, and C) in the nanocomposite. Moreover, the quantitative analysis of the EDX data indicates that the molar ratio of Cu to Se in the synthesized material is approximately unity, thereby suggesting the formation of stoichiometric CS nanoparticles.

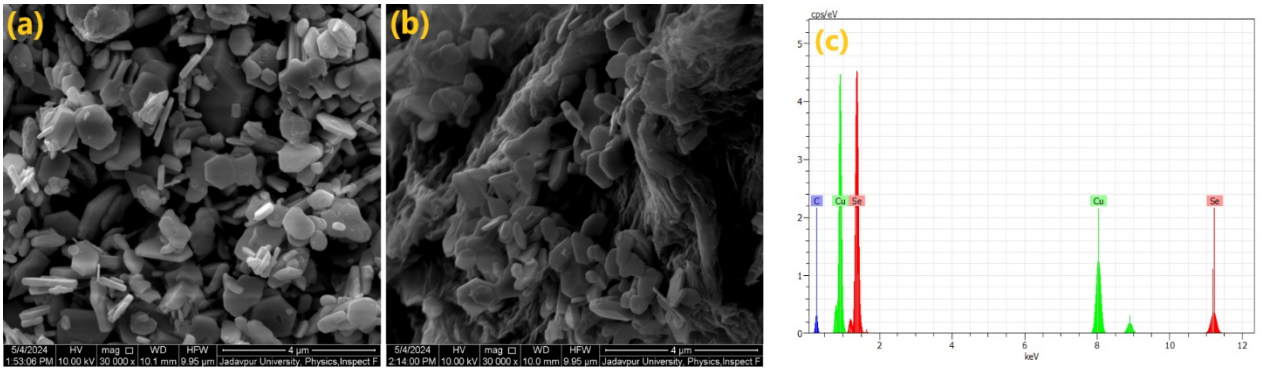

Fig. 7.3: FESEM image of (a) CS and (b) RCS nanocomposite (c) EDX spectra of the RCS nanocomposite.

➲ ***TEM Study***

The transmission electron microscopy (TEM) microstructures illustrated in Fig. 7.4(a) elucidate the distribution of CS nanoparticles. Fig. 7.4(b) indicates that the nearly hexagonal morphology of the CS nanometric particles is uniformly dispersed across the wrinkled two-dimensional reduced graphene oxide (rGO) layers[23]. This configuration facilitates the establishment of a close interface characterized by minimal particle aggregation, resulting in the formation of an intimate bond between the CS nanoparticles and the rGO layers[24]. The formation of this intimate bonding is anticipated to enhance the transfer of charge carriers, thereby mitigating their recombination. The high-resolution transmission electron microscopy (HRTEM) image presented in Fig. 7.4(c) corresponds to the interplanar spacing of the hexagonal CS lattice. Furthermore, Fig. 7.4(d) displays the selected area electron diffraction (SAED) pattern of the CS nanoparticles, with concentric diffraction rings, indicating the polycrystalline nature of the specimen.

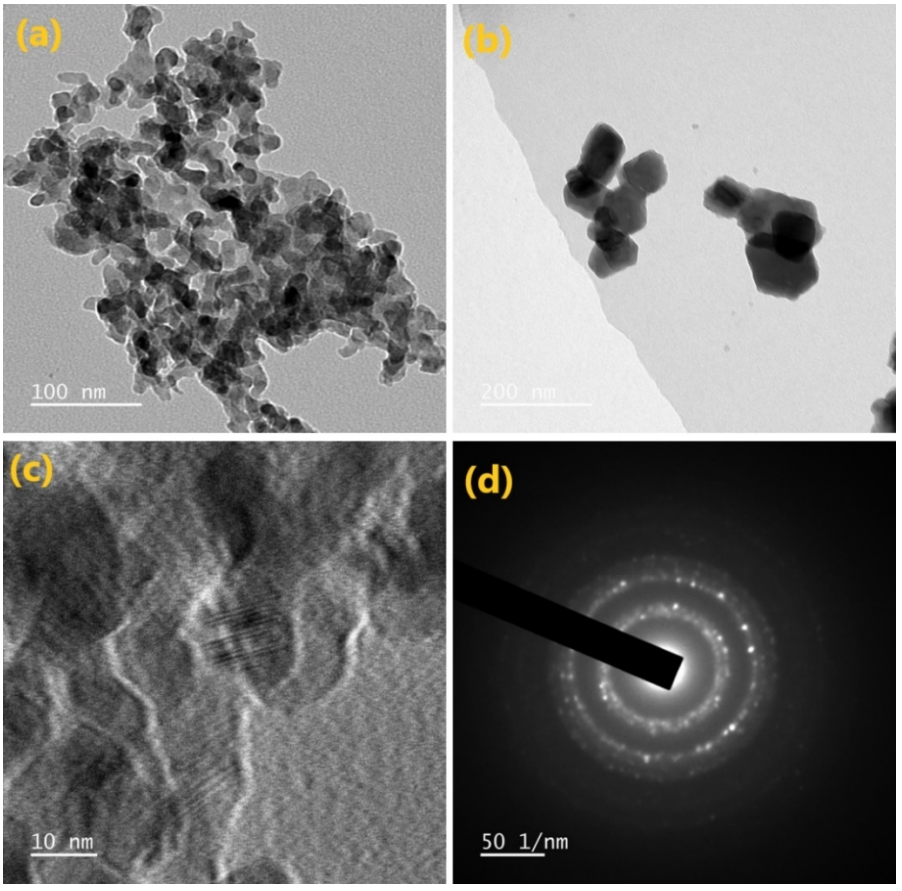

Fig.7.4: TEM images of (a) CS and (b) RCS nanocomposite. (c) High-resolution TEM and (d) SAED pattern of CS nanoparticles over rGO layers.

➲ *XPS Study*

An X-ray Photoelectron Spectroscopy (XPS) investigation of the RCS nanostructures was conducted to analyze the surface chemical composition and the oxidation states of the metallic ions present. The presence of copper (Cu), selenium (Se), carbon (C), and oxygen (O) in the RCS nanocomposite was confirmed by the survey spectrum within the energy range of 0-1200 eV, as illustrated in Fig. 7.5(a). The XPS peak corresponding to C 1s for the RCS composite was deconvoluted into four constituent Gaussian peaks, as shown in Fig. 7.5(b), with binding energies centered around 283.86 eV, 285.17 eV, 287.26 eV, and 290.03 eV. These peaks are attributed to the C=C, C-OH, C=O, and O-C=O bonds, respectively[25]. The observation of relatively low-intensity oxygenated functional groups suggests their partial elimination, alongside the presence of restored graphitic segments within the composite material[22]. This phenomenon has significant implications; on one hand, the restored graphitic layers facilitate electron transfer, while on the other hand, the presence of O_2^- containing functional groups is likely to promote strong interactions between the nanocomposite and the aqueous solution during photocatalytic degradation[26,27].

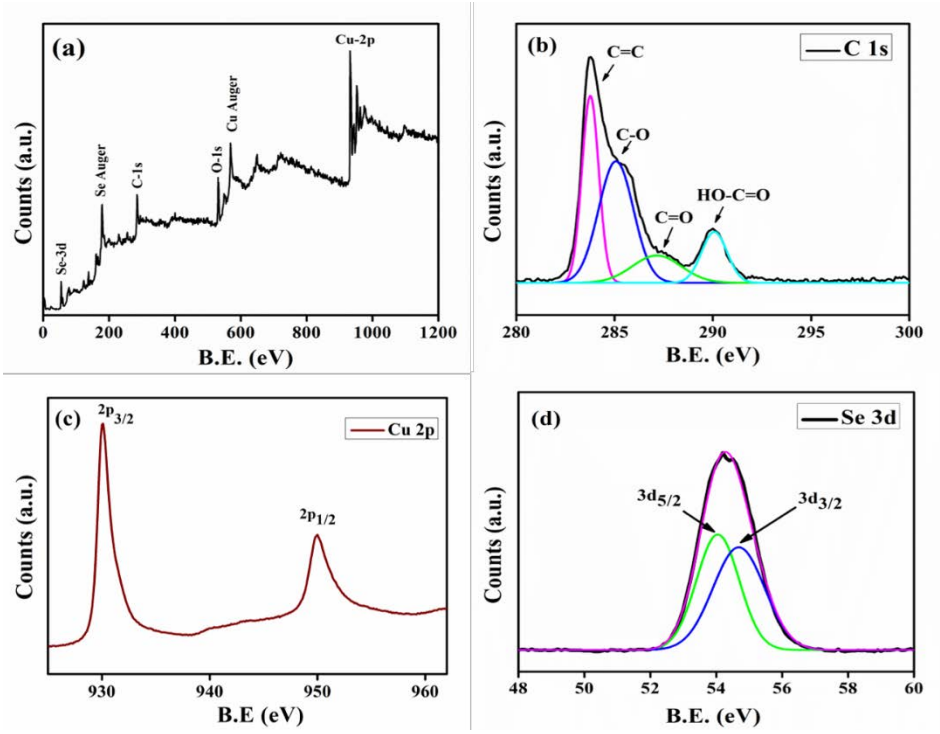

Fig. 7.5: (a) XPS survey and (b) C 1s spectrum of the RCS nanocomposite. The HR-XPS spectrum of (c) Cu-2p and (d) Se-3d states.

The high-resolution X-ray photoelectron spectroscopy (XPS) data for the Cu 2p region, as illustrated in Fig. 7.5c, reveals two distinct peaks at 932.5 eV and 952.4 eV. The

energy difference between these states is 19.9 eV, which aligns with previously reported values for the Cu $2p_{3/2}$ and Cu $2p_{1/2}$ states[28]. These peaks can be attributed to the Cu^{2+} state present in CuSe nanostructures.

Lastly, Figure 7.5(d) presents a detailed scan of the Se 3d core level, which has been deconvoluted into two doublets resulting from spin-orbit coupling (j = 3/2, 5/2) with a splitting of 0.86 eV, observed at binding energies of 54.86 eV and 54 eV, respectively. These results are consistent with the existing literature, thereby confirming the 2^- oxidation state of selenium in CuSe[29,30].

Thus, X-ray photoelectron spectroscopy (XPS) analysis supports the sample's chemical purity, while the electronic states of the component elements validate the development of an RCS nanocomposite. Furthermore, the XPS analysis provides information about the surface chemical states of copper (Cu), selenium (Se), and carbon (C), which together form our heterostructure photocatalyst. This photocatalyst has the ability to serve as an electron capture and transfer medium during the photocatalytic degradation process, which will be discussed in the subsequent section.

7.4.2. Optical Properties

➲ *UV-visible Spectroscopy*

The UV-visible absorbance spectra of as-synthesized CS and RCS nanocomposite presented in Fig. 7.6(a) were recorded in the wavelength range 250-800 nm to study their optical properties. The optical band gap (E_g) of the nano-catalysts was derived employing Tauc's equation (Eq. 7.1) in the fundamental absorption edge of the UV-visible absorption spectroscopy. According to Tauc's equation[31]:

$$\left(\alpha h\nu\right)^n = A\left(h\nu - E_g\right) \qquad (7.1)$$

where α is the absorption coefficient, E_g is the bandgap, h is Planck's constant, ν is frequency, A is a constant, and n = 2 and ½ corresponds to the allowed direct and indirect optical transition, respectively.

By analyzing Tauc's plot (Fig. 7.6b), the estimated values of the bandgap for the CS and RCS were found to be 2.60 eV and 2.21 eV, respectively, which were close to the reported values[32]. The broader absorption band and the reduced bandgap of the rGO attached material, compared to pristine CS, indicate an enhancement in photon

absorption and an increase in the generation of electron-hole pairs for the photocatalytic experiment.

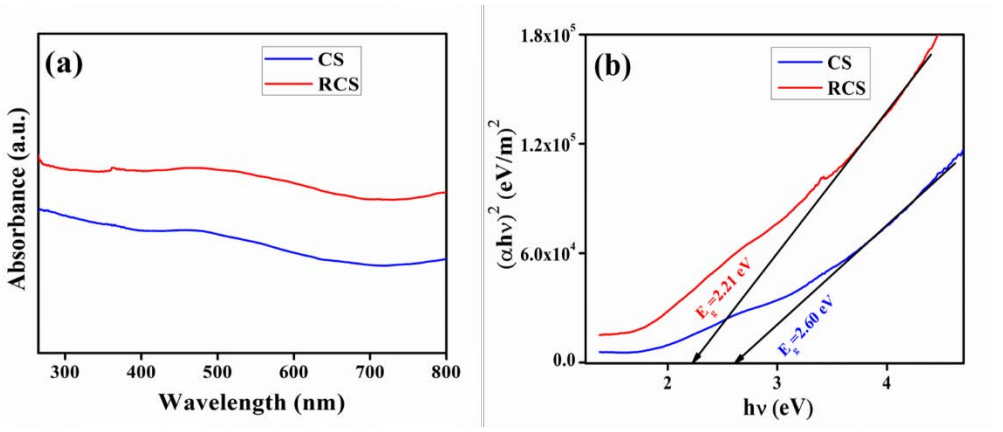

Fig. 7.6: (a) Optical absorption spectra of pure CS and RCS composite. (b) Tauc's plot for the optical band gap of pure CS and RCS nanocomposite.

7.4.3. BET Surface Area Studies

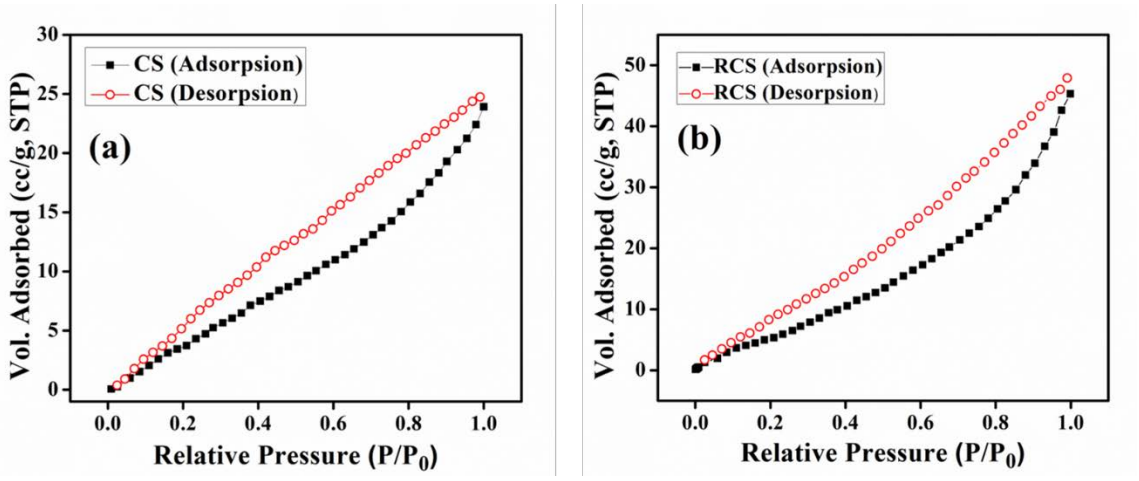

Fig. 7.7: N_2 adsorption-desorption isotherms for (a) CS and (b) RCS nanocomposite.

The N_2 adsorption-desorption isotherms (Fig. 7.7) at 77 K (-196 °C) were also measured to determine the Brunauer-Emmett-Teller (BET) specific surface of pure CS and RCS nanocomposite[33]. The BET study estimated the specific surface area of virgin CS and RCS composites to be 28.33 m^2g^{-1} and 46.57 m^2g^{-1}, respectively, demonstrating a larger surface area in the graphene-based composite[34,35]. In photocatalytic applications, a higher absorbance cross-section is always preferred since the larger the surface area, the greater the photo-absorption and, as a result, the diffusion of molecules. Figure 7.7 shows

that the graphene composite is expected to satisfy those requirements, as demonstrated in the following.

7.4.4. Electrical Properties

➲ ***Current-Voltage (I-V) Measurements***

To interpret the electronic charge transport properties of the synthesized materials, the current-voltage (I-V) characteristics of the fabricated Schottky devices (Al/CS/ITO and Al/RCS/ITO), as presented in the preceding chapter (§ 6.3.4), were analyzed by applying a direct current (dc) bias voltage of ±1 V at room temperature under both dark and illuminated (~1000 W/m^2) conditions. The dc conductivity (σ), which serves as an indicator of charge flow, was derived from the linear region of the diode characteristic curves (Fig. 7.8(a)) for both devices examined under various conditions (Table 7.1). The notable increase in current density following light irradiation underscores the photo-responsive characteristics of the materials. The photosensitivity (S), defined as $S = I_v / I_d$ (where $I_v = I_l - I_d$ is the photo-induced current and I_d is the current under dark), was further calculated for both devices[36]. The graphene-based device, which exhibits superior absorption capabilities, demonstrated higher sensitivity compared to its counterpart composed of pristine CS (Table 7.1). Moreover, the elevated conductivity of the composite material indicated in Table 7.1 suggests an enhancement in charge transport as well as improved mobility. Carrier mobility is a critical factor for any semiconducting material, as it determines the rate at which charge carriers, namely electrons and/or holes, traverse the intricate network before reaching the active sites where they ultimately recombine. Given that reduced graphene oxide (rGO) provides increased electron mobility (approximately 10^4 cm^2/Vs at 300 K), it is anticipated to facilitate the movement of charge carriers and the separation of electron-hole pairs through its high-quality two-dimensional network[37].

To elucidate the inclusive influence of reduced graphene oxide (rGO) in the charge transport mechanism and photodegradation process, the current-voltage (I-V) characteristics were further analyzed by interpreting the effective carrier mobility (μ_{eff}) and lifetime (τ) based on semiconductor theory. For this purpose, the logarithm of current (log I) was plotted against the logarithm of voltage (log V) for positive voltages, as depicted in Fig. 7.8(b). In this plot, two distinct linear regions can be identified, suggesting the presence of different conduction mechanisms.

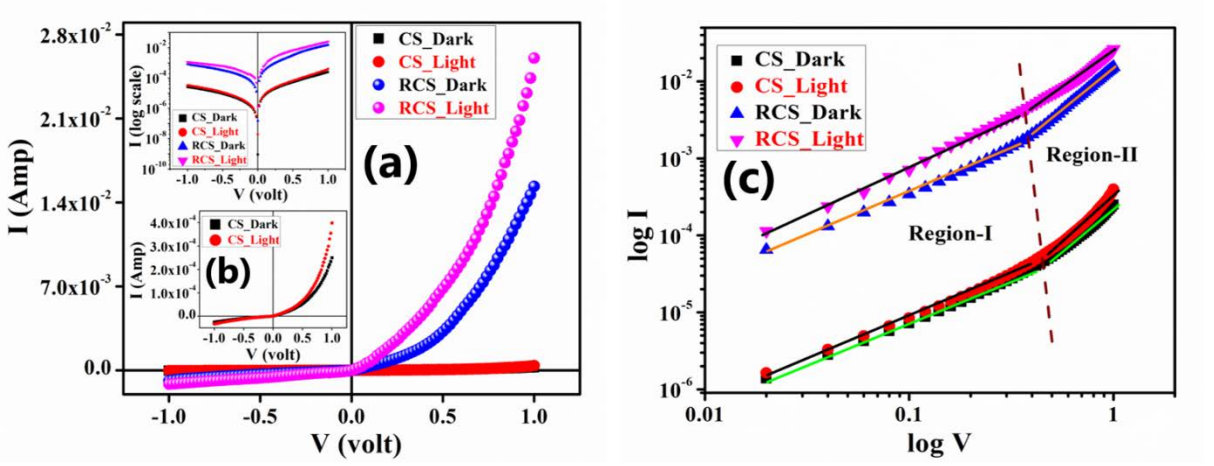

Fig. 7.8: (a) Current-voltage (I-V) characteristic curves of CS and RCS (b) I-V curve of CS (inset) and (c) I-V plot in logarithmic scale for the pure CS and RCS composite-based Schottky diodes under the dark and light conditions.

In a metal-semiconductor junction, interfacial trap states significantly influence the conduction behavior of charge carriers, thereby modifying the current-voltage (I-V) characteristic curves. In the low bias regime (Region I), Ohmic behavior ($I \propto V$) is observed, characterized by a slope of approximately unity. In this region, the current primarily results from the charge carriers that are intrinsic to the material under investigation[38]. Progressing to Region II, as illustrated in Fig. 7.8(b), the injected carriers from the contacts interact with the intrinsic carriers at intermediate potential difference values, resulting in the formation of a spatially distributed charge field. In this context, the motion of charge carriers is predominantly influenced by this field, and their mobility principally dictates the quadratic current ($I \propto V^2$) observed in this region[39,40].

➲ *Estimation of the Charge Transport Parameters*

To obtain a comprehensive understanding of the charge transport mechanism, the current-voltage (I-V) characteristics were further analyzed by determining the effective carrier mobility (μ_{eff}) and lifetime (τ) from region II [Fig. 7.8(b)], based on the space-charge limited current (SCLC) theory[39]. Figures 7.9(a) and 7.9(b) illustrate the current (I) versus voltage squared (V^2) plots for the SCLC region for the CS and RCS composites, respectively. The dielectric constant of the synthesized materials, the mobility (μ_{eff}), and the lifetime or transient time (τ) of the charge carriers were estimated using the following equations:

$$\varepsilon_r = \frac{C_0 d}{\varepsilon_0 A_{eff}} \tag{7.2}$$

$$I = \frac{9\mu_{eff}\varepsilon_0\varepsilon_r A_{eff}}{8}\left(\frac{V^2}{d^3}\right) \tag{7.3}$$

$$\tau = \frac{9\varepsilon_0\varepsilon_r A_{eff}}{8d}\left(\frac{V}{I}\right) \tag{7.4}$$

The comprehensive explanation of all symbols utilized in the previously mentioned equations can be found in Chapter 2 (§ 2.7.2). Additionally, Figure 7.10 presents the plot depicting the capacitance (C) versus frequency (f) characteristics for both CuSe and rGO-CuSe films.

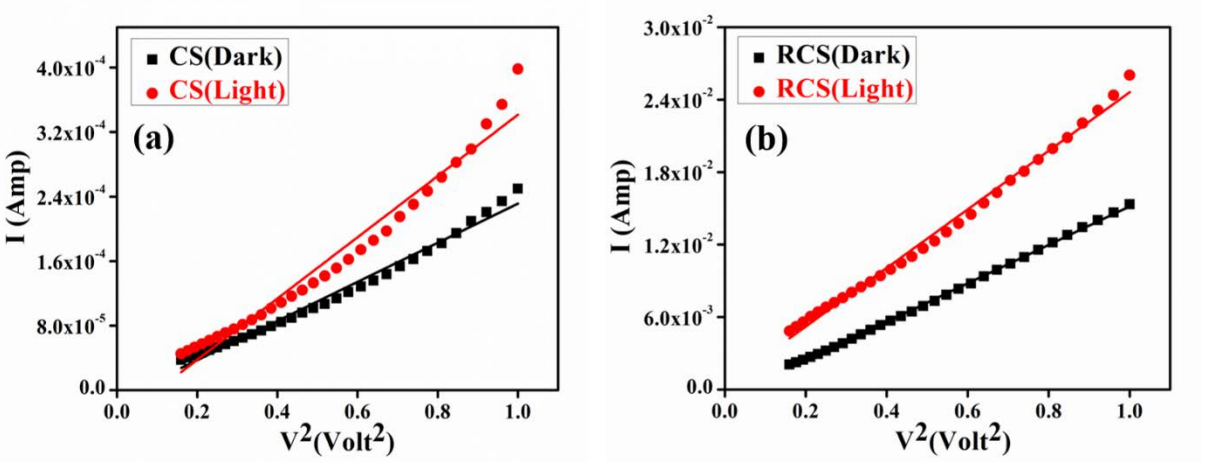

Fig. 7.9: The current (I) vs. voltage^2 (V^2) plot for the SCLC region for (a) CS and (b) RCS composite.

The estimated values of μ_{eff} and τ are presented in Table 7.1. The enhanced mobility of graphene and its significant contribution to the efficient transfer of charge carriers is demonstrated in our findings. The graphene-based composite exhibited superior carrier mobility and lifetime compared to the as-synthesized CS nanoparticles. These results are consistent with previously reported data for the reduced graphene oxide (rGO)-based inorganic composite[41,42]. Under both dark and light conditions, the carrier mobility was significantly increased by nearly 15 to 20 times (Table 7.1). This enhancement in mobility, as well as in lifetime, could lead to improved charge transfer efficiency and consequently, enhanced photocatalytic activity.

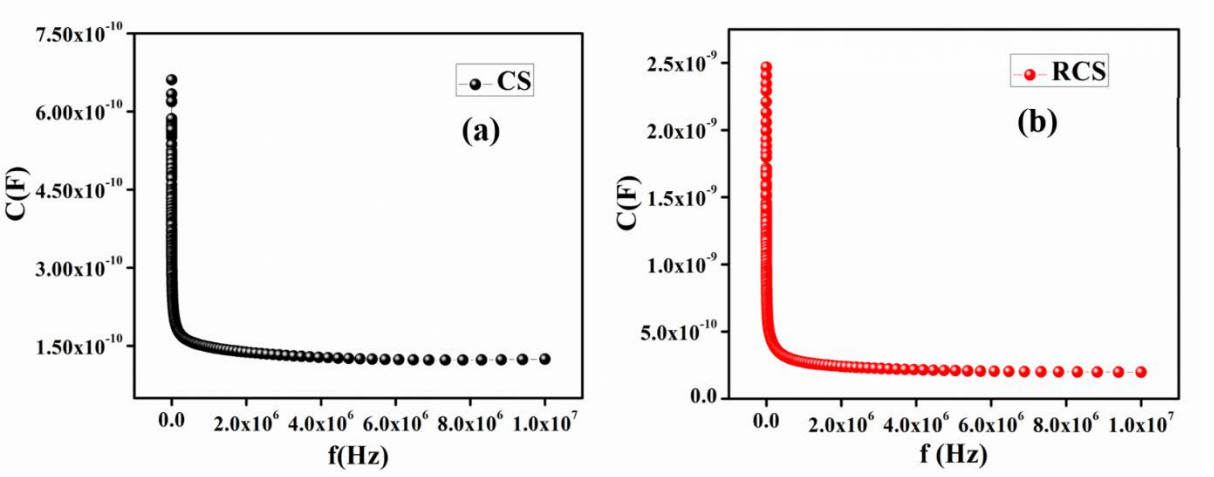

Fig. 7.10: Capacitance (C) vs. frequency (f) plot for (a) CuSe and (b) rGO-CuSe thin film.

Table 7.1: *Charge transport parameters*

Sample	Photo-sensitivity	Conductivity (σ) (Sm^{-1})		Mobility (μ_{eff}) ($m^2V^{-1}s^{-1}$)		Lifetime (τ) (s)	
Condition	-	**Dark**	**Light**	**Dark**	**Light**	**Dark**	**Light**
CS	0.70	1.24×10^{-5}	1.47×10^{-5}	1.74×10^{-6}	2.72×10^{-6}	4.15×10^{-7}	2.67×10^{-7}
RCS	1.04	6.45×10^{-4}	1.72×10^{-3}	6.43×10^{-5}	9.78×10^{-5}	1.11×10^{-8}	7.36×10^{-9}

➲ *Transient Photocurrent Measurements and Nyquist Plots*

To investigate the photo-electrochemical properties of the synthesized catalysts, transient photo-response spectra and electrochemical impedance spectroscopy (EIS), Nyquist plots were obtained and are presented in Fig. 7.11(a) and Fig. 7.11(b), respectively[43]. As anticipated, the photocurrent intensity of the reduced graphene oxide (rGO) composite (RCS) was significantly higher than that of the pristine CS. This finding indicates that the incorporation of rGO into the CS nanoparticles enhances the separation of the photo-generated electrons and holes and promotes their rapid transport through the two-dimensional graphene channels[44]. Additionally, the EIS Nyquist spectra, a robust method for assessing conductance and charge transfer capabilities, exhibited a substantially smaller diameter of the semi-circular arc for the RCS composite compared to the pristine CS [Fig. 7.11(b)]. This observation corroborates the assertion that the addition of rGO markedly reduces the charge transfer resistance within the composite

material, thereby facilitating the migration of electrons and holes to the active sites during the degradation process, as discussed further below.

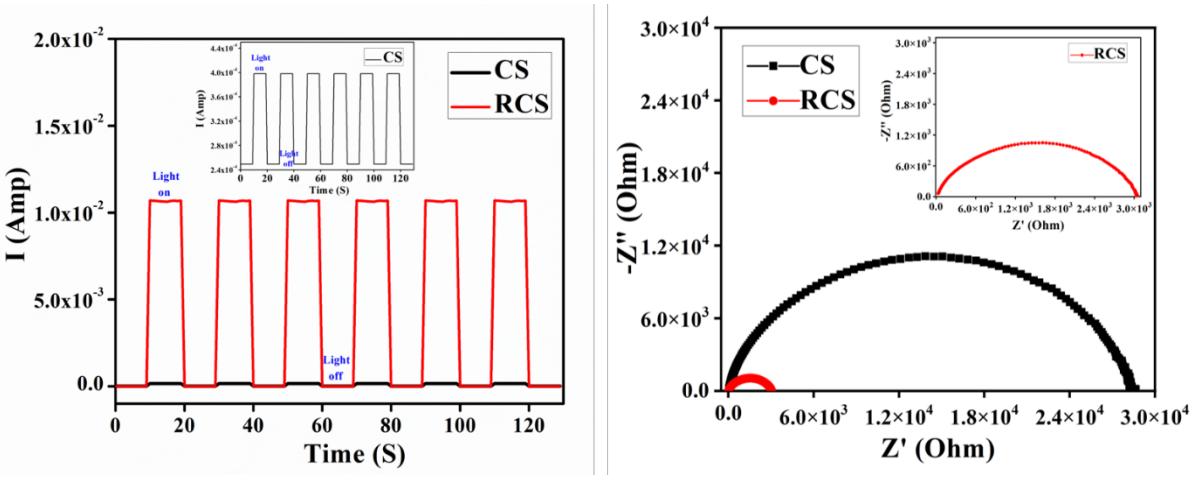

Fig. 7.11: (a) Transient photocurrent response and (b) EIS Nyquist plots of pristine CS (inset) and RCS composite.

7.4.5. Photocatalytic Activity

➲ *Photo-degradation Process*

The photocatalytic performance of the synthesized samples was evaluated through the photocatalytic degradation of Methylene Blue (MB) under solar-simulated visible light irradiation. In a typical experimental setup, 30 mg of the samples and 1 mL of hydrogen peroxide (H_2O_2) were dispersed in 100 mL of a 100 ppm MB aqueous solution. The resultant mixed suspensions were magnetically stirred for 30 minutes in the absence of light to achieve adsorption-desorption equilibrium. Following this, the mixed suspensions were subjected to visible light irradiation produced by a solar simulator (Abet Technologies, Model 10500) while maintaining ambient conditions and continuous stirring. At regular time intervals, 3 mL aliquots of the suspensions were extracted and centrifuged to remove suspended impurities. The absorption of MB in the filtrate was subsequently analyzed using a UV-Vis spectrometer, and the degradation process was assessed.

For the recyclability test, the catalyst was extracted following the degradation cycle through centrifugation and subsequently washed with isopropyl alcohol, followed by millipore water, before being reused in the subsequent cycle. In this study, all experiments were conducted in triplicate to assess their catalytic activity.

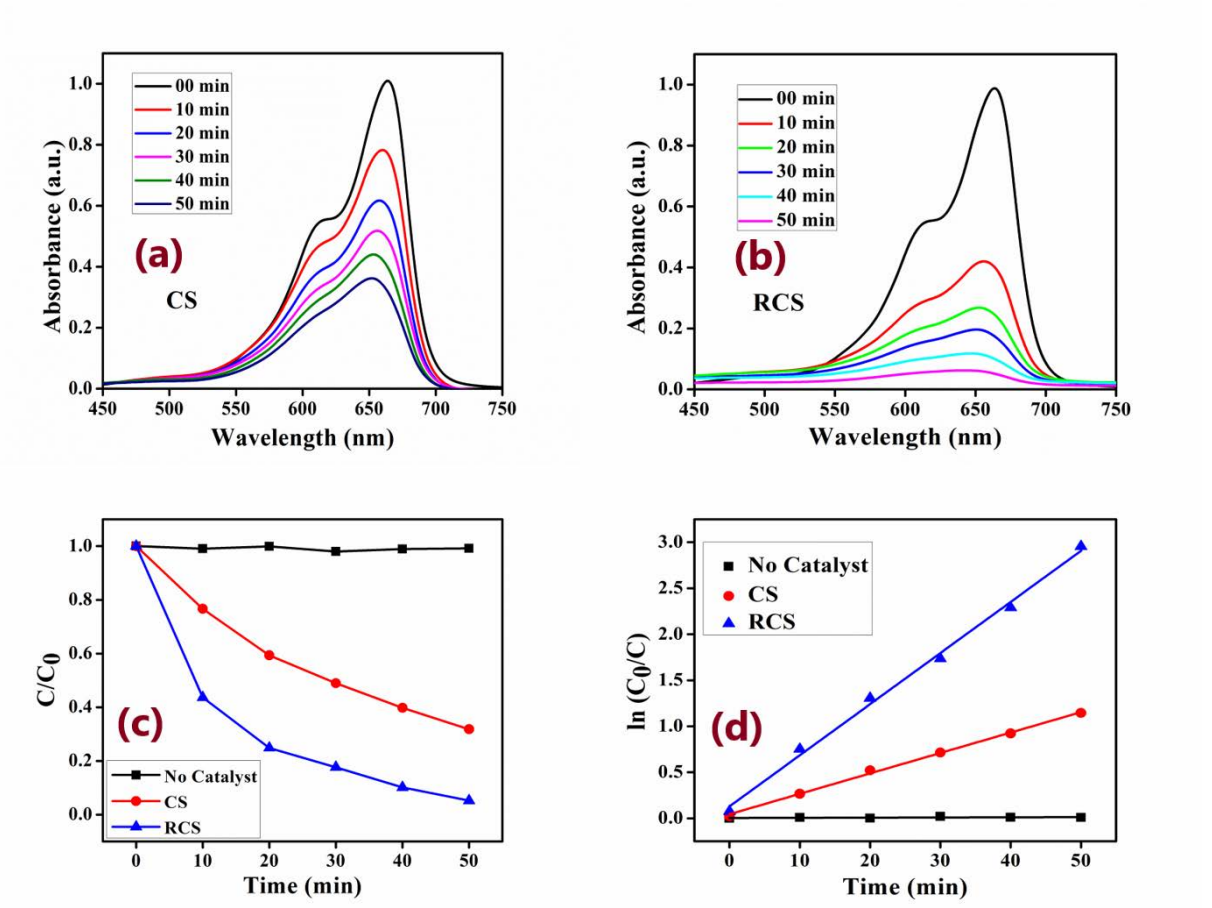

Fig. 7.12: Absorbance spectra of aqueous MB solution at different intervals of time in the presence of (a) CS and (b) RCS nanocomposite under solar irradiations. (c) Photocatalytic degradation behaviour of MB solution (d) ln (C_0/C) vs. Time plot for MB solution in presence of CS and RCS catalysts.

➲ *Photo-degradation Behaviour and Performances*

The photocatalytic degradation of Methylene Blue (MB) under simulated solar light irradiation was employed to investigate the photocatalytic behavior of pristine CS and RCS nanocomposite. The degradation process was monitored by observing the principal absorption peak of the MB aqueous solution, which is centered at 663.5 nm, utilizing a UV-Vis spectrometer [Fig. 7.12(a)]. The analysis of the degradation process was conducted using the equation:

$$Degradation = \left(\frac{C_0 - C_t}{C_0} \times 100\right) \% \qquad (7.5)$$

represent the concentrations of Methylene Blue (MB) at time zero and at time t, respectively[45]. The linear relationship between ln(C_0/C) and illumination time (in minutes) [Fig. 7.12(c)] for both pure CS and RCS composite materials indicates the presence of pseudo-first-order degradation kinetics[46]. Under solar light irradiation for a duration of 50 minutes, no significant change in the MB concentrations was observed for

catalyst-free suspensions. Following the introduction of the pure CS catalyst, the MB solution exhibited a reduction of up to 68% from its initial concentration. In contrast, the RCS nanocomposite demonstrated a notable degradation of 95%, attributable to the synergistic effects of CS nanoparticles and reduced graphene oxide (rGO) [Fig. 7.12(b)]. Moreover, the recycling test [Fig. 7.12(d)] indicated that the degradation efficiency of the RCS catalyst remains relatively stable even after three consecutive cycles of use.

➲ *Adsorption of MB by the Photocatalysts*

The adsorption of Methylene Blue (MB) onto the photocatalysts was assessed prior to the degradation experiments, as the pre-adsorption of dyes facilitates the migration of charge carriers. The adsorption experiments were conducted by continuously stirring 100 mL of an aqueous MB solution with 30 mg of each catalyst (CS and RCS) for a duration of 30 minutes under dark conditions[47]. Figure 7.13 illustrates the adsorption profiles of the aqueous MB solution as a function of time in the dark for both the pristine CS and the RCS composite. The pristine CS exhibited no adsorption in the dark, as evidenced by the concentration of the MB solution remaining virtually unchanged. Furthermore, the RCS composite likewise demonstrated negligible adsorption behavior towards MB, recording less than 1% adsorption after 30 minutes of stirring. These findings suggest that the adsorption of MB by the catalysts would not significantly influence the photo-induced degradation process, which will be discussed in the subsequent sections.

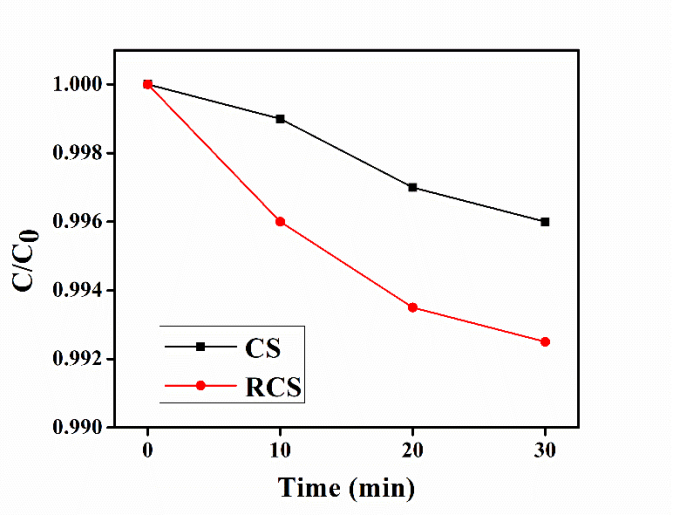

Fig. 7.13: The adsorption profiles of aqueous MB solution on the pristine CS and the RCS composite, as a function of time in the dark.

➲ *Optimization of the rGO Content in the Composites*

To identify the optimal composite photocatalyst for maximizing photocatalytic activity, RCS composites with varying amounts of reduced graphene oxide (rGO) were synthesized and labelled as "RCS(x%)", where x denotes the weight percentage of rGO (0%, 1%, 3%, 5%, and 7%). Figure 7.14 shows the change in Methylene Blue (MB) concentration (C/C0) over a 50-minute period under visible-light irradiation with different catalysts. It was noted that there was no significant change in MB concentration in catalyst-free suspensions. When the pristine CS catalyst was introduced, the MB solution's concentration reduced by up to 68%. In contrast, the degradation of the MB solution reached 78%, 86%, 95%, and 91% with RCS composites containing 1%, 3%, 5%, and 7% rGO, respectively. These findings indicate that the photocatalytic activity of the RCS composites increased initially, then decreased with higher rGO content. Among the samples tested, the composite with 5% rGO exhibited the highest photocatalytic activity, achieving a degradation rate of 95%.

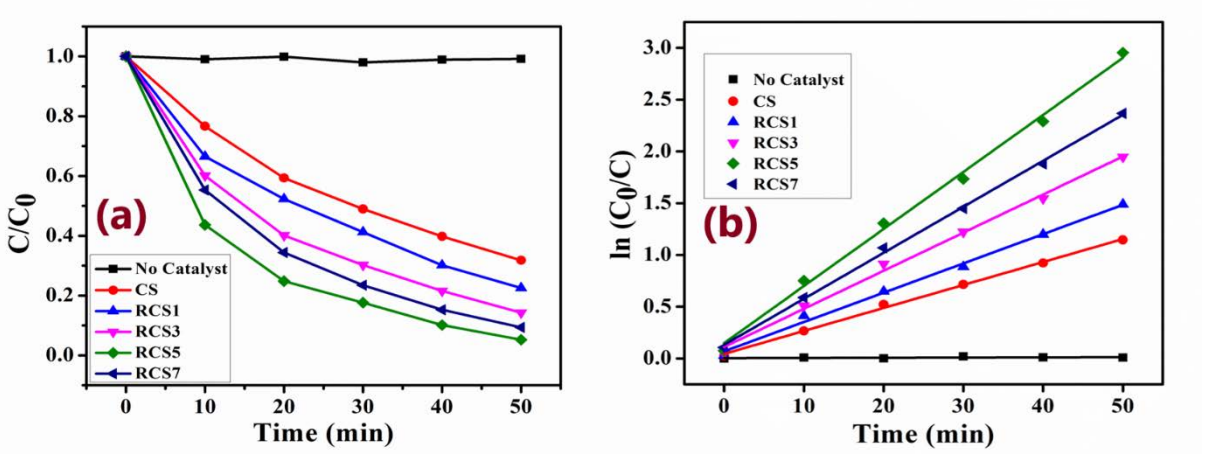

Fig. 7.14: (a) Changes in concentration vs. time and (b) ln (C_0/C) vs. time plot in the presence of different catalysts under visible-light irradiation.

➲ *Photo-degradation Mechanism*

To elucidate the synergy between reduced graphene oxide (rGO) and CuSe (CS) in the composite material, the photocatalytic decomposition process was systematically analyzed. Under visible light irradiation, interfacial excitons are generated at the surface of CS nanoparticles, subsequently separating into free electrons in the conduction band (CB) and holes in the valence band (VB). However, the rapid recombination of these photogenerated electrons and holes prior to their arrival at the active sites results in

suboptimal photocatalytic activity. The attachment of CS nanoparticles to rGO facilitates the efficient separation of the photoinduced electron in the CB of CS at the graphene interface, leaving behind a hole in the VB of CS, attributed to their favourable energy levels (Fig. 7.15)[48]. Consequently, the photogenerated electrons in CS can traverse the rGO platform to readily reach the active sites, where they reduce dissolved O_2 in the aqueous medium to produce the highly reactive superoxide radical anion ($O_2^{\bullet-}$), which can further interact with H_2O to form hydroxyl radicals ($OH^{\bullet}$)[49]. Concurrently, the photoinduced holes may also engage with H_2O or OH^-, oxidizing them to generate $OH^{\bullet}$ [50]. These $O_2^{\bullet-}$, $OH^{\bullet}$, and the photogenerated holes collaboratively contribute to the decomposition process of the MB solution[51,52]. A schematic representation of the photocatalytic mechanism of the rGO-CS photocatalysts is illustrated in Fig. 7.15.

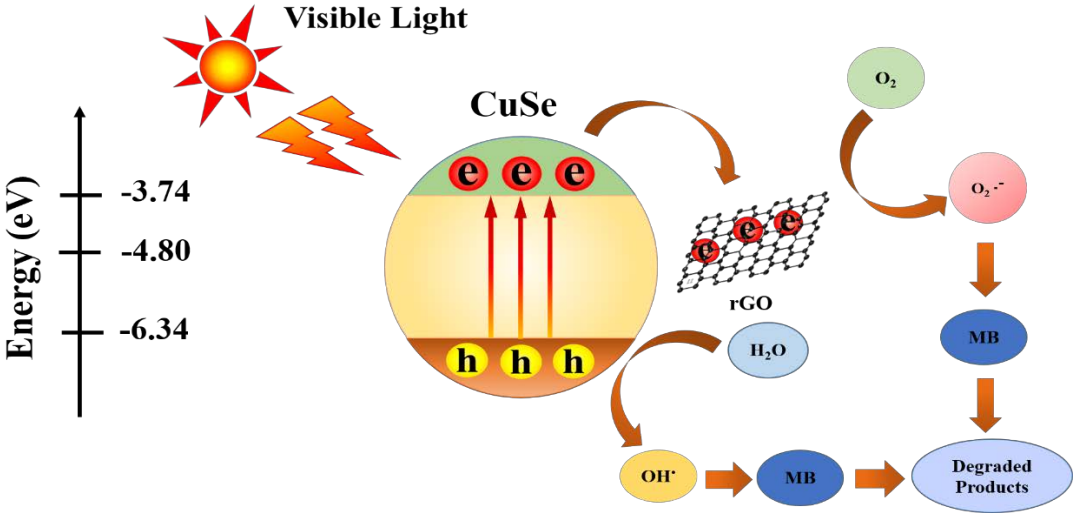

Fig. 7.15: A plausible mechanism of the photocatalytic degradation process of MB containing RCS catalyst under solar light irradiation.

7.5. Conclusion

The CS nanoparticles were successfully synthesized, and the incorporation of the reduced graphene oxide (rGO) sheet with CS was corroborated by X-ray diffraction (XRD), transmission electron microscopy (TEM), field emission scanning electron microscopy (FESEM), X-ray photoelectron spectroscopy (XPS), photoluminescence (PL), and ultraviolet-visible (UV-Vis) spectroscopic data. The charge transport dynamics and the significance of the enhanced carrier mobility of the photocatalysts in the degradation of Methylene Blue (MB) were investigated. The graphene composite demonstrated

significantly higher photocatalytic activity compared to the bare CS under visible-light irradiation. The increased mobility of the graphene-based composite material facilitated the rapid transfer of photoinduced charges between active sites and target molecules during the degradation process. The strong interfacial contact, coupled with enhanced visible light absorption and reduced electron-hole pair recombination, primarily contributed to the improved photocatalytic performance of the composite materials. In conclusion, our findings illuminate the design and charge transfer mechanisms of the graphene-semiconductor-based RCS composite material, which presents a promising photocatalyst with potential applications in wastewater treatment.

***

References

1. R. Al-Tohamy, S. S. Ali, F. Li, K. M. Okasha, Y. A.-G. Mahmoud, T. Elsamahy, H. Jiao, Y. Fu and J. Sun, *Ecotoxicol Environ Saf*, 2022, **231**, 113160.

2. V. Selvaraj, T. Swarna Karthika, C. Mansiya and M. Alagar, *J Mol Struct*, 2021, **1224**, 129195.

3. D. Liu, C. Li, C. Zhao, Q. Zhao, T. Niu, L. Pan, P. Xu, F. Zhang, W. Wu and T. Ni, *Chemical Engineering Journal*, 2022, **438**, 135623.

4. Y. Zhao, R. Li, L. Mu and C. Li, *Cryst Growth Des*, 2017, **17**, 2923–2928.

5. T. Ni, Z. Yang, H. Zhang, L. Zhou, W. Guo, L. Pan, Z. Yang, K. Chang, C. Ge and D. Liu, *J Colloid Interface Sci*, 2022, **615**, 650–662.

6. Z. Zhang, W. Wang, L. Wang and S. Sun, *ACS Appl Mater Interfaces*, 2012, **4**, 593–597.

7. U. G. Akpan and B. H. Hameed, *J Hazard Mater*, 2009, **170**, 520–529.

8. D. Liu, H. Li, R. Gao, Q. Zhao, Z. Yang, X. Gao, Z. Wang, F. Zhang and W. Wu, *J Hazard Mater*, 2021, **406**, 124309.

9. T. Aarthi and G. Madras, *Ind Eng Chem Res*, 2007, **46**, 7–14.

10. A. A. Faremi, P. A. Olubambi and S. S. Oluyamo, *Mater Lett*, 2022, **314**, 131868.

11. P. Patel, R. G. Solanki, P. Gupta, KM Sujata and B. Balachandran, *MRS Adv*, 2023, **8**, 960–968.

12. B. Barman and P. K. Kalita, *Opt Mater (Amst)*, 2023, **138**, 113642.

13. A. Saxena, W. Liyanage, J. Masud, S. Kapila and M. Nath, *J Mater Chem A Mater*, 2021, **9**, 7150–7161.

14. Q. Shu, W. Qiu, M. Luo and L. Xiao, *Materials Today Sustainability*, 2022, **17**, 100094.

15. S. Sonia, P. S. Kumar, D. Mangalaraj, N. Ponpandian and C. Viswanathan, *Appl Surf Sci*, 2013, **283**, 802–807.

16. H. Sun, S. Liu, G. Zhou, H. M. Ang, M. O. Tadé and S. Wang, *ACS Appl Mater Interfaces*, 2012, **4**, 5466–5471.

17. K. Thakur and B. Kandasubramanian, *J Chem Eng Data*, 2019, **64**, 833–867.

18. S. Saxena, T. A. Tyson, S. Shukla, E. Negusse, H. Chen and J. Bai, *Appl Phys Lett*, 2011, **99**, 013104.

19. W. Liu, J. Cai and Z. Li, *ACS Sustain Chem Eng*, 2015, **3**, 277–282.

20. B. Liu, X. Liu, J. Liu, C. Feng, Z. Li, C. Li, Y. Gong, L. Pan, S. Xu and C. Q. Sun, *Appl Catal B*, 2018, **226**, 234–241.

21. Y.-L. Chen, Z.-A. Hu, Y.-Q. Chang, H.-W. Wang, Z.-Y. Zhang, Y.-Y. Yang and H.-Y. Wu, *The Journal of Physical Chemistry C*, 2011, **115**, 2563–2571.

22. S. D. Perera, R. G. Mariano, K. Vu, N. Nour, O. Seitz, Y. Chabal and K. J. Balkus, *ACS Catal*, 2012, **2**, 949–956.

23. J. Zhang, K. Sun, A. Kumbhar and J. Fang, *The Journal of Physical Chemistry C*, 2008, **112**, 5454–5458.

24. S. Pan and X. Liu, *J Solid State Chem*, 2012, **191**, 51–56.

25. C. Xu, X. Wang and J. Zhu, *The Journal of Physical Chemistry C*, 2008, **112**, 19841–19845.

26. Q. Li, B. Guo, J. Yu, J. Ran, B. Zhang, H. Yan and J. R. Gong, *J Am Chem Soc*, 2011, **133**, 10878–10884.

27. M. Gao, X. Wu, H. Qiu, Q. Zhang, K. Huang, S. Feng, Y. Yang, T. Wang, B. Zhao and Z. Liu, *RSC Adv*, 2018, **8**, 20661–20668.

28. M. Chandra, K. Bhunia and D. Pradhan, *Inorg Chem*, 2018, **57**, 4524–4533.

29. J. F. Moulder and Jill. Chastain, *Handbook of x-ray photoelectron spectroscopy: a reference book of standard spectra for identification and interpretation of XPS data*, Physical Electronics Division, Perkin-Elmer Corp., 1992.

30. Z. Zhu, Z. Li, X. Xiong, X. Hu, X. Wang, N. Li, T. Jin and Y. Chen, *J Alloys Compd*, 2022, **906**, 164316.

31. J. Tauc, R. Grigorovici and A. Vancu, *physica status solidi (b)*, 1966, **15**, 627–637.

32. J. Yaseen, F. Saira, M. Imran, M. Fatima, H. E. Ahmed, M. Z. Manzoor, M. Rasheed, I. Nisa, K. Mehmood and Z. Batool, *RSC Adv*, 2024, **14**, 6896–6905.

33. P. Madhusudan, J. Zhang, B. Cheng and G. Liu, *CrystEngComm*, 2013, **15**, 231–240.

34. M. Nouri, R. Yousefi, N. Zare-Dehnavi and F. Jamali-Sheini, *Colloids Surf A Physicochem Eng Asp*, 2020, **586**, 124196.

35. R. Dhahiya, N. Chauhan and A. Kumar, *physica status solidi (a)*, 2024, **221**, 2300638.

36. Q. Yang, X. Guo, W. Wang, Y. Zhang, S. Xu, D. H. Lien and Z. L. Wang, *ACS Nano*, 2010, **4**, 6285–6291.

37. H. Zhang, B. Gao, B. Sun, G. Chen, L. Zeng, L. Liu, X. Liu, J. Lu, R. Han, J. Kang and B. Yu, *Appl Phys Lett*, 2010, **96**, 123502.

38. İ. Taşçıoğlu, U. Aydemir and Ş. Altındal, *J Appl Phys*, DOI:10.1063/1.3468376.

39. I. Ullah, M. Shah, M. Khan and F. Wahab, *J Electron Mater*, 2016, **45**, 1175–1183.

40. M. Soylu and B. Abay, *Physica E Low Dimens Syst Nanostruct*, 2010, **43**, 534–538.

41. M. Das, J. Datta, A. Dey, R. Jana, A. Layek, S. Middya and P. P. Ray, *RSC Adv*, 2015, **5**, 101582–101592.

42. M. Das, J. Datta, R. Jana, S. Sil, S. Halder and P. P. Ray, *New Journal of Chemistry*, 2017, **41**, 5476–5486.

43. D. Liu, C. Li, T. Ni, R. Gao, J. Ge, F. Zhang, W. Wu, J. Li and Q. Zhao, *Appl Surf Sci*, 2021, **555**, 149677.

44. I. Zamudio-Torres, E. Ramírez-Morales, G. Pérez-Hernández, M. G. Hernández-Cruz and L. Rojas-Blanco, *Desalination Water Treat*, 2022, **266**, 276–283.

45. S. Khanchandani, S. Kundu, A. Patra and A. K. Ganguli, *The Journal of Physical Chemistry C*, 2013, **117**, 5558–5567.

46. J.-M. Herrmann, *Catal Today*, 1999, **53**, 115–129.

47. T. Liu, L. Wang, X. Lu, J. Fan, X. Cai, B. Gao, R. Miao, J. Wang and Y. Lv, *RSC Adv*, 2017, **7**, 12292–12300.

48. D. K. Padhi and K. Parida, *J. Mater. Chem. A*, 2014, **2**, 10300–10312.

49. L. Huang, F. Peng, H. Yu and H. Wang, *Solid State Sci*, 2009, **11**, 129–138.

50. M. Wang, L. Sun, Z. Lin, J. Cai, K. Xie and C. Lin, *Energy Environ Sci*, 2013, **6**, 1211.

51. H. Wang, Y. Wu, P. Wu, S. Chen, X. Guo, G. Meng, B. Peng, J. Wu and Z. Liu, *Front Mater Sci*, 2017, **11**, 130–138.

52. Z. Zhang, S. Zhai, M. Wang, H. Ji, L. He, C. Ye, C. Wang, S. Fang and H. Zhang, *J Alloys Compd*, 2016, **659**, 101–111.

***

Summary and Future Outlook

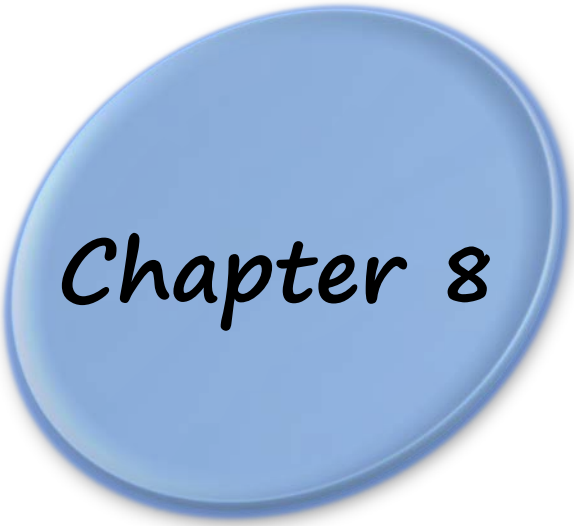

8.1. Summary

In the culmination of this thesis, which consists of seven comprehensive chapters, we have meticulously explored various facets of materials science, with a particular focus on charge transport kinetics and photocatalytic degradation—areas that remain relatively underexplored. Despite the extensive scope of materials science, our endeavour aimed to effectively communicate our experimental findings and the underlying rationale for these results through a systematic examination presented across the seven chapters.

The significance of carbon nanomaterials like graphene and carbon nanotube as versatile materials with multifaceted applications has been widely acknowledged within the contemporary scientific community. Over the past decade, extensive research has elucidated its considerable potential; however, numerous aspects remain to be explored. Consequently, a thorough understanding of carbon materials properties is essential for their effective application across various domains, including solar cells, supercapacitors, and photocatalysis. In this endeavour, we sought to achieve a comprehensive understanding of reduced graphene oxide (rGO) and carbon nanotube (CNT), encompassing the production methods of graphene, reduction techniques of graphene oxide, and the integration of CNT and rGO with other semiconductor compounds.

Our investigation was motivated by a significant gap in the literature regarding the direct interpretation of the conductivity and mobility of carbon nanomaterials (GO, rGO and CNT). Although numerous studies have examined carbon composites for various photo-induced applications, the underlying reasons for the unique characteristics of graphene oxide and CNT remain unaddressed. By elucidating these fundamental aspects, we aimed to provide researchers with a scientific and strategic framework for the application of carbon nanocomposites across diverse fields.

Central to our research was the exploration of the applicability of carbon nanomaterials in composite materials and their potential benefits. Prior to application, we aimed to extract charge transport parameters, particularly the mobility (μ) of charge carriers. This required the fabrication of metal-semiconductor junction-based Schottky diodes utilizing the synthesized materials. By analyzing current-voltage (I-V) characteristics and applying thermionic emission (TE) theory, we estimated the mobility and lifetime or transit times (τ) of charge carriers. These parameters were critical in assessing the efficacy of integrating carbon nanomaterials into various photo-induced applications, particularly in the decolorization of dye wastewater. Our investigation

further encompassed the degradation of wastewater utilizing two distinct carbon nanomaterials in conjunction with two different copper-based nanocomposites: the synthesis of carbon nanotube-copper sulfide composites (CNT-CuS) and reduced graphene oxide-copper selenide composites (rGO-CuSe). However, prior to the application of these materials, a foundational understanding of carbon and its derivatives, as well as copper nanomaterials and their composites, was essential. Therefore, in Chapter 1, we provided an extensive overview of these materials, thereby establishing the groundwork for our subsequent analyses.

In Chapter 2, we present a theoretical overview of various characterization techniques. Furthermore, we conducted a comprehensive exploration of Schottky barrier diodes (SBDs), encompassing their theoretical principles, fabrication techniques, and insights into electrical properties, as well as impedance spectroscopy. This chapter offers a thorough understanding of SBDs, ranging from their theoretical foundations to practical applications, thereby establishing a framework for further analysis.

In Chapter 3, we synthesized copper-based chalcogenide, specifically Copper Sulfide (CuS), utilizing two distinct methods. The structural, optical, and electrical properties of the materials were thoroughly analyzed. Schottky barrier diodes were fabricated, and the charge transport properties were examined through current-voltage measurements and impedance spectroscopy. We estimated the mobility (μ) and transit times (τ) of the charge carriers. The particle size and crystallinity resulting from the different synthesis methods significantly enhance device performance and charge transport. This highlights the charge transport characteristics of CuS-based photovoltaic devices and provides a deeper understanding of the synthesis procedure-dependent conduction mechanisms. In this chapter, we demonstrate that the solvothermally synthesized nanomaterial exhibited superior charge transport properties compared to the co-precipitation synthesis method.

Continuing our exploration, Chapter 4 concentrated on the investigation of carbon nanotube-copper sulfide (CNT-CuS) nanocomposites, with the objective of enhancing charge transfer in optoelectronic devices. Employing an equivalent circuit model, we analyzed the metal-semiconductor interfaces, illuminating the complex interplay between materials and charge transfer mechanisms.

In Chapter 5, we explored the influence of elevated carrier mobility in carbon nanotube-copper sulfide (CNT-CuS) nanocomposites on efficient charge transfer and the photodecomposition of Rhodamine B (RhB). Through a comprehensive analysis of the structural, optical, and electrical properties, we elucidated the underlying mechanisms that govern charge transport and photocatalytic activity within these nanocomposites. We examined the dynamics of charge transport and emphasized the significance of enhanced carrier mobility in the photocatalytic degradation of RhB. Our findings indicated that the CNT composite demonstrated superior photocatalytic activity compared to bare CuS under visible-light irradiation. This improved performance was attributed to the elevated mobility of the carbon nanotube-based composite, which facilitates the rapid movement of photoinduced charges between active sites and target molecules during the degradation process.

Chapter 6 presented an analysis of the charge transport properties of reduced graphene oxide-copper selenide (rGO-CuSe) based Schottky diodes, achieved by varying the rGO content on bare CuSe substrates. The performance of the fabricated diodes was evaluated through the incorporation of different weight percentages of rGO. Space charge limited current theory was employed to ascertain various charge transport properties, including carrier mobility, transit time, and diffusion length, thereby offering valuable insights for the advancement of electronic device applications.

In Chapter 7, we examined the influence of elevated carrier mobility in reduced graphene oxide-copper selenide (rGO-CuSe) nanocomposites on rapid charge transfer and the visible-light-driven degradation of Methylene Blue dye. Through the application of various material characterization techniques, we acquired a comprehensive understanding of the structural, optical, and electrical properties of these heterostructures, thereby elucidating their potential applications in wastewater treatment. We explored the dynamics of charge transport and emphasized the significance of enhanced carrier mobility in the photocatalytic degradation of Methylene Blue. Our findings demonstrated that the graphene composite exhibited superior photocatalytic activity in comparison to bare copper selenide under visible-light irradiation. Key microscopic parameters, such as charge carrier mobility and transit time, were identified as critical determinants influencing catalytic activity. This improved performance was attributed to the superior mobility of the graphene-based composite,

which facilitated the rapid transport of photoinduced charges between active sites and target molecules during the degradation process.

In conclusion, this thesis seeks to advance the dynamic field of materials science by elucidating the complexities of carbon composites and copper-based semiconducting nanomaterials. Employing a multidisciplinary approach that integrates theoretical insights, experimental investigations, and advanced characterization techniques, this work aspires to facilitate the development of novel materials with improved functionalities and applications across a range of disciplines.

8.2. Future Outlook

We intend to expand our research to delve deeper into the various conduction mechanisms of Schottky contacts, emphasizing the critical importance of precise understanding regarding the Schottky interface. Charge transport properties is influenced by the shape and the size of the materials. In the other case the heterostructure of two materials can improve the charge transfer kinetics. As the charge transport parameters affect the photo catalytic degradation process our further investigation will about the shape dependent and heterostructure based photo catalytic degradation of some azo and non azo dyes for wastewater treatments.

➲ ***Shape dependent photocatalytic activity of copper-based chalcogenides***

The physical and chemical properties of micro- and nano-materials are significantly influenced by their geometrical shapes and crystallographic planes. In recent years, extensive efforts have been dedicated to developing effective strategies for the synthesis of various morphologies of copper-based nano crystals, including cubic, octahedral, and rhombic dodecahedral forms. The atomic arrangement on the surface of these inorganic compounds plays a crucial role in determining their crystal shapes, which, in turn, significantly influences the photocatalytic activity. Different shape like spherical, cubic, rod like, nanowire have different specific surface area. These shape-dependent particles have different charge transport parameters like carrier mobility and transit time; the impact of these parameters upon the degradation process should be investigated further.

➲ ***Metal oxide-rare earth materials heterostructure for photocatalytic degradation***

Metal oxides are extensively employed as electrode materials for the detection of various substances. Zirconium oxide (ZrO_2), a type of metal oxide characterized by a fluorite structure, can be functionalized with phosphonic acid groups and utilized as an electron transport layer. Additionally, it exhibits remarkable chemical stability and high mechanical strength, rendering it suitable for applications in machinery, electronics, biomedicine, and chemistry. Lanthanum-doped ZrO_2 is a significant material with various applications, including use in electronic devices, thermal barrier coatings, photoluminescence, and electrochemical detection. When the doped cations possess a larger ionic size and high ionic character, they typically serve as stabilizers. Lanthanum oxide (La_2O_3), a prominent member of the rare earth oxide family. The ionic radius of La^{3+} is larger than that of Zr^{4+}, making lanthanum oxide (La_2O_3) an effective stabilizer for ZrO_2. Doping allows trivalent rare earth ions to occupy cation positions within zirconium oxide. This process generates specific oxygen vacancies, which subsequently enhance conductivity. The enhancement in conductivity is dependent on various charge transport parameters which have a pivotal role in the photo catalytic degradation process. So, La doped ZrO_2 should be a better candidate for the photocatalytic degradation.

The primary objectives of this research endeavour are to enhance the understanding of charge transport mechanisms in shape-dependent copper chalcogenides and oxides, as well as in rare earth material-doped metal oxide-based Schottky diode devices. This will be achieved through advanced characterization techniques, with the ultimate aim of optimizing device performance for a range of electronic and optoelectronic applications.

***

List of Publications, Conference and Workshop

List of Publications

▪ Journal Publications

1. "Investigation of particle size-dependent charge transport phenomena in copper sulphide (CuS) synthesized via solvothermal and co-precipitation methods" - **Mainak Das,** Dhananjoy Das, Ramjan Sk, Supravat Ghosh, Partha Pratim Ray; Optical Materials, 156 (2024): 115916.

2. "Investigation of charge transfer in optoelectronic devices: a study of carbon nanotube-copper sulfide nanocomposites using equivalent circuit models for metal–semiconductor interfaces" - **Mainak Das**, Dhananjoy Das, Supravat Ghosh, Ramjan Sk, Animesh Biswas and Partha Pratim Ray; Journal of Materials Science: Materials in Electronics, 35 (2024): 1143.
3. "Development of hierarchical copper sulfide-carbon nanotube (CuS-CNT) composites and utilization of their superior carrier mobility in efficient charge transport towards photodegradation of Rhodamine B under visible light"- **Mainak Das**, Dhananjoy Das, Sayantan Sil, Partha Pratim Ray, *Nanoscale Advances*, 5 (2023): 3655-3663.

4. "Effect of Higher Carrier Mobility of the Reduced Graphene Oxide-Zinc Telluride Nanocomposite on Efficient Charge Transfer Facility and the Photodecomposition of Rhodamine B" - Dhananjoy Das, **Mainak Das**, Sayantan Sil, Puspendu Sahu, and Partha Pratim Ray; *ACS Omega*, 7 (2022): 26483-94.

5. "Investigating carrier mobility in hollow and mesoporous ZnSe/ZnTe heterostructures: microscopic observations of swift charge transfer and visible-light-driven dye decomposition"- Dhananjoy Das, **Mainak Das**, Saikat Shyamal, Sayantan Sil, Puspendu Sahu, Partha Pratim Ray, *Journal of Photochemistry and Photobiology A: Chemistry*, 449 (2024): 115421.

6. "Exploring reduced graphene oxide-zinc telluride nanocomposites for enhanced charge transfer in optoelectronic devices: a study of the metal–semiconductor interfaces via equivalent circuit model"- Dhananjoy Das, **Mainak Das**, Animesh Biswas, Puspendu Sahu, and Partha Pratim Ray, *Journal of Materials Science: Materials in Electronics,* 34 (2023): 1574.

7. "Investigating the effect of lead substitution on the optical, electrical, and photoresponse properties of Quasi-2D double perovskites"- Vishal Singh, **Mainak Das**, Krishnakanta Mondal, Sourabh Barua, Dirtha Sanyal, Partha Pratim Ray, Joydeep Dhar, Journal of Physics and Chemistry of Solids, 192 (2024): 112082.

8. "Comparison of Electrical Conductivity and Schottky Behavior of 4-[2-(9-anthryl) vinyl] pyridine Based Two 1D Coordination Polymers of Zn (II) and Cd (II)" - Ersad Hossain, Ramjan Sk, **Mainak Das**, Joydeb Goura, Sourav Roy, Partha Pratim Ray, Mohammad Hedayetullah Mir, Antonio Frontera, Subrata Mukhopadhyay; *European Journal of Inorganic Chemistry*, 27 (2024): e202300736.

9. "Fabrication and Characterization of Metal/Semiconductor Junction Devices Using Four Benzaldehyde Derivatives" - Prantika Das, **Mainak Das**, Partha Pratim Ray, Saikat Kumar Seth; *ChemistrySelect*, 9 (2020): e202303361.

10. "Application of a distinctly bent, trinuclear, end-to-end azide bridged, mixed valence cobalt (iii/ii/iii) complex in the fabrication of photosensitive Schottky barrier diodes" - Sudip Bhunia, **Mainak Das**, Snehasis Banerjee, Michael GB Drew, Partha Pratim Ray, Shouvik Chattopadhyay; *RSC advances*, 14 (2024): 11185-11196.

11. "Development of a novel Cd(II) metal complex for solvent-sensitive detection of Zn(II) and Mg(II) with the formation of Cd(II)–Zn(II)/Cd(II)–Mg(II) complexes and their application in effective Schottky devices" - Dibyendu Sathapat, **Mainak Das**, Manik Das, Uttam Kumar Das, Arijit Bag, Soumik Laha, Partha Pratim Ray, Bidhan Chandra Samanta, Tithi Maity; *New Journal of Chemistry*, 48 (2024): 1837-1849.

12. "An experimental approach to ensure energy quenching and fluorescence resonance energy transfer of excitons from P3HT to CuInSe2" - Animesh Biswas, Baishakhi Pal, **Mainak Das**, Ramjan Sk, Animesh Layek, Partha Pratim Ray; *Materials Letters*, 338 (2023): 134066.

13. "Magnetic and Electric Properties of Pyrazole-Based Metal–Organic Frameworks Grafted With a Sulfonic Moiety" - Sayan Saha, **Mainak Das**, Krishna Sundar Das, Raktim Datta, Sukhen Bala, Jun-Liang Liu, Partha Pratim Ray, Raju Mondal; *Crystal Growth & Design*, 23 (2023): 1104-1118.

14. "The synthesis and combined electrical–magnetic and toxic dye sequestration properties of a Cr (iii)-metallogel" - Krishna Sundar Das, **Mainak Das**, Sayan Saha, Amit Adhikary, Sukhen Bala, Partha Pratim Ray, Raju Mondal; *Materials Advances*, 4 (2023): 6367-6380.

15. "Harnessing the hydrogen evolution reaction (HER) through the electrical mobility of an embossed Ag (i)-molecular cage and a Cu (ii)-coordination polymer" - Ananya Debnath, Sangharaj Diyali, **Mainak Das**, Subhra Jyoti Panda, Debasish Mondal, Debasis Dhak, Chandra Shekhar Purohit, Partha Pratim Ray, Bhaskar Biswas; *Dalton Transactions*, 52 (2023): 8850-8856.

16. "Schottky Device Fabrication of Linear Dicarboxylato-Bridged Mn(II) and Co(II) Coordination Polymers: Experimental and Theoretical Insights" - Ersad Hossain, Ramjan Sk, **Mainak Das**, Partha Pratim Ray*****, Antonio Frontera*****, Mohammad Hedayetullah Mir*****, Subrata Mukhopadhyay; Crystal Growth & Design 24 (2024): 7597-7604.

17. "Combined experimental and theoretical studies of conformationally diverse (thio) semicarbazone-based semiconducting materials" - Anangamohan Panja, **Mainak Das**, Narayan Ch Jana, Paula Brandão, Rosa M Gomila, Joaquín Ortega-Castro, Antonio Frontera, Partha Pratim Ray; *CrystEngComm*, 25 (2023): 2133-2143.

18. "Supramolecular Framework-Driven Electrical Conductivities and Hydrogen Evolution Activities of Hybrid Nickel (II)–Cerium (IV) Complex Salts Cooperativity" - Sangharaj Diyali, Nilankar Diyali, **Mainak Das**, Mayank Joshi, Partha Pratim Ray, Md Selim Arif Sher Shah, Angshuman Roy Choudhury, Bhaskar Biswas; *Crystal Growth & Design*, 22 (2022): 7590-7602.

19. "Synthesis and crystal structures of two tri- and tetra-heterometallic Ni(II)–Mn(II)/Ni(II)–Co(III) complexes from two different Ni(II)-containing metalloligands: effective catalytic oxidase activity and Schottky device approach" - Manik Das, **Mainak Das**, Subham Ray, Uttam Kumar Das, Soumik Laha, Partha Pratim Ray, Bidhan Chandra Samanta, Tithi Maity; *New Journal of Chemistry,* 46 (2022); 21103-21114.

20. "Synthesis, characterization and multi-dimensional application approach for two distinctive tetra nuclear, first-time reported, Fe^{3+}/Hg^{2+} and Fe^{3+}/Cd^{2+} clusters from a new Fe^{3+} containing metalloligands" - Soumik Laha, Dibyendu Sathapathi, **Mainak Das**, Manik Das, Partha Pratim Ray, Arijit Bag, Bidhan Chandra Samanta, Uttam Kumar Das, Tithi Maity; New Journal of Chemistry, 46 (2022); 16730-16742.

21. "De novo synthesis of hybrid d–f block metal complex salts for electronic charge transport applications"- Shreya Mahato, Amit Mondal, **Mainak Das**, Mayank Joshi, Partha Pratim Ray, Angshuman Roy Choudhury, C Malla Reddy, Bhaskar Biswas; *Dalton Transactions*, 51 (2022); 1561-1570.

22. "Schottky Device Fabrication of Linear Dicarboxylato-Bridged Mn(II) and Co(II) Coordination Polymers: Experimental and Theoretical Insights" - Ersad Hossain, Ramjan Sk, **Mainak Das**, Partha Pratim Ray,* Antonio Frontera,* Mohammad Hedayetullah Mir,* and Subrata Mukhopadhyay; *Cryst. Growth Des.*, 24 (2024), 7597−7604.

▪ Conference Proceedings

1. “Investigation of the metal–semiconductor interface by equivalent circuit model in zinc phthalocyanine (ZnPc) based Schottky diodes and its charge transport properties”- Dhananjoy Das, **Mainak Das**, Puspendu Sahu, Partha Pratim Ray; *Materials Today: Proceedings*, (2023), In Press, Corrected Proof.

***

▪ List of Conferences Attended

1. "Hydrothermal synthesized copper sulfide (CuS) nanoparticles for fabrication of shottky diode and its photosensing applications" – participated in the ***Advances in smart materials, chemical & biochemical Engineering (CHEMSMART-22)***, organized By the Department of Chemical Engineering, National Institute of Technology Rourkela, Rourkela, India, on 16-18 December 2022.
2. "One-pot Hydrothermal Synthesis of Copper Sulfide (CuS) Nanoparticles and Fabrication of Shottky Diode for Photosensing Applications" - participated and presented in the ***International Conference on Nanotechnology: Opportunities & Challenges (ICNOC-2022)*****,** organized by the Department of Applied Sciences & Humanities, Faculty of Engineering & Technology, Jamia Millia Islamia, New Delhi, India on November 28-30, 2022.
3. "Improvement in device performance of copper sulfide (CuS) nanoparticles synthesized by hydrothermal method over the co-precipitation method"- presented in the ***7th International Conference on Nanoscience and Nanotechnology (ICONN-2023)*****,** organised by the Department of Physics and Nanotechnology, SRM Institute of Science and Technology, India, during March 27- 29, 2023.
4. "Development of copper sulfide-carbon nanotube (CuS-CNT) composites and utilization of its superior carrier mobility in efficient charge transport towards photodegredation of Rhodamine B under visible light" – presented in the a one-day seminar in ***"COMMEMORATION OF CENTENARY BIRTH ANNIVERSARY OF PROF. SHYAMAL SENGUPTA"***, organized by the Condensed Matter Physics Research Centre & Department of Physics, Jadavpur University, during February 7th , 2024.
5. "Investigation Of Charge Transport Properties Of RGO-CuSe-Based Schottky Diode By Tuning Graphene Content" - participated and presented in the ***68th DAE Solid State Physics Symposium(DAE SSPS 2024)***, organized by Bhava Atomic Research Centre Mumbai, Department od Atomic Energy, Goverenment of India, on December 18-22, 2024.

***

▪ Workshops Attended

1. "***1st DFT-M: Workshop/Hands-on-Training on Density Functional Theory Modelling of Materials: Nanoparticles, Thin Films, Unit cells using Quantum Espresso***"- organized by Centre for Advanced Computational Studies, New Delhi, India; during 14th September - 20th September 2023.
2. "***1st Workshop/Hands-on-Training on Rietveld Refinement of X-Ray Diffraction data (RRD) (using FullProf Software Package)***"- organized by Centre for Advanced Computational Studies, New Delhi, India; during 1st – 7th January 2024 via Online Mode.

***

Mainak Das.
30/04/2025

Publications, Conference and Workshop Certificates

Optical Materials 156 (2024) 115916

Contents lists available at ScienceDirect

Optical Materials

journal homepage: www.elsevier.com/locate/optmat

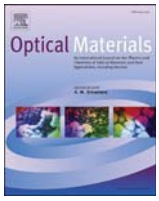

Research Article

Investigation of particle size-dependent charge transport phenomena in copper sulphide (CuS) synthesized via solvothermal and co-precipitation methods

Mainak Das, Dhananjoy Das, Ramjan Sk, Supravat Ghosh, Partha Pratim Ray *

Department of Physics, Jadavpur University, Kolkata, 700032, India

ARTICLE INFO

Keywords:
CuS nanoparticles (NPs)
Schottky diode (SD)
Electronic charge transport
Photo-response
Space charge limited current (SCLC)

ABSTRACT

In this present work, copper (II) sulfide (CuS) nanoparticles (NPs) were synthesized via co-precipitation [CuS(co-pr)] and solvothermal [CuS(solv)] methods. The structural, optical, and electrical properties of these materials were analyzed and compared. It was observed that the particle size and crystallinity varied depending on the synthesis method employed. Further, two individual metal-semiconductor junction devices based on CuS(co-pr) and (CuS(solv) were fabricated. Then the current vs. voltage (I–V) measurements were performed. The comparative study of the electrical parameters like photo response, rectification ratio, barrier height and ideality factor were performed between the two synthesized CuS NPs based devices. Under no light condition, the rectification ratio for CuS(solv) increased by 28 % more than that of CuS(co-pr). The photo response for CuS (solv) also enhanced by 146 %. For a better understanding of junction and carrier transport properties space charge limited current (SCLC) theory is incorporated. The interfacial resistance of the devices was studied by Nyquist plots obtained from the impedance spectroscopy and were also fitted by equivalent circuit model and explained the mechanism of charge transport through the Schottky interface. The transit time and carrier mobility were improved for CuS(solv) than CuS(co-pr). Thus, the solvothermally synthesized CuS-based device could be assigned as it possesses lesser number of lattice defects, better crystallinity and larger particle size along with its better film properties leading to better performance.

1. Introduction

Transition metal chalcogenides have garnered significant attention as electrode materials due to their exceptional chemical and physical properties. Notably, compounds such as CoS, MnS, NiS, and MoS_2 have been explored for their application in supercapacitors [1–4] and other electronic devices. Among these, copper sulfide (CuS), commonly known as 'covellite' stands out as a promising candidate owing to its low cost, abundance, and environmental friendliness [5]. CuS has demonstrated metal-like electronic conductivity and high theoretical capacity and finds utility in various optoelectronic devices and supercapacitors [6]. In recent years, copper sulfide (CuS) has emerged as an earth-abundant transition metal sulfide with several advantageous properties such as non-toxicity, high chemical stability, ease of regeneration, biocompatibility, and a unique optical property which encourages the preparation and study of CuS materials. CuS has a bandgap ranging from 1.3 eV to 2.4 eV [7] and is commonly utilized as a semiconducting material that exhibits a broad variety of application possibilities, including solar cells [8], gas sensors [9], supercapacitors [10], catalysts [11], field-effect transistors [12], memristors [13], and biosensors [14].

Numerous studies, including the reflux method [15], solvothermal [16], sol-gel [17], hydrothermal [18], sonochemical method [19], co-precipitation [20], and microwave-assisted method [21], have investigated the synthesis of this metal chalcogenide (CuS), and its applications in optoelectronic devices. For instance, Dutrizac et al. described a direct metal sulfurization technique involving the heating of copper and sulfur under vacuum at 450 °C [22]. Additionally, Y. Ni et al. utilized microwave irradiation to efficiently synthesize CuS nanoparticles (NPs) using $CuCl_2$ and Na_2S [23]. Armelao et al. introduced a novel method for CuS nanoparticle synthesis based on the fast nucleation of the sulfide by reacting thioacetic acid with water and copper carboxylates [24]. Other synthesis routes include thermolysis [25], physical vapor deposition [26], and template-assisted growth [27].

* Corresponding author.
E-mail address: parthapray@yahoo.com (P.P. Ray).

https://doi.org/10.1016/j.optmat.2024.115916
Received 16 June 2024; Received in revised form 28 July 2024; Accepted 1 August 2024
Available online 5 August 2024
0925-3467/© 2024 Elsevier B.V. All rights are reserved, including those for text and data mining, AI training, and similar technologies.

J Mater Sci: Mater Electron (2024) 35:1143

Investigation of charge transfer in optoelectronic devices: a study of carbon nanotube-copper sulfide nanocomposites using equivalent circuit models for metal–semiconductor interfaces

Mainak Das[1], Dhananjoy Das[1], Supravat Ghosh[1], Ramjan Sk[1], Animesh Biswas[1,2], and Partha Pratim Ray[1,*]

[1] *Department of Physics, Jadavpur University, Kolkata 700032, India*
[2] *Department of Physics, Sreegopal Banerjee College, Mogra, Hooghly 712148, India*

Received: 4 April 2024
Accepted: 1 June 2024
Published online: 14 June 2024

© The Author(s), under exclusive licence to Springer Science+Business Media, LLC, part of Springer Nature, 2024

ABSTRACT

This study outlines the synthesis of copper sulfide (CuS) nanoparticles and their composites with carbon nanotubes (T-CuS) via a solvothermal reaction. X-ray diffraction techniques were employed to characterize the crystal structure of the synthesized materials. Thin films of both CuS and T-CuS were deposited using vacuum coating techniques to construct Schottky devices. Atomic force microscopy (AFM) and field emission scanning electron microscopy (FESEM) were utilized to examine the topography and surface morphology of the deposited films, enabling analysis of metal–semiconductor (MS) junction formation. The interfacial characteristics of MS junctions in Al/CuS and T-CuS/ITO designs were investigated using AC impedance spectroscopy (IS) over a frequency range of 40 Hz to 10 MHz. Bias-dependent impedance spectroscopy within a ± 1.0 V range was conducted to determine the equivalent circuit for the MS junction Schottky diodes (SDs). Parameters such as on/off ratio, series resistance, ideality factor, and barrier height of the fabricated diodes were derived from current–voltage (*I*–*V*) characteristics. Additionally, characteristics related to charge transport, including photosensitivity and conductivity, were calculated. The results indicate an enhanced performance of carbon nanotube-based Schottky devices, likely attributed to the strong interaction and synergy between CNTs and CuS nanoparticles.

1 Introduction

In recent years, the usage of compound semiconductors in electronic and optoelectronic devices has witnessed a notable increase, primarily propelled by the growing demand for solar energy solutions [1]. Copper metal chalcogenide semiconductors, exemplified by copper oxide (CuO), copper selenide (CuSe), and copper telluride (CuTe), have garnered attention owing to their favorable attributes, encompassing low environmental

Address correspondence to E-mail: parthapray@yahoo.com

https://doi.org/10.1007/s10854-024-12876-y

Nanoscale Advances

ROYAL SOCIETY OF CHEMISTRY

PAPER

View Article Online
View Journal | View Issue

Check for updates

Cite this: *Nanoscale Adv.*, 2023, **5**, 3655

Development of hierarchical copper sulfide–carbon nanotube (CuS–CNT) composites and utilization of their superior carrier mobility in efficient charge transport towards photodegradation of Rhodamine B under visible light†

Mainak Das,[a] Dhananjoy Das,[a] Sayantan Sil[b] and Partha Pratim Ray *[a]

In this work, the synthesis of visible light sensitive copper sulfide (CuS) nanoparticles and their composites with carbon nanotubes (T-CuS) *via* a solvothermal technique is reported. The synthesized nanoparticles (NPs) and their composites were significantly characterized by powder X-ray diffraction (PXRD), scanning electron microscopy, transmission electron microscopy, X-ray photoelectron spectroscopy, UV-vis spectroscopy, photoluminescence (PL) spectroscopy and thermogravimetric analysis (TGA). The effect of carbon nanotubes (CNTs) on the crystallinity, microstructures, photo-absorption, photo-excitation, thermal stability and surface area of CuS was investigated. The current–voltage (*I vs. V*) characteristics of both CuS and T-CuS based Schottky diodes were measured to determine the charge transport parameters like photosensitivity, conductivity, mobility of charge carriers, and transit time. The photocatalytic performance of bare CuS and T-CuS in the decomposition of Rhodamine B dye was studied using a solar simulator. The T-CuS composite showed higher photocatalytic activity (94%) compared to bare CuS (58%). The significance of charge carrier mobility in transferring photo-induced charges (holes and electrons) through complex networks of composites and facilitating the photodegradation process is explained. Finally, the reactive species responsible for the Rhodamine B degradation were also identified.

Received 29th March 2023
Accepted 30th May 2023

DOI: 10.1039/d3na00204g

rsc.li/nanoscale-advances

Open Access Article. Published on 31 May 2023. Downloaded on 2/13/2025 12:01:50 PM.
This article is licensed under a Creative Commons Attribution-NonCommercial 3.0 Unported Licence.

Introduction

Organic dyes and pigments discharged into water sources, mostly by the paint and textile industries, are causing serious environmental issues and harming the ecosystem in other ways.[1] Over the last few decades, various biological and physicochemical experiments based on physical as well as chemical adsorption approaches have been conducted to decompose these industrial pollutants. However, these processes often produce secondary pollutants and are not cost-effective from the economic viewpoint.[2] The photocatalytic approach based on semiconductor materials has demonstrated significant efficiency in wastewater purification among all advanced oxidation techniques known to exist.[3] There are some well-known semiconducting photocatalysts, namely TiO_2 and ZnO, which have been widely used to decompose organic pollutants, but their use is hindered due to their wide range bandgaps, which are 3.2 eV and 3.37 eV for TiO_2 and ZnO, respectively, limiting their light absorption mainly in the ultraviolet (UV) region of the solar spectrum.[4,5] This reduces the redox reactions with the impurities and significantly affects the rate of degradation.[6]

On the other hand, copper(II) sulfide (CuS) has a narrow direct bandgap of 2.29 eV, due to which it can efficiently capture visible light from the solar spectrum, making it practically function as a 'visible-light-driven photocatalyst'. It also has excellent optical and electronic properties which show great potential in many fields like solar cells,[7] energy storage,[8] gas sensors,[9] biosensors[10] and photocatalysis.[11] Copper sulfide has some excellent features, such as its environmentally friendly and non-toxic nature, low cost, biocompatibility, higher physical and chemical stability and ease of recyclability which

[a]*Department of Physics, Jadavpur University, Kolkata 700032, India. E-mail: parthapray@yahoo.com*

[b]*Department of Physics, University of Engineering and Management, University Area, Action Area III, B/5, Newtown, Kolkata 700160, India*

† Electronic supplementary information (ESI) available: Device fabrication method, calculation of bandgap and dielectric constant, weight (%) test of CNT, charge transfer characteristics of CNT, adsorption of RhB by the catalysts, photodegradation process, function of H_2O_2 in the degradation process, optimization of the composite material with different CNT content, identification of reactive species, recycling test, photocatalytic activity of a non-azo dye, Fig. S1–S9, and eqn (S1) and (S2). See DOI: **https://doi.org/10.1039/d3na00204g**

© 2023 The Author(s). Published by the Royal Society of Chemistry

ACS OMEGA

http://pubs.acs.org/journal/acsodf

Article

Effect of Higher Carrier Mobility of the Reduced Graphene Oxide−Zinc Telluride Nanocomposite on Efficient Charge Transfer Facility and the Photodecomposition of Rhodamine B

Dhananjoy Das,[§] Mainak Das,[§] Sayantan Sil,[§] Puspendu Sahu,[§] and Partha Pratim Ray*[,§]

Cite This: *ACS Omega* 2022, 7, 26483−26494

Read Online

ACCESS | Metrics & More | Article Recommendations | Supporting Information

ABSTRACT: The synthesis of solar-light-responsive zinc telluride (ZnTe) nanoparticles and their composite with reduced graphene oxide (rGO−ZnTe) via a simple hydrothermal reaction is reported. The synthesized nanostructures were comprehensively characterized by a combination of X-ray diffraction and photoelectron spectroscopy, electron microscopy, UV−vis spectroscopy, photoluminescence spectroscopy and thermogravimetric analysis. The effects of graphene oxide on the crystallinity, microstructure, photo-excitation, light absorption, surface area and thermal stability of ZnTe were studied. The current−voltage (I−V) characteristics for both as-synthesized ZnTe and rGO−ZnTe composite-based Schottky devices were measured to estimate the charge transport parameters such as dc conductivity, photosensitivity, carrier's mobility and lifetime. The photocatalytic performance of both the materials in the degradation of an azo dye (Rhodamine B) was subsequently investigated using simulated solar light. The rGO−ZnTe composite exhibited a higher photocatalytic activity (66%) as compared to the as-synthesized ZnTe (23%), essentially due to the synergy between rGO sheets and ZnTe nanoparticles. The role of the carrier's mobility in the transportation of photo-induced charges (electrons and holes) through the complex network of the composite materials and thus facilitating the photo-degradation process is explained. In the end, the responsible reactive species for the decomposition of Rhodamine B was also interpreted.

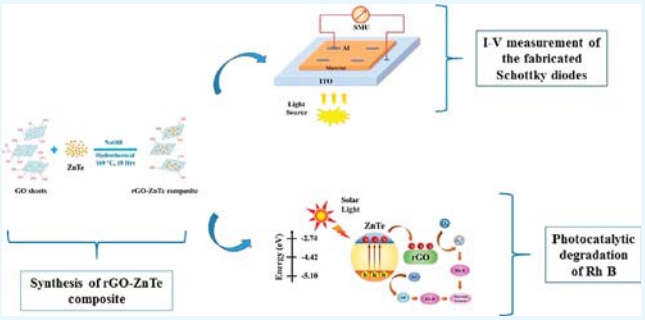

Downloaded via JADAVPUR UNIV on February 13, 2025 at 12:20:59 (UTC).
See https://pubs.acs.org/sharingguidelines for options on how to legitimately share published articles.

INTRODUCTION

Dye wastewater released into water bodies mainly by textile industries is becoming a major environmental concern, causing several ecological problems.[1] In the past few decades, different physicochemical and biological attempts based on chemical and physical adsorption techniques have been made to degrade these industrial effluents, but they are not cost-effective from an economical point of view and often produce secondary pollutants.[2] Among all advanced oxidation methods known to date, the photocatalytic route based on semiconducting materials has shown considerable efficiency in wastewater decontamination processes.[3] Thus far, a large number of compound semiconductors have been investigated for organic dye decomposition since they possess an excellent larger absorbance cross-section and higher environmental stability.[4] Although the semiconductor materials have excellent potential in the area of organic dye decolorization, they suffer from the shortcomings of having wide band gaps and a comparatively shorter life span of excitons, limiting the usage of these semiconductors in practical applications.[5] As an example, TiO_2, which is one of the most promising materials for the decomposition of many organic pollutants, responds only in the UV region of the electromagnetic spectrum, attributed to its wide band gap (∼3.2 eV).[6] This causes fewer redox reactions with the pollutants and detrimentally affects its degradation efficiency.[7]

On the other hand, zinc telluride (ZnTe), which is an important group II−VI compound semiconductor having a direct band gap of ∼2.26 eV, has shown immense potential in a wide range of applications in solar cells,[8] light-emitting diodes,[9] optoelectronic devices,[10] CO_2 reductions,[11] and in wastewater treatment.[12] The solution-processed ZnTe nanostructures demonstrate a few excellent features, namely, low production cost, large surface area, good environmental stability, excellent reusability and prominent visible-light absorption, which make them a prospective photocatalyst. However, they also have an inherent shortcoming that the fast electron (e^-)−hole (h^+) recombination in ZnTe nanomaterials is responsible for their weak photocatalytic performance, particularly under visible light irradiation. Several attempts were made to decrease the electron−hole recombination in these materials and thus

Received: April 20, 2022
Accepted: June 14, 2022
Published: July 23, 2022

ACS Publications

© 2022 The Authors. Published by American Chemical Society

J Mater Sci: Mater Electron (2023) 34:1574

Exploring reduced graphene oxide-zinc telluride nanocomposites for enhanced charge transfer in optoelectronic devices: a study of the metal–semiconductor interfaces via equivalent circuit model

Dhananjoy Das[1], Mainak Das[1], Animesh Biswas[1,2], Puspendu Sahu[1], and Partha Pratim Ray[1,*]

[1] *Department of Physics, Jadavpur University, Kolkata 700032, India*
[2] *Department of Physics, Sreegopal Banerjee College, Mogra, Hoogly 712148, India*

Received: 29 June 2023
Accepted: 10 July 2023
Published online: 24 July 2023

© The Author(s), under exclusive licence to Springer Science+Business Media, LLC, part of Springer Nature 2023

ABSTRACT

This study presents the synthesis of zinc telluride (ZnTe) nanoflakes and their composite with reduced graphene oxide (RGO-ZnTe) through a simple hydrothermal reaction. The crystal structure of the synthesized materials was characterized using X-ray Diffraction techniques. Subsequently, the Metal-Semiconductor (MS) based Schottky devices were fabricated by depositing the ZnTe and RGO-ZnTe thin films and Aluminium electrodes via vacuum coating methods. The surface morphology and topography of the deposited films were investigated using field emission scanning electron microscopy (FESEM) and atomic force microscopy (AFM) techniques, respectively, to study the formation of MS junctions. The interfacial properties of the MS junctions in the Al/ZnTe/ITO and Al/RGO-ZnTe/ITO configurations were analyzed using ac impedance spectroscopy over a frequency range of 50 Hz–10 MHz. Thereafter, the bias-dependent impedance spectrometry was also conducted within a voltage range of $\pm$ 0.6 V to establish the equivalent circuits for the fabricated MS junction Schottky diodes (SDs). The diode parameters, including on/off ratio, ideality factor, barrier height and series resistance were determined by measuring the current–voltage (*I–V*) characteristics of the fabricated SDs. Further, the charge transport parameters, such as dc conductivity and photosensitivity, were also estimated. The findings indicate that the Schottky devices based on the RGO-ZnTe composites exhibit enhanced device performance compared to those based on pristine ZnTe, attributed to the synergistic effects between the RGO sheets and ZnTe nanoflakes.

Address correspondence to E-mail: parthapray@yahoo.com

https://doi.org/10.1007/s10854-023-10978-7

Journal of Photochemistry & Photobiology, A: Chemistry 449 (2024) 115421

Contents lists available at ScienceDirect

Journal of Photochemistry & Photobiology, A: Chemistry

journal homepage: www.elsevier.com/locate/jphotochem

Investigating carrier mobility in hollow and mesoporous ZnSe/ZnTe heterostructures: Microscopic observations of swift charge transfer and visible-light-driven dye decomposition

Dhananjoy Das [a], Mainak Das [a], Saikat Shyamal [a], Sayantan Sil [b], Puspendu Sahu [a], Partha Pratim Ray [a,*]

[a] Department of Physics, Jadavpur University, Kolkata 700032, India
[b] Department of Physics, University of Engineering and Management, University Area, Action Area III, B/5, Newtown, Kolkata 700160, India

ARTICLE INFO

Keywords:
Semiconductor
Hydrothermal
Heterostructure
Schottky diode
Mobility
Photocatalysis

ABSTRACT

We report herein a one-pot hydrothermal approach to synthesize zinc selenide (ZnSe)/zinc telluride (ZnTe) heterostructures - a set of common cation-based photocatalysts. The crystal structure and phase purity of the heterostructures were verified by powder X-ray diffraction (PXRD) analysis, while field emission scanning electron microscopy (FESEM), transmission electron microscopy (TEM), and X-ray photoelectron spectroscopy (XPS) techniques were employed to study their morphology, microstructures, and surface electronic states, respectively. Notably, a detailed XPS analysis was conducted to discern the chemical species present on the surface of the photocatalyst, providing valuable insights into the compound's stability in an aqueous medium. Furthermore, the synthesized hybrid structures were utilized to fabricate Schottky barrier diodes, enabling a study of their electrical and dielectric properties using the Spatial-charge-limited conduction (SCLC) mechanism. The key charge transport parameters for all the photocatalysts, namely, carriers' mobility and transit time, influencing the photo response and consequently, dye degradation were estimated. Notably, the ZnSe/ZnTe heterostructure, comprising 50 % ZnSe and 50 % ZnTe, exhibited the highest mobility (3.36×10^{-6} S/m in the dark, increasing to 1.70×10^{-5} S/m in light) and proved to be the most effective photocatalyst for degrading Rhodamine B (with up to ~ 78 % degradation over 60 min of solar light irradiation) - underscoring the pivotal role of carriers' mobility in governing the photocatalytic activity. Moreover, the ZnSe/ZnTe heterostructure demonstrated a remarkable reduction in the photo-corrosion process, a key challenge affecting the photocatalytic activity of numerous materials. Our discussion highlighted the efficient separation of photoinduced electron-hole pairs in the ZnSe/ZnTe heterostructure, facilitated by the synergistic effects of ZnSe and ZnTe, leading to the achievement of the highest photocatalytic performance.

1. Introduction

Wastewater released by the textile industry is a major cause of ecological imbalances and environmental concerns. Azo dyes, commonly used in textile production, contain high levels of aromatic rings and strong colours, making them harmful and carcinogenic to both humans and animals [1]. In recent decades, various biological and physio-chemical methods have been adopted to degrade these complex dyes; however, many of these methods are not cost-effective and they often produce hazardous by-products [2]. Among the various Advanced Oxidation Processes (AOPs), photo-induced catalytic decomposition has garnered significant attention from researchers due to its economical and green approach to environmental remediation. Metal oxides and sulphides, including TiO_2 [3], ZnO [4], ZnS [5], CdS [6], ZnSe [7], WO_3 [8] and CeO_2 [9] have been employed to bleach the industrial effluents through photocatalytic decomposition methods. However, these single metal oxides or sulphides suffer from several shortcomings, such as a low surface-to-volume ratio, broad optical bandgaps, and short lifetimes of photo-generated electron-hole pairs that limit the number of excitons produced upon light illumination [10]. Even if the excitons are produced, their rapid recombination hinders an efficient degradation process. For example, ZnO, despite having a higher hydroxyl ion-generating

* Corresponding author.
E-mail address: parthap.ray@jadavpuruniversity.in (P. Pratim Ray).

https://doi.org/10.1016/j.jphotochem.2023.115421
Received 10 June 2023; Received in revised form 3 December 2023; Accepted 15 December 2023
Available online 17 December 2023
1010-6030/© 2023 Elsevier B.V. All rights reserved.

Materials Letters 338 (2023) 134066

Contents lists available at ScienceDirect

Materials Letters

journal homepage: www.elsevier.com/locate/matlet

An experimental approach to ensure energy quenching and fluorescence resonance energy transfer of excitons from P3HT to $CuInSe_2$

Animesh Biswas [a,b], Baishakhi Pal [a], Mainak Das [a], Ramjan Sk [a], Animesh Layek [a,*], Partha Pratim Ray [a]

[a] Department of Physics, Jadavpur University, Kolkata 700032, India
[b] Department of Physics, Sreegopal Banerjee College, Mogra, Hooghly 712148, India

ARTICLE INFO

Keywords:
Nanocomposite
Optical materials and properties
Absorption and emission spectra
Energy quenching
Stern-Volmer method
Förster's distance

ABSTRACT

This letter reports the paramount fluorescence resonance energy transfer mechanism for photo induced charge transfer from P3HT to solvothermally derived $CuInSe_2$. The HOMO (-4.85 eV) and LUMO (-3.38 eV) energy states of $CuInSe_2$ (electrical conductivity = 1.1x 10^{-7} Scm^{-1}) are determined from cyclic voltammetry and optical study. This HOMO-LUMO position agrees to select P3HT polymer as possible donor of excitons. Steady-state luminescence study of composite (P3HT:$CuInSe_2$) demonstrates possibility of successful charge transfer. Stern–Volmer analysis of absorption and emission spectroscopy ensures static energy quenching phenomena. The Förster distance (R_0) of critical energy transfer is estimated as 3.61 nm. The average distance between donor–acceptor (r_{avg} = 4.71 nm) is<8 nm and within the range $0.5R_0 < r < 1.5R_0$ (1.81 nm < r < 5.42 nm), which ensures energy transfer from P3HT to $CuInSe_2$.

1. Introduction

In recent past $CuInSe_2$ (CIS) composite and its application as electron acceptors in photovoltaics has become more popular because of its semiconductor nature with narrow band gap, non-toxicity, high reproducibility, tuneable optical energy gap, and good stability [1]. In order to attain higher performance of organic–inorganic solar cell, conjugated polymer like poly(3-hexylthiophene) (P3HT) is appreciated yet as electron donor. Extensive studied had been performed by several scientists and researchers on energy harvesting from the P3HT: $CuInSe_2$ composite based solar cells [2]. The understanding of underline physics of resonance energy transfer by quenching phenomena is an obvious commissioning task of charge transfer from donor to acceptor. However, the underline charge transport mechanism by fluorescence resonance energy transfer theory within this composite is not reported so far. Hence the field remain unexplored.

In this letter the solvothermally derived $CuInSe_2$ is composited with P3HT to study the state of quenching which is highly responsible for understanding the hopping of excitons from donor to acceptor [3]. Even though CIS's applications in Schottky diode has been reported earlier [4], perhaps this is the first approach to report the quenching phenomena and photo-induced charge transfer by utilizing FRET mechanism within the composite P3HT:$CuInSe_2$.

In this context, solvothermally derived CIS is characterized accordingly and the energy band positions are determined to find out the organic P3HT as appreciable donor with respect to CIS one. To get better insight the mechanism of energy quenching and the physics behind of hopping of excitons from donor to acceptor, the optical spectral (absorption and emission) analyses are performed pertinently. The analysis deserves a thorough inspection which is carried out by employing Stern-Volmer theory and Förster's equation for non-radiative energy transfer [5,6].

2. Materials & methods

Poly(3-hexylthiophene) (P3HT) purchased from Sigma-Aldrich. Flake like $CuInSe_2$ is derived by Solvothermal technique (reported elsewhere) [4].

FESEM and EDAX spectroscopy are performed with a FEI make Inspect F-50 scanning electron microscope equipped with energy-dispersive X-ray analysis system. Bruker D8 Advanced PXRD is used to record diffraction. The absorption spectra are obtained from Perkin Elmer Lambda 365 spectrophotometer. Fluorescence spectra are recorded via Perkin Elmer LS-45 fluorimeter. The electrical conductivity (σ) is

* Corresponding author.
E-mail address: alayek.physics@jadavpuruniversity.in (A. Layek).

https://doi.org/10.1016/j.matlet.2023.134066
Received 14 December 2022; Received in revised form 2 February 2023; Accepted 14 February 2023
Available online 16 February 2023
0167-577X/© 2023 Elsevier B.V. All rights reserved.

CRYSTAL GROWTH & DESIGN

pubs.acs.org/crystal

Article

Magnetic and Electric Properties of Pyrazole-Based Metal−Organic Frameworks Grafted With a Sulfonic Moiety

Published as part of a Crystal Growth and Design virtual special issue on Molecular Magnets and Switchable Magnetic Materials

Sayan Saha, Mainak Das, Krishna Sundar Das, Raktim Datta, Sukhen Bala, Jun-Liang Liu, Partha Pratim Ray,* and Raju Mondal*

Cite This: *Cryst. Growth Des.* 2023, 23, 1104−1118

Read Online

ACCESS | Metrics & More | Article Recommendations | Supporting Information

Downloaded via JADAVPUR UNIV on February 13, 2025 at 11:58:31 (UTC).
See https://pubs.acs.org/sharingguidelines for options on how to legitimately share published articles.

ABSTRACT: We report herein two multifunctional metal−organic frameworks (MOFs) that exhibit excellent mutually inclusive electrical and magnetic properties. Accordingly, two cobalt and nickel based MOFs (**Co-MOF**, **Ni-MOF**) were generated using a flexible bispyrazole based ligand and 2-sulphono terephthalic acid. The idea is to generate paramagnetic metal ion based magnetic MOFs, which can also be used to fabricate electrical devices by utilizing the immobilized free sulfonic groups and encapsulated H-bonded water clusters for active charge species generation and transportation. Further support comes from the intriguing structural features of the MOFs that include extensive H-bonded water clusters, free sulfonic acid moiety, or *syn-anti* bridged carboxylates, which make them highly suitable candidates for generating electrical and magnetic materials. Further complementary support for their candidature comes from the high thermal, chemical, and physical stability of the MOFs. The impedance spectroscopy data and *I*−*V* results unequivocally support the suitability of the MOFs for electronic device fabrication showing a befitting conductivity value of 1.80×10^{-4} S/m with an ideality factor of 1.06 for **Ni-MOF**. Interestingly, the **Co-MOF** shows a light-dependent behavior with conductivity values of 9.09×10^{-5} S/m (dark) and 6.31×10^{-4} S/m (light) and ideality factors of 0.78 (dark) and 0.92 (light). The MOFs, fitted with a free sulfonic acid moiety and extensive H-bonded water clusters, show high potential for proton exchange membrane fuel cells (PEMFCs) development with corroborating proton conductivity values of 1.95×10^{-3} S/cm and 5.80×10^{-4} S/cm for **Ni-MOF** and **Co-MOF**, respectively, at 95% relative humidity and 85 °C. Moreover, the interesting structural aspects like *syn-anti* bridged carboxylates prompt us to explore the magnetic behavior of the MOFs. The **Ni-MOF** shows some interesting antiferromagnetic behavior. The **Co-MOF** reveals intriguing single molecule magnet behavior with a U_{eff} value of 34 K and moderate relaxation time of 3.5×10^{-8} s.

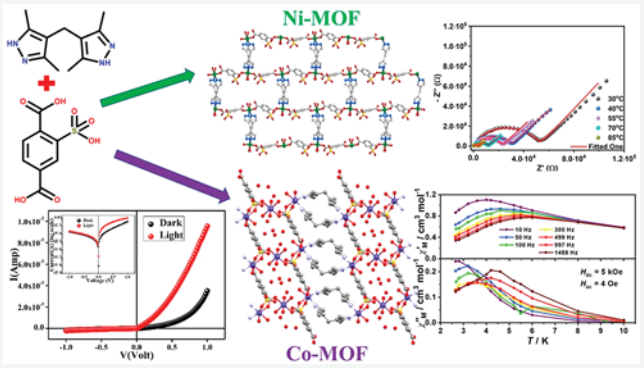

INTRODUCTION

Notwithstanding their unprecedented fanfare as the next big thing in the field of alternative energy, metal−organic frameworks (MOFs) remain a highly interesting class of multifunctional inorganic polymeric materials.[1] The unique blend of mutually inclusive features of inorganic chemistry, polymer science, and porous materials makes a paradigm shift for MOFs, in terms of exploiting the same benefits of precise and meticulous synthetic fundamentals but diversifying the outlook of commercial or industrial interests with a widening range of applications encompassing catalysis, magnetism, sensing, electrical device fabrications, biomedical utilities.[2−4] In the early years, the researchers, in pursuit of porous absorbent materials, were more interested in optimizing and improving the physical features of MOFs like pore size, surface area, dimensionality, or topology.[5] Subsequently, the investigations were more focused on the resultant empty space or the surface features of the network and less on what these networks were actually made of, viz., the organic functional groups of the linker and nodal metal ions.[6] Ironically, the fates of traditional inorganic compounds mostly depend on the characteristic features of the comprising metal ions and organic functional groups and their mutual interactions.[7] Coincidently,

Received: October 31, 2022
Revised: December 22, 2022
Published: January 17, 2023

ACS Publications

© 2023 American Chemical Society

https://doi.org/10.1021/acs.cgd.2c01251
Cryst. Growth Des. 2023, 23, 1104−1118

Journal of Physics and Chemistry of Solids 192 (2024) 112082

Contents lists available at ScienceDirect

Journal of Physics and Chemistry of Solids

journal homepage: www.elsevier.com/locate/jpcs

Investigating the effect of lead substitution on the optical, electrical, and photoresponse properties of Quasi-2D double perovskites

Vishal Singh [a], Mainak Das [b], Krishnakanta Mondal [c], Sourabh Barua [d], Dirtha Sanyal [e,f], Partha Pratim Ray [b,**], Joydeep Dhar [a,*]

[a] Department of Chemistry, Birla Institute of Technology, Mesra, Ranchi, 835215, India
[b] Department of Physics, Jadavpur University, Kolkata, 700032, India
[c] Department of Physics and Astrophysics, University of Delhi, New Delhi, 110007, India
[d] Department of Physics, Central University of Punjab, Bathinda, 151401, India
[e] Variable Energy Cyclotron Centre, 1/AF, Bidhannagar, Kolkata, 700064, India
[f] Homi Bhabha National Institute, Training School Complex, Anushakti Nagar, Mumbai, 400094, India

ARTICLE INFO

Keywords:
A. semiconductors
C. positron annihilation spectroscopy D. defects
D. optical properties D. electrical properties

ABSTRACT

Quasi-2-dimensional (2D) halide perovskites have recently attracted attention due to their higher operational stability as alternatives to 3-dimensional (3D) perovskites having exceptional optoelectronic and charge transport properties. To reduce the lead content, here following the double perovskite approach lead is substituted with silver and bismuth simultaneously, and three quasi-2D perovskites, with general formula $(C_7H_{10}N)_2Pb_{(1-2x)}Ag_xBi_xBr_4$, ($0 \leq x \leq 0.5$) were prepared. The optical studies show that the partially lead substituted sample has the lowest optical band gap, aptly supported by the theoretical calculations. The powder X-ray diffraction technique along with field-emission scanning electron microscopy suggests enhancement in crystallinity along with the decrease in grain boundaries with the substitution of lead. The improvement in crystallinity with concomitant reduction in grain boundaries has led to the decrease in point defects as identified from the positron annihilation lifetime spectroscopy and coincidence Doppler broadening analysis. The tuned band gap, improved crystal quality along with lower defects jointly contributed to the enhancement in electrical properties of the perovskites with varying lead percentages. Finally, the photoresponse of all the materials was studied after fabricating metal (Al)-semiconductor (MS) junction thin film photodetector devices.

1. Introduction

In the past decade, organometal halide perovskites have garnered increasing attention in optoelectronic devices since the first report of solar cell fabrication using methylammonium lead iodide ($MAPbI_3$) by Miyasaka & co-workers in 2009 [1]. As per the latest reports of the National Renewable Energy Laboratory (NREL), the photon-to-current conversion efficiency of perovskite solar cells has reached 26.1 % [2]. These active materials have become one of the top choices in the field of optoelectronic and electronic devices because they come with the benefits of having long carrier diffusion length, high carrier mobility, band gap tunability with high light absorption coefficient, high photoluminescence quantum yield, low exciton binding energies, low trap densities and thus minimal non-radiative recombination [3,4]. Also, the ease of fabrication in the solution phase along with the requirement of low-temperature processability makes it an excellent choice for device manufacturing [5].

The most studied 3D organometal halide perovskites are of the type ABX_3, with A being a monovalent organic or inorganic cation occupying the corner of a unit cell with a divalent metal cation B and six halide anion (X^-) forming an octahedron, positioning at the body center and the face center positions within an ideal cubic lattice, respectively [6]. Despite all the beneficial features suitable for commercialization, these 3D perovskites are yet to be realized due to the degradation this class of material suffers. Organo metal hybrid perovskite easily decomposes as the large organic cations like methylammonium (MA^+), formamidinium (FA^+) show poor stability against external environmental stimuli due to the hygroscopic nature of the ammonium salt incorporated in the

* Corresponding author.
** Corresponding author.
E-mail addresses: parthap.ray@jadavpuruniversity.in (P.P. Ray), joydeepdhar@bitmesra.ac.in (J. Dhar).

https://doi.org/10.1016/j.jpcs.2024.112082
Received 21 February 2024; Received in revised form 13 April 2024; Accepted 2 May 2024
Available online 6 May 2024
0022-3697/© 2024 Elsevier Ltd. All rights are reserved, including those for text and data mining, AI training, and similar technologies.

RSC Advances

PAPER

View Article Online
View Journal | View Issue

Check for updates

Cite this: *RSC Adv.*, 2024, **14**, 11185

Application of a distinctly bent, trinuclear, end-to-end azide bridged, mixed valence cobalt(III/II/III) complex in the fabrication of photosensitive Schottky barrier diodes†

Sudip Bhunia, [a] Mainak Das, [b] Snehasis Banerjee, [c] Michael. G. B. Drew,[d] Partha Pratim Ray *[b] and Shouvik Chattopadhyay *[a]

A mixed-valence trinuclear cobalt(III)-cobalt(II)-cobalt(III) complex, $[(\mu\text{-}1,3\text{-}N_3)Co_3L(N_3)_3]\cdot MeOH$ has been synthesized using a tetradentate N_2O_2 donor 'reduced Schiff base' ligand, H_2L {1,3-bis(2-hydroxybenzylamino)2,2-dimethylpropane} and azide as anionic co-ligand. The complex has been characterised by elemental analysis, IR, UV-vis spectroscopy and single-crystal X-ray diffraction studies *etc.* The cobalt(III)-cobalt(II)-cobalt(III) skeleton in the complex is non-linear and non-centrosymmetric. The redox behavior of the complex was studied by using Cyclic Voltammetry (CV). The complex is found to be a semiconductor material as confirmed by determining the band gap of this complex by experimental as well as theoretical studies. The band gap in the solid state has been determined experimentally. The conductivity of the synthesized complex based device improves considerably in illumination conditions from the non-illuminated conditions. The complex has also been used to fabricate Schottky barrier diodes.

Received 23rd February 2024
Accepted 16th March 2024

DOI: 10.1039/d4ra01406e

rsc.li/rsc-advances

Open Access Article. Published on 08 April 2024. Downloaded on 2/13/2025 11:51:22 AM.
This article is licensed under a Creative Commons Attribution-NonCommercial 3.0 Unported Licence.

Introduction

Many di- and poly-nuclear complexes of transition and non-transition metals have interesting photochemical and photophysical properties, with potential applications in light-emitting diodes, luminescent probes, photovoltaic devices, solar cells, memory devices, field effect transistors *etc.*[1–8] If a compound of a transition or a non-transition metal shows good semiconducting properties, along with a rectifying nature in a metal–semiconductor junction, it may be used to fabricate a Schottky diode, which is a well-known opto-electronic device. In the last few years, our group has synthesized and characterized a lot of compounds of transition and non-transition metals showing notable semiconducting properties.[9–21] These semiconducting materials have been utilized for the fabrication of different opto-electronic devices.[9–21] Different N,O-donor Schiff bases and their reduced analogues have been used as ligands for the synthesis of these compounds.

Focusing on cobalt, carboxylate-bridged trinuclear mixed valence complexes are very common.[22–38] In these complexes, the central cobalt is in the +2 state and is present in the O_6 donor environment, whereas terminal cobalt centers are in the +3 state and are present in N_3O_3 or N_2O_4 donor environments. The Co(III)–Co(II)–Co(III) angle is not less than 150° (if not more) in most of the cases and the complexes may be considered as linear trinuclear Co(III)–Co(II)–Co(III) complexes.[22–38] The bridging carboxylates are *trans* to one another in most of the cases,[17,28–32,36–38] although cis orientations are also found in some cases.[23,24,28,39] Few such complexes were also used to fabricate opto-electronic devices.[13,14,40,41] In the present work, we have synthesized a distinctly bent trinuclear mixed valence cobalt complex, where the terminal cobalt centers are bridged by an end-to-end azide group. The structure of the complex has been confirmed by single crystal X-ray diffraction analysis. The band gap of the synthesized material in the solid state has been determined by experimental measurements and compared with the theoretical value obtained from DFT calculations. The band gap indicates that the complex belongs to the semiconductor family. The conductivities of such complexes have not been explored widely. We therefore concentrated on the electric

[a]*Department of Chemistry, Inorganic Section, Jadavpur University, Kolkata 700032, India. E-mail: shouvik.chattopadhyay@jadavpuruniversity.in; shouvik.chem@gmail.com; Tel: +91 3324572941*

[b]*Department of Physics, Jadavpur University, Kolkata 700032, India. E-mail: parthap.ray@jadavpuruniversity.in; Fax: +91 3324138917*

[c]*Department of Higher Education, (University Branch) Government of West Bengal, Bikash Bhavan, Salt Lake, Kolkata-91, India*

[d]*School of Chemistry, The University of Reading, P. O. Box 224, Whiteknights, Reading RG6 6AD, UK*

† Electronic supplementary information (ESI) available: Physical measurement, X-ray crystallography, Hirshfeld surface analysis, noncovalent interactions, band gap measurement from CV, device fabrication, electrical characterization, BVS calculation, Fig. S1–S7 and Tables S1–S3. CCDC 2305257. For ESI and crystallographic data in CIF or other electronic format see DOI: https://doi.org/10.1039/d4ra01406e

© 2024 The Author(s). Published by the Royal Society of Chemistry

NJC

ROYAL SOCIETY OF CHEMISTRY

PAPER

View Article Online
View Journal | View Issue

Check for updates

Cite this: *New J. Chem.*, 2024, **48**, 1837

Published on 20 December 2023. Downloaded by Jadavpur University on 2/13/2025 11:52:21 AM.

Development of a novel Cd(II) metal complex for solvent-sensitive detection of Zn(II) and Mg(II) with the formation of Cd(II)–Zn(II)/Cd(II)–Mg(II) complexes and their application in effective Schottky devices†

Dibyendu Sathapat,[a] Mainak Das,[b] Manik Das,[a] Uttam Kumar Das,[c] Arijit Bag,[d] Soumik Laha,[e] Partha Pratim Ray,[b] Bidhan Chandra Samanta[f] and Tithi Maity *[a]

Received 6th October 2023,
Accepted 19th December 2023

DOI: 10.1039/d3nj04660e

rsc.li/njc

The novel mononuclear Cd(II) metalloreceptor Cd[$\mathbf{L}H_2I_2$] (complex **1**), derived by the reaction of the Schiff base ligand 6,6′-(1E,1′E)(ethane-1,2 diylbis(azaneylidene))bis(methaneylylidene)bis(2-ethoxyphenol) ($\mathbf{H_2L}$) and CdI_2, was successfully used to detect Zn(II) and Mg(II) in semi-aqueous and aqueous media, respectively, among several competitive cations. The single crystal data analysis revealed that the asymmetric unit of complex **1** consists of one ligand, $\mathbf{H_2L}$, and two I-ions, compensating the +2 oxidation state of Cd. The optically monitored sensing of Zn(II) and Mg(II) by complex **1** was further assessed by utilizing UV and fluorescence spectroscopic techniques. The remarkable enhancement of the fluorescence intensity of complex **1**-Zn(II) and complex **1**-Mg(II) in the presence of CH_3COO^- and $SO_4^=$ indicated that a heteronuclear bridging complex could be obtained if two separate reactions of complex **1** with $(CH_3COO)_2Zn$ and $MgSO_4$ could be carried out. Interestingly, two different single crystals of Cd–Zn (complex **2**) and Cd–Mg (complex **3**) were obtained after conducting two separate reactions of complex **1** with Zn(II) and Mg(II). Single crystal data analysis showed that complex **2** is an octanuclear Zn(II)/Cd(II) complex with the presence of acetate and an hydroxy group, and both metal centers are in the +2 oxidation state. The IR and NMR spectra results confirmed the formation of complexes **2** and **3**. The SPX and EDX studies confirmed the presence of Zn(II) and Mg(II) in complex **2** and complex **3**, respectively. The limit of detection for sensing of both was measured in the nanomolar range. Although it is well-known that mononuclear Cd complexes are effective Schottky devices, there have been few reports of investigation of heteronuclear Cd(II) complexes as candidates for effective Schottky devices, or determination of the values of device performance, conductivity, and device parameters with heteronuclear Cd complexes **2** and **3**. Surprisingly, all the results indicated that a potential Schottky device could be produced due to the efficacy of complex **2** with respect to complex **3**. The effectiveness of the device would be satisfactory because of the lower band gap value and the presence of weak intramolecular π–π stacking interactions in complex **2**.

Introduction

The novel design and development of chemosensors for selective and sensitive detection of metal cations is important because this selection process plays a vital role in medicine, living systems, and environmental processes.[1–5] Several organic ligands with N and O donor centers have been successfully utilized as chemosensors for metal cation detection because this recognition phenomenon leads to high sensitivity, easy visualization, and a short response time.[6–11]

Great importance is given to the synthesis of metalloligands in organic chemosensor development because they possess the

[a] *Department of Chemistry, Prabhat Kumar College, Contai, Purba Medinipur, West Bengal, India. E-mail: titlipkc2008@gmail.com*
[b] *Department of Physics, Jadavpur University, Kolkata, India*
[c] *Department of Chemistry, School of Physical Science, Mahatma Gandhi Central University, Bihar, India*
[d] *School of Natural and Applied Sciences, Maulana Abul Kalam Azad University of Technology, West Bengal, India*
[e] *IICB, Kolkata, West Bengal, India*
[f] *Mugberia Gangadhar Mahavidyalaya, Purbamedinipur, West Bengal, India*

† Electronic supplementary information (ESI) available. CCDC 2246285 and 2246286. For ESI and crystallographic data in CIF or other electronic format see DOI: https://doi.org/10.1039/d3nj04660e

CrystEngComm

PAPER

View Article Online
View Journal | View Issue

Check for updates

Cite this: *CrystEngComm*, 2023, **25**, 2133

Combined experimental and theoretical studies of conformationally diverse (thio)semicarbazone-based semiconducting materials†

Anangamohan Panja, *[ab] Mainak Das,[c] Narayan Ch. Jana, [b] Paula Brandão, [d] Rosa M. Gomila, [e] Joaquín Ortega-Castro, [e] Antonio Frontera *[e] and Partha Pratim Ray*[c]

This study reports the synthesis and characterization of two closely related semicarbazone/thiosemicarbazone-based organic compounds: *N*-(2-hydroxy-3-methoxy-5-methylbenzylidene) semicarbazide (**1**) and *N*-(2-hydroxy-3-methoxy-5-methylbenzylidene)thiosemicarbazide (**2**). Structural studies revealed the conformational diversity in these systems as compound **1** crystallized as only one conformer, while compound **2** crystallized as a mixture of two conformers. DFT calculations in combination with the quantum theory of atoms in molecules (QTAIM) and natural bond orbital (NBO) analyses revealed that the energy difference between the two conformers was larger in compound **1**, while the difference between both conformers was very small in the thiosemicarbazide derivative (**2**), in line with the X-ray crystallographic characterizations. The synthesized compounds were tested for their electrical conductivity behaviour *via* current density–voltage measurements, as well as impedance spectroscopy, which revealed that both compounds were semiconducting in nature, arising from the charge transport through space *via* π···π contacts, and could be useful for the fabrication of electrical devices, particularly **1**, in which the conductivity fell by a higher order of magnitude than observed in similar organic semiconductors tested earlier. Moreover, the combined experimental and theoretical studies showed the importance of the non-covalent interactions on the stability of the different conformers, thereby guiding the possible isolations of different polymorphic forms of such conformationally diverse semicarbazone/thiosemicarbazone systems through the selective stabilization of a particular conformer by varying the reaction conditions.

Received 10th February 2023,
Accepted 7th March 2023

DOI: 10.1039/d3ce00137g

rsc.li/crystengcomm

Published on 07 March 2023. Downloaded by Jadavpur University on 2/13/2025 12:12:54 PM.

Introduction

Conformational versatility owing to various spatial dispositions of the constituent subunits has a tremendous impact on the possible isolation of different solid-state structures and in turn the properties of the organic solid.[1,2] This has been best demonstrated in the field of crystal engineering in the search for active polymorphic forms of pharmaceutical drugs/ingredients, in which different polymorphs derived from the same molecule may exhibit diverse physical and chemical properties.[3–5] Therefore, it is necessary to understand the factors that affect the conformational flexibility of a particular molecule, which is crucial for the deliberate design of novel crystalline materials with desired properties and functions.[6–8] In this context, the non-covalent interactions play a crucial role, and their knowledge is highly desirable. The most studied among such interactions is hydrogen bonding.[9–11] Besides the strong intra- or intermolecular hydrogen bonds, other interactions, like π···π and C–H···X (O/N/π) interactions, also help to stabilize the correct and active conformations.[12–19] Among many such identified organic synthons so far, semicarbazones/thiosemicarbazones deserve a special mention as the presence of several hydrogen bond acceptor

[a] *Department of Chemistry, Gokhale Memorial Girls' College, 1/1 Harish Mukherjee Road, Kolkata-700020, India. E-mail: ampanja@yahoo.co.in*
[b] *Department of Chemistry, Panskura Banamali College, Panskura RS, WB 721152, India*
[c] *Department of Physics, Jadavpur University, Raja S. C. Mallick Road Jadavpur, Kolkata700 032, India. E-mail: parthapray@yahoo.com*
[d] *Department of Chemistry, CICECO-Aveiro Institute of Materials, University of Aveiro, 3810-193 Aveiro, Portugal*
[e] *Department of Chemistry, Universitat de les Illes Balears, Crta. de Valldemossa km 7.5, 07122 Palma de Mallorca (Baleares), Spain. E-mail: toni.frontera@uib.es*

† Electronic supplementary information (ESI) available: Supplementary data including device fabrication and characterization, electrical characterization, IR and ^{1}H and ^{13}C NMR spectral data, bond distances, hydrogen bonds, packing diagrams and solid-state calculations. CCDC 2239945 and 2239946 for **1** and **2** contain the supplementary crystallographic data for this paper. For ESI and crystallographic data in CIF or other electronic format see DOI: **https://doi.org/10.1039/d3ce00137g**

NJC

PAPER

View Article Online
View Journal | View Issue

Check for updates

Cite this: *New J. Chem.*, 2022, **46**, 21103

Published on 12 October 2022. Downloaded by Jadavpur University on 2/13/2025 12:21:33 PM.

Synthesis and crystal structures of two tri- and tetra-heterometallic Ni(II)–Mn(II)/Ni(II)–Co(III) complexes from two different Ni(II)-containing metalloligands: effective catalytic oxidase activity and Schottky device approach†

Manik Das,[a] Mainak Das,[b] Subham Ray,[a] Uttam Kumar Das,[c] Soumik Laha,[d] Partha Pratim Ray,[b] Bidhan Chandra Samanta[e] and Tithi Maity *[a]

Received 18th July 2022,
Accepted 11th October 2022

DOI: 10.1039/d2nj03535a

rsc.li/njc

Using two different metalloligands [NiLA] and [NiLB], developed using two different N_2O_2 donor Schiff bases, H_2LA 6,6′-((1*E*,1′*E*)-((2,2-dimethylpropane-1,3-diyl)bis(azaneylylidene))bis(2-methoxyphenol) and H_2LB 6,6′-((1*E*,1′*E*)-((2,2 (2-ethoxyphenol), two new tetra- and trinuclear heterometallic complexes, $[(NiLA)_2(CH_3COO)_2(SCN)_2(Co)_2]$ (complex **1**) and $[(NiLB)_2(SCN)_2Mn]$ (complex **2**), have been synthesized. The two newly formed complexes have primarily been characterized using several spectroscopic techniques. According to the single-crystal structural study, the metalloligand portion is shared by both crystals. Complex **1** is a tetranuclear complex where Ni(II) is connected to Co(II) *via* acetate and phenoxide bridging, whereas complex **2** is a trinuclear complex where each Ni(II) center is coordinated to Mn(II) *via* phenoxide bridging only. It is interesting to note that the thiocyanate moiety in complex **1** is linked to Co(II), whereas in complex **2**, it is linked to Ni(II) as a secondary anionic residue. Following structural analysis, both complexes were exposed to catecholase-like activity to test their ability to aerially oxidize 3,5-di-*tert*-butylcatechol. The calculated turnover numbers (K_{cat}) 355 h^{-1} and 286 h^{-1} for complexes **1** and **2**, respectively, unveiled that complex **1** is more susceptible to this catalytic process. The generation of Ni(I) in complex **1** is more favorable than the formation of Mn(I) in complex **2** during catalysis and this is the factor responsible for the higher susceptibility of complex **1** towards the catalytic process. To determine whether both the studied complexes can function as effective Schottky devices, the band gap values for complexes **1** and **2** were used to calculate the diode parameters. The results show that complex **1** will function as a better Schottky device than the complex **2**.

Introduction

Organometallic chemistry has long given special attention to the creation and development of heteronuclear complexes with N, O donor tetradentate ligands. In terms of catalytic, magnetic, biomedical, gas storage, and sensing activities, the metal complexes with N, O donor tetradentate ligands have multiple applications that are significant for the study of chemical science.[1–6] In the past, numerous heterometallic complexes have been created by directly mixing a metal centre with an N_2O_2 donor Schiff base ligand.[7–9] These Schiff bases are widely used in coordination chemistry research due to their simple synthesis procedures, one-pot condensation of a diamine with substituted salicylaldehyde derivatives, and their exceptional complexing power. The creation of a metalloligand by utilizing an N_2O_2 donor Schiff base ligand and a metal salt has recently emerged as a common method for creating heterometallic complexes.[10–12] The anionic component of second metal salts plays a key role in modulating the nuclearity as well as the topologies of these heterometallic complexes through the various forms of coordination to the metal centers in this newly emerging pathway, in addition to providing the consequent complex charge.[13–16] These structural differences, which emerge from anion dependency, may control the properties of

[a] *Department of Chemistry, Prabhat Kumar College, Contai, Contai, Purba Medinipur, West Bengal, India. E-mail: titlipkc2008@gmail.com*
[b] *Department of Physics, Jadavpur University, Kolkata, India*
[c] *Department of Chemistry, School of Physical Sciences, Mahatma Gandhi Central University, Bihar, India*
[d] *IICB, Kolkata, West Bengal, India*
[e] *Mugberia Gangadhar Mahavidyalaya, Purbamedinipur, West Bengal, India*

† Electronic supplementary information (ESI) available. CCDC 2176941 and 2176942. For ESI and crystallographic data in CIF or other electronic format see DOI: https://doi.org/10.1039/d2nj03535a

Check for updates

EurJIC
European Journal of Inorganic Chemistry

Research Article
doi.org/10.1002/ejic.202300736

Chemistry Europe
European Chemical Societies Publishing

www.eurjic.org

Comparison of Electrical Conductivity and Schottky Behavior of 4-[2-(9-anthryl)vinyl]pyridine Based Two 1D Coordination Polymers of Zn(II) and Cd(II)

Ersad Hossain,[a] Ramjan Sk,[b] Mainak Das,[b] Joydeb Goura,[c] Sourav Roy,[d] Partha Pratim Ray,*[b] Mohammad Hedayetullah Mir,*[e] Antonio Frontera,[f] and Subrata Mukhopadhyay*[a]

With the increase in demand of electronic devices in the modern civilization, research in material science is being projected to grow in faster rate. In this facet, coordination polymer (CP) based electronic device is one of the promising candidates to the material researchers. Herein, two new Zn(II) and Cd(II) based one-dimensional (1D) CPs, denoted as [Zn(4-avp)$_2$(5-nip)]·(solvent)$_x$ (**1**) and [Cd(4-avp)(5-nip)(CH$_3$OH)] (**2**) have been synthesized using relatively less explored highly conjugated polycyclic aromatic hydrocarbon (PAH) based monodentate ligand, 4-[2-(9-anthryl)vinyl]pyridine (4-avp) and bidentate linker 5-nitroisophthalic acid (H$_2$5-nip). In this instance, the CP **1** creates 1D chain polymer, while CP **2** is made up with 1D ladder polymer. It is interesting to note that both the CPs exhibit semiconducting nature and generate metal-semiconductor (MS) junction Schottky barrier diodes (SBDs). However, Cd-based CP **2** shows higher charge transport as compared to Zn-CP **1**, which could be due to stronger π···π contacts as well as larger size of Cd metal in CP **2**. The experimental results are well corroborated with theoretical density of states (DOS) calculations.

Introduction

In the past few decades, the design and fabrication of coordination polymers (CPs) have drawn enormous attention of material scientists because of their exceptional stabilities and unique molecular architectures, which lead to distinctive properties along with desire applications.[1–8] Metal ions or metal clusters combined with organic ligands form these hybrid materials.[9–15] Therefore, the nature of the metal core and ligating ligands play the pivotal role in the molecular characteristics and applications. However, it is not always easy to attain requisite molecular structures with fair stability. In order to achieve desired molecular structures along with characteristics features, sometimes mixed-ligand system, i.e. combination of *O*-donor and *N*-donor ligands is employed.[16–18] Thus, metal salts or organic linkers are carefully chosen in the designing of CPs based on the specific application. Actually, there is a crucial connection between material qualities, structural architectures, and their prospective applications. These crystalline materials are engineered by rational construction and scientific judgment, which facilitate their characterizations and help to highlight significant structure-property relationship. Besides, various supramolecular interactions, including van der Waals contacts, π···π stacking, halogen bonding, and hydrogen bonding interactions become occasionally essential for building higher-dimensional supramolecular architecture that dictates structure-property correlation.[19–21] The self-assembled constructions are occasionally different and superior to the disassembled version in regard to the application of the materials. It is noteworthy to mention that these inorganic-organic hybrid materials have a wide spectrum of applications, including molecular storage and separation, water harvesting, energy technology, electro-catalysis, photo-catalysis, temperature-dependent magnetism, drug delivery, fabrication of electronic devices and photoactuating smart materials.[22–28]

Among the CPs, their uses in electrical conductivity and optoelectronic device applications are particularly interesting in terms of both energy and technological aspects. Nonetheless, in CPs, charge transport is largely hampered by the inadequate prolonged electronic coupling between the ligands and the metal ions.[29–31] Consequently, the most important aspect is to modify the electrical coupling between the organic ligands and metal centers in order to promote delocalization and increase

[a] *E. Hossain, Prof. S. Mukhopadhyay*
Department of Chemistry
Jadavpur University, Kolkata 700 032, India
E-mail: ju_subrata@yahoo.co.in

[b] *R. Sk, M. Das, Prof. P. P. Ray*
Department of Physics
Jadavpur University, Kolkata 700 032, India
E-mail: partha@phys.jdvu.ac.in

[c] *Dr. J. Goura*
Chemistry Department
Delhi University, Delhi 110 007, India

[d] *Dr. S. Roy*
Solid State and Structural Chemistry Unit
Indian Institute of Science, Bangalore 560 012, India

[e] *Dr. M. H. Mir*
Chemistry Department
Aliah University, New Town, Kolkata 700 160, India
E-mail: chmmir@gmail.com

[f] *Prof. Dr. A. Frontera*
Departament de Quimica, Universitat de les Illes Balears, Crta de Valldemossa km 7.5, 07122 Palma de Mallorca (Baleares), Spain

Supporting information for this article is available on the WWW under https://doi.org/10.1002/ejic.202300736

© 2024 Wiley-VCH GmbH

Dalton Transactions

ROYAL SOCIETY OF CHEMISTRY

COMMUNICATION

View Article Online
View Journal | View Issue

Check for updates

Cite this: *Dalton Trans.*, 2023, **52**, 8850

Received 7th April 2023,
Accepted 6th June 2023

DOI: 10.1039/d3dt01073b

rsc.li/dalton

Published on 09 June 2023. Downloaded by Jadavpur University on 2/13/2025 12:02:32 PM.

Harnessing the hydrogen evolution reaction (HER) through the electrical mobility of an embossed Ag(I)-molecular cage and a Cu(II)-coordination polymer†

Ananya Debnath, [a] Sangharaj Diyali, [a] Mainak Das,[b] Subhra Jyoti Panda,[c] Debasish Mondal,[d] Debasis Dhak,[d] Chandra Shekhar Purohit, [c] Partha Pratim Ray [b] and Bhaskar Biswas *[a]

A structurally characterized porous Ag(I)-molecular cage Ag_{MOC} and a Cu(II)-coordination polymer Cu_{CP} with a pre-synthesized ligand 1,3-bis(((*E*)-2-methoxybenzylidene)amino)propan-2-ol and its parental amine with thiocyanate are reported to harness electrical mobility-driven hydrogen evolution activity. Porosity-induced electrically conductive Ag_{MOC} emerges as a better electrocatalyst with a Tafel slope of 104 mV per decade over Cu(II)-polymer's slope of 128 mV per decade. The electrochemical stability and durability of the designed electrocatalysts in harnessing the HER activity are also examined under experimental conditions.

The coordination chemistry of metal ions in coupling with synthetic ligands having unique topicity, denticity, and backbone flexibility holds great promise in the progress of futuristic functional materials.[1–3] Nowadays, the diversity in metal–ligand coordination ranging from metal complexes to metal–organic frameworks to coordination polymers to composite materials is considered a cornerstone to understanding a material's structure and activity relationship.[4–7] Despite the numerous fundamental applications of coordination-driven compounds, discrete (or finite) molecular coordination complexes composed of an internal void provide an exciting avenue in materials science.[8] Typically, metal–organic cages (MOCs), an alternative term for discrete molecular coordination complexes, adopt the same constituent as a MOF, but the designed individual complexes are typically monodisperse in size, structure, and molecular weight.[9] Notably, MOCs with distinct porosity and morphology attract great interest because of their significant applications in molecular electronics, smart catalysis, *etc.*[8] In contrast, coordination polymers (CPs) composed of polymeric frameworks of metal–ligand complexes emerge as an important class of functional molecules for their immaculate contributions to the fields of catalysis, magnetism, optoelectronics, *etc.*[2,3] It is well documented that discrete MOCs or polymeric coordination complexes or structurally diversified molecular composites can be steered by the judicious selection of appropriate metal and polydentate ligands under ambient conditions. Noteworthy, electrical transport properties of coordination compounds have attracted ample interest in tuning the electrocatalytic performance and semiconducting properties in optoelectronic devices.[10] Consequently, electronic devices are decorated with rationally designed metal complexes, MOFs, MOCs, CPs, 3d–4f hybrid salts, and composite materials to probe the performance of real electrical devices. However, the most alluring prospect of fabricating MOCs and CPs for electrical conduction remains in the rudimentary stage, demanding a rigorous investigation in this field. Nonetheless, the electric transport properties of a material inherently correlate with the electrochemical properties, expressing its distinct corollary in numerous fundamental applications like the production of carbon-free energy. The electrochemical production of hydrogen from water splitting has emerged as a novel strategy for the efficient production of carbon-free energy, although only 4% of hydrogen has been acquired to date through the water splitting process.[11] To date, numerous molecular electrocatalysts as homogeneous and heterogeneous catalysts have been reported, which have enormous potential in hydrogen production.[12] Recently, Huang *et al.* reported a copper(II)-benzene hexathiol-based coordination polymer as a smart hydrogen evolution electrocatalyst in an acid medium with ~95 mV dec^{-1} Tafel slope, highlighting Cu-edge sites on the surface as a crucial parameter for its superior HER activity.[13] In addition, Prof. Shi and his group designed different bimetallic nickel-M^{II} cage-derived molecular frameworks with biphenyl-3,3′,5,5′-tetracar-

[a]*Department of Chemistry, University of North Bengal, Darjeeling-734013, India. E-mail: bhaskarbiswas@nbu.ac.in, icbbiswas@gmail.com*
[b]*Department of Physics, Jadavpur University, Kolkata-700032, India*
[c]*Department of Chemical Sciences, National Institute of Science Education and Research, Bhubaneswar 752050, India*
[d]*Department of Chemistry, Sidho-Kanho-Birsha University, Purulia-723104, India*

†Electronic supplementary information (ESI) available. CCDC 2232715 and 2232716 for AgMOC and CuCP. For ESI and crystallographic data in CIF or other electronic format see DOI: https://doi.org/10.1039/d3dt01073b

This journal is © The Royal Society of Chemistry 2023

Check for updates

ChemistrySelect

Research Article
doi.org/10.1002/slct.202303361

Chemistry Europe
European Chemical Societies Publishing

www.chemistryselect.org

Fabrication and Characterization of Metal/Semiconductor Junction Devices Using Four Benzaldehyde Derivatives

Prantika Das[+],[a] Mainak Das[+],[a] Partha Pratim Ray,[a] and Saikat Kumar Seth*[a]

Four benzaldehyde derivatives [ALD-1: compound (**1**), ALD-2: compound (**2**), ALD-5: compound (**3**), ALD-6: compound (**4**)] were taken to investigate their optical band gap by UV-vis spectroscopy. Semiconducting devices were fabricated using these compounds to study their electrical properties. The current-voltage (I–V) characteristics graph was obtained. Furthermore, the diode parameters were extracted by conventional methods to analyze the charge transport mechanism. From the dielectric study, a low dielectric constant was observed. Moreover, each compound's mobility and transit time were derived to compare the device performance of benzaldehyde derivatives.

Introduction

Organic semiconductors have been the subject of extensive research in recent years as an important development has been observed in the field of modern electronic devices containing organic materials to a great extent.[1] As the organic materials possess easily tuneable electronic and processing properties, they are promising materials in electronic device fabrication.[2] Nowadays, several organic devices such as Schottky diodes, organic light-emitting diodes, organic field effect transistors, photovoltaic (PV), and solar cells are fabricated and characterized using organic semiconductors and their derivatives.[3–8] Furthermore, extensive research has been implemented for applying semiconducting organic materials to electronic devices and various condensed matter physics applications. Conventionally, the interfacial properties of metal/semiconductor (MS) contact significantly influence device performance, reliability, and stability. In addition, the electrical parameters of the metal/semiconductor interface may control the contact resistance.[9–12] Therefore, the structural and chemical characteristics of organic materials and metal/semiconductor interface are important for the charge carrier transport in organic material based Schottky diodes.[13]

Organic compounds containing benzaldehyde as a substitution are found in many plants in combined or non-combined forms. Benzaldehyde compounds are a great topic of research as they show high antimicrobial phenomena, they are eminent candidates for practical applications such as the development of novel antimicrobial drugs and disinfectants.[14–16] However, as per the literature survey, the research works related to exploring the optical and electrical properties of benzaldehyde compounds are very few.

In the present study, we are interested in investigating four benzaldehyde derivatives' optical and electrical properties. The optical band gap of four compounds was found to be in the range of wide band gap semiconductor ($E_g > 2$ eV).[17] Due to the fact of having a wide band gap, the compounds are employed to fabricate Schottky diodes by spin coating method on ITO-coated glass substrates along with the vapour deposition of aluminium. The conductivity of the devices was measured and an I–V characteristics graph was obtained. The dielectric constant, mobility of charges, and transit time were calculated in addition to the diode parameters.

Results and Discussion

Optical bandgap

The optical bandgap of compounds (**1**) & (**2**) was already reported.[18] The allowed direct bandgap of (**1**) & (**2**) is 4.08 eV and 3.61 eV respectively and the allowed indirect bandgap of (**1**) & (**2**) is 3.99 eV and 3.43 eV respectively. The bandgap of compounds (**3**) & (**4**) has been calculated in the present work. The allowed direct bandgap of (**3**) & (**4**) is found to be 3.36 eV (Figure S1a) and 3.76 eV (Figure S1b) respectively whereas their indirect bandgap is calculated as 3.29 eV (Figure S2a) and 3.64 eV (Figure S2b). From the results, it can be inferred that the title compounds belong to wide bandgap semiconductors.

Electrical characterization

The measurement of the direct optical band gap from the absorbance spectrum suggests that the complex salts might have been employed as semiconducting in nature. It inspires to fabrication of thin film semiconducting devices. So, four Metal-Semiconductor (MS) devices as Al/ALD-1/ITO (device-A), Al/ALD-2/ITO (device-B), Al/ALD-5/ITO (device-C) and Al/ALD-6/ITO (device-D) were fabricated. To investigate the electrical proper-

[a] *P. Das,[+] M. Das,[+] Prof. P. P. Ray, Dr. S. K. Seth*
Department of Physics
Jadavpur University
Kolkata 700032, India
E-mail: saikatk.seth@jadavpuruniversity.in

[+] *Contributed equally.*

Supporting information for this article is available on the WWW under https://doi.org/10.1002/slct.202303361

© 2024 Wiley-VCH GmbH

CRYSTAL GROWTH & DESIGN

pubs.acs.org/crystal

Article

Supramolecular Framework-Driven Electrical Conductivities and Hydrogen Evolution Activities of Hybrid Nickel(II)−Cerium(IV) Complex Salts Cooperativity

Published as part of a Crystal Growth and Design virtual special issue on Noncovalent Interactions: Celebrating Prof. Guru Row

Sangharaj Diyali, Nilankar Diyali, Mainak Das, Mayank Joshi, Partha Pratim Ray, Md. Selim Arif Sher Shah, Angshuman Roy Choudhury,* and Bhaskar Biswas*

Cite This: *Cryst. Growth Des.* 2022, 22, 7590−7602

Read Online

ACCESS | Metrics & More | Article Recommendations | Supporting Information

ABSTRACT: This work highlights the design, synthesis, structural characterization, electrical conductivities, and hydrogen evolution activities of a new pair of hybrid 3d(Ni)-4f(Ce) block metal complex salts, $[Ni(phen)_2(NO_3)]_2[Ce(NO_3)_6]$ (**1**) and $[Ni(bpy)_3]$-$[Ce(NO_3)_6][Ce(NO_3)_2(H_2O)_5]NO_3$ (**2**) containing phen and bpy ligands; [phen = 1,10-phenanthroline and bpy = 2,2′-bipyridine]. Crystal structural analysis divulges that complex salt **1** adopts two units of monocationic Ni(II) complex with one dianionic Ce(IV) complex unit while complex salt **2** exists in an association of one unit of dicationic Ni(II) complex with two complex units of Ce along with a counteranionic nitrate. The Ni(II) ions exist in distorted bicapped square pyramidal coordination geometry, while the Ni(II) center in **2** exists in an octahedral geometry. The cerium ion in **1** exists in dodecahedron geometry while the first and second Ce ions hold dodecahedral and tricapped trigonal prism coordination geometries, respectively. Supramolecular interactions reveal that predominant nonclassical forces like O···H, N···H, $\pi\cdots\pi$, O···π, and O···O are interactive to shape highly ordered crystalline frameworks. Complex salt **2** exhibits a unique formation of the supramolecular cage-type framework by the cerium complex units, leading to the inclusion of Ni(II)-complex units into the supramolecular cages. The complex salts (**1**, **2**) were employed to fabricate the Schottky devices to unveil the fate of the hybrid salts in charge transport applications. Carrier mobility (μ) for **1** and **2** were determined as 3.02×10^{-6} and 8.022×10^{-5} $m^2\ V^{-1}\ s^{-1}$ with respective transit time(τ) of 2.60×10^{-7} and 9.67×10^{-9} s attributing the excellent candidature of complex salt **2** in transport properties. The hybrid salts were also found to be highly active electrocatalysts for proton reduction in 1 M aqueous KOH solution at room temperature. The overpotential values of **1** and **2** were determined to be 730 mV and 687 mV at a current density of 10 mA cm^{-2} with 0.081 s^{-1} and 0.225 s^{-1} as turnover frequencies. The supramolecular interactions−driven crystalline framework sheds light on the electrical conductivities and casting the hydrogen evolution activities for the newly designed hybrid d−f type complex salts.

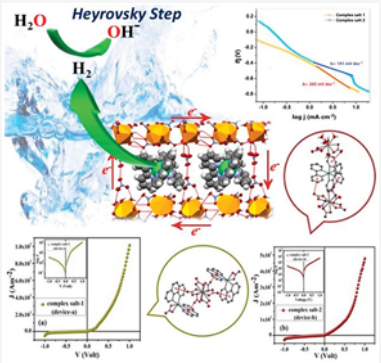

Downloaded via JADAVPUR UNIV on February 13, 2025 at 12:14:06 (UTC).
See https://pubs.acs.org/sharingguidelines for options on how to legitimately share published articles.

INTRODUCTION

In coordination chemistry, the design of novel homo-/heterometallic composite-based hybrid materials for synthetic chemists has been revealed as a promising vector in technological applications.[1−5] In view of the various structural and functional diversity of this type of material, it has been observed as an auspicious candidate in power cell technology, novel single molecular magnets (SMMs) and magnetic spintronics, fascinating and imminent catalysts, alloys, and composites, while bioanalyses and imaging also deliver insightful electrical and optical properties and so on.[6−10] Considering the important properties of 3d and 4f block elements, their coupling counterparts may allow the conception and advancement of new functional properties in the future[11−13] as is well depicted in the research fields of magnetism and electrical conductivity.[14−17] A literature survey yields shreds of evidence on electrical conductivities of the crystalline material as one of the vital aspects of the evolution of smart and functional electrical devices.[18,19] Indeed, the intrinsic electronic properties of crystalline materials feature the evolution of electrical conductivities, but the nature of the electrolytes, the orientation of molecules, and their supramolecular architecture are also well-known to deliver superiority in the charge transport phenomenon.[20−22] More-

Received: October 3, 2022
Revised: November 9, 2022
Published: November 28, 2022

ACS Publications

© 2022 American Chemical Society

Materials Advances

ROYAL SOCIETY OF CHEMISTRY

PAPER

View Article Online
View Journal | View Issue

Check for updates

Cite this: *Mater. Adv.*, 2023, 4, 6367

The synthesis and combined electrical–magnetic and toxic dye sequestration properties of a Cr(III)-metallogel†

Krishna Sundar Das,[a] Mainak Das,[b] Sayan Saha,[a] Amit Adhikary,[a] Sukhen Bala,[a] Partha Pratim Ray *[b] and Raju Mondal *[a]

Materials based on typical inorganic compounds, along with their embodied metal-specific features like redox, magnetic, catalytic and spectroscopic properties, in their as-synthesized economical, end-user friendly and commercially viable gel states, have manifold practical and strategic advantages. Along these lines, the work presented herein aims to explore the usefulness of porous gel-based inorganic compounds, in their original as-synthesized states, for probing their combined electrical, magnetic and adsorption properties. Accordingly, we have synthesized and thoroughly characterized a benzene dicarboxylic acid based Cr(III)-metallogel for magnetic and electrical device fabrication. The metallogel shows an interesting NMOP morphology and is thoroughly characterized using various microscopic and spectroscopic techniques. Furthermore, rheological studies on the resultant metallogel reveal its interesting thixotropic behaviour. The Cr-gel has been successfully utilized for fabricating an electrical Schottky barrier diode with a befitting conductivity value of 1.61×10^{-2} S cm^{-1}. Moreover, the free immobilized azide group, featuring in-built charge-separated resonance structures, acts as a proton carrier facilitator-cum-transporter and shows an impressive proton conductivity value of 3.3×10^{-4} S cm^{-1} at 95% relative humidity and 85 °C. The presence of paramagnetic chromium ions also renders a special physicochemical property, namely magnetism, to the system. The porous and magnetic nature of the as-synthesized metallogel was also evaluated. DC magnetic susceptibility data confirm the antiferromagnetic nature of the material. Gas sorption studies, on the other hand, confirm the porous nature and show the selective CO_2 uptake ability of the xerogel. Subsequently, the as-synthesized, by default porous, magnetic metallogel was utilized as an adsorbent for removing toxic organic dyes like methylene blue, rhodamine B and crystal violet. Interestingly, the as-prepared metallogel also enables the substantial release of the adsorbed dye molecules for re-use. To the best of our knowledge, this kind of electrical–magnetic Cr-gel based wastewater treatment technique was not reported hitherto in the literature but has a huge potential application in adsorbent based environmental remediation as well as in magnetic or electrical device fabrication.

Received 1st September 2023,
Accepted 30th October 2023

DOI: 10.1039/d3ma00645j

rsc.li/materials-advances

Open Access Article. Published on 03 November 2023. Downloaded on 2/24/2025 12:38:11 PM.
This article is licensed under a Creative Commons Attribution-NonCommercial 3.0 Unported Licence.

Introduction

Metallogels, comprising typical inorganic metal–ligand coordination bonds, have emerged as some of the front runners in the field of new-age inorganic materials.[1–4] A crucial hurdle that thwarts the metallogels from being the predominant materials is the step that involves arresting a relatively heavy metal-coordinated network in its less-ordered gel state while using nothing more than a common low-molecular-weight ligand for gelation.[5–7] The consequential low-success rates play a major role in deterring inorganic chemists from conducting metallogelation studies. Two other contributing factors of this apathy would be: (a) for inorganic compounds, metallogelation mostly happens serendipitously rather than by design and (b) low structural predictability, which is deduced from guessing various possible self-assembly methods.[8,9] The gel state, by default, represents the short range ordering of gelators and solvent molecules in nanoscale dimensions. Naturally, the studies of their self-assembly also demand nano-level instrumentation and nanostructural techniques such as scanning electron microscopy (SEM), transmission electron microscopy (TEM), atomic force microscopy (AFM) and X-ray photoelectron

[a] *School of Chemical Sciences, Indian Association for the Cultivation of Science, Raja S. C. Mullick Road, Kolkata 700032, India. E-mail: icrm@iacs.res.in*
[b] *Department of Physics, Jadavpur University, Raja S. C. Mullick Road, Jadavpur, Kolkata 700 032, India*

† Electronic supplementary information (ESI) available. See DOI: https://doi.org/10.1039/d3ma00645j

© 2023 The Author(s). Published by the Royal Society of Chemistry

NJC

ROYAL SOCIETY OF CHEMISTRY

PAPER

View Article Online
View Journal | View Issue

Check for updates

Cite this: *New J. Chem.*, 2022, **46**, 16730

Published on 01 August 2022. Downloaded by Jadavpur University on 2/13/2025 12:22:15 PM.

Synthesis, characterization and multi-dimensional application approach for two distinctive tetra nuclear, first-time reported, Fe^{3+}/Hg^{2+} and Fe^{3+}/Cd^{2+} clusters from a new Fe^{3+} containing metalloligand†

Soumik Laha,[a] Dibyendu Sathapathi,[b] Mainak Das,[c] Manik Das,[b] Partha Pratim Ray,[c] Arijit Bag,[d] Bidhan Chandra Samanta,[e] Uttam Kumar Das *[f] and Tithi Maity *[b]

Received 7th July 2022,
Accepted 19th July 2022

DOI: 10.1039/d2nj03357g

rsc.li/njc

A new mononuclear Fe^{3+} metalloligand **MC1** [$FeLN_3(H_2O)$], developed by using the N_2O_2 donor Schiff base ligand H_2L, has been successfully used to detect and remove Hg^{2+} and Cd^{2+} from several transition metal ions with the formation of two unusual hetero metallic μ-oxo Fe^{3+}–Hg^{2+}/Cd^{2+} clusters, [(Fe_2^{3+})-(μ-O)$L_2Cl_4(Hg_2^{2+})$] (**MC2**) and [(Fe_2^{3+})(μ-O)$L_2I_4Cd_2^{2+}$] (**MC3**) [(where H_2L is 6, 6′-(1E, 1′E) (ethane-1, 2 diylbis(azaneylidene))bis(methaneylylidene))bis(2-ethoxyphenol)]. All three complexes were identified by X-ray single-crystal data analysis along with a range of spectral studies. In **MC1**, the Fe^{3+} is coordinated with deprotonated H_2L, one water molecule, and one azide ion as a secondary anionic residue, forming an octahedral geometry. Interestingly, **MC2** and **MC3** are isostructural, where each asymmetric unit contains deprotonated H_2L, one Fe^{3+} and Hg^{2+}/Cd^{2+} metal center, two Cl^-/I^- and two Fe^{3+} centers are connected by a μ-O bridge to form tetranuclear complexes. As the band gap energy values of **MC1**, **MC2**, and **MC3** (3.07 eV, 2.69 eV, and 2.55 eV, respectively) are in the visible region so all the three complexes are exposed to investigate their potentiality to be effective Schottky devices and at the same time a thorough inspection has been carried out to check their catalytic behaviour in aqueous medium in terms of methylene blue (MEB) dye degradation under visible light irradiation. A thorough inspection reveals the better MB dye degradation potentiality of **MC3** in comparison to **MC2** in the presence of H_2O_2. At the same time, the investigation of the device performances, conductivity, and device parameters disclose more effectiveness of **MC3** in comparison to **MC2** in a better Schottky device. The effectiveness of **MC3** in both applications may be attributed to its lower band gap value.

Introduction

During the last few decades, the fabrication and development of high nuclearity μ-oxo bridged supramolecular metal complexes have received a special priority in chemical science research not only for their distinctive and gorgeous structures but also for their catalytic activity in oxidation reactions.[1–8] A literature survey discloses that in most of the developed μ-oxo bridged homonuclear complexes, generally, two macrocyclic metal moieties are connected by a μ-oxo bridge.[9–13] The presence of a hetero-metallic centre (M–M′) in the oxo-bridged complex may alter the topologies or introduce unusual coordination environments, which may influence the physical properties of the mother homo-nuclear complex from which the hetero-nuclear complex is formed. In oxo bridged development research, very few reports have been found where a hetero nuclear oxo-bridge is formed.[14,15] However, interestingly, no reports are found wherein two hetero-nuclear simple Schiff base motifs are connected by a μ-oxo bridge to form a unique and attractive multi-nuclear complex. Not only that, the development of metal clusters along with the presence of the oxo group is very rare. Apart from this, the removal of environmentally or physically concerned

[a] *IICB, Kolkata, West Bengal, India*
[b] *Department of Chemistry, Prabhat Kumar College, Contai, Contai, Purba Medinipur, West Bengal, India. E-mail: titlipkc2008@gmail.com*
[c] *Department of Physics, Jadavpur University, Kolkata, India*
[d] *School of Natural and Applied Sciences, Maulana Abul Kalam Azad University of Technology, West Bengal, India*
[e] *Mugberia Gangadhar Mahavidyalaya, Purbamedinipur, West Bengal, India*
[f] *Department of Chemistry, School of Physical Sciences, Mahatma Gandhi Central University, Bihar, India. E-mail: uttamkumardas@mgcub.ac.in*

† Electronic supplementary information (ESI) available: CCDC 2128297, 2128298, 2128300. For ESI and crystallographic data in CIF or other electronic format see DOI: https://doi.org/10.1039/d2nj03357g

 This journal is © The Royal Society of Chemistry and the Centre National de la Recherche Scientifique 2022

Dalton Transactions

ROYAL SOCIETY OF CHEMISTRY

PAPER

View Article Online
View Journal | View Issue

Check for updates

Cite this: *Dalton Trans.*, 2022, **51**, 1561

De novo synthesis of hybrid d–f block metal complex salts for electronic charge transport applications†‡

Shreya Mahato,[a] Amit Mondal,[b] Mainak Das,[c] Mayank Joshi,[d] Partha Pratim Ray,[c] Angshuman Roy Choudhury,[d] C. Malla Reddy*[b] and Bhaskar Biswas*[a]

The advent of d–d type complex salts for designing smart functional materials with versatile utility inspired us to develop a novel type of M(II)–Ce(IV) complex salts [M(II) = Cu and Zn ions]. In this study, we present for the first time a holistic approach to design and prepare metal complex salts of the novel hybrid d–f block type, $[Cu(bpy)_2]_2[Ce(NO_3)_6]_2$ (**1**), $[Cu(phen)_2(NO_3)]_2[Ce(NO_3)_6](HNO_3)$ (**2**), $[Zn(bpy)_2(NO_3)][ClO_4]$ (**3**), and $[Zn(phen)_2(NO_3)]_2$ $[Ce(NO_3)_6]$ (**4**); [bpy = 2,2′-bipyridine; phen = 1,10-phenanthroline]. The intrinsic structural and morphological properties of the compounds have been revealed by employing a suite of analytical and spectroscopic methods. X-ray structural analysis reveals that the copper(II) centres in the cationic complex units of **1** and **2** adopt a highly distorted tetrahedral and a rare bicapped square pyramidal coordination geometry, respectively. The zinc(II) ions in both **3** and **4** adopt the rare bicapped square pyramidal geometry while the cerium(IV) ions in **1**, **2** and **4** exist in a dodecahedral geometry. Investigation of supramolecular interactions reveals that intermolecular O···H and O···π short contacts bind the complex units in **1**, while predominant π···π interactions, along with O···H and O···π short contacts, produce the binding force among the complex units in **2**. We further employed the complex salts (**1–4**) to construct Schottky devices to reveal the role of these new complex salts in the charge-transport phenomenon. The carrier mobilities (μ) for salts **1–4** were determined to be 1.76×10^{-6}, 9.02×10^{-6}, 1.86×10^{-8}, and 4.31×10^{-8} $m^2\ V^{-1}\ s^{-1}$, with respective transit times (τ) of 439, 85, 4.17×10^3, and 1.79×10^3 ns, which suggest that complex salt **2** is the best candidate with the highest transport properties among all the complex salts. A crystal engineering perspective sheds light on the charge-transport properties of the complex salts, emphasizing the attribution of the best performance of **2** to its predominant π···π interactions. The synthesis of this new type of complex salts, their physicochemical properties and their charge-transport applications envisage great promise for the development of novel crystalline materials with smart functionalities.

Received 16th August 2021,
Accepted 13th December 2021

DOI: 10.1039/d1dt02722k

rsc.li/dalton

Published on 15 December 2021. Downloaded by Jadavpur University on 2/13/2025 12:22:50 PM.

Introduction

The design of metal-incorporating crystalline materials is an emerging field of research owing to the promising properties of these novel solids for technological applications.[1–4] Homo/heterometallic-composite-based hybrid materials of varied dimensions and multiple functionalities have emerged, giving rise to a wealth of advanced functional materials such as novel single molecular magnets (SMMs) and magnetic spintronics,[5] smart optics and electronics,[6] emerging catalysts,[7] alloys and composites,[8] efficient lighting, and materials for solar-energy conversion,[9] bio-analyses, imaging,[10] *etc.*[11–13]

In light of the peculiar properties of the transition metals and lanthanide elements, the coupling of transition metals with lanthanides within a single molecular compartment may facilitate the design of new functional properties with great

[a]*Department of Chemistry, University of North Bengal, Darjeeling 734013, India. E-mail: bhaskarbiswas@nbu.ac.in*
[b]*Department of Chemical Sciences, Indian Institute of Science Education and Research Kolkata, Nadia 741246, India*
[c]*Department of Physics, Jadavpur University, Kolkata 700032, India*
[d]*Department of Chemical Sciences, Indian Institute of Science Education and Research, Mohali, Sector 81, Knowledge City, S. A. S. Nagar, Manauli PO, Mohali, Punjab 140306, India*

†Electronic supplementary information (ESI) available: Experimental information such as FT-IR, UV-Vis, cyclic voltammograms for the complex salts, EPR spectra, FESEM microscopy images and EDX plots, ESI-MS spectrum, supramolecular architectures, EPR parameter table, bond distance, bond angle parameters, *etc.* CCDC CCDC 1479047 for complex salt **2**, 1479048 for complex salt **1**, 1524682 for complex salt **4** and 1524683 for complex salt **3**. For ESI and crystallographic data in CIF or other electronic format see DOI: 10.1039/d1dt02722k

‡Prof. B. Biswas dedicates this work in the memory of his father Radhakanta Biswas who passed away on 4th April 2021.

CRYSTAL GROWTH & DESIGN

pubs.acs.org/crystal Article

Schottky Device Fabrication of Linear Dicarboxylato-Bridged Mn(II) and Co(II) Coordination Polymers: Experimental and Theoretical Insights

Published as part of Crystal Growth & Design special issue "Honoring Professor Jagadese J. Vittal and his Contributions to Functional Molecular Crystals."

Ersad Hossain, Ramjan Sk, Mainak Das, Partha Pratim Ray,* Antonio Frontera,* Mohammad Hedayetullah Mir,* and Subrata Mukhopadhyay

Cite This: *Cryst. Growth Des.* 2024, 24, 7597−7604 Read Online

ACCESS | Metrics & More | Article Recommendations | Supporting Information

ABSTRACT: In this study, we report the syntheses of two new coordination polymers (CPs) of Mn(II) and Co(II), $[Mn(4\text{-avp})_2(adc)(H_2O)]\cdot(solvent)_x$ (**1**) and $[Co(4\text{-avp})_2(adc)(CH_3OH)_2]$ (**2**), respectively, using relatively less explored linear linker acetylenedicarboxylic acid (H_2adc) and polyaromatic hydrocarbon (PAH)−based monodentate *N*-donor ligand 4-[2-(9-anthryl)-vinyl]pyridine (4-avp). CP**1** creates a two-dimensional (2D) structure in this instance, while CP**2** is made up of a 1D chain polymer. It is of interest that CP**1** and CP**2** exhibit semiconducting behavior and behave as Schottky barrier diodes. However, CP**1** exhibits higher conductivity and better Schottky diode formation when compared to CP**2**, which relates to the charge transportation through space via $\pi\cdots\pi$ interactions present in CP**1**. The experimental results are well validated by theoretical density functional theory (DFT) prediction based on band gap and density-of-state (DOS) calculations. It is noteworthy that fabrication of Mn/Co-based Schottky devices appears to be inadequate in the literature. Thus, this work showcases a new direction for the development of electronic device fabrication.

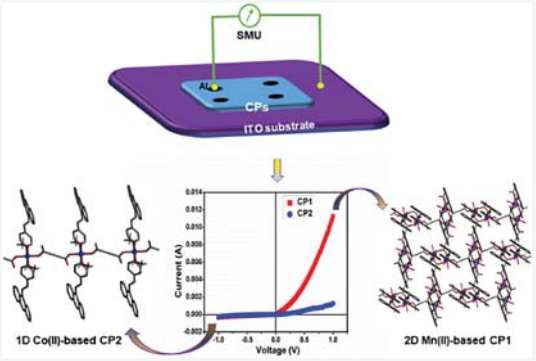

INTRODUCTION

The versatility of crystal structure and its wide range of applications in crystal engineering have led to a new path in the solid-state chemistry in recent years.[1−4] The underlying concept of crystal engineering revolves around the deliberate design and manipulation of the structure of crystalline materials at the atomic or molecular level to achieve desired properties.[5−10] The discipline relies on the fundamental understanding of intermolecular interactions, such as hydrogen bonding, halogen bonding, $\pi\cdots\pi$ stacking, C−H$\cdots\pi$ interactions, van der Waals forces, and coordination bonds, which govern the assembly of molecules into crystalline solids.[11−14] By strategically selecting building blocks and controlling their arrangements, crystal engineering aims to create materials with tailored functionalities. Key aspects of crystal engineering include the prediction and characterization of the crystal structures.

One prominent subset of crystal engineering is the study of coordination polymers (CPs), also known as metal−organic frameworks (MOFs). The CPs are inorganic−organic solid-state hybrid materials that are formed through the self-assembly of metal ions or clusters with organic ligands, resulting in extended networks with intriguing structural diversity and tunable properties.[15−17] CPs exhibit a wide range of characteristic features, including large surface area and diverse chemical functionalities spanning gas storage and separation, catalysis, drug delivery, sensing, light harvesting, ion exchange, and beyond.[18−23] Besides, the production of electronic and optoelectronic devices based on CPs is a quickly developing sector. However, the fabrication of CPs with good charge mobility and conductivity is one of the biggest hurdles. CPs typically do not offer an effective conjugation pathway for charge transport because of the combination of hard metal ions and redox-inactive organic ligands. However, new ideas have been developed in recent decades for the production of CPs with high electrical conductivity.[24−26] Different strategies have been adopted in

Received: June 14, 2024
Revised: August 20, 2024
Accepted: August 22, 2024
Published: August 31, 2024

Downloaded via JADAVPUR UNIV on February 24, 2025 at 13:07:44 (UTC).
See https://pubs.acs.org/sharingguidelines for options on how to legitimately share published articles.

ACS Publications © 2024 American Chemical Society

https://doi.org/10.1021/acs.cgd.4c00818
Cryst. Growth Des. 2024, 24, 7597−7604

Materials Today: Proceedings 102 (2024) 165–170

Contents lists available at ScienceDirect

Materials Today: Proceedings

journal homepage: www.elsevier.com/locate/matpr

Investigation of the metal–semiconductor interface by equivalent circuit model in zinc phthalocyanine (ZnPc) based Schottky diodes and its charge transport properties

Dhananjoy Das, Mainak Das, Puspendu Sahu, Partha Pratim Ray *

Department of Physics, Jadavpur University, Kolkata 700 032, India

ARTICLE INFO

Article history:
Available online 25 April 2023

Keywords:
Phthalocyanines
Semiconductors
Schottky diodes
Impedance spectroscopy
Conductivity
Mobility

ABSTRACT

In this report, the ZnPc-based metal–semiconductor (MS) junction Schottky devices (Al/ZnPc/ITO) were fabricated using an effusion cell coating unit. To study the formation of the MS junction, the surface morphology of the deposited ZnPc thin film was investigated using field-emission scanning electron microscope (FESEM) images. The interfacial properties of the MS junction of the Al/ZnPc/ITO configuration were studied using the ac impedance spectroscopy technique within the frequency range of 50 Hz–10 MHz at room temperature (300 K). The bias-dependent impedance spectroscopy was carried out within the voltage range of ±1 V to establish the equivalent circuit of the MS junction Schottky diodes (SDs). The current vs. voltage (I-V) measurements of the fabricated SDs were also conducted to deduce the diode parameters, namely on/off ratio, photosensitivity, ideality factor, barrier height, and series resistance. The charge transport parameters including dc conductivity, mobility and transit time of the charge carriers were also estimated employing the spatial-charge limited current (SCLC) theory, which illustrates the enhanced carrier's mobility and consequently, the device performance after light irradiation.
Copyright © 2023 Elsevier Ltd. All rights reserved.
Selection and peer-review under responsibility of the International Conference on Advances in Smart Materials, Chemical & Biochemical Engineering.

1. Introduction

In recent times, the use of organic semiconductors in optoelectronic devices has significantly increased to meet the growing demand for solar energy harvesting. Compared with their inorganic counterparts, organic materials have a low environmental impact and relatively low production costs with unlimited abundance. Among the variety of organic semiconductors, phthalocyanines (Pcs) manifest various excellent features such as non-toxicity, ease of processing, higher physical and thermal stability, and broadly visible light absorbance – which make them a promising candidate for numerous optoelectronic applications, namely, light-emitting diodes [1], solar cells [2], sensors [3]. Amidst many metal-phthalocyanines, the deep bluish-green colored zinc phthalocyanine (ZnPc) has been extensively studied as a promising material for its excellent photoconductive and photo-responsive properties [4].

However, the potential of the organic zinc phthalocyanine (ZnPc) for prospective optoelectronic device applications still has to be investigated by examining its electrical charge transport parameters and equivalent circuit model of the interfaces present. Understanding the Schottky barrier diodes would be an excellent start to assess the electronic conduction through the metal–organic semiconductor interfaces and subsequently, the performance of the device. In this work, an analysis is reported on the charge transport properties of the ZnPc-based Schottky devices, in which a thin layer of ZnPc was sandwiched between the aluminium (Al) and indium tin oxide (ITO) electrodes. The bias-dependent impedance spectroscopy of the Al/ZnPc/ITO configuration was studied to investigate different interfacial properties. The I-V measurement was also carried out under dark and light conditions to analyze the photo-responsive properties and charge transport mechanism within the MS junction ZnPc-based Schottky devices.

* Corresponding author.
E-mail addresses: parthapray@yahoo.com, parthap.ray@jadavpuruniversity.in (P. Pratim Ray).

https://doi.org/10.1016/j.matpr.2023.04.274
2214-7853/Copyright © 2023 Elsevier Ltd. All rights reserved.
Selection and peer-review under responsibility of the International Conference on Advances in Smart Materials, Chemical & Biochemical Engineering.

NATIONAL INSTITUTE OF TECHNOLOGY ROURKELA

(An Institution of National Importance)

CHEMSMART-22

Certificate of Participation

This is to Certify that the Paper titled

Hydrothermal synthesized copper sulfide (CuS) nanoparticles for fabrication of shottky diode and its photosensing applications

has been presented by the author(s)

MAINAK DAS

from

JADAVPUR UNIVERSITY

In one of the technical sessions of An International Conference on ADVANCES IN SMART MATERIALS, CHEMICAL & BIOCHEMICAL ENGINEERING (CHEMSMART-22) organized by the Department of **Chemical Engineering, NIT Rourkela,** during **December 16-18, 2022.**

Dr. Krunal Gangawane
Convener–CHEMSMART-22

Prof. Abanti Sahoo
Chairman –CHEMSMART-22

CHEMSMART-22

ICNOC-2022

International Conference
on
Nanotechnology: Opportunities & Challenges

CERTIFICATE OF PARTICIPATION

This is to certify that

Mainak Das

participated and presented a paper titled

One-pot Hydrothermal Synthesis of Copper Sulfide (CuS) Nanoparticles and Fabrication of Shottky Diode for Photosensing Applications

in the International Conference on Nanotechnology: Opportunities & Challenges (ICNOC-2022) in online mode, organized by Department of Applied Sciences & Humanities, Faculty of Engineering & Technology, Jamia Millia Islamia, New Delhi, India on November 28-30, 2022.

Prof. Zishan Husain Khan
Organizing Chair

Prof. Nafis Ahmad
Organizing Secretary

Dr. Mukesh Prartap Singh
Organizing Secretary

ICONN 2023

NAAC A++

Category 1 with 12B Status

(2022) Ranked 19th University

(2023) World Ranking one among 41 Indian Universities

(2023) World Ranking one among 75 Indian Universities

(2021) Ranked 4th

(2023) World Ranking one among 14 Indian Universities

SRM INSTITUTE OF SCIENCE & TECHNOLOGY (Deemed to be University u/s 3 of UGC Act, 1956)

SRM INSTITUTE OF SCIENCE AND TECHNOLOGY

Kattankulathur - 603 203, Tamil Nadu, India.

7th International Conference on Nanoscience and Nanotechnology (ICONN-2023)

(Virtual Conference) March 27 - 29, 2023

Certificate of Participation

This is to certify that Mr. / Ms. / Dr. **Mainak Das** has participated and presented a paper entitled **Improvement in device performance of copper sulfide (CuS) nanoparticles synthesized by hydrothermal method over the co-precipitation method** in the 7th International Conference on Nanoscience and Nanotechnology (ICONN-2023) organized by Department of Physics and Nanotechnology, SRM IST, India during March 27- 29, 2023, in association with Shizuoka University, Japan; National Yang Ming Chiao Tung University, Taiwan; GNS Science, New Zealand; University of Rome Tor Vergata, Italy; Asian Consortium on Computational Materials Science (ACCMS), Japan; Indian Ceramic Society; Indian Physics Association (IPA); Solar Energy Society of India (SESI); Innovation, Science & Technology Foundation - Tirupati (ISTF-T) and co-sponsored by Defence Research and Development Organization (DRDO), India; Council of Scientific & Industrial Research (CSIR), India; The Indian Science Congress Association (ISCA) and Springer Nature.

Head
Department of Physics and Nanotechnology
SRM IST, KTR

Chairperson
School of Applied Sciences
SRM IST, KTR

Shizuoka University Japan | NYCU, Taiwan | GNS Newzealand | University of Rome Tor Vergata, Italy | Solar Energy Society of India | ACCMS | Indian Ceramic Society | Indian Physics Association | DRDO | CSIR | SPRINGER NATURE

1331

A one-day seminar in

"COMMEMORATION OF CENTENARY BIRTH ANNIVERSARY OF PROF. SHYAMAL SENGUPTA"

Condensed Matter Physics Research Centre
Estd. 1990

Organised by

Condensed Matter Physics Research Centre & Department of Physics, Jadavpur University

CERTIFICATE OF PARTICIPATION

This certificate has been awarded to ***Mainak Das*** *of Dept. Of Physics, Jadavpur University in appreciation of his oral presentation titled* ***Development of copper sulfide-carbon nanotube (CuS-CNT) composites and utilization of its superior carrier mobility in efficient charge transport towards photodegradation of Rhodamine B under visible light*** *at the one day seminar in "Commemoration Of Centenary Birth Anniversary Of Prof. Shyamal Sengupta" held at Jadavpur University, Kolkata, India on 7th February 2024.*

07.02.2024

H.O.D. Dept. Of Physics, JU

7/02/2024

Co-Ordinator CMPRC, JU

68th DAE Solid State Physics Symposium

Organised by: Bhabha Atomic Research Centre, Mumbai

Sponsored by: Board of Research in Nuclear Sciences (BRNS)

Department of Atomic Energy, Government of India

CERTIFICATE

of Participation

Mainak Das

JU Kolkata

has presented a paper and participated in this symposium, held at Bhabha Atomic Research Centre, Mumbai

during 18- 22 December 2024

L. M. Pant
Convener
DAE SSPS 2024

Jitendra Bahadur
Scientific secretary
DAE SSPS 2024

Himal Bhatt
Scientific secretary
DAE SSPS 2024

RegNo: i0002

Dated: 22 Dec 2024

1ST DFT-M ONLINE HANDS-ON-TRAINING ON

DENSITY FUNCTIONAL THEORY MODELLING OF MATERIALS

(NANOPARTICLES, THIN FILMS, UNIT CELLS USING QUANTUM ESPRESSO)

Centre for Advanced Computational Studies, New Delhi, India

(Registered under Ministry of SME, Government of India for Research and Experimental Development on Natural Sciences and Engineering)
(ISO 9001:2015 Certification for Hands-on-Training on Computational Science including DFT calculation of Materials, Molecular Docking and Dynamics)
DATE: 14TH SEPTEMBER – 20TH SEPTEMBER 2023
Website: https://aimsdelhi.com, Email: admin@aimsdelhi.com

Certificate of Participation

This is to certify that

Mainak Das, Research Scholar, Jadavpur University, West Bengal

has actively participated in the **1st Workshop on Density Functional Theory Modelling of Materials (DFT-M)** organized by the Centre for Advanced Computational Studies, Delhi from **14th – 20th September 2023** via Online Mode.

Hands-on-Training program included 7 Interactive Sessions by DR. **NIKHIL AGGARWAL** on Density Functional Theory Modelling of Materials at Nanoscale using Quantum Espresso and Burai Software applications.

Dr. Nikhil Aggarwal
Head of the Department & Convener

Certificate No.: 2023/DFT-M/W/1/94

1ST ONLINE HANDS-ON-TRAINING ON

RIETVELD REFINEMENT OF X-RAY DIFFRACTION (RRD)

(USING FULLPROF SOFTWARE PACKAGE)

Centre for Advanced Computational Studies, New Delhi, India

(Registered under Ministry of SME, Government of India for Research and Experimental Development on Natural Sciences and Engineering)
(**ISO 9001:2015** Certification for Hands-on-Training on Computational Science including DFT calculation of Materials, Molecular Docking and Dynamics)
Website: https://aimsdelhi.com, Email: admin@aimsdelhi.com

Certificate of Participation

This is to certify that

MAINAK DAS, Research Scholar, Jadavpur University, West Bengal

has actively participated in the **1st Hands-on-Training on Rietveld Refinement of X-Ray Diffraction data (RRD)** organized by the Centre for Advanced Computational Studies, Delhi from **1st – 7th January 2024** via Online Mode. Training program had 7 Interactive Sessions by DR. **NIKHIL AGGARWAL** on Rietveld Refinement of X-Ray Diffraction data using **FullProf** Software Package.

Dr. Nikhil Aggarwal
Head of the Department & Convener

ISO Accreditation Body: United Ackreditering Services Limited, United Kingdom

Certificate No.: 2023/RRD/W/1/134